

**INVESTIGATION OF PHYSICO-CHEMICAL PROPERTIES
OF FAST REACTOR METALLIC FUELS**

By

SANTU KAITY

CHEM01201604002

Bhabha Atomic Research Centre, Mumbai

A thesis submitted to the

Board of Studies in Chemical Sciences

In partial fulfillment of requirements

for the Degree of

DOCTOR OF PHILOSOPHY

of

HOMI BHABHA NATIONAL INSTITUTE

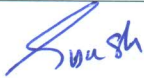
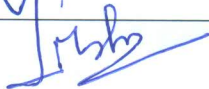


March, 2021

Homi Bhabha National Institute

Recommendations of the Viva Voce Committee

As members of the Viva Voce Committee, we certify that we have read the dissertation prepared by **Mr. Santu Kaity** entitled "**Investigation of physico-chemical properties of fast reactor metallic fuels**" and recommend that it may be accepted as fulfilling the thesis requirement for the award of Degree of Doctor of Philosophy.

Chairman - Prof. Smruti Dash		Date: 04/06/2021
Guide / Convener - Prof. S.C. Parida		Date: 04/06/2021
Examiner - Prof. C.K. Behera		Date: 04-06-2021
Member 1 - Prof. Ratikant Mishra		Date: 4/6/2021
Member 2 - Prof. S.K. Ghosh		Date: 4/6/2021
Member 3 - Prof. Vinita G. Gupta		Date: 04/06/2021
Technology Advisor - Dr. Sudhir Mishra		Date: 4/06/2021

Final approval and acceptance of this thesis is contingent upon the candidate's submission of the final copies of the thesis to HBNI.

I/We hereby certify that I/we have read this thesis prepared under my/our direction and recommend that it may be accepted as fulfilling the thesis requirement.

Date: 04/06/2021

Place: Mumbai



Signature

Guide

डॉ. एस. सी. परिडा / Dr. S. C. PARIDA

अध्यक्ष, उत्पाद विकास प्रभाग / Head, Product Development Division

भारत सरकार / Government of India

भाभा परमाणु अनुसंधान केंद्र / Bhabha Atomic Research Centre

ट्रॉम्बे, मुंबई - 400065, Trombay, Mumbai - 400 085.

STATEMENT BY AUTHOR

This dissertation has been submitted in partial fulfillment of requirements for an advanced degree at Homi Bhabha National Institute (HBNI) and is deposited in the Library to be made available to borrowers under rules of the HBNI.

Brief quotations from this dissertation are allowable without special permission, provided that accurate acknowledgement of source is made. Requests for permission for extended quotation from or reproduction of this manuscript in whole or in part may be granted by the Competent Authority of HBNI when in his or her judgment the proposed use of the material is in the interests of scholarship. In all other instances, however, permission must be obtained from the author.

Santu Kaity
Santu Kaity

DECLARATION

I, hereby declare that the investigation presented in the thesis has been carried out by me. The work is original and has not been submitted earlier as a whole or in part for a degree / diploma at this or any other Institution / University.

Santu Kaity
Santu Kaity

List of Publications arising from the thesis

Journals

1. "Structural, microstructural and thermal analysis of U-(6-x)Zr-xNb alloys (x = 0, 2, 4, 6)", **S. Kaity**, J. Banerjee, S.C. Parida, V. Bhasin, J. Nucl. Mater. 504 (2018) 234-250.
2. "Studies on fuel-cladding chemical interaction between U-10wt%Zr alloy and T91 steel", **S. Kaity**, J. Banerjee, S.C. Parida, A. Laik, C.B. Basak, V. Bhasin, J. Nucl. Mater. 513 (2019) 16-32.
3. "Structural, microstructural and thermal analysis of U-(6-x)Zr-xMo alloys (x = 0, 2, 4, 6)", **S. Kaity**, J. Banerjee, S.C. Parida, P.G. Behere, V. Bhasin, J. Nucl. Mater. 532 (2020) 152046.
4. "Molar heat capacity of uranium-rich U-Zr-Nb and U-Zr-Mo alloys", **S. Kaity**, J. Banerjee, S.C. Parida, P.G. Behere, V. Bhasin, J. Nucl. Mater. 541 (2020) 152427.

Conferences

1. "Microstructural investigation of U-Zr-Nb alloy by SEM", **S. Kaity**, K. Bhandari, J. Banerjee, S.C. Parida, K.B. Khan, Proceedings of International Conference on Electron Microscopy & XXXVIII Annual Meeting of EMSI (EMSI-2017), July 17-19, 2017, IGCAR, Kalpakkam, India, pp. 204-206.

2. "Thermal analysis of U-6Zr alloy", **S. Kaity**, S.K. Swarnkar, J. Banerjee, S.C. Parida, Proceedings of the 21st DAE-BRNS Symposium on Thermal Analysis (THERMANS-2018), Jan 18-20, 2018, Goa University, Goa, India, p 146.
3. "Thermal analysis of U-rich U-Zr-Mo alloys", **S. Kaity**, J. Banerjee, S.C. Parida, V. Bhasin, Proceedings of the 22nd DAE-BRNS Symposium on Thermal Analysis (THERMANS-2020), Jan 30-Feb 01, 2020, BARC, Mumbai, India, pp. 120-122.

Santu Kaity
Santu Kaity

**Dedicated to
God**

ACKNOWLEDGEMENTS

First and foremost, I wish to express my sincere gratitude and heartfelt thanks to my supervisor, **Prof. S.C. Parida**, for his invaluable guidance, suggestions and continuous encouragement during the progress of my research work.

I express my deep sense of gratitude to **Shri Vivek Bhasin** (Director, NFG), **Shri P.G. Behere** (Head, RMD), **Dr. T.R.G. Kutty**, (Ex-Head, FPES, RMD), **Dr. Joydipta Banerjee** (Head, FPES, RMD), **Dr. Sudhir Mishra** (Head, FD&MS, RMD) for their valuable suggestions and encouragement during the entire course of the work. I would also like to thank members of the doctoral committee: **Dr. (Smt.) Smruti Dash**, **Dr. Ratikant Mishra**, **Dr. S.K. Ghosh** and **Dr. (Smt.) Vinita G. Gupta** for spending their valuable time and offering their valuable suggestions and comments during the progress of my research work.

I wish to express my special thanks to **Dr. C.B. Basak**, **Dr. Arijit Laik**, **Shri M.T. Saify**, **Shri Buddhadeb Kanrar**, **Shri Suraj Kumar** for their help and support during the course of the research work. I would like to thank **Shri M.S. Nawge**, **Shri D.A. Kamble** and **Shri S.K. Swarnkar** for extending their helping hand in numerous ways. I owe many thanks to **Shri S. Moorthy** for helping me to carry out quartz encapsulations of various samples. I would also like to thank **Dr. Pradeep Samui**, **Dr. C. Nandi**, **Shri Koushik Bhandari**, **Shri R. Rakesh** for their help and support. I would like to extend special thanks to all my fellow members of Radiometallurgy Division and Nuclear Fuels Group for their assistance and support.

At last but not the least, I thank my **parents**, **parent-in-laws**, **brothers**, **sisters** and my all **family members**, **relatives**, **teachers and friends** for their encouragement and support. I am grateful to my wife **Tanusri** and my daughter **Anishka** for their consistent support throughout my research work.

Santu Kaity
Santu Kaity

CONTENTS

	Page No.
Summary	I-II
List of Figures	III-X
List of Tables	XI-XII
Chapter 1 Introduction	1-29
1.1. Nuclear power programme in India	1
1.2. Background and history of metallic fuel in fast reactor	3
1.3. Various aspects of metallic fuel	6
1.4. Alloying element(s) in metallic fuel	9
1.5. Alloy characteristics, phase stability & literature information	12
1.5.1. Uranium metal	12
1.5.2. Uranium alloyed with Zr and Nb metals	12
1.5.2.1. The Uranium-Zirconium system	12
1.5.2.2. The Uranium-Niobium system	14
1.5.2.3. The Uranium-Zirconium–Niobium system	15
1.5.3. Uranium alloyed with Zr and Mo metals	18
1.5.3.1. The Uranium-Molybdenum system	18
1.5.3.2. The Uranium-Zirconium–Molybdenum system	19
1.6. Thermophysical properties of nuclear fuel	22
1.7. Cladding material for metallic fuelled fast reactor	24
1.8. Fuel-cladding chemical interaction	26
1.9. Research goals and objectives of the present work	28
Chapter 2 Experimental Techniques	30-47
2.1. Introduction	30

2.2.	Alloy sample preparation	30
2.2.1.	Alloy melting	30
2.2.2.	Heat treatment	31
2.2.3.	Impurity Analysis	32
2.3.	Characterization techniques	32
2.3.1	X-ray Diffraction (XRD)	32
2.3.2.	Metallographic practice	34
2.3.3.	Scanning Electron Microscopy (SEM) & Energy Dispersive Spectroscopy (EDS)	35
2.4.	Thermal analysis and thermo-physical properties measurement	36
2.4.1.	Differential thermal analysis (DTA)	36
2.4.2.	Differential scanning calorimetry (DSC)	38
2.4.3.	Heat capacity	40
2.4.3.1.	Molar heat capacity measurement using DSC	41
2.4.4.	Thermal expansion	42
2.4.4.1.	Bulk thermal expansion using dilatometry	44
2.5.	Microhardness measurement	45
2.6.	Fuel-cladding chemical compatibility test	45
2.6.1.	Differential thermal analysis (DTA)	46
2.6.2.	Diffusion couple experiment	46
Chapter 3	Structural, microstructural characterization and thermal properties of U-(6-x)Zr-xNb alloys (x = 0, 2, 4, 6 wt%)	48-89
3.1.	Introduction	48
3.2.	Experimental procedure	48
3.3.	Terminology and notations for various phases	48

3.4.	Results	49
3.4.1.	Structural Characterization	49
3.4.1.1.	Furnace-cooled samples	49
3.4.1.2.	Water-quenched samples	53
3.4.2.	Microstructural characterization	56
3.4.2.1.	Furnace-cooled samples	56
3.4.2.2.	Water-quenched samples	58
3.4.3.	Differential thermal analysis	60
3.4.3.1.	Furnace-cooled sample	60
3.4.3.2.	Water-quenched sample	63
3.4.4.	Dilatometry	65
3.4.5.	Molar heat capacity	67
3.4.6.	Microhardness	69
3.5.	Discussion	70
3.6.	Summary and Conclusions	88
Chapter 4	Structural, microstructural characterization and thermal properties of U-(6-x)Zr-xMo alloys (x = 0, 2, 4, 6 wt%)	90-122
4.1.	Introduction	90
4.2.	Experimental procedure	90
4.3.	Results	90
4.3.1.	Structural Characterization	90
4.3.1.1.	Furnace-cooled samples	90
4.3.1.2.	Water-quenched samples	91
4.3.2.	Microstructural characterization	97
4.3.2.1.	Furnace-cooled samples	97

4.3.2.2. Water-quenched samples	99
4.3.3. Differential thermal analysis	101
4.3.3.1. Furnace-cooled sample	101
4.3.3.2. Water-quenched sample	103
4.3.4. Dilatometry	104
4.3.5. Molar heat capacity	105
4.3.6. Microhardness	108
4.4. Discussion	108
4.5. Summary and conclusions	121
Chapter 5 Phase stability of U-(6-x)Zr-xNb & U-(6-x)Zr-xMo alloys under near-equilibrium condition (x = 0, 2, 4, 6 wt%)	123-144
5.1. Introduction	123
5.2. Experimental procedure	123
5.3. Results	124
5.3.1. U-Zr-Nb alloys (Zr+Nb = 6 wt%)	124
5.3.1.1 Structural Characterization	124
5.3.1.2. Microstructure	126
5.3.1.3. Differential thermal analysis	129
5.3.2. U-Zr-Mo alloys (Zr+Mo = 6 wt%)	131
5.3.2.1 Structural Characterization	131
5.3.2.2. Microstructure	132
5.3.1.3. Differential thermal analysis	134
5.4. Discussion	136
5.5. Summary and conclusions	144
Chapter 6 Fuel-cladding chemical interaction (FCCI) between U-Zr	145-178

	alloy and T91 steel cladding	
6.1.	Introduction	145
6.2.	Experimental procedure	145
6.3.	Results	146
6.3.1.	Structural & microstructural characterization of U–10Zr	146
6.3.2.	Chemical interaction by differential thermal analysis	148
6.3.3.	Diffusion couple experiment	153
6.3.3.1.	Interfacial reaction in U–10Zr/T91 at 823 K	153
6.3.3.2.	Interfacial reaction in U–10Zr/T91 at 923 K	156
6.3.3.3.	Interfacial reaction in U–10Zr/T91 at 973 K	160
6.3.3.4.	Interfacial reaction in U–10Zr/T91 at 1003 K	161
6.4.	Discussion	164
6.4.1.	Differential thermal analysis	164
6.4.2.	Interfacial reactions in U–10Zr/T91 couples	169
6.4.2.1.	Kinetics of the interfacial reaction	173
6.4.3.	Interfacial reactions in U–6Zr/T91 couples	175
6.5.	Summary and conclusions	177
Chapter 7	Summary, Conclusions and Future Scope	179-185
References		186-198

LIST OF FIGURES

Fig. 1.1:	Cross-sections of conceptual fuel pin design for metallic fuels; (a) U–Pu–Zr ternary and (b) U–Pu binary alloy (not to scale)	9
Fig. 1.2	Phase diagram of U–Zr system	13
Fig. 1.3	Phase diagram of U–Nb system	15
Fig. 1.4	Isothermal section of U–Zr–Nb phase diagram at 894 K	16
Fig. 1.5	Phase diagram of U–Mo system	19
Fig 1.6	Ternary Equilibrium phase diagrams of U–Zr–Mo at (a) 923 K and (b) 1273 K	20
Fig. 2.1	Schematic representation of DTA	38
Fig. 2.2	Schematic representation of heat flux DSC	39
Fig. 2.3	Schematic diagram of the diffusion couple-fixture assembly for U–Zr/T91 couples.	47
Fig. 3.1	X-ray diffraction patterns of furnace-cooled alloy samples.	51
Fig. 3.2	Magnified XRD data of furnace-cooled U–6Zr alloy showing low intensity (111) and (112) peaks of δ -UZr ₂ phase	51
Fig. 3.3	Rietveld refinement of XRD data of furnace-cooled (a) U–6Zr alloy showing experimental (blue dots), calculated (black line) and difference pattern (bottom line) along with the peak positions of α -U & δ -UZr ₂ phases, and (b) U–2Zr–4Nb alloy showing experimental (blue dots), calculated (black line) and difference pattern (bottom line) along with peak positions of α & γ_3 phases.	52
Fig. 3.4	X-ray diffraction patterns of water-quenched alloy samples	54
Fig. 3.5	Rietveld refinement of XRD data of water-quenched (a) U–6Zr alloy	55

showing experimental (blue dots), calculated (black line) and difference pattern (bottom line) along with the peak positions of orthorhombic α' phase, (b) U-6Nb alloy showing experimental (blue dots), calculated (black line) and difference pattern (bottom line) along with the peak positions of monoclinic α'' phase.

- Fig. 3.6** (a & b) SEM micrographs & Intensity profiles of U-M α , Zr-L α X- 57
ray lines on the lamellar structure of furnace-cooled U-6Zr alloy; (c,
d & e) SEM micrographs of furnace-cooled U-4Zr-2Nb,
U-2Zr-4Nb and U-6Nb alloys, respectively; (f) Magnified
micrograph of U-2Zr-4Nb alloy showing very fine lamellar.
- Fig. 3.7** SEM micrographs at different magnification for water-quenched 59
alloy samples, (a & b) U-6Zr, (c & d) U-4Zr-2Nb, (e & f) U-6Nb
showing martensitic structures.
- Fig. 3.8** (a & b) DTA curves of furnace-cooled alloy samples during heating 62
and cooling cycles, respectively at scanning rate of 10 K min⁻¹, (c)
DTA curves of repeat runs at scanning rate of 5 K min⁻¹, (d)
Magnified view of DTA peak of U-6Nb alloy at 1 K min⁻¹.
- Fig. 3.9** (a) DTA curves of water-quenched alloy samples during heating 64
cycle at scanning rate of 10 K min⁻¹, (b) DTA curves of repeat run at
scanning rate of 5 K min⁻¹.
- Fig. 3.10** (a) Thermal expansion curves of alloy samples, (b & c) Expansion 66
curves of U-6Zr alloy at different heating rates, the first derivative
plots of the expansion curves are shown in inset.
- Fig. 3.11** Measured molar heat capacity data of U-6Zr, U-2Zr-4Nb and 69

U–6Nb alloys.

- Fig. 3.12** (a) SEM micrograph of equilibrium cooled U–6Zr sample showing δ -phase and α -matrix, (b & c) Typical EDS spectra of δ -phase (dark phase) and α -matrix (bright phase), respectively, showing the elemental composition; (c) DTA curves of step-cooled U–6Zr sample during heating cycle at scanning rate of 5 K min⁻¹. 73
- Fig. 3.13** Molar heat capacity data of various U-rich U–Zr alloys of similar compositions as a function of temperature for comparison with the present data of U–6Zr alloy. 84
- Fig. 3.14** The experimental and calculated molar heat capacities of U–6Zr, U–2Zr–4Nb and U–6Nb alloys along with the reported molar heat capacities of pure constituent elements (i.e., U, Zr and Nb) are plotted collectively as a function of temperature. 84
- Fig. 4.1** (a) X-ray diffraction patterns of furnace-cooled alloy samples, (b) Magnified XRD data of U–6Mo alloy showing low intensity peaks of orthorhombic α U phase along with bcc γ -phase. 93
- Fig. 4.2** Rietveld refinement of XRD data of furnace-cooled (a) U–4Zr–2Mo alloy showing experimental (blue dots), calculated (black line) and difference pattern (bottom line) along with the peak positions of α -U & γ phases, and (b) U–2Zr–4Mo alloy showing experimental (blue dots), calculated (black line) and difference pattern (bottom line) along with the peak positions of α & γ phases. 94
- Fig. 4.3** (a) X-ray diffraction patterns of water-quenched alloy samples, and (b) Magnified XRD data of U–6Mo alloy showing (110) peak of bcc 95

γ -phase.

- Fig. 4.4** Rietveld refinement of XRD data of water-quenched (a) U-4Zr-2Mo 96 alloy showing experimental (blue dots), calculated (black line) and difference pattern (bottom line) along with the peak positions of orthorhombic α' phase, (b) U-2Zr-4Mo alloy showing experimental (blue dots), calculated (black line) and difference pattern (bottom line) along with the peak positions of monoclinic α'' phase.
- Fig. 4.5** (a & b) SEM images & intensity profiles of U-M α , Zr-L α X-ray 98 lines on the lamellar structure of furnace-cooled U-6Zr alloy; (c, d & e) SEM images & U-M α , Zr-L α , Mo-L α X-ray lines scan on the furnace-cooled U-4Zr-2Nb alloy; (f & g) Micrographs of U-2Zr-4Mo at various magnifications showing fine lamellar structure; (h & i) SEM images of U-6Mo alloys showing partial decomposition of γ -phase and magnified view of the decomposition product.
- Fig. 4.6** SEM micrographs at different magnification for water-quenched 100 alloys, (a & b) U-6Zr, (c & d) U-4Zr-2Mo, (e) U-2Zr-4Mo and (f) U-6Mo alloys.
- Fig. 4.7** (a & b) DTA curves of furnace-cooled alloys in heating and cooling 102 cycles, respectively, at scanning rate of 10 K min⁻¹, (c) DTA curves of repeat runs at scanning rate of 5 K min⁻¹.
- Fig. 4.8** (a) DTA curves of water-quenched alloy samples during heating 103 cycle at scanning rate of 10 K min⁻¹, (b) DTA curves of repeat run at scanning rate of 5 K min⁻¹.

- Fig. 4.9** (a) Thermal expansion curves of alloy samples, (b) Thermal expansion curves of the first run and repeat run of U-6Mo alloy. 106
- Fig. 4.10** Measured molar heat capacity data of U-6Zr, U-4Zr-2Mo and U-2Zr-4Mo alloys. 107
- Fig. 4.11** A comparison among molar heat capacity data of present U-Zr-Mo alloys with that of U-Mo alloys reported in the literature. 117
- Fig. 4.12** The experimental and calculated molar heat capacities of U-6Zr, U-2Zr-4Mo and U-4Zr-2Mo alloys along with the reported molar heat capacities of pure constituent elements (i.e., U, Zr and Mo) are plotted collectively as a function of temperature. 118
- Fig. 5.1** XRD patterns of step-cooled U-6Zr, U-4Zr-2Nb, U-2Zr-4Nb and U-6Nb alloys. 125
- Fig. 5.2** Magnified XRD data of step-cooled U-6Zr alloy showing few non overlapping low intensity peaks of δ -UZr₂ phase. 125
- Fig. 5.3** SEM micrographs of step-cooled alloys at different magnifications (a & b) U-6Zr alloy showing α -U and δ -UZr₂ phases; (c & f) U-4Zr-2Nb, (d & g) U-2Zr-4Mo, (e & h) U-6Nb alloy showing alternative layers of α -U and γ -phases. 127
- Fig. 5.4** (a) Electron forescatter image of U-4Zr-2Nb alloy; (b) experimental EBSD pattern on the phase as indicated by arrow; (c) indexed EBSD pattern on b correspond to solute-rich bcc γ -phase (Im-3m); (d) EDS spectrum on that phase showing their chemical composition. 129
- Fig. 5.5** (a) DTA curves of step-cooled of U-6Zr, U-4Zr-2Nb, U-2Zr-4Nb and U-6Nb alloys during heating, and (b) DTA curves of repeat runs 130

at scanning rate of 5 K min⁻¹

- Fig. 5.6** XRD patterns of step-cooled U-6Zr, U-4Zr-2Mo, U-2Zr-4Mo and U-6Mo alloys. 131
- Fig. 5.7** SEM micrographs of step-cooled alloys at different magnifications (a & b) U-6Zr alloy showing α -U and δ -UZr₂ phases; (c & f) U-4Zr-2Nb, (d & g) U-2Zr-4Mo, (e & h) U-6Nb alloy showing formation of various phases. 133
- Fig. 5.8** (a) DTA curves of step-cooled U-6Zr, U-4Zr-2Mo, U-2Zr-4Mo and U-6Mo alloys samples during heating at scanning rate of 5 K min⁻¹, (b) DTA curves of repeat runs at scanning rate of 5 K min⁻¹. 135
- Fig. 5.9** The vertical sections of ternary U-Zr-Nb diagram at (a) 4 wt% Zr and (b) 2 wt% Zr as reported by Dwight and Mueller. The composition of U-4Zr-2Nb and U-2Zr-4Nb are shown by lines. The (Zr+Nb)-rich bcc γ phases in U-Zr-Nb alloys is represented by γ_3 . 139
- Fig. 5.10** Isothermal section of ternary U-Zr-Mo phase diagrams at (a) 773 K, (b) 848 K, (c) 923 K and (d) 973 K. The compositions of U-Mo-Zr alloys in this study are marked by dots. 141
- Fig. 6.1** XRD pattern of U-10Zr alloy showing peaks of orthorhombic α -U phase. 147
- Fig. 6.2** (a) SEM micrograph of U-10Zr alloy, (b) A representative EDS spectrum showing chemical composition. 147
- Fig. 6.3** DTA thermograms of U metal, T91 steel, U-10Zr alloy. 148
- Fig. 6.4** DTA curves of (a & b) U+T91 composite, and (c & d) U-10Zr+T91 composite in both heating and cooling cycles at a scanning rate of 10 150

K min⁻¹.

- Fig. 6.5** Microstructures of reaction products of (a & b) U+T91, and (c & d) U-10Zr+T91 composites at different magnifications showing different phases (i.e., bright, grey and dark). 151
- Fig. 6.6** (a-b) Electron foreshatter images of U+T91 reaction products after DTA run; (c-d) experimental EBSD patterns of phases as indicated by arrows; (e-f) indexed EBSD patterns on c and d correspond to UFe₂ (Fd-3m) and U₆Fe (I4/mcm) phases, respectively; (g-h) EDS spectra of respective phases showing their chemical composition. 154
- Fig. 6.7** (a-b) Electron foreshatter images of U-10Zr+T91 reaction product; (c-e) experimental EBSD patterns of various phases as indicated by arrows; (f-h) indexed EBSD patterns on c, d and e correspond to Zr(Fe,Cr)₂ (P6₃/mmc), UFe₂ (Fd-3m) and U₆Fe (I4/mcm) phases, respectively; (i-K) EDS spectra of respective phases showing their chemical composition. 155
- Fig. 6.8** (a & b) SEM micrographs of U-10Zr/T91 couple at 823 K for 1500 h, (c) intensity profiles of U-Mα, Zr-Lα, Fe-Kα and Cr-Kα X-ray lines along line AB marked in Fig. 6.8b 156
- Fig. 6.9** Fig. 6.9 (a & b) SEM image of U-10Zr/T91 couple at 923 K for 1000 h, (c & d) intensity profiles of U-Mα, Zr-Lα, Fe-Kα and Cr-Kα X-ray lines along line CD and EF in Fig. 6.9a and Fig. 6.9b, respectively. 158
- Fig. 6.10** (a) The electron foreshatter image of the diffusion couple annealed at 923 K for 1000 h; (b-d) the experimental EBSD patterns of different layers as indicated by arrows; (e-g) the indexed EBSD patterns on b, c and d correspond to Zr (P6₃/mmc), UFe₂-type phase 159

(Fd-3m) and Fe (Im-3m), respectively.

- Fig. 6.11** (a & b) SEM images of U-10Zr/T91 diffusion couple annealed at 973 K for 500 h, (c) intensity profiles of U-M α , Zr-L α , Fe-K α and Cr-K α X-ray lines along the line GH marked in Fig. 6.11b. 160
- Fig. 6.12** (a & b) SEM images of U-10Zr/T91 couple annealed at 1003 K for 200 h, showing the interface with stable Zr-rich layer, (c) intensity profiles of U-M α , Zr-L α , Fe-K α and Cr-K α X-ray lines along the line IJ marked in Fig. 6.12b. 162
- Fig. 6.13** (a) SEM images of U-10Zr/T91 diffusion couple at 1003 K for 200 h, showing the interface with broken Zr-rich layer, (b) magnified image marked with different reaction layers, (c) X-ray line profiles of U, Zr, Fe and Cr along the line KL marked in Fig. 6.13b. 163
- Fig. 6.14** Phase diagram of U-Fe system 164
- Fig. 6.15** Plot of w^2/t versus $1/T$ for the combined width of UFe₂-type and Zr-rich reaction layers. 175
- Fig. 6.16** (a & b) SEM image of U-6Zr/T91 diffusion couple at 973 K for 500 h, (c) intensity profiles of U-M α , Zr-L α , Fe-K α and Cr-K α X-ray lines along the line MN marked in Fig. 6.16b. 176
- Fig.6.17** (a) Microstructure of U-6Zr/T91 diffusion couple annealed at 1023 K for 100 h showing almost complete meltdown of couple, (b) Magnified micrograph showing the formation of U₆Fe, U(Fe,Cr)₂ and Zr(Fe,Cr)₂ phases. 177

LIST OF TABLES

Table 1.1	The various metallic fuelled fast reactors with their fuel compositions operated earlier.	5
Table 1.2	Intercomparison of important properties of mixed uranium plutonium oxide (MOX), carbide (MC), nitride (MN) and metallic fuels for fast reactor.	7
Table 1.3	Crystallographic data of various phases in the U–Zr system	14
Table 1.4	Crystallographic data of different phases in the U–Nb system	15
Table 1.5	Crystallographic data of various phases in the U–Mo system	19
Table 1.6	Chemical composition of T91 cladding steel (wt %)	25
Table 2.1	Impurities content (C, O, N) in the alloy samples	32
Table 3.1	Lattice parameter, phase fraction of different phases formed in furnace-cooled samples	53
Table 3.2	Lattice parameter of phases formed in water-quenched alloy samples	56
Table 3.3	Chemical composition of water-quenched alloys by EDS	60
Table 3.4	Experimental molar heat capacity data of U–6Zr, U–2Zr–4Nb and U–6Nb alloys	68
Table 3.5	Microhardness data of different U–Zr–Nb alloy samples	70
Table 3.6	Thermodynamic functions for U–6Zr alloy.	85
Table 3.7	Thermodynamic functions for U–2Zr–4Nb alloy.	85
Table 3.8	Thermodynamic functions for U–6Nb alloy	86
Table 3.9	Reported data of thermodynamic functions for uranium metal	86
Table 4.1	Lattice parameter, phase fraction of different phases formed in furnace-cooled samples	93

Table 4.2	Lattice parameter of phases formed in water-quenched alloys	95
Table 4.3	EDS results of chemical composition of water-quenched alloys	99
Table 4.4	Experimental molar heat capacity data of U-4Zr-2Mo and U-2Zr-4Mo alloys	107
Table 4.5	Microhardness data of different U-Zr-Mo alloy samples	108
Table 4.6	Thermodynamic functions for U-4Zr-2Mo alloy	119
Table 4.7	Thermodynamic functions for U-2Zr-4Mo alloy.	119
Table 5.1	Lattice parameter, phase fraction of phases formed in step-cooled U-6Zr, U-4Zr-2Nb, U-2Zr-4Nb and U-6Nb alloys under near-equilibrium condition.	126
Table 5.2	Elemental compositions of various phases formed in different alloys	128
Table 5.3	Lattice parameter, phase fraction of phases formed in step-cooled U-6Zr, U-4Zr-2Mo, U-2Zr-4Mo and U-6Mo alloys.	132
Table 5.4	Elemental compositions of various phases formed in different alloys.	134
Table 6.1	Annealing temperature & time of the diffusion couple experiments	146
Table 6.2	DTA peaks for various phase transitions of U, U-10Zr and T91 during heating	149
Table 6.3	Phase transformation sequences of U+T91 and U-10Zr+T91 composites samples	168

Chapter 7

Summary, Conclusions and Future Scope

The present study is a part of metallic fuel development programme for future fast breeder reactor in India. The out-of-pile properties data of metallic fuels are scanty and therefore, there is a need to augment the database on those properties. Most of the work reported on metallic fuels was carried out with 10wt%Zr addition in the uranium metal. Moreover, the present composition of alloy containing 6wt%Zr is new without much international experience. Hence, the present study has generated a database on phase stability, phase transformation, microstructure, thermophysical properties, fuel-cladding chemical compatibility of U-6wt%Zr alloys which are very useful to the fuel-designer to optimize various design features and to predict in-reactor fuel performance. The alloying elements Nb and Mo were also combined with U-Zr alloy to obtain metallic fuels of U-Zr-Nb and U-Zr-Mo alloys which are expected to have better thermal properties. In this thesis, the potential metallic fuel systems, namely, binary U-Zr, U-Nb, U-Mo and ternary U-Zr-Nb, U-Zr-Mo alloys with total alloying content limiting to 6wt% have been investigated extensively for their phase stability, microstructure evolution, phase transformation and thermal properties. The major findings of this thesis are summarized in the following section.

1. Investigation on the phase stability of various heat treated U-(6-x)Zr-xNb and U-(6-x)Zr-xMo alloys ($x = 0, 2, 4, 6$ wt%) revealed significant variation on their microstructures, crystal structures, lattice parameters, phase fractions depending on heat treatment conditions and alloy compositions. The furnace-cooled U-6Zr alloy consists of complete lamellar structure with partitioning of Zr in the alternative layers which originates from the invariant monotectoid, eutectoid type of reactions. The XRD analysis revealed formation of α -phase along with small fraction of δ -UZr₂ phase. The replacement of Zr in U-6Zr alloy with Nb leads to formation of fine lamellar structure of

α -phase and γ -phase with partitioning of solute elements. The α -phases are considered as supersaturated with alloying constituent(s) and the γ -phases are rich in solute content. The replacement of Zr with Mo also leads to formation of similar type of lamellar structure of α -phase and γ -phase with partitioning of solute elements. The formation of probable intermetallic phases i.e., γ' -U₂Mo and Mo₂Zr phases were not observed which attributes to sluggish diffusion of solute elements. In furnace-cooled U-6Mo alloy, the high temperature bcc γ -phase undergoes partial decomposition leading to substantial amount of retained γ -phase at room temperature (RT). It was found out that the furnace-cooled alloys are far from their equilibrium state predicted by equilibrium phase diagrams because of sluggish diffusion.

The water quenching of the alloys leads to formation of various non-equilibrium orthorhombic (α'), monoclinic (α'') structures via diffusionless shear dominated martensitic transformation. In U-6(Zr+Nb) alloys, a total alloying content of 6wt% (Zr or Nb or both) is not sufficient to retain the high temperature bcc γ -phase at RT by water quenching from 1173 K. In U-6(Zr+Mo) alloys, high temperature bcc γ -phase is almost fully retained in a metastable state only in case of water-quenched U-6Mo alloy. This attributes to better gamma stabilization power of Mo as compared to Zr or Nb.

2. The phase stability of the alloys under near-equilibrium condition has been demonstrated when the samples were subjected to step cooling from 1173 K with isothermal holding at various temperatures. The phase stability of step-cooled U-6Zr alloy reveals biphasic microstructure of distinct α -U and δ -UZr₂ phases as expected from equilibrium phase diagram. The step-cooled U-Zr-Nb, U-6Nb alloys attained biphasic microstructure comprised of almost solute free α -U phase and solute enriched bcc γ phase under near-equilibrium condition. In step-cooled alloys, the α -U phase has almost negligibly

solubility of alloying elements (i.e., Zr or Nb or Mo) and the solute content in solute enriched bcc γ phase is found to be significantly higher when compared to that in furnace-cooled samples. The phase stability of step-cooled U–Zr–Mo alloys become complicated by appearance of multiphase microstructure with α -U, ZrMo_2 intermetallic and various solute enriched phases. The formation of ZrMo_2 phase may lead to decrease in solute content in the bcc γ phase and therefore, the precipitation of such type of phases is always undesirable. In the step-cooled U–Zr–Nb and U–Zr–Mo alloys, no δ - UZr_2 phase formation was observed which indicates that the δ - UZr_2 phase formation can be eliminated by replacing Zr with Nb or Mo. Unlike furnace-cooled alloy, the step-cooled U–6Mo alloy attained a microstructure consisting of α -U and γ - U_2Mo as depicted in the equilibrium phase diagram.

3. In the present thesis, DTA technique has been extensively used to investigate the phase transformation sequences and solidus temperature of the alloys which are useful input to evaluate their thermal performance. The solidus/liquidus temperatures of U–6Zr alloy are found to be $\sim 1465/1548$ K. The gradual replacement of Zr in U–6Zr alloy with Nb increases the solidus/liquidus temperatures whereas replacement of Zr by Mo decreases the solidus/liquidus temperatures. Therefore, Mo addition as an alloying element in the fuel is not an attractive option for increasing the solidus temperature of fuel.
4. The phase transformation sequences and the transformation temperatures of the alloys vary significantly depending on their phase stability resulting from variations in heat treatment. The U–6Zr alloy follows the phase transformation sequences of $\alpha + \delta \rightarrow \alpha + \gamma_2 \rightarrow \beta + \gamma_2 \rightarrow \gamma_1 + \gamma_2 \rightarrow \gamma$ at 860, 946, 975 K and 993 K, respectively. All the intermediate transition was not observed in case of furnace-cooled alloy. The replacement of Zr with Nb or Mo leads to disappearance of phase transformation associated with δ - UZr_2 phase. In presence of Nb and Mo, the furnace-cooled alloys form the single bcc γ -

phase at remarkably lower temperature than U–Zr alloy which is always beneficial for fuel application. However, the phase transformation temperatures of step-cooled alloys differ significantly from furnace-cooled alloys. In the step-cooled alloys, the single bcc γ -phase forms at relatively higher temperature as compared to furnace-cooled alloys. The furnace cooling of the sample does not allow sufficient time for the complete segregation of alloying constituent in α and γ_3 phase like step-cooled samples and therefore the solute content in the α -phase might be higher than the solubility limit leading to formation of supersaturated α -U phase. It is well known that the alloying constituents Nb and Mo are effective stabilizer of γ phase and therefore γ -phase appears at a lower temperature via $\alpha + \gamma \rightarrow \gamma$ transition. In step-cooled U–Zr–Mo alloys, the single γ -phase forms at relatively higher temperature because of formation of $ZrMo_2$ which has higher thermally stability. Apart from all these phase transformation, few additional exothermic transitions observed in water-quenched alloys could be attributed to the non-equilibrium martensitic to equilibrium phase transformation. The present results of microstructure evolution, phase transformation behaviour of the various heat treated alloys will be useful to understand the phase stability of U–6wt%(Zr,Nb/Mo) alloy system.

5. Heat capacity data is an important parameter of nuclear fuel. Heat capacity data of the alloys indicate that the addition of 6wt% alloying element (Zr or Nb or Mo) into uranium metal leads to decrease in molar heat capacity. The gradual replacement of Zr in U–6Zr alloy with equivalent amount of Nb or Mo leads to decrease in molar heat capacity value. The molar heat capacity data of U–Zr–Nb and U–Zr–Mo alloys are useful to calculate their thermal conductivity. The thermodynamic functions such as molar enthalpy increment $H_m^0(T) - H_m^0(298.15 \text{ K})$ and molar entropy increment $S_m^0(T) - S_m^0(298.15 \text{ K})$ of the alloys have been evaluated using measured heat capacity data. The thermodynamic data like molar heat capacity, molar enthalpy increment, and

molar entropy increment will be useful for thermodynamic assessment of phase diagrams of these multi-component systems. In general, the metallic alloy system with a relatively low heat capacity will limit the stored energy in the fuel and therefore, exhibits inherent passive safety characteristics. The lower heat capacities of U–Zr–Nb and U–Zr–Mo alloys leads to less amounts of stored energy in the fuel and therefore, the above ternary alloys based metallic fuel will offer an added advantage.

6. The coefficient of thermal expansion (CTE) is another important parameter of nuclear fuel. The replacement of small amount of Zr in U–6Zr alloy with Nb or Mo does not have any remarkable effect on the overall thermal expansion except the phase transformation temperatures. However, the thermal expansion gradually decreases with further increasing Nb or Mo content in the alloys. Thermal expansion of metallic alloy fuel has two different aspects. There is a concern that the relatively higher CTE of metallic fuel and phase transformation may lead to faster contact with the cladding leading to accumulation of stresses resulting in the deformation of the cladding. At the same time, the higher thermal expansion of metallic fuel has the benefit of a strong negative reactivity feedback to the core during an over-power transient event due to enhanced neutron leakage. Thus, higher thermal expansion of metallic fuel provides added advantage in terms of inherent safety characteristics. Therefore, the U–Zr alloy with limited amount of Nb or Mo may offer the advantages of better inherent safety characteristics and lesser stress on the cladding.

7. The chemical interaction between the metallic fuel and steel cladding is considered as a potential problem area as there is possibility of low melting eutectic formation between fuel and cladding components. The eutectic liquefaction temperatures between U/U–Zr alloy and T91 steel are found to be identical (i.e., 995 K). From this observation, one can conclude that presence of Zr (~ 10wt%) in the fuel or Cr, Mo etc. in the cladding steels

will not have much effect on eutectic reaction temperature of fuel-cladding interaction since the main contributors to the fuel-cladding eutectic reaction are U of the fuel and Fe of the cladding. The interdiffusion between U–Zr and T91 resulted in the formation of three distinct reaction zones at the interface: UFe₂-type intermetallic, a Zr-rich layer and a Zr-depleted layer. The alloying element Zr in the fuel plays a crucial role in fuel-cladding interdiffusion through the formation of Zr-rich diffusion barrier layer at the interface. This observation agrees with those made by some other researchers that Zr in the fuel moves out towards the surface and acts as a reaction barrier between fuel and cladding. Our experiments were carried out under isothermal condition, but under temperature gradient, the diffusion of Zr to the surface is expected to be more than the present values. Although the Zr-enrichment at the surface is expected to improve the fuel-cladding interaction, it will correspondingly bring down the solidus temperature of the fuel, which is a small set back. But as per our observation, most of the Zr moves from the outer region, where the temperatures are less. Therefore, composition at the center-line, the highest temperature zone of the fuel, is expected to remain unchanged by Zr diffusion. Based on the diffusion couple experiments at various temperatures, it can be concluded that the compatibility of U–Zr alloy and T91 steel cladding seems to be good at reactor operating temperature due to the formation of Zr-rich barrier layer at the interface. However, at any accidental condition if the fuel-cladding interfacial temperature reaches above the eutectic liquefaction temperature (995 K), the U–Zr fuel will no longer remain compatible with T91 cladding due to liquid phase formation.

Suggestions for future work

This thesis reports an extensive study on phase stability, phase transformation, thermophysical properties, fuel-cladding chemical compatibility of various U-based alloys. It has been realized that there is plenty of scope for further investigation. Some of them are

listed below: (1) evaluations of thermal diffusivity and thermal conductivity of U–Zr–Nb and U–Zr–Mo alloys and investigation of their chemical compatibility with T91 cladding, (2) investigation on phase stability and thermophysical properties of the U based alloys containing Pu, (3) The design and safety analysis of metal fuel system requires an understanding of irradiation behaviour and its quantitative evaluation on the margin of fuel pin failure. The modeling and simulation of the irradiation behaviour provides a basis for them. Therefore, post-irradiation examination (PIE) of the above alloys needs to be carried out to understand their behaviour after irradiation to various burnup levels, (4) It will be interesting to conduct similar type of extensive studies with U-based alloys with total alloying content limited to 10 wt.%, (5) Since, rare earth fission products migrate to the surface and react with cladding, their effects have to be studied extensively, (6) To reduce the repository burden of radioactive waste is to separate minor actinides from water reactor fuels and burn minor actinides in fast reactors since metal fueled fast reactors facilitate effective transmutation of minor actinides. A study in this regard has to be initiated.

SUMMARY

Metallic alloys are recognized as promising candidate fuels for fast breeder reactors (FBRs). In recent years, special attention has been paid to the development of metallic fuels for future FBRs in India due to their high breeding potential. The present work is a part of metallic fuel development programme. Metallic fuels with alloying content of ~6wt%Zr is preferred for future FBRs in India with an objective of achieving higher breeding ratio. Hence, the present study is aimed at generating a database on phase stability, phase transformation, microstructure, thermophysical properties and fuel-cladding chemical compatibility of U-6wt%Zr alloy, which are very useful to predict in-pile fuel performance. The alloying elements Nb and Mo were also combined with U-Zr alloy due to their various attractive features. In this thesis, the potential metallic fuel systems, namely, binary U-Zr, U-Nb, U-Mo and ternary U-Zr-Nb, U-Zr-Mo alloys with total alloying content limiting to 6wt% have been investigated for their phase stability, microstructure evolution, phase transformation and thermal properties. Investigation on the phase stability of various heat treated U-(6-x)Zr-xNb and U-(6-x)Zr-xMo alloys (x = 0, 2, 4, 6 wt%) revealed significant variation on their microstructures, crystal structures, lattice parameters depending on heat treatment and alloy compositions. The microstructures of furnace-cooled alloys are far from their equilibrium state predicted by equilibrium phase diagrams because of sluggish diffusion of solute elements. The water quenching of the alloys leads to formation of various non-equilibrium structures like distorted orthorhombic, monoclinic via diffusionless shear dominated martensitic transformation. The high temperature bcc γ -phase is retained in a metastable state only in water-quenched U-6Mo alloy indicating better gamma stabilization power of Mo as compared to Zr or Nb. The phase stability of the alloys under near-equilibrium condition has been demonstrated when the samples were subjected to step cooling from 1173 K with isothermal holding at various temperatures. The phase stability of

step-cooled alloys revealed the formation various phases as expected from equilibrium phase diagram and the formation of probable intermetallic phases i.e., δ -UZr₂, γ -U₂Mo and Mo₂Zr phases was also observed. The formation of ZrMo₂ phase may reduce the solute content in the bcc γ phase and therefore, the precipitation of such type of phases is always undesirable. The gradual replacement of Zr in U-6Zr alloy with Nb, increases the solidus temperatures whereas, replacement of Zr by Mo decreases the solidus temperatures. Therefore, Mo addition is not an attractive option for increasing the solidus temperature of fuel. The phase transformation sequences and the transformation temperatures of the alloys vary significantly depending on their phase stability resulting from variations in heat treatment. The gradual replacement of Zr in U-6Zr alloy with equivalent amount of Nb or Mo leads to decrease in molar heat capacity value. The lower molar heat capacity leads to less amount of stored energy in the fuel and therefore, U-Zr-Nb and U-Zr-Mo alloy based metallic fuel will offer an added advantage. The replacement of small amount of Zr in U-6Zr alloy with Nb or Mo does not have any remarkable effect on the overall thermal expansion. However, the thermal expansion gradually decreases with further increase in Nb or Mo content in the alloys. The microhardness data show substantial variation depending on the alloy composition and phase content. The chemical interaction between U-Zr alloy fuel and T91 steel cladding has been investigated by differential thermal analysis and diffusion couple test. The eutectic liquefaction temperature between U-Zr alloy and T91 steel are found to be ~995 K. The interdiffusion between U-Zr and T91 resulted in the formation of UFe₂-type phase, a Zr-rich layer and a Zr-depleted layer at the interface. The compatibility between U-Zr alloy and T91 steel seems to be good at reactor operating temperature due to formation of Zr-rich barrier layer at the interface. However, at any accidental condition if the fuel-cladding interfacial temperature reaches above the eutectic liquefaction temperature (995 K), the U-Zr fuel will no longer remain compatible with T91 cladding due to liquid phase formation.

Chapter 1

Introduction

1.1. Nuclear power programme in India

Nuclear energy is considered as a safe, economically viable and environmentally benign source of energy. Nuclear power is an inevitable option to meet the ever increasing energy demand and sustainable energy supply. The Indian nuclear programme was conceptualized based on a unique sequential three-stage programme and associated technologies through optimum utilization of indigenous resource of modest uranium and abundant thorium. This sequential three-stage programme is predicated on the closed fuel cycle approach, where the spent fuel of one stage is reprocessed to generate fuel for the subsequent stage and thus multiplies the energy potential of fuel and reduces the quantity of radioactive waste. The main goals in the three-stage Indian nuclear power programme are:

- to maximize energy potential from domestic resources of uranium and thorium,
- energy security and sustainability of nuclear power,
- to minimize green house gas emissions while meeting the massive demand of electricity.

The first stage of Indian nuclear programme comprises of Pressurized Heavy Water Reactors (PHWR) fuelled by natural uranium having 0.7% fissionable ^{235}U isotope and remaining 99.3% fertile ^{238}U . Furthermore, a small quantity of ^{239}Pu formed by transmutation of ^{238}U would be used in the second stage. The second stage comprises of Fast Breeder Reactors (FBRs) and fuels based on ^{238}U mixed with ^{239}Pu recovered by reprocessing spent fuel of the first stage. In FBRs, ^{239}Pu as main fissile element undergoes fission producing energy, while ^{238}U present in the fuel undergoes transmutation to produce additional ^{239}Pu . FBRs are designed to “breed” more fuel

Chapter 1: Introduction

than they consume. In addition to this, a blanket of fertile ^{232}Th will be introduced around the FBR core to undergo transmutation through neutron capture reactions leading to the formation of fissile ^{233}U for use in the third stage. The third stage will use a self-sustaining ^{232}Th - ^{233}U fuel cycle in the thermal breeder reactors where the vast thorium reserves can be utilized. The growing energy demand of developing India warrants faster growth of nuclear power where fast reactor could play a significant role. Hence, development of fast reactor and their utilization for effective use of limited resources of natural uranium and also for breeding of ^{233}U from thorium blanket and later using U^{233} in reactors are essential steps for Indian nuclear power program [1]. Furthermore, closing the fuel cycle is an essential requirement for the growth of nuclear power at a faster pace. Fast reactors are being considered for nuclear power generation, in addition to transmutation of long-lived fission products to minimize nuclear waste.

In the late 1960's, the first decision was taken by Department of Atomic Energy (DAE), India, to build a Fast Reactor in collaboration with France; since their Liquid Metal cooled Fast Breeder Reactor (LMFBRs) RAPSODIE and its high power version FORTISSIMO demonstrated progress in fast reactor engineering operation. Thus, Fast Breeder Test Reactor (FBTR), India's first breeder reactor, was built on the lines of the French Rapsodie-Fortissimo reactor, with modifications [2, 3]. Accordingly, FBTR was successfully commissioned at Indira Gandhi Centre for Atomic Research (IGCAR), Kalpakkam, and went critical on 18th Oct 1985 [3]. FBTR is a 40 MWt loop type, sodium cooled fast reactor and hyper-stoichiometric uranium-plutonium mixed carbides containing 70% (Mark-I) and 55% (Mark-II) PuC are being used as the fuels. The first commercial fast reactor in India, prototype fast breeder reactor (PFBR), is under commissioning. PFBR will use mixed oxide fuel with 21% and 28% PuO_2 as the driver fuel with rated power generation capacity of 500 MWe. However, the future fast breeder reactors

Chapter 1: Introduction

(FBR's) will utilize metallic fuel because of its high breeding potential, low fuel doubling time and better safety features. Therefore, it has been decided that the first four FBRs will use mixed oxide fuel and subsequent FBRs will utilize metallic fuel [1].

1.2. Background and history of metallic fuel in fast reactor

The concept of fast breeder reactor (FBR) was first introduced by Fermi and Zinn in the year 1945-1946. Fast neutron spectrum reactors, commonly known as fast reactors, are the most efficient system for the effective utilization of uranium resources. The fast reactor has the potential to function either as breeder to achieve the net creation of fissile fuel or as a transmuter to convert the long lived minor actinides and other radioisotopes to short lived ones [4]. The first FBR was Clementine, developed by Los Alamos Scientific Laboratory, USA and it began operation in 1949 with cast delta-stabilized plutonium fuel rods. At the initial stage, the fast breeder reactors used metallic fuels as the preferred choice and most of the earliest fast reactors during 1945-1960 were fueled with metallic forms [5]. Metallic fuels were selected for fuelling various fast reactors including Clementine, LAMPRE-I, and LAMPRE-II developed by Los Alamos Scientific Laboratory, USA; EBR-I (Experimental Breeder Reactor I in Idaho), EBR-II (Experimental Breeder Reactor II) developed by Argonne National Laboratory, USA; FERMI (Enrico Fermi Reactor located near Detroit, Michigan) developed by Atomic Power Development Associates, USA and DFR (Dounreay Fast Reactor in UK) developed by United Kingdom Atomic Energy Authority [5]. The fuels used in these reactors are mainly based on uranium, plutonium alloys. The first prototype FBR, Clementine, was fuelled with cast delta-stabilized plutonium rods in mild steel cladding. In LAMPRE-I and LAMPRE-II reactors, molten eutectic Pu-2.3wt% Fe alloy fuel in tantalum capsules was used. EBR-I was fuelled with unalloyed uranium and U-2Zr and Pu-1.25Al alloys (in wt%). U-0.1Cr and U-9.1Mo alloys

Chapter 1: Introduction

were used as fuel element in DFR while U-10Mo alloy was employed for the Enrico Fermi Reactor. The various metallic fuelled fast reactors with their fuel compositions operated earlier are presented in Table 1.1 [5-7]. However, world-wide interest shifted toward ceramic fast reactor fuel in the late 1960's, before the full potential of the metallic fuel could be ascertained. This was primarily due to the excellent stability of ceramic fuels under neutron irradiation over metallic fuels and available established and proven technology. The development work of the metallic fuels was further continued throughout the 1970's in experimental breeder reactor II (EBR-II) of Argonne National Laboratory fueled with the metallic uranium-fissium alloy, i.e. U-5wt% Fs [8-10]. Fissium is an equilibrium composition of fission product elements remaining after the pyrometallurgical reprocessing cycle designed for the EBR-II and consists of 2.5Mo, 1.9Ru, 0.3Rh, 0.2Pd, 0.1Zr and 0.01Nb (in wt%). In EBR II, MK-I design with U-5Fs alloy fuel had limited space for fuel swelling and very little plenum volume to accommodate fission gas. As a result, the fuel pins failed at relatively low fuel burnup (3 at.%) from stress rupture of the austenitic stainless steel cladding [8]. Burnup is a measure of the fraction of fissionable atoms that have undergone fission. The MK-II design with U-5Fs alloy, first clad with SS304 and subsequently with SS316, allowed fuel swelling by reducing areal smeared density to 75% and also by providing more plenum volume with a plenum-to-fuel volume ratio of about 0.6 to accommodate fission gas. Over 30000 MK-II fuel pins were irradiated in EBR-II and qualified for 8 at.% burnup which was sufficiently below the ultimate burnup capability [7]. In the 1980s, the EBR-II reactor was upgraded to a driver core of U-10Zr fuel (Mark-III/IIIA design) with more swelling-resistant cladding (cold-worked D9 and SS316) and more plenum volume with plenum-to-fuel volume ratio of 1.45. The Mark-III/IIIA driver fuel was qualified for 10 at.% burnup due to swelling of the SS316 fuel assembly hardware. Assembly made of ferritic/martensitic

Chapter 1: Introduction

steel HT9 was to be included in future designs to allow greater fuel utilization. However, these tests never came to fruition because of terminal shut-down of the EBR-II reactor in 1994.

Table 1.1 Various metallic fuelled fast reactors with their fuel compositions operated earlier.

Reactor	Fuel Composition (wt %)	Operation period	Location
Clementine	Pu	1946–1952	USA
EBR-I	U (MK-I) U–2Zr (MK-II) U–2Zr (MK-III) Pu–1.25Al (MK-IV)	1951–1963	USA
LAMPRE-I	Pu–2.3Fe (Molten)	1961–1963	USA
DFR	U–0.1Cr (MK-II) U–9.1Mo (MK-IIA, B, C) U–9.1Mo (MK-IIIA, B, C)	1959 – 1977	UK
EBR-II	U–5Fs (MK-I, MK IA) U–5Fs (MK-II) U–10Zr (Mark-III) U–10Zr (Mark-IV) U–20Pu–10Zr (Mark-V/-VA)*	1965–1994	USA
Fermi	U–10Mo	1963–1972	USA

*Conversion to Mark-V/-VA was never begun before EBR-II was terminally shut down in 1994.

Only qualification assemblies of U–10Zr fuel with HT9 cladding were fabricated for the Mark-IV design; no standard driver fuel assemblies were made. U–Zr fuel rods (in experiments and qualification assemblies) and U–Pu–Zr fuel rods (in experiments) in SS316, D9 or HT9 cladding reached terminal burnup values of 15–20 at.%. In addition to EBR-II, irradiations of U–10Zr fuel

rods and U–Pu–Zr fuel rods with HT9 cladding were conducted in the Fast Flux Test Facility (FFTF), USA, to burnup values above 14 at.% and 9 at.%, respectively [7].

1.3. Various aspects of metallic fuel

Metallic alloys are recognized as one of the promising candidate fuels for FBRs. The notable success obtained from irradiation and testing of metallic fuels in both the experimental breeding reactor-II (EBR-II) and the fast flux test facility (FFTF) during 1960 to 1990 makes them attractive option as fast reactor fuel. In general, the basic thermal and neutronic performances of metallic fuels based on U–Zr, and U–Pu–Zr alloys are better than the conventional uranium-plutonium mixed oxide or high density mixed carbide ceramic fuels in fast reactor. Table 1.2 [11, 12] shows an inter-comparison of the various properties and behavior of different fast reactor fuels e.g., uranium plutonium mixed oxide (MOX), carbide (MC), nitride (MN) and metallic fuels. Metallic fuels have high fissile and fertile atom densities, which in turn offer relatively higher breeding ratio and lower doubling time [8]. The breeding ratio is defined as the ratio of the number of fissionable atoms produced compared to the number of fissionable atoms consumed in a breeder reactor. Doubling time is defined as the time required for a particular breeder reactor to double the initial fissile inventory. Metallic fuel has high thermal conductivity and relatively low heat capacity, which offer additional safety benefit. It has simplified fabrication process involving melting and casting route in which the problem of handling radiotoxic dust hazard could be avoided. Furthermore, metallic fuel can be simply recycled using either melt-refining or electro-refining process (i.e., pyrometallurgical reprocessing) with actinide recycle potential. The processes have ability to effectively remove a majority of fission products and return uranium, plutonium, and minor actinides into the fuel cycle, leading to an economical and proliferation-resistant reprocessing scheme. Moreover, the volume of radioactive

Chapter 1: Introduction

waste generated in the pyro-reprocessing of metallic fuel is expected to be lower than those encountered in aqueous reprocessing of ceramic fuel. In the Integral Fast reactor (IFR) concepts with metallic fuel, reprocessing and refabrication can be co-located in a single plant and therefore the capital investment to set up such facility is low. Also, being an integrated facility, there will neither be any additional cost of transportation nor any chance of proliferation.

Table 1.2 Inter-comparison of important properties of mixed uranium plutonium oxide (MOX), carbide (MC), nitride (MN) and metallic fuels for fast reactor [11, 12].

Properties	U-19Pu-10Zr	(U _{0.8} Pu _{0.2})O ₂	(U _{0.8} Pu _{0.2})C	(U _{0.8} Pu _{0.2})N
Theoretical Density (g/cc)	15.73	11.04	13.58	14.32
Melting point (K)	1400	3083	2750	3070
Structure	Multiphase ($\alpha+\delta+\zeta+\gamma$)	Fluorite	NaCl	NaCl
Thermal Conductivity (W/mK)	40	2.6	18.8	15.8
1000K		2.4	21.2	20.1
2000 K				
Breeding ratio	1.35-1.4	1.1-1.15	1.2-1.25	1.2 - 1.25
Handling	Inert atmosphere	Air	Inert atmosphere	Inert atmosphere
Fabrication/irradiation experience	Limited	Large good	Limited	Very little
Swelling	High	Moderate	High	High
Compatibility				
Cladding	Eutectics	Average	Carburization	Good
Coolant	Good	Average	Good	Good
Dissolution and reprocessing amenability	Demonstrated Pyroprocessing on pilot plant scale	Demonstrated aqueous process on industrial scale and pyro-processes on pilot scale	Dissolution not simple. Not yet demonstrated on industrial scale	Dissolution easy, Risk of C ¹⁴ in waste management

Chapter 1: Introduction

However, there are three major shortcomings in metallic fuels which may suppress them from achieving their full potential [8]. The issues are:

- Low solidus temperature of metallic fuel
- High swelling rate and
- Susceptibility to chemical and mechanical interaction with cladding material.

In recent years, special attention has been paid to the development of metallic fuel for future FBRs in India where two design concepts of metallic fuel have been proposed. These two concepts are: (a) sodium-bonded fuel pin with ternary U–Pu–Zr alloy as fuel and (b) mechanically bonded fuel pin with binary U–Pu alloy as fuel [13-16]. Fig. 1.1a shows the cross-section of conventional sodium bonded fuel pin where sodium metal acts as a thermal bond between the fuel (U–Pu–Zr) and cladding material. On the other hand, the cross-section of a proposed mechanically bonded fuel pin is presented in Fig. 1.1b where a thin zirconium layer is used in between fuel and cladding and semicircular grooves, placed diametrically opposite direction, are purposely given in the fuel slug to accommodate irradiation induced fuel swelling and also to facilitate early release of fission gasses. U–Zr alloy is proposed to be used as the blanket material for sodium bonded fuel pin, whereas, uranium is the proposed blanket material for mechanically bonded fuel pin. T91 grade steel (modified 9Cr1Mo steel) is chosen here as the cladding material in both the designs. Smear Density (S.D.) is considered as a key design parameter to achieve high burnup. “Smear density”, a dimensionless parameter, is the effective density of the fuel if the fuel were uniformly smeared or spread throughout the inside of the cladding. Fuel porosity is also reflected in the S.D. It is generally expressed (in percentage) by the following relation [7]: $S. D. = (\% \text{ of theoretical density}) \times (\text{square of fuel outer diameter}) / (\text{square of the cladding inner diameter})$. For higher target burnup, the smear density should be

lowered to accommodate fuel swelling as well as to facilitate release of fission gases to plenum. Low smeared density can be attained by using a large fuel-cladding gap or highly porous fuel [17]. The smeared density of the fuel could vary between 75% and 80% depending upon the residence time of the fuel in the reactor or burnup. In EBR II, the smeared density of 75% was chosen for U–Pu–Zr fuel pin.

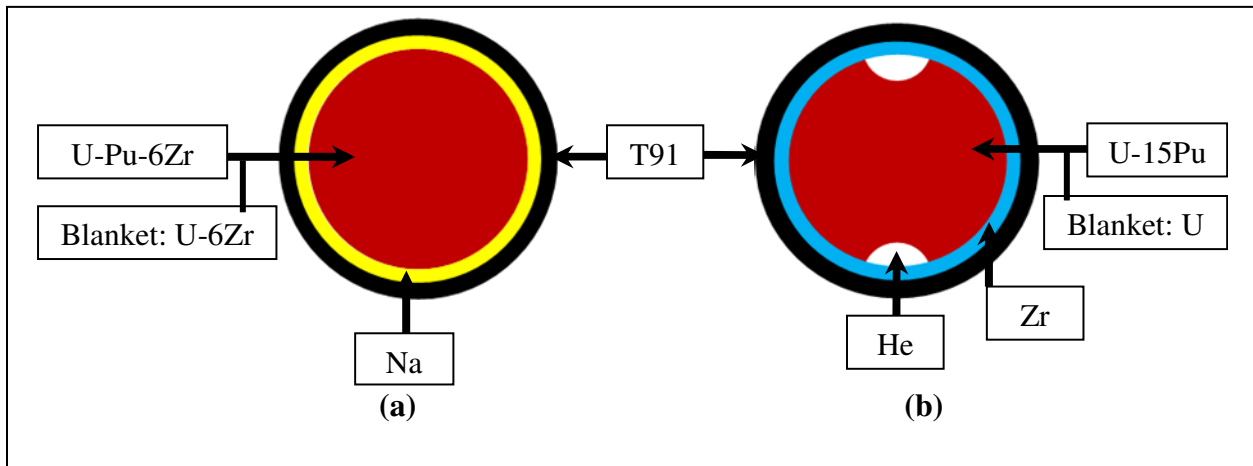


Fig. 1.1 Cross-sections of conceptual fuel pin design for metallic fuels; (a) U–Pu–Zr ternary and (b) U–Pu binary alloy (not to scale).

1.4. Alloying element(s) in metallic fuel

Uranium is the major constituent element in metallic fuel and therefore the selection of appropriate uranium alloys is crucial. Uranium metal has three allotropes: α -, β - and γ -phases between room temperature and its melting point. The α -U phase with base-centered orthorhombic structure is stable up to 941 K; β -U phase with tetragonal crystal structure is stable in the temperature range from 941 K to 1049 K and the γ -phase having symmetric body-centered cubic structure is stable from 1049 K up to the melting point. The α -U phase exhibits poor dimensional stability in the form of anisotropic growth and swelling during irradiation due to its

Chapter 1: Introduction

anisotropic orthorhombic crystal structure and making it undesirable as a fuel. On the other hand, the “ γ -stabilized” uranium alloys with isotropic cubic symmetry are always attractive fuel candidates due to their good irradiation characteristics [18, 19]. The alloying elements considered for fuel should have high degree of solubility within the isotropic γ -phase and ability to stabilize the γ -phase over wider temperature range [20]. Transition metals, particularly 4d and 5d elements in Group IV, through VIII, form solid solutions with γ -U phase and their γ -stabilizing power increases with atomic number as d-electrons participate in bonding through hybridization with s and p atomic orbitals [19]. The solubility of these elements decreases with increasing size difference with uranium atom, and the increased bond strength promotes different intermetallic compound formation. The transition group elements e.g. Zr, Nb, Mo, and Ti are generally chosen as alloying constituents with uranium because of their high degree of solid solubility in bcc γ -uranium [21]. Metallic fuels based on U–Zr and U–Pu–Zr alloys are selected as fuel candidates for FBRs and most of the irradiation experiments of metallic fuel were carried out with U–Zr based alloys. Zr is selected as an alloying element due to the following reasons [8]:

- Zr increases the solidus temperature
- It stabilizes the isotropic gamma phase over a wider temperature range
- It helps to mitigate the fuel-cladding chemical interaction.
- Uranium alloyed with Zr has better dimensional stability during thermal cycling.

Furthermore, the allowable concentration of Zr is limited to about 10 wt% in metallic fuel because too much addition of Zr would result in the formation of an alloy whose liquidus temperatures may exceed the softening point of the quartz molds used for fuel fabrication [8].

The properties of the U–Zr alloys as a fuel material can be further refined with the addition of Nb or Mo due to their various attractive features [22-26], some of which are given below.

Chapter 1: Introduction

1. Both Nb and Mo are effective stabilizer of bcc γ -phase of uranium to a lower temperature.
2. Both Nb and Mo have higher thermal conductivity than Zr.
3. Unlike Zr, both Nb and Mo have bcc crystal structure up to their melting point.
4. Nb does not form any intermetallic compound with uranium.
5. Nb increases the solidus temperature.
6. Mo decreases the density of uranium to a lesser degree than other alloying elements.
7. Uranium alloyed with Nb and Mo improve oxidation/corrosion resistance which may provide an added advantage to these alloys and handling of the alloys in presence of oxygen/moisture impurities becomes relatively easier during fabrication. It may be noted here that both U, Zr are reactive in nature, forming surface oxide layer in presence of oxygen/moisture.

Therefore, it is a logical step to combine requisite quantity of Nb or Mo as alloying elements with U–Zr alloy in order to obtain metallic fuels of ternary U–Zr–Nb and U–Zr–Mo alloys which are expected to have improved thermal properties and better irradiation stability. It is noteworthy to mention from the neutronics point of view that all the alloying constituents i.e., Zr, Nb, Mo may reduce the breeding gain of the fuel due to the parasitic neutron capture. Furthermore, the substantial addition of Nb is also undesirable because of its induced radioactivity. Hence, total amount of alloying constituents should be restricted to a minimum fraction in order to achieve higher breeding ratio [27]. It may be noted here that the metallic fuels with relatively low Zr (~6 wt%) is preferred for future FBRs in India with an objective of achieving higher breeding ratio [13, 15]. From this prospective, the combined addition of total alloying elements i.e., Zr and Nb (or Mo) in the uranium alloys is restricted to 6wt% in the present investigation. On account of this, investigation on the phase stability and the knowledge of various thermophysical properties of uranium-rich binary U–Zr, U–Nb, U–Mo and ternary

U–Zr–Nb, U–Zr–Mo alloys, with total alloying content being restricted to 6 wt%, are essential and must be well-known in order to predict their performance as fuel material.

1.5. Alloy characteristics, phase stability and relevant literature information

1.5.1. Uranium metal

The α -U phase has base-centered orthorhombic structure (space group Cmcm) with a two-atom motif at each lattice site and the atoms form corrugated sheets, which comprise the (010) planes. The orthorhombic crystal of α -U contains 4 atoms per unit cell and the coordinate of four atoms are given as $(0, y, \frac{1}{4})$, $(0, -y, \frac{3}{4})$, $(\frac{1}{2}, y+\frac{1}{2}, \frac{1}{4})$ and $(\frac{1}{2}, \frac{1}{2} -y, \frac{3}{4})$; where $y = 0.1025$. The lattice parameter of α -U at room temperature are $a = 2.852 \text{ \AA}$, $b = 5.865 \text{ \AA}$, and $c = 4.945 \text{ \AA}$ [28]. The crystal structure of β -U phase is complex tetragonal lattice (space group $P4_2/mnm$) with 30 atoms per unit cell and lattice parameter are $a = 10.52 \text{ \AA}$ and $c = 5.57 \text{ \AA}$ [29]. The crystal structure of β -U phase is a layer structure composed of two densely populated main layers (B and C) with one less populated subsidiary layer (A) with AB AC type stacking. The irradiation behavior of β -U is not satisfactory for its use as reactor fuel and it exhibits swelling similar to α -U phase [30]. The γ -U phase has isotropic body centered cubic (BCC) structure (space group $Im\bar{3}m$) with 2 atoms per unit cell and lattice parameter $a = 3.474 \text{ \AA}$ [29].

1.5.2. Uranium alloyed with Zr and Nb metals

1.5.2.1. The Uranium-Zirconium system

The assessed U–Zr equilibrium diagram is shown in Fig. 1.2 [31]. The U–Zr binary system is characterized by the five solid phases e.g., α -U (orthorhombic), β -U (tetragonal), γ -U (bcc), δ -UZr₂ (hexagonal) and α -Zr (hcp). The only intermetallic in the U–Zr system is δ -UZr₂ phase, a complex phase with modified C32 (A1B2-type) structure and the homogeneity range of the δ -UZr₂ phase was found to be 66.5-80.2 at% Zr at 823 K. At high temperatures, Zr

Chapter 1: Introduction

has complete solid solubility in bcc γ -U phase, forming a continuous series of solid solutions whereas Zr has limited solubility in both α -U and β -U phases. The maximum solubility of Zr in α -U phase is slightly higher than 0.5 at.% at 935 K and decreases to 0.2 at.% at 773 K. The β -U exhibits the maximum solubility of around 1.1 at.% Zr at 966 K. The crystallographic data of various phases in U–Zr system are summarized in Table 1.3. In the high temperature γ -phase of U–Zr system, a miscibility gap exists where γ -phase undergoes phase separation, forming two bcc phases with different Zr-content represented by γ_1 (rich in uranium) and γ_2 (rich in Zr). The maximum of the miscibility gap exists at ~ 993 K and ~ 14 wt%Zr. It could be seen from the phase diagram that U–Zr system exhibits four invariant reactions i.e., monotectoid ($\gamma \leftrightarrow \beta + \gamma_2$ at 966 K), eutectoid ($\beta \leftrightarrow \alpha + \gamma_2$ at 935K) and peritectoid ($\alpha + \gamma_2 \leftrightarrow \delta$ -UZr₂ at 890 K) and eutectoid ($\gamma \leftrightarrow \delta$ -UZr₂ + α -Zr at 879 K).

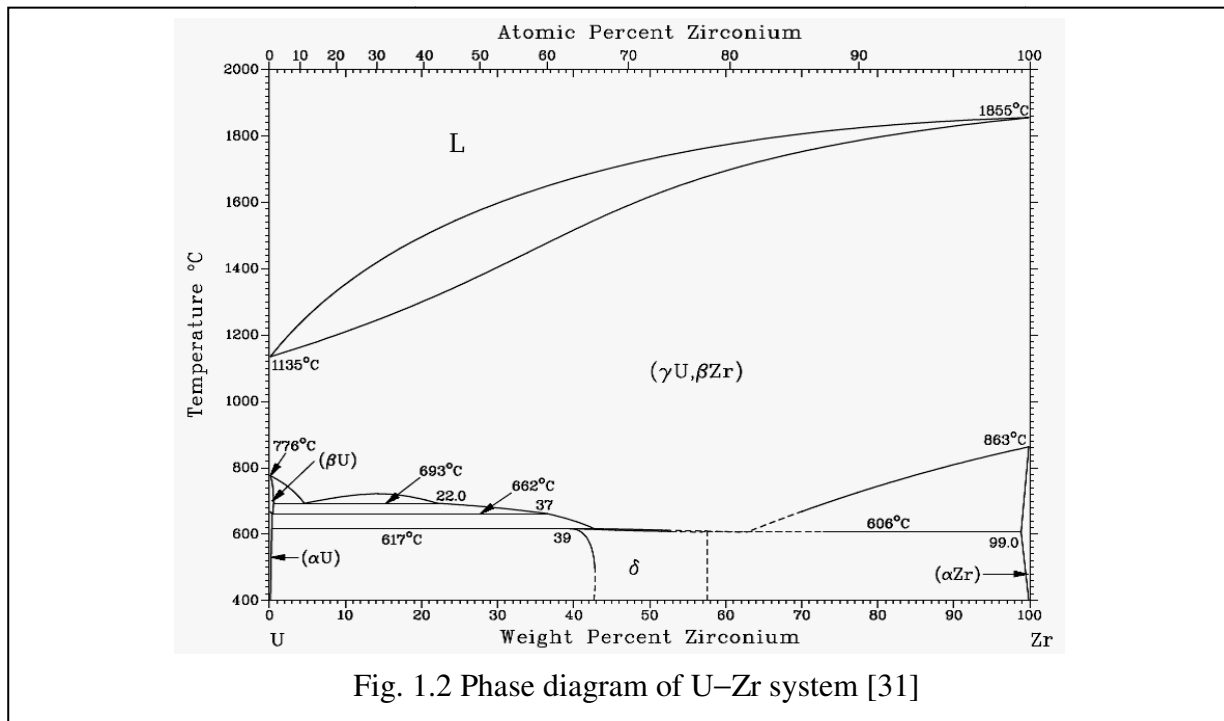


Fig. 1.2 Phase diagram of U–Zr system [31]

Phase	Approximate composition at.%Zr	Space group	Pearson symbol	Prototype
α -U	0 - 0.5	Cmcm	oC4	α U
β -U	0 - 1.1	P4 ₂ /mnm	tP30	β U
γ (U,Zr)	0 - 100	Im-3m	cI2	W
δ -UZr ₂	63 - 78	P6/mmm	hP3	A1B2
α -Zr	99.6 - 100	P6 ₃ /mmc	hP2	Mg

1.5.2.2. The Uranium-Niobium system

The assessed phase diagram of U–Nb system is presented in Fig. 1.3 [32]. The U–Nb system is characterized by the three solid phases e.g., α -U (orthorhombic), β -U (tetragonal), γ (U, Nb) (bcc). There is no intermetallic compound in the U–Nb system which is considered as a unique feature for this system. There is complete solid solubility of Nb in the bcc γ -U phase and forming a continuous solid solution, γ (U,Nb), at high temperature. Like U–Zr system, Nb also has limited solubility in both α -U and β -U phases. At lower temperatures, the γ (U,Nb) phase separates into two phases along a miscibility gap and forming one U-rich bcc phase (γ_1) and another Nb-rich bcc phase (γ_3). In the U–Nb binary system, the miscibility gap is represented by γ_1 and γ_3 . The term γ_3 is adopted for the Nb-rich bcc phase in U–Nb system to avoid confusion with the γ_2 (Zr-rich bcc phase) of the U–Zr system. The crystallographic data of phases formed in U–Nb system are summarized in Table 1.4. As per the phase diagram, U–Nb system has two invariant reactions i.e., monotectoid ($\gamma \leftrightarrow \beta + \gamma_3$ at 923K) and eutectoid ($\beta \leftrightarrow \alpha + \gamma_3$ at 913K). It may be noted here that the phase diagram of U–Nb system was also assessed by Koike et al. [33] and there are two different opinions for the monotectoid reaction [34]. According to phase diagram reviewed by Massalski [32], the monotectoid reaction of the $\gamma \leftrightarrow \beta + \gamma_3$ at 923K is

Chapter 1: Introduction

adopted. On the other hand, the monotectoid reaction $\gamma \leftrightarrow \alpha + \gamma_3$ at 920 K is adopted according to the phase diagram reviewed by Koike et al. [33]. According to them, two invariant reactions are eutectoid ($\beta \leftrightarrow \alpha + \gamma_3$ at 937 K) and monotectoid ($\gamma \leftrightarrow \alpha + \gamma_3$ at 920 K).

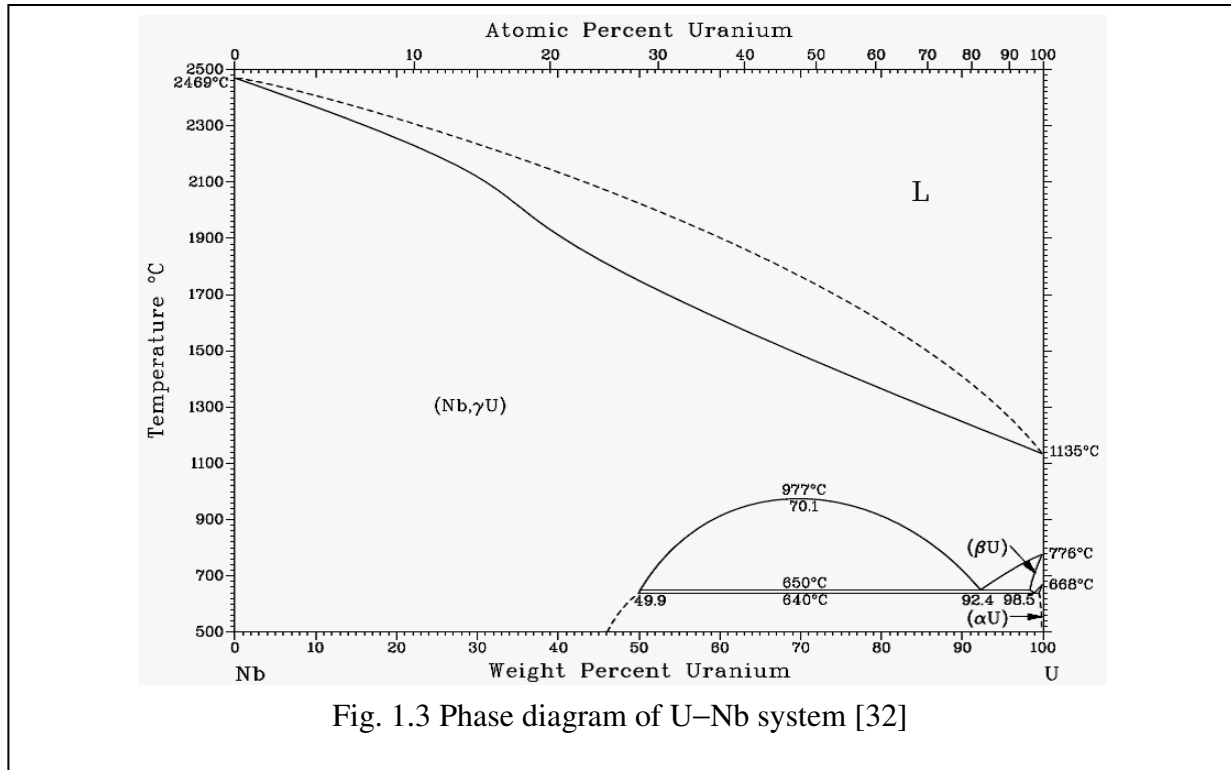


Fig. 1.3 Phase diagram of U–Nb system [32]

Table 1.4 Crystallographic data of different phases in the U–Nb system [32, 33]

Phase	Composition at.%Nb	Space group	Pearson symbol	Prototype
α -U	0 - < 1	Cmcm	oC4	α U
β -U	0 - < 2	P4 ₂ /mnm	tP30	β U
γ (U,Nb)	0 - 100	Im-3m	cI2	W

1.5.2.3. The Uranium-Zirconium–Niobium system

Dwight and Mueller [22] thoroughly investigated the U–Zr–Nb system using metallography, resistivity measurements, XRD and presented isothermal sections, vertical sections and three-dimensional isometric model of ternary equilibrium diagram. According to

them, the U–Zr–Nb alloys exhibit continuous solid solutions of γ -phase at high temperature. Addition of both Zr and Nb stabilize bcc γ -phase to lower temperatures. The miscibility gaps of $\gamma_1 + \gamma_2$ in the U–Zr and $\gamma_1 + \gamma_3$ in the U–Nb binary systems tend to close with addition of third element (Zr or Nb). The major part of uranium-rich corner of the ternary diagram exhibits the equilibrium phases of α -U and γ . No new ternary phases were observed by Dwight and Mueller. A representative isothermal section of ternary phase diagram is presented in Fig. 1.4.

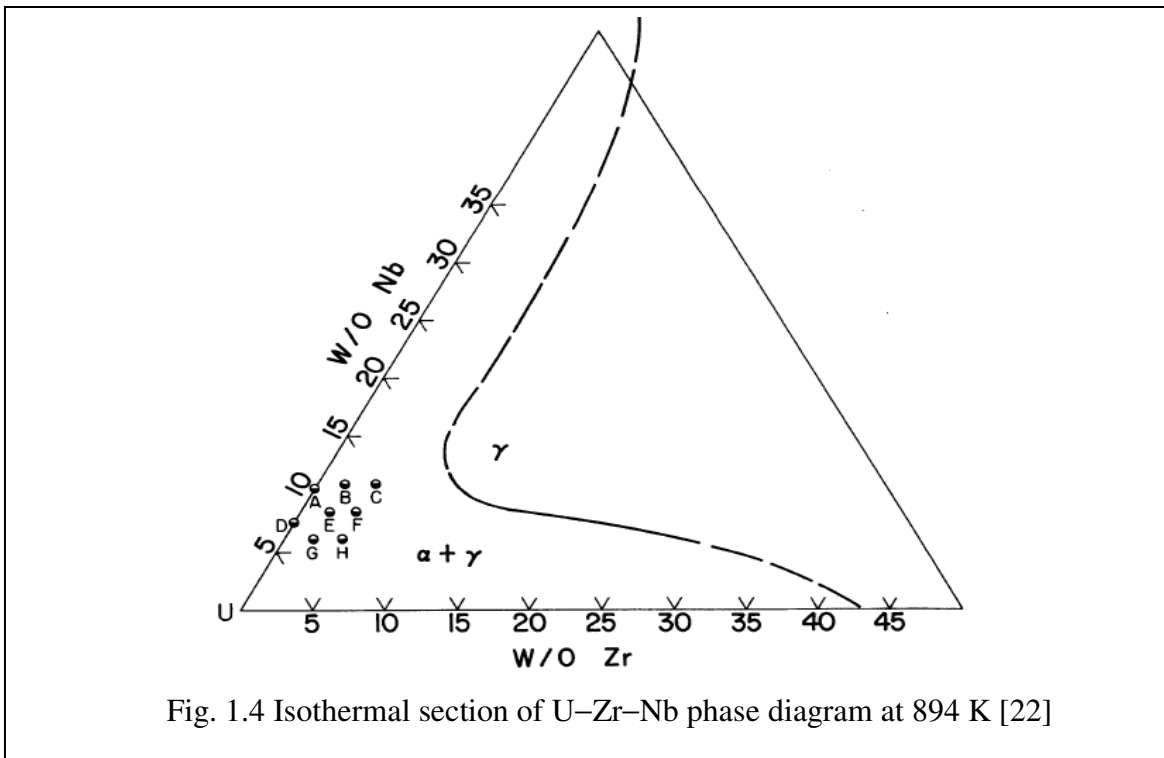


Fig. 1.4 Isothermal section of U–Zr–Nb phase diagram at 894 K [22]

It is noteworthy to mention that uranium alloyed with Zr and Nb undergo series of phase transformations from high temperature bcc γ -phase to a variety of equilibrium and non-equilibrium intermediate phases by diffusional and/or martensitic mechanisms depending upon alloy composition, cooling rate, quenching, aging etc. Several studies on the phase transformations of uranium-rich binary U–Zr, U–Nb and ternary U–Zr–Nb alloys have been reported in the literature. In an earlier study, Lagerberg [35] examined the phase transformations

Chapter 1: Introduction

of U-rich U–Zr alloys (Zr = 0.5, 2 and 5wt%) by means of metallography, thermal analysis and reported the time temperature-transformation(TTT) diagram for U–2Zr alloy. Hills et al. [36] studied the effect of cooling rate on the decomposition of γ -phase in U–Zr alloys (2.5, 5, 10, 15, 20, 30, 40 and 50 at.%) where the formation of δ -UZr₂ phase was not revealed for U-rich alloys. The microstructural evaluation, phase transformation, and thermal properties of various U-rich U–Zr alloys (Zr = 2, 5, 7, 10 wt%) have been thoroughly investigated by Basak et al. [37-40]. They reported martensitic phase of metastable α' (distorted orthorhombic) and the associated intermediate phases for U–Zr alloy. The sequences of various phase transformations in U–Zr alloys have been studied by few authors using differential scanning calorimeter (DSC) [41, 42]. In few recent investigations, the formation of intermetallic δ -UZr₂ phase in as-cast U-rich U–Zr alloys has been highlighted by microstructural investigations [43-45]. The phase transformation behavior of U-rich U–Nb system was also investigated by many authors. Tangri and Chaudhuri [46] reported appearance of metastable phases i.e., α' (orthorhombic), α'' (monoclinic), γ° (tetragonal) in the U-rich U–Nb alloy. The phase transformation behavior of high temperature bcc γ -phase during continuous cooling, rapid quenching and isothermal aging, the formation of metastable martensitic structures and their decomposition on aging in U-rich U–Nb alloy system were reported in the earlier studies [23, 47-51]. One of the unique features reported for U-rich U–Nb alloys is that the metastable α'' and γ° phases exhibit shape memory effect (SME) [48].

On the other hand, the investigation reported on the ternary U–Zr–Nb alloy mainly emphasizes U–2.5%Zr–7.5%Nb (Mulberry Alloy) (in wt%). In U–2.5Zr–7.5Nb alloy, several non-equilibrium intermediate phases like γ^{\diamond} (cubic, unit cell parameter is twice that of γ phase), γ° (tetragonal), α'' (monoclinic) and equilibrium phases of γ_3 (bcc) + α (orthorhombic) were

Chapter 1: Introduction

found to be formed owing to various heat treatments like quenching or isothermal aging at different temperatures [18, 52]. Lopes et al. [20, 53] studied phase transformation, thermal and mechanical behaviours of γ -stabilized U–2.5Zr–7.5Nb alloy and its kinetic transformation diagram was determined by combining calorimetry and dilatometry. Pais et al. [54] reported the phase and microstructural characterization of U–2.5Zr–7.5Nb and U–3Zr–9Nb alloys at 573 K and 873 K isotherms. Masrukan et al. [55] investigated the effect of Nb on phase stability, microstructure and hardness of U–Zr–Nb alloys by varying Nb content (i.e., 2, 5 and 8 wt%) while Zr being fixed at 6%. Ghoshal et al. [27] studied microstructural and structural investigation and phase transformation of U-rich U–Zr, U–Nb, U–Zr–Nb alloys and reported various metastable phases α' (orthorhombic), α'' (monoclinic), γ° (tetragonal) in water-quenched alloys.

1.5.3. Uranium alloyed with Zr and Mo metals

1.5.3.1. The Uranium-Molybdenum system

The equilibrium diagram of U–Mo system is shown in Fig. 1.5 [32]. The U–Mo system has five solid phases e.g., α -U (orthorhombic), β -U (tetragonal), γ -U, (bcc), γ' -U₂Mo (tetragonal) and Mo (bcc). There is only slight solubility of Mo in the α -U and β -U phases, however, Mo has maximum solubility of ~41 at.% in bcc γ phase and forming a substitutional solid solution with bcc structure. The only intermetallic in the U–Mo system is γ' -U₂Mo phase having tetragonal structure. At ~838 K, the γ phase undergoes a eutectoid decomposition reaction, transforming to the α -U and γ' -U₂Mo phases. The crystallographic data of various phases in U–Mo system are presented in Table 1.5.

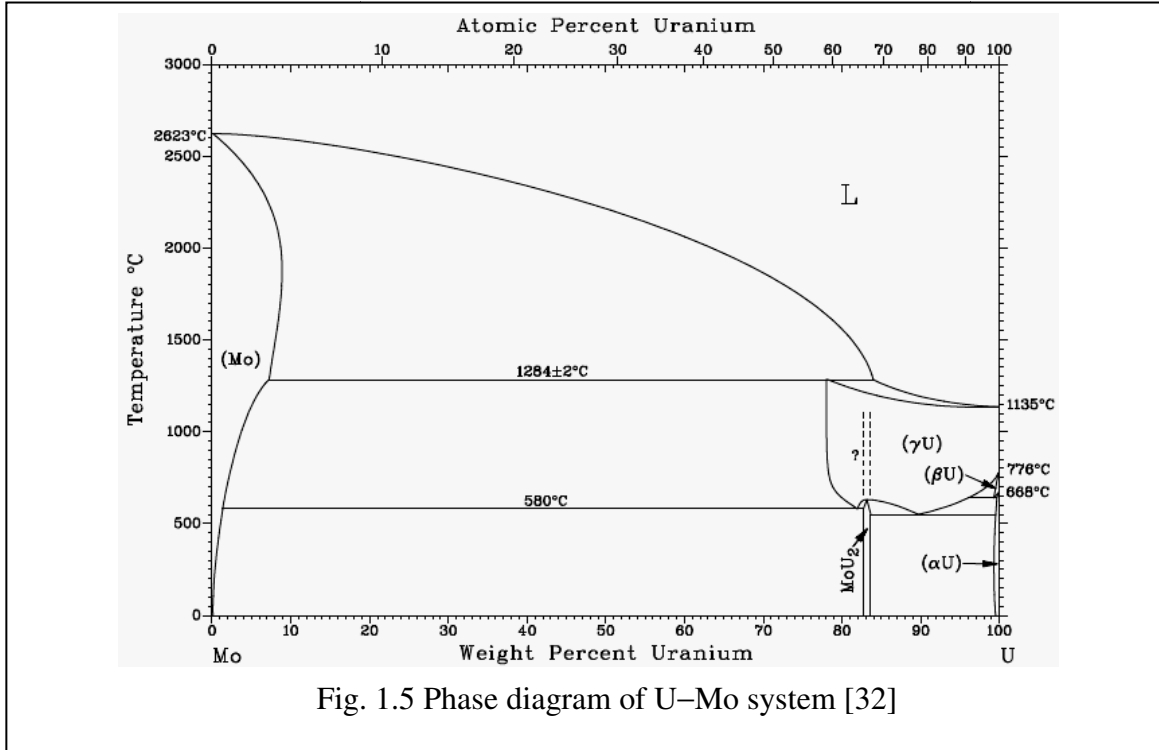


Fig. 1.5 Phase diagram of U–Mo system [32]

Table 1.5 Crystallographic data of various phases in the U–Mo system

Phase	Approximate composition at. %Mo	Space group	Pearson symbol	Prototype
α-U	0 - < 1	Cmcm	oC4	αU
β-U	0 - < 2	P4 ₂ /mnm	tP30	βU
γ-U	0 - 41	Im-3m	cI2	W
γ'-U ₂ Mo	~33.3	I4/mmm	tI6	MoSi ₂
Mo	98-100	Im-3m	cI2	W

1.5.3.2. The Uranium-Zirconium–Molybdenum system

The phase diagram of ternary U–Zr–Mo system was reported by Ivanov et al. [56]. The representative equilibrium diagrams of U–Zr–Mo system at 923 K and 1273 K were presented in Figs 1.6 [56, 57]. The U–Zr–Mo system exhibits various solid phases e.g., α-U (orthorhombic), β-U (tetragonal), γ-U (bcc), δ-UZr₂ (hexagonal), γ'-U₂Mo (tetragonal), ZrMo₂ (cubic), α-Zr (hcp)

Chapter 1: Introduction

and Mo (bcc). As per the phase diagram, U-rich part of U–Zr–Nb system exhibits solid solutions of γ -phase at higher temperature. At relatively lower temperature, the U-rich U–Zr–Mo alloys may consist of two or three phases with α -U, γ -U and Mo_2Zr phases. It may be noted here that binary phase diagram of Zr–Mo system consists of Mo_2Zr intermetallic phase at ranges from 33 to 40 at% Zr.

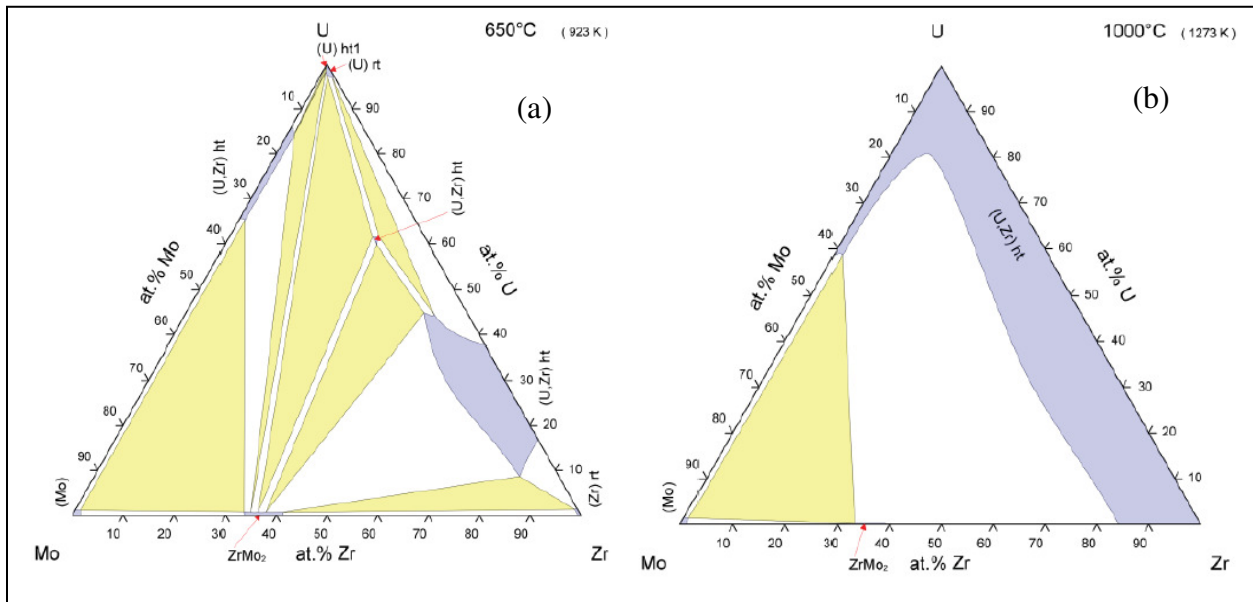


Fig 1.6 Ternary Equilibrium phase diagrams of U–Zr–Mo at (a) 923 K and (b) 1273 K [56]

Like U–Zr–Nb alloys, uranium alloyed with Zr and Mo undergo phase transformations from high temperature bcc γ -phase. The phase stability of U–Mo alloys after different heat treatments have been reported by many authors. Hills et al. [58] studied the effect of cooling rate on the decomposition of bcc γ -phase in U-rich U–Mo alloys (2.5 to 15 at% Mo) in which a number of metastable phases e.g., α' (orthorhombic), α'' (monoclinic) γ^o (tetragonal) were reported for various compositions. Similar types of metastable phases along with the variation in lattice parameters in water-quenched U–Mo alloys were also reported by Tangri et al. [59]. Burkes et al. [60] reported the microstructural and phase analyses of DU–Mo alloys (7-12 wt%

Chapter 1: Introduction

Mo) where no significant degree of phase decomposition or crystallographic ordering of bcc γ -phase was observed and they also determined the lattice parameter of γ -phase as a function of the Mo concentration. Sinha et al. [61, 62] investigated the stability of bcc γ -phase as a function of Mo in U–Mo alloys and reported the amount of Mo required to metastabilize γ -phase at room temperature under furnace cooling condition. Kim-Ngan et al. [63] investigated the stabilization and decomposition of splat-cooled cubic γ -phase U–Mo alloys and demonstrated the amount of Mo required to stabilize the γ -phase in the as-obtained state of ultrafast cooled U–Mo alloys. Neogy et al. [64, 65] reported U–9Mo alloy as a “sluggish” eutectoid system where the γ -phase can be retained at low temperatures even without rapid cooling like water quenching. According to them, the metastable γ -phase of an aged sample decomposes through discontinuous precipitation reaction (or the cellular reaction) mechanism. Ageing studies of U–Mo alloy at different temperature was also reported by other authors [66-68]. The structural properties of U–5.4Mo and U–10Mo alloys were reported by Lee et al. [69] and Seong et al. [70] using neutron diffraction technique.

However, studies particularly on ternary U–Zr–Mo alloys are found to be limited in the literature. Woolum [30] examined the phase evolution and stability of several ternary U–Zr–Mo alloys containing 7, 10wt% Mo and 2, 5, 10wt% Zr after casting and heat treatment. The U–Zr–Mo alloys exhibited similar microstructural characteristics with a solid solution matrix phase and the intermetallic precipitates distributed in the matrix as well as along the grain boundaries. The phase stability in the U–10Mo alloys with varying Zr concentration of 0.5-20 wt% at room temperature has been examined by Eriksson [57] after heat treatment at 1173 K and 923 K. It was reported that γ -U phase remained stable for alloys containing less than 1wt.% Zr

Chapter 1: Introduction

whereas a significant quantity of intermetallic Mo_2Zr phase formation was revealed for alloys containing 2 wt.% or more Zr. The as-cast and heat treated ternary U–Zr–Mo alloys with total alloying content (Zr+Mo) of 12 wt% were investigated in terms of the crystal structure, microstructure and hardness by Morais et. al. [71]. Although, there are many reports available for U-rich U–Zr, U–Nb and U–Mo alloys, studies on U–Zr–Nb and U–Zr–Mo alloy systems are limited in the literature and requires further investigation. Moreover, the literature data particularly of U–6(Zr+Nb) and U–6(Zr+Mo) alloy systems of our interest are sparse. The present study aims to fill the existing research gaps on structural and microstructural characteristics of U–6(Zr+Nb) and U–6(Zr+Mo) alloy systems.

1.6. Thermophysical properties of nuclear fuel

The in-pile performance of nuclear fuels is strongly dependent on their thermophysical properties. The knowledge of thermophysical properties of the fuel as a function of temperature are essential and must be well known in order to effectively model and predict fuel performance under normal and off-normal irradiation conditions [15]. The data on out-of-pile thermophysical properties such as melting point/solidus temperature, thermal conductivity, coefficient of thermal expansion, specific/molar heat capacity etc. of the fuel are important for fuel design and safety analysis. The variations of these properties as a function temperature are dependent on chemical composition, phase content, and microstructure of fuels. The solidus temperature, thermal conductivity, heat capacity, and coefficient of thermal expansion of nuclear fuels are required to evaluate their thermal performance. The solidus temperature of the fuel is considered as an important safety temperature and it depends on the fuel composition (at fixed pressure). The thermal conductivity of fuel plays major role in deciding the temperature profile which in turn influences various important processes such as swelling, grain growth, fission gas release etc.

Chapter 1: Introduction

[11]. The thermal conductivity also determines the maximum linear heat rating (LHR) of the fuel without causing center melting. Molar/specific heat capacity is an intensive property that determines/quantifies the amount of heat required to raise the fuel's temperature. The molar heat capacity data can be used to estimate the stored energy in the fuel during any potential accident scenarios, to calculate thermal conductivity of fuel using the experimentally measured data of thermal diffusivity and density. It is considered as a basic thermodynamic parameter commonly used to estimate the various thermodynamic functions like molar enthalpy increment, molar entropy increment of the fuels as a function of temperature. The coefficient of thermal expansion (CTE) is an important parameter for nuclear fuel materials. The thermal expansion data are useful to understand the stresses occurring between fuel and cladding on change in temperature [11]. Significant variation between thermal expansion data of fuel and cladding may cause accumulation of stresses during the thermal cycling and that may lead to cladding deformation. When the fuel element is brought to power, the gap between fuel and cladding is related to the difference between their coefficients of thermal expansion. Hence, precise knowledge of CTE data of the fuel is necessary/essential for modeling fuel performance in nuclear reactor. The CTE data can be utilized to evaluate the variation of fuel density as a function of temperature. Higher thermal expansion leads to a higher volume increase and that causes lowering of the density of the fuel system. This in turn increases the neutron leakage of the reactor core and allows for negative feedback of the system. Considering the usefulness of those properties for reactor application, few important thermophysical properties such as solidus temperature, thermal expansion, heat capacity of the alloy samples have been measured and presented in this thesis.

The physical properties such as density, thermal conductivity, thermal expansion, specific heat capacity of various U-rich U–Zr, U–Nb and U–Mo alloys have been discussed in an earlier

Chapter 1: Introduction

report edited by Fackelmann et al. [72]. In a recent work, Balakrishnan et al.[73] reported the solidus and liquidus temperatures of the U–Zr system using spot-technique. Thermal expansion of a series of U-rich U–Zr and U–Mo alloys after different heat treatments have been studied earlier by Saller et al. [74] using dilatometer. The thermal expansion data of as-cast U-rich U–Zr alloys was also studied by Basak et al. [37] using dilatometer. The molar/specific heat capacity data of different U–Zr alloys were reported in the literature by Fedorov and Smirnov [75] (for 5.42, 21, 37.48, 50.89, 75.62 wt% Zr compositions), Takahashi et al. [76] (for 5.87, 17.11, 49.64, 79.5 wt% Zr) and Matsui et al. [77] (for U–8.74Zr). In a recent paper, the specific heat capacities of U–Zr, U–Nb, and U–Zr–Nb alloys with total of 7 wt% alloying element were measured by Dash et al. [78]. The heat capacity data of few binary U-rich U–Mo alloys were also reported by Parida et al. [79] (for U–8Mo alloy) and Matsui et al. [77] (for U–9.15Mo alloy). The specific heat capacity, coefficient of linear thermal expansion, and other thermophysical properties of DU–10Mo were reported by Burkes et al. [21]. Although, there are few literature reports available for U-rich binary U–Zr, U–Nb, U–Mo alloys, the thermophysical investigation particularly on U–Zr–Nb, U–Zr–Mo alloy systems are limited in the literature. In the present thesis, a systematic study on the evaluation of various thermophysical properties of U–6(Zr+Nb) and U–6(Zr+Mo) alloys has been carried out.

1.7. Cladding material for metallic fuelled fast reactor

Until the 1970s, austenitic stainless steels were used for fast reactor structural material and as fuel cladding. High void swelling limits the use of the austenitic steels as cladding and other in-core applications. The higher target burnup conditions for liquid-metal-cooled fast reactor offer a challenge for engineers and designers to develop a suitable structural and cladding material with better strength and lower void swelling. Ferritic/martensitic steels with 9–12% Cr

Chapter 1: Introduction

such as HT9, T91 etc. are contemplated as possible structural and/or cladding materials. T91 grade steel is proposed to be used as the cladding of metallic fuel for future fast reactor in India. T91 cladding material is a low carbon 9Cr-1MoVNb steel having ferritic-martensitic structure [80, 81]. This type of steel is considered a potential cladding material for future fast reactor due to its excellent irradiation resistance to void swelling in comparison to austenitic stainless steels, lower thermal expansion coefficient and higher thermal conductivity than those of austenitic stainless steels [80, 82-84]. The composition of T91 is given in the Table 1.6.

C	Mn	P	S	Si	Cu	Ni	Cr	Mo	Al	Nb	V	Ti	N	Fe
0.099	0.368	0.015	0.0013	0.209	0.068	0.197	9.161	0.882	0.008	0.079	0.207	0.003	0.0457	balance

The normalizing of T91 steel was carried out by heating at 1323 K for 75 min followed by cooling in air. Then the steel was tempered at 1043 K for 70 min followed by air cooling. Normalizing consists of austenitizing by annealing the steel above the equilibrium temperature where ferrite (bcc structure) transforms to austenite (fcc structure), which is followed by cooling in air. This heat treatment leads to formation of martensite (body-centered tetragonal structure). Normalized steel is then tempered to enhance toughness and ductility. The tempering of the steel leads to formation of $M_{23}C_6$ ($M = Cr, Fe, \text{ and } Mo$) and MX ($M = V \text{ and } Nb, \text{ and } X = C \text{ and } N$) precipitates in ferrite (bcc) matrix. During irradiation, the high-energy neutron in a fast reactor displaces atoms from their normal positions and forming vacancies and interstitials. The 'displacement damage' is expressed/measured as displacements per atom (dpa). The mechanical properties of a material can be affected significantly by the irradiation damage. The progressive damage with both irradiation dose and temperature may cause agglomeration of vacancies and

Chapter 1: Introduction

interstitials into voids, dislocation loops and these processes finally lead to swelling. Swelling is defined as $\Delta V/V_0$, where ΔV and V_0 are volume change and original volume, respectively. In addition, the irradiation-induced segregation and precipitation may also occur. The swelling characteristic of various steels has been demonstrated in the EBR-II and FFTF and it was observed that the extent of swelling is significantly higher in austenitic stainless steel (316 SS) compared to ferritic or ferritic/martensitic steels [80, 81].

1.8. Fuel-cladding chemical interaction

Apart from phase stability and thermophysical properties of metallic fuels, the knowledge of chemical compatibility between fuel and cladding is also essential for their successful application in fast reactor. The chemical compatibility between fuel and cladding also known as fuel-cladding chemical interaction (FCCI) is considered as one of the major concerns in the application of the metallic fuel in fast reactors. During irradiation, the fuel material undergoes swelling and the fuel comes in direct contact with the cladding material after achieving few at.% burnup. This in turn promotes interdiffusion between fuel and cladding components, resulting to develop an interdiffusion layers with various possible intermetallic phases which may adversely affect the structural integrity of cladding [85]. Furthermore, the load bearing capability of the cladding tube may be reduced because of thinning of cladding caused by the formation of the interfacial diffusion layer. FCCI is of prime importance since it may limit the life of fuel pin by forming a low melting eutectic between fuel and cladding components at temperatures substantially lower than the melting point of the fuel alloys. From the standpoint of accident transients, there is a possibility of accelerated rate of cladding attack, once eutectic liquefaction occurs at the interface. Hence, eutectic liquefaction temperature arising from FCCI at the fuel-cladding interface is considered as a crucial safety parameter to set cladding temperature limit for

Chapter 1: Introduction

the use of metallic fuels in fast reactors. For reliable and smooth reactor operation, the fuel elements must be resistant to breaching even in case of overpower transients. FCCI is a multi-component diffusion problem in which a number of alloying elements of both fuel and cladding materials are involved. FCCI, a complex phenomena, depends on various factors like fuel composition, type of cladding materials of different grades, fuel-cladding interfacial temperature, linear power rating, burnup, fission products etc. [86, 87]. Generally, FCCI can be mitigated in two possible ways i.e. either by alloying of uranium or by using a suitable barrier layer in between fuel and cladding. Zr metal was found to be a suitable choice to mitigate the FCCI problem in metallic fuel. The best way to examine FCCI is to conduct the chemical compatibility test with the help of diffusion couple experiment at various temperatures which are relevant to both normal and off-normal thermal events of reactor. Another approach to investigate the chemical compatibility is by differential thermal analysis in which the reaction temperature can be measured accurately. In the present investigation, the fuel-cladding chemical compatibility between U–Zr alloy and T91 steel cladding has been tested using both the approaches.

The diffusion behaviour of U–Zr alloy with Fe, Fe–Cr, Fe–Ni–Cr, austenitic (SS316 and D9), ferritic-martensitic (HT9) were investigated by many authors [85, 88-93] in order to examine their chemical compatibility. It may be noted here that high void swelling of austenitic steels cladding at high burnup make them unsuitable for use in metallic fuel application and therefore the FCCI problem of metallic fuel with austenitic type cladding steels might be largely of academic interest [8]. On the other hand, FCCI between U–Zr alloy and ferritic/martensitic steels such as HT9 and T91 is of prime importance as these steels are more suitable for high burn-up application due to their excellent swelling resistance characteristics. The literature data on the interdiffusion behaviour between ferritic/martensitic steels and U–Zr alloy mainly

Chapter 1: Introduction

emphasizes on HT9 cladding steel and U–10Zr alloy fuel. The interdiffusion behaviour between U–10Zr alloy and HT9 in the temperature range 973-1073 K was reported by Keiser et al. [91, 92], Lee et al. [93], Ryu et al. [94], Kim et al.[95], and Yang et al. [96]. On the other hand, the diffusion behaviour between U–10Zr and T91 was investigated only at 1013 K and 1073 K by Ryu et al. [94]. It appears that the systematic investigations particularly on the chemical interaction between U–Zr alloy and T91 steel are limited and hence requires further detailed investigation. Therefore, a detail investigation on FCCI between these two materials was carried out in the present investigation.

1.9. Research goals and objectives of the present work

The present work is a part of metallic fuel development programme for future fast reactors in India. Metallic fuels with relatively low alloying content (Zr ~6 wt%) is preferred with an objective of achieving higher breeding potential. From that prospective, the total alloying elements i.e., Zr and Nb (or Mo) in the uranium alloys is restricted to 6wt% in the present investigation. An in-depth knowledge on phase stability, phase transformation and thermophysical properties of fuel materials are essential in order to effectively design and predict their performance under normal and off-normal irradiation conditions. Therefore, a detailed study on the phase stability, microstructure evolution, phase transformation, thermophysical properties, microhardness of U–Zr–Nb alloys with total alloying content of 6 wt% has been investigated and discussed in chapter 3. A similar study on U–Zr–Mo alloys with 6 wt% alloying content has been carried out and presented in Chapter 4. The effects of Nb and Mo additions on the various properties of U–Zr alloys have been addressed in these chapters. It is also essential to know the equilibrium phase(s) of a fuel along with the equilibrium phase transformation behaviour. Therefore, the phase stability and phase transformations of those alloys under near-

Chapter 1: Introduction

equilibrium condition has been investigated and described in Chapter 5. The fuel material should have good chemical compatibility with the cladding. The fuel-cladding chemical interaction is considered as one of the major issues in metallic fuelled fast reactor. To address this issue, the compatibility test between U–Zr alloy and T91 steel under normal and accidental conditions has been extensively investigated and presented in chapter 6. Finally all the findings are summarized in chapter 7.

Chapter 2

Experimental techniques

2.1. Introduction

The techniques/methods employed for preparation of alloys and their characterization and thermo-physical property evaluation are briefly described in this chapter. A DC arc-melting furnace has been used to prepare the uranium based alloys. The alloy samples have been thoroughly characterized using techniques like X-ray Diffraction (XRD), Scanning Electron Microscopy (SEM) equipped with Energy Dispersive X-ray Spectroscopy (EDS). The phase transformation behaviour of the samples has been determined using Differential Thermal Analyzer (DTA). The thermo-physical properties like thermal expansion and molar heat capacity of the samples have been measured by dilatometer and Differential Scanning Calorimeter (DSC), respectively. The hardness data of the samples has been measured using a microhardness tester. The fuel-cladding chemical compatibility studies of selected alloy samples have been conducted using diffusion couple experiment.

2.2. Alloy sample preparation

2.2.1. Alloy melting

The alloy samples were prepared by alloying nuclear grade uranium with Zr, Nb and Mo with appropriate weight percentage. Nuclear grade uranium rod and crystal bar of zirconium produced at BARC were used for alloy preparation. Niobium and molybdenum pure metal rods were procured from Alfa Aesar. The chemical purity of these alloying elements is better than 99.9%. Alloying was performed by melting these constituent elements in an electric arc-melting furnace in high purity argon atmosphere (purity 99.999% supplied by M/s Six Sigma Gases India Pvt. Ltd., Mumbai, India) in a copper hearth and tungsten electrode. In the DC mode of arc

Chapter 2: Experimental techniques

melting furnace, the tungsten electrode acts as cathode and the bottom of the furnace acts as anode. There are three major parts in the arc furnace: power source (TIG-600Amp), vacuum pumps and chiller unit. The vacuum unit consists of rotary and diffusion pumps. The chiller unit circulates the cold water to both the copper hearth and the electrodes. Melting of samples occurs by the heat of electric arc struck between a tungsten electrode and metals placed in the crucible. After the melting and solidification, the arc-melted ingots were inverted and re-melted repeatedly for at least 6 times to ensure chemical homogeneity. Before actual melting operation, the furnace chamber was evacuated (upto $\sim 1 \times 10^{-5}$ mbar) and then thoroughly flushed with high purity argon gas repeatedly to remove the oxygen/moisture impurity in the chamber. In general, melting of any U, Zr containing alloy sample poses difficulty owing to their extreme reactivity to traces amount of oxygen. Hence, proper precaution was taken prior to actual alloy sample preparation by melting a sacrificial Zr button, which acts as an oxygen getter.

2.2.2. Heat treatment

For heat treatment, the as-cast alloy samples were wrapped in tantalum foil and then encapsulated in evacuated quartz tubes. Each tube was evacuated and flushed with helium gas for several times before it was sealed. The sealed samples were then homogenized at 1173 K for 50 h and then quenched in water kept at room temperature. After homogenization and quenching, the samples are referred to as water-quenched samples. The homogenization and subsequent quenching were carried out to bring in complete chemical and microstructural uniformity in the samples and also to check the possibility of retention of high temperature phase at room temperature. Each sample was then cut into two pieces for further heat treatment. One piece of sample with tantalum wrapping was again sealed in evacuated quartz capsule after purging with helium and then heated at 1173 K followed by slowly cooling to room temperature keeping the

Chapter 2: Experimental techniques

sample inside furnace. After this treatment, the samples are referred to as furnace-cooled samples. The alloys were also subjected to various other treatments as per the requirement and those details will be discussed afterwards.

2.2.3. Impurity Analysis

The carbon, oxygen and nitrogen (C, O, N) impurities content in the alloy samples were analyzed. Carbon content in the alloys was analyzed by carbon analyzer using combustion technique. Oxygen and nitrogen contents were determined by oxygen-nitrogen sequential analyzer based on inert gas fusion technique. The results of the analysis are presented in Table 2.1. It was found that the samples are having approximately 400-550 ppm of C, 150-210 ppm of O and <50 ppm of N impurities.

Sample	C (ppm)	O (ppm)	N (ppm)
U-6Zr	400	150	<50
U-4Zr-2Nb	420	150	<50
U-2Zr-4Nb	480	170	<50
U-6Nb	410	160	<50
U-4Zr-2Mo	550	210	<50
U-2Zr-4Mo	520	150	<50
U-6Mo	490	160	<50

2.3. Characterization techniques

2.3.1 X-ray Diffraction (XRD)

X-ray diffraction (XRD) is a powerful analytical technique primarily used for phase identification of a crystalline material and information on unit cell dimensions. Each crystalline solid has its own characteristic XRD pattern which may be used as a 'fingerprint' for its identification [97]. The technique is used to characterize materials based on their X-ray

Chapter 2: Experimental techniques

diffraction patterns. In general, the crystals, with their regularly repeating structures, are capable of diffracting radiation which has a wavelength similar to interatomic separations, $\sim 2\text{--}3 \text{ \AA}$ [98]. In other words, the crystalline materials act as three-dimensional diffraction gratings for X-ray which has wavelengths similar to the spacing of planes in a crystal lattice. The X-ray wavelengths commonly used for diffraction are in the range of $0.7\text{--}2.3 \text{ \AA}$ for the study of crystal structures and atomic spacing. When an incident beam of monochromatic X-rays interacts with a crystalline material, the scattering of X-rays occurs primarily from electrons of atoms within the material. The scattered X-rays undergo constructive and destructive interference and this process is known as diffraction. X-ray diffraction is related to constructive interference of monochromatic X-rays and crystalline sample. In a periodic arrangement of atoms in crystalline material, the diffraction of monochromatic X-rays takes place only at particular angles of incidence which satisfy Bragg's law.

$$n \lambda = 2d_{hkl} \sin\theta \quad (2.1)$$

where n is an integer, the order of the reflection, λ is the wavelength of the X-ray beam and d is the spacing between diffracting planes ($h k l$), θ is the angle of incidence at which diffraction occurs, also called the Bragg angle. When the geometry of the incident X-rays impinging the sample satisfies the Bragg's law, a peak in intensity in the diffracted X-rays occurs because of constructive interference. The directions of diffractions are determined solely by the shape and size of the unit cell of the material. The intensities of diffracted beams depend on the positions of the atoms within the unit cell [97]. However, most of the materials are not used as single crystals, but polycrystalline forms where many tiny crystallites oriented in all possible directions. Hence, the X-ray beam will interact with all possible interatomic planes of a polycrystalline material with randomly oriented crystallites. If the experimental angle is systematically changed, all

Chapter 2: Experimental techniques

possible diffraction peaks from the sample will be detected. A typical X-ray diffractometer consists of three basic elements i.e., an X-ray tube, a sample holder, and an X-ray detector. The X-rays produced by a cathode ray tube are filtered to make monochromatic, collimated to concentrate, and then directed toward the specimen. A detector records and processes this diffracted X-ray signal and converts the signal to a count rate. A typical diffraction pattern of a sample is basically a plot of 2θ (horizontal axis) vs. intensity (vertical axis). The XRD diffraction pattern can be used for phase identification, to determine unit cell parameters, preferred orientation, crystallite size and microstrain etc.

In the present work, samples were characterized by powder X-ray Diffraction (XRD) technique using a Rigaku Miniflex-600 X-ray diffractometer with Bragg-Brentano focusing geometry and crystal curved graphite monochromator. Cu $K\alpha$ radiation ($\lambda = 1.5406 \text{ \AA}$) was used for XRD measurement. The data was collected within the $20\text{--}100^\circ$ range with scan rate of 1°min^{-1} at 40 kV and 15 mA for phase identification and quantification. Specimens for XRD analysis were prepared by cutting with a slow speed cut-off wheel and then carefully polished to get a mirror finish. The uranium based alloys are reactive in nature and a thin oxide layer may form on the surface of the samples in air. To avoid this, the XRD examinations were conducted immediately after polishing. The X-Ray diffraction (XRD) patterns were analyzed by Rietveld refinement method using 'MAUD' program [99].

2.3.2. Metallographic practice

For metallographic sample preparation, the heat treated alloy samples were cut into pieces using slow speed SiC abrasive cut-off wheel with water as coolant. The samples were then mounted with cold mounting self-setting resin and then grounded in water resistant SiC abrasive paper of different grit size under constant flow of water. Water is used here as coolant and the

Chapter 2: Experimental techniques

wet grinding in flowing water is recommended here to avoid any unwanted heat generation and to avoid fire hazard of pyrophoric fine powder from uranium alloys generated during grinding. Final grinding was carried out in 2400 grit paper using water as coolant which is followed by polishing up to 1 μm surface finish using diamond slurry in alcohol based lubricating media. The polished samples were subjected to electrolytic etching to reveal their microstructure. For electro-etching, an etching pot made of SS 304 was used as cathode and 10% oxalic acid aqueous solution was chosen as electrolyte. Electro-etching was carried out by applying a constant potential of $\sim 3\text{-}4\text{V}$ for 3-5 s. After that, the samples were properly cleaned with soap solution and alcohol and made them ready for microstructural investigation.

2.3.3. Scanning Electron Microscopy (SEM) & Energy Dispersive Spectroscopy (EDS)

Scanning electron microscope (SEM) is one of the most versatile equipments used for investigating the microstructure of materials. SEM produces an image by scanning the surface of a sample with a focused electron beam. The beam electrons interact with the constituent elements in the sample, producing various signals including secondary electrons (SE), backscattered electrons (BSE), diffracted backscattered electrons (EBSD), X-Rays, Auger electrons, cathodoluminescence and heat. The signals of secondary electrons and backscattered electrons are normally used for producing images of samples. The secondary electrons (SEs) are electrons ejected from atoms in the specimen by inelastic scattering with beam electrons. Backscattered electrons (BSE) are beam electrons that are reflected or back-scattered out of the specimen by elastic scattering with specimen atoms. SEs are the primary signals to observe morphology and topography on samples while BSEs provide elemental contrasts in multiphase samples and easily discriminate the phases with compositional variations. The characteristic X-rays that are emitted from sample atoms due to electron-sample interaction can be detected in X-

Chapter 2: Experimental techniques

ray energy-dispersive spectroscopy (EDS) and the x-ray signals are used for compositional analysis to map the distribution and estimate the abundance of elements in the sample.

In the present investigation, scanning electron microscope was operated at acceleration potential of 20 kV for microstructural and elemental analyses. For various microstructural features, both SE and BSE images of the samples were thoroughly analyzed. SE images were recorded using Everhart–Thornley (E-T) secondary electron detector and BSE images were recorded using solid state back scattered electron detector. The energy dispersive spectroscopy (EDS) with Peltier-cooled silicon drift detector (SDD) (50 mm²) has been utilized for elemental analysis. The EDS was operated in various modes like point analysis, line scan and elemental mapping to identify the composition of phases and elemental distribution in the samples.

2.4. Thermal analysis and thermo-physical properties measurement

Thermal analysis (TA) is a group of analytical techniques in which a physical property of a substance is monitored against time or temperature whilst the substance is subjected to a controlled temperature programme [100]. Thermal properties describe the response of a material to the application of heat. The various properties that can change include mass, energy, dimension, phase change, mechanical behavior etc. The most common techniques are differential thermal analysis (DTA), differential scanning calorimetry (DSC), thermogravimetric analysis (TGA), Dilatometer etc. In the present investigation, physical properties like the solidus/liquidus temperatures, solid-state phase transformation temperatures, coefficient of thermal expansion, and molar heat capacity of the samples were determined using thermal analysis techniques.

2.4.1. Differential thermal analysis (DTA)

DTA is a thermal analysis technique in which temperature differences between sample and reference material recorded during programmed heating and cooling cycles. Sample and

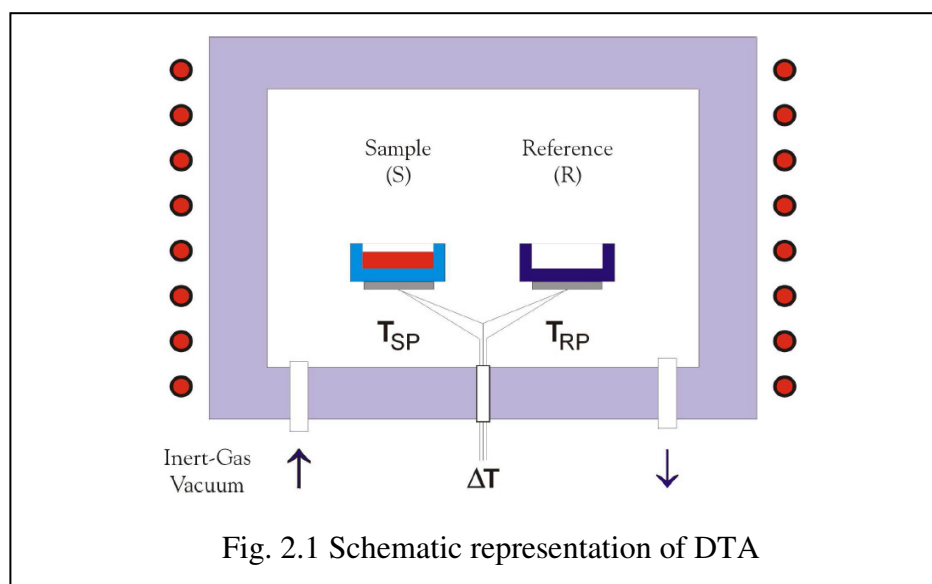
Chapter 2: Experimental techniques

reference material are symmetrically placed and heated in one furnace. The temperature difference between sample and reference (ΔT) are recorded by two thermocouples in contact with the underside of the sample and the reference crucibles. The reference material chosen for DTA experiment should satisfy the following criteria: it should not undergo any thermal events over the selected temperature range, should not react with any component of equipment, and should have similar heat capacity and thermal conductivity to the sample. The use of reference material may be avoided by keeping the reference crucible empty. The temperature difference (ΔT) should be zero when no thermal event occurs in the sample and $\Delta T \neq 0$ during any thermal event occurred in the sample. ΔT is negative for an endothermic and positive for an exothermic thermal event. The DTA curve is a plot of ΔT versus temperature (T) or time (t). Generally, the output from the thermocouple is recorded as e.m.f. and hence, the ΔT in DTA curve is expressed as the e.m.f. (μV) in most cases. A schematic of DTA equipment are presented in Fig. 2.1.

In the present study, the DTA equipment (Model No. Setsys Evolution 24, combined TG/DTA/DSC; make: M/s Setaram Instrumentation, France) has been extensively used to determine the various phase transformation temperatures and solidus/liquidus temperatures of uranium based alloys. For DTA experiments, a small piece of sample of ~ 200 mg was cut from each heat treated alloy and then the surface of the sample was properly cleaned to remove oxide layer. The sample was loaded into Al_2O_3 crucible with an inner coating layer of Y_2O_3 . The thin coating of Y_2O_3 inside Al_2O_3 crucible was purposely used to provide a diffusion barrier between the sample and crucible particularly at higher temperature. Uranium-based alloys are highly reactive in nature and hence highly purity inert atmosphere is essential for carrying out DTA of these alloys. Before the actual experiment, the furnace and sample chambers were evacuated with a standard mechanical pump and backfilled with high purity argon gas repeatedly to remove

Chapter 2: Experimental techniques

oxygen/air impurity from the analyzing chamber. During the actual experiment, highly purified argon flowing at 20 ml min^{-1} was used as carrier gas in the sample chamber and the protective gas in the furnace chamber. In addition to that, commercially available moisture/oxygen trap system was installed in the argon gas line for further purification. It may be noted here that the DTA equipment used for the present study was installed inside leak tight glove-box with inert cover gas and this arrangement may also help to minimize the oxidation of sample. The rate of heating and cooling were programmed mostly at 5 or 10 K min^{-1} . The temperature calibration is considered as an important step in DTA operations and calibration was carried out with standard materials. The recorded thermograms of heating and cooling cycles of all the samples were presented and analyzed.

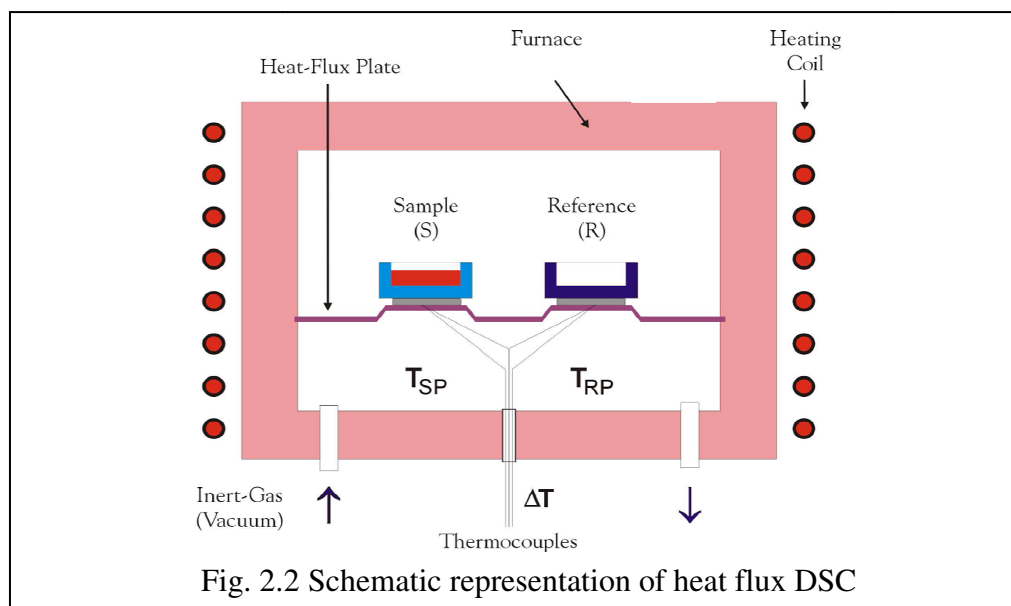


2.4.2. Differential scanning calorimetry (DSC)

Differential Scanning Calorimetry (DSC) measures the change of the difference in the heat flow rate (Power) to the sample and to a reference material while they are subjected to a controlled temperature program. There are two basic types of DSC: the power-compensated DSC and the heat flux DSC. The primary measurement signal is temperature difference (in form of a

Chapter 2: Experimental techniques

voltage) and the resulting heat flow rate Φ is proportional to the temperature difference. The power compensation DSC consists of two identical micro-furnaces, one for sample and other for reference. Both the furnaces are separately heated and the DSC unit always maintains a thermal null state ($\Delta T=0$). When a thermal event takes place in the sample, there will be an increment or decrement of the temperature in reference furnace. The compensating heating power is supplied to the furnaces to maintain sample temperature same as that of reference. The compensating heating power is actually the heat flow rate difference. On the other hand, a heat-flux DSC unit consists of one furnace and two crucibles (one for sample and other for reference) with thermocouples like DTA unit. The sample and reference materials in respective crucibles are placed in the same furnace. Unlike DTA, the sample and reference crucible in heat-flux DSC are connected with a low resistance heat-flow path via a metal disk and the heat flux DSC is also called quantitative DTA. A schematic of heat-flux DSC equipment are presented in Fig. 2.2.



Both DTA and heat-flux DSC are similar in measuring thermal event and used to determine the liquidus/solidus line and other phase transition points. DTA can operate at higher temperature

(>1000°C), or in aggressive environments, where true heat-flux DSC may not be able to operate. On the other hand, DSC equipment can be utilized for measuring quantitative data for energy and thermodynamic parameters such as enthalpy and specific heat etc. In the present study, heat-flux DSC was utilized mainly for measuring heat capacity of the alloys.

2.4.3. Heat capacity

Heat capacity of a substance is defined as the amount of heat required to raise the temperature of the substance by unit degree. When a heat input ΔQ raises the temperature of a substance by ΔT , then the approximate mathematical expression of heat capacity is given by

$$C = \lim_{\Delta T \rightarrow 0} \left(\frac{\Delta Q}{\Delta T} \right) \quad (2.2)$$

The heat capacity at constant volume (C_v) can be defined as

$$C_v = \lim_{\Delta T \rightarrow 0} \left(\frac{\Delta Q}{\Delta T} \right)_v = \lim_{\Delta T \rightarrow 0} \left(\frac{\Delta U}{\Delta T} \right)_v = \left(\frac{\partial U}{\partial T} \right)_v \quad (2.3)$$

The heat capacity at constant pressure (C_p) can be defined as

$$C_p = \lim_{\Delta T \rightarrow 0} \left(\frac{\Delta Q}{\Delta T} \right)_p = \lim_{\Delta T \rightarrow 0} \left(\frac{\Delta H}{\Delta T} \right)_p = \left(\frac{\partial H}{\partial T} \right)_p \quad (2.4)$$

where 'U' and 'H' denote the internal energy and enthalpy of the system.

It is really difficult to keep the volume constant of a solid during temperature change and hence, direct measurement of C_v is difficult and it can be determined theoretically. Most of the experiments carried out in the laboratory are at constant pressure and the experientially measured heat capacity is basically C_p . The heat capacity per unit mass of substance is normally considered as the specific heat of the substance and is expressed as $C_p = C/m$ where m is the mass of the sample. The specific heat capacity is defined as the quantity of heat required to raise the temperature of unit mass of the substance by one Kelvin. Similarly, the molar heat capacity ($C_{p,m}$) is defined as the amount of heat energy required to raise the temperature of one mole of a

Chapter 2: Experimental techniques

substance by one Kelvin. The molar heat capacity of a substance ($C_{p,m}$) is obtained by multiplying the specific heat capacity with molecular mass of the sample.

The molar heat capacities at constant volume ($C_{v,m}$) and at constant pressure ($C_{p,m}$) of a solid material are thermodynamically related as

$$C_{p,m} - C_{v,m} = \frac{V_m \alpha^2 T}{\beta} \quad (2.5)$$

where V_m , α , β represent the molar volume, thermal expansion coefficient, compressibility, respectively and T temperature in K. In the present investigation, a heat flux type DSC has been employed for the measurements of molar heat capacity.

2.4.3.1. Molar heat capacity measurement using differential scanning calorimeter (DSC)

Measurement of molar heat capacity of the alloy samples were carried out using a heat flux-type DSC (Netzsch DSC 404 F3). The temperature and energy calibration of the instrument were accomplished by measuring melting point and enthalpy of fusion of high purity standard metals e.g., In, Bi, Sn, Zn, Al, Ag and Au. The molar heat capacity measurements were carried out after sectioning the samples into small discs of ~10–100 mg with a flat surface in order to facilitate perfect thermal contact with crucible. Two identical Pt-Rh metallic crucibles with an Al_2O_3 liner (PtRh/ Al_2O_3) and covering lids were used as containers for sample and reference materials. PtRh crucibles with Al_2O_3 liner were purposely chosen for getting the advantages of metallic crucible and to prevent reaction between the sample and crucible material. The Classical three-step method in the continuous heating mode was employed for molar heat capacity measurement and the synthetic sapphire was used as the reference material. After the sample loading, the DSC chamber was evacuated and backfilled with high purity argon gas for several times to remove oxygen/air impurity. The high purity argon gas used for measurement was passed through a moisture/oxygen trap system for further purification. The measurement was

Chapter 2: Experimental techniques

carried out by three consecutive runs. The first run was conducted by keeping both sample and reference crucibles empty and the heat flow as a function of temperature was recorded. In the second run, the heat flow data was recorded by loading synthetic sapphire into the sample side, keeping the crucible in the reference side empty. The third run was carried out by loading the actual sample into the sample crucible and keeping the reference crucible empty. For all the three runs, heat flow as a function of temperature was recorded in the temperature range of 323-823 K using a scanning rate of 10 Kmin⁻¹ and high purity argon as a carrier gas with a constant flow rate of 50 ml min⁻¹. The heat capacity of sample, C_p at a given temperature was determined by comparing the recorded data of heat flow rates of the blank, sample and reference runs.

The molar heat capacity of the sample, $C_{p,m}^0(T)_{\text{Sample}}$, was calculated using the following equation:

$$C_{p,m}^0(T)_{\text{Sample}} = \frac{C_p^0(T)_{\text{Ref}} \cdot (\Phi_{\text{Sample}} - \Phi_o) \cdot m_{\text{Ref}}}{(\Phi_{\text{Ref}} - \Phi_o) \cdot m_{\text{Sample}}} \times M_{\text{Sample}} \quad (2.6)$$

where $C_p^0(T)_{\text{Ref}}$ is the specific heat capacity of reference material sapphire, and m_{Sample} and m_{Ref} represent mass values of sample and reference, respectively, and Φ_o , Φ_{Sample} and Φ_{Ref} are the respective heat flow rate for blank, sample and reference runs. M_{Sample} is molar mass of the sample. The accuracy of the DSC measurements was checked by measuring the molar heat capacities of standard molybdenum metal (SRM) in the temperature of 323–1073 K with a heating rate of 10 K min⁻¹ and found to be within $\pm 1.5\%$ of the reported values.

2.4.4. Thermal expansion

The thermal expansion of a material is defined as relative change in dimension per unit temperature rise. It is also known as bulk thermal expansion. The bulk thermal expansion coefficient (α_l) is defined as

Chapter 2: Experimental techniques

$$\alpha_l = \frac{L_T - L_0}{L_0 (T - T_0)} = \frac{\Delta L}{L_0 \Delta T} \quad (2.7)$$

where L_T represents the length of the material at temperatures T and L_0 represent reference length of the material at reference temperature T_0 . α_l has units of reciprocal temperature $^{\circ}\text{C}^{-1}$ or K^{-1} . The parameter is called linear coefficient of thermal expansion. Similarly, the volume change of a material with temperature can be expressed as

$$\alpha_v = \frac{\Delta V}{V_0 \Delta T} \quad (2.8)$$

where α_v represents the volume coefficient of thermal expansion. ΔV and V_0 indicate the volume change and the original volume, respectively.

From the atomic perspective, thermal expansion of a material can be attributed to an increase in the average interatomic distance between the atoms. This origin of thermal expansion can be best explained using potential energy versus interatomic spacing curve for a solid. The atoms in the crystal vibrate about their mean positions in equilibrium. The vibrational amplitude increases with increase in temperature of the material. The average interatomic distance is defined by the mean position of atomic vibration. The increase in average value of interatomic separation with rising temperature is due to asymmetric (anharmonic) nature of interatomic interaction potential, rather than the increase in atomic vibration amplitude. In other words, the increase in the average value of interatomic separation, i.e. thermal expansion is associated with the asymmetric (anharmonic) shape of interatomic potential. In general, higher atomic bonding energy leads to a deeper and narrower potential energy trough. As a result of that the increase in interatomic spacing with a given rise in temperature will be lower and causing smaller value of thermal expansion. Thermal expansion of a solid depends on the nature of the chemical bond, mass of the vibrating atoms, crystal structure, melting point etc. The bulk thermal expansion of a

Chapter 2: Experimental techniques

material can be determined directly by measuring the change of dimension with temperature and the expansion data is used to calculate the coefficient of thermal expansion. In this study, bulk thermal expansion has been measured using dilatometry.

2.4.4.1. Bulk thermal expansion using dilatometry

Thermal expansion of the alloy samples has been measured employing a high temperature vertical dilatometer (make: SETARAM Instrumentation, France; model: Setsys Evolution 24). Specimen of approximately 5 mm × 5 mm × 10 mm size were cut from the alloys and then properly cleaned to remove surface oxide layer. The sample was placed inside a sample holder-push rod assembly which is made of Al₂O₃ and a nominal load of 10 g was chosen to be applied by the push rod over the sample. Like DTA/DSC experiment, the analyze chamber was evaluated and purged with high purity argon gas for several times in order to remove oxygen impurity before heating the sample. The sample was then subjected to a controlled temperature program up to 1173 K with a heating rate of 10 K min⁻¹ and high purity argon atmosphere at a dynamic gas flow rate of 20 ml min⁻¹ was maintained throughout the experiment to avoid surface oxidation. The change in length of the sample with temperature was transmitted through the frictionless push rod to a linear variable differential transformer (LVDT) that converts the linear motion into the electrical signals. A blank run was also conducted without keeping any sample in identical experimental condition, to find the expansion of sample holder, push rod etc. which accounted for the expansion of the system. The recorded data of the blank run are needed for correcting the values of overall expansion. The dilatometer unit was calibrated by measuring the linear thermal expansion of NIST standard reference material (SRM) Tungsten and measured values were found within ± 1% of the reported data. The thermal expansion data of the sample

Chapter 2: Experimental techniques

alloy samples are presented by plotting length change (%) versus temperature and the average coefficient of thermal expansion (CTE) was determined using the following expression:

$$\alpha = \frac{L_2 - L_1}{L_1 (T_2 - T_1)} \quad (2.9)$$

where 'L₂' and 'L₁' represent length at temperatures 'T₂' and 'T₁', respectively.

2.5. Microhardness measurement

Hardness is generally defined as the resistance of a material to plastic indentation. It can be described as the ability of a material to resist permanent indentation or deformation when in contact with an indenter under load [101]. In microhardness testing, the applied loads are less than 1 kgf, and indentations can be observed only with the aid of a microscope. Knoop and Vickers (low-load) tests with a diamond indenter of specific geometry are in this category. In the present study, the microhardness of the metallographically prepared samples was measured using a microhardness tester (Model: Durascan 10, make: EMCO test, Austria) with the help of a Vickers diamond pyramid indenter. A load is applied smoothly, without impact, and held in contact for few seconds. After the removal of force/load, both diagonals of the indentation are measured accurately, and the average of the diagonal is taken to calculate the hardness value. The hardness (H) is related to the indentation diagonal by the following expression:

$$H_{(VHN)}(\text{kg mm}^{-2}) = \frac{1.854 \times P}{d^2} \quad (2.10)$$

where P is the applied load (kg) and d is the average diagonal (mm).

In this study, a load of 200 g was applied for dwell time of 10 s. Hardness values were measured at 8-10 different locations on each sample and the average value with standard deviation was presented as Vickers Hardness Number (VHN) throughout the thesis.

2.6. Fuel-cladding chemical compatibility test

The chemical compatibility between few selected U–Zr alloys and T91 steel has been

examined by two methods (i) differential thermal analysis and (ii) diffusion couple experiment.

2.6.1. Differential thermal analysis (DTA)

To investigate the chemical reaction between U–Zr alloy and T91 steel, DTA experiments were conducted by placing small discs of U–Zr and T91 one on top of the other in sample crucible. For these studies, total sample of ~200 mg was used by maintaining the ratio of U–Zr and T91 of approximately 5:1 to simulate fuel rich part of fuel-cladding system. Al₂O₃ crucible with an inner coating layer of Y₂O₃ was selected here to avoid any unwanted reaction between sample and crucible material. The experiment was carried out using highly purified argon carrier gas flowing at 20 ml min⁻¹ and both heating and cooling rates were programmed at 10 K min⁻¹. The other precautions for carrying out DTA experiment of reactive U-based samples were already mentioned in the section 2.4.1. A similar DTA experiment was also carried out with U metal and T91 steel for comparison. Thermograms recorded for both heating and cooling cycles were analyzed. After the DTA run, the reaction products were characterized by energy dispersive spectroscope (EDS) and electron back scattered diffraction (EBSD) attached to SEM.

2.6.2. Diffusion couple experiment

To carry out diffusion couple tests, U–Zr alloy was cut into discs of 3 mm thickness and T91 steel rod of the similar diameter was cut into 0.5 mm thick discs. The surfaces of all the samples were metallographically prepared by polishing up to 1 μm surface finish. For preparing diffusion couple, a disc of U–Zr alloy was sandwiched between two discs of T91 steel and these couples would be referred to as U–Zr/T91 couples. The components of the diffusion couples were placed inside fixtures of Inconel 600 in order to ensure intimate contact during heating. Any unwanted chemical interaction between couples and fixture was avoided by placing tantalum foil between them. The arrangement in diffusion couple-fixture assembly is shown

Chapter 2: Experimental techniques

schematically in Fig. 2.3. The fixtures containing these couples were encapsulated in quartz tube in helium atmosphere. Before encapsulation, the inside of the quartz tube was evacuated and purged with helium gas repeatedly to remove oxygen impurity. The diffusion couples were then annealed in a resistance heating furnaces at various temperatures in the range of 823–1003 K for duration up to 1500 h. The heat treatment schedule will be presented afterward in Chapter 6. Subsequent to annealing, the couples were mounted in cold setting resin and then sectioned using a slow speed diamond cutting wheel. The exposed cross sections were metallographically polished and the extent of diffusion reaction and phases formed at the interfaces were thoroughly characterized using SEM/EDS. The X-ray line scans of U, Zr, Fe, and Cr were acquired across the interfaces of the couples to measure the depth of penetration of each element accurately.

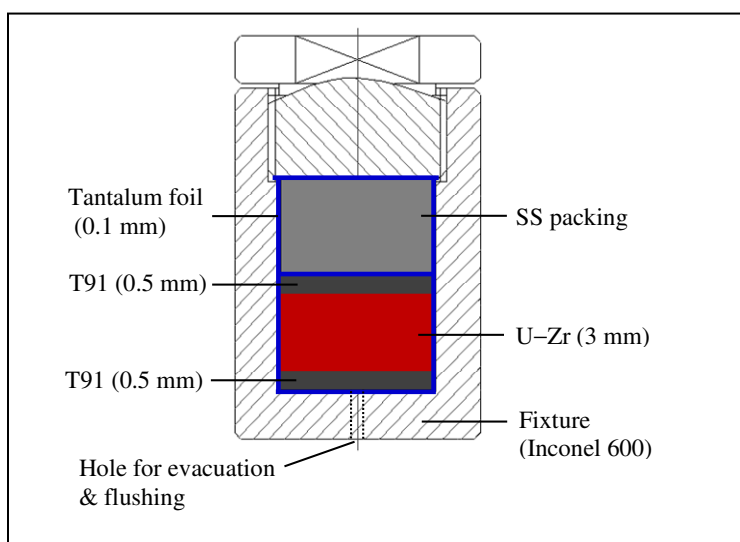


Fig. 2.3 Schematic diagram of the diffusion couple-fixture assembly for U-Zr/T91 couples.

Chapter 3

Structural, microstructural characterization and thermal properties of U-(6-x)Zr-xNb alloys (x = 0, 2, 4, 6 wt%)

3.1. Introduction

Uranium-Zirconium-Niobium (U-Zr-Nb) alloy system can be considered as a promising nuclear fuel for fast breeder reactors and other reactors such as research reactors, test reactors, and advanced high flux reactors, due to their various favourable properties. In the present investigation, U-6Zr, U-4Zr-2Nb, U-2Zr-4Nb and U-6Nb alloys with total alloying content of 6 wt% were chosen by gradually replacing Zr in U-6Zr alloy with equivalent amount of Nb in order to address effect of Nb addition. U-6Zr is considered here as the reference composition from the prospective of its application in future fast reactor. This chapter describes the structural and microstructural characterization, thermal analysis, thermophysical property evaluation, phase transformation behaviour and microhardness data of these alloys. All these results have been highlighted and compared with the reference composition of U-6Zr alloy.

3.2. Experimental procedure

The detailed experimental procedure related to sample preparation, heat treatment, structural and microstructural characterization, thermal analysis, thermophysical properties measurement, and microhardness of U-6Zr, U-4Zr-2Nb, U-2Zr-4Nb and U-6Nb alloys have been presented in Chapter 2. The present chapter mainly deals with furnace-cooled and water-quenched alloys.

3.3. Terminology and notations for various phases

Uranium alloys undergo various phase transformations from high temperature bcc γ phase to different equilibrium and martensitic phases depending upon their thermal history, alloy composition. In the present study, the various terminology and notations used for describing

different equilibrium and martensitic phases of U-Zr, U-Nb and U-Zr-Nb alloys are summarized as follows. Several variants of gamma phase are described by using the notations e.g., γ , γ_1 , γ_2 , γ_3 , and γ° . The term γ describes the high temperature equilibrium bcc phase for all the U-Zr, U-Nb and U-Zr-Nb alloys and this bcc- γ phase can be stabilized at lower temperature as metastable phase by proper alloying and cooling conditions. As mentioned earlier in Section 1.5.2 of Chapter 1, the terms γ_1 and γ_2 , two bcc phases with different compositions, define the miscibility gap in the U-Zr binary system. The miscibility gap in the U-Nb binary system is represented by γ_1 and γ_3 . The term γ_1 is applicable for U-rich bcc phase of both the U-Zr and U-Nb systems, γ_2 represents Zr-rich bcc phase for U-Zr system whereas the Nb-rich bcc phase of U-Nb system is designated as γ_3 . Similarly, (Zr+Nb)-rich bcc phases in ternary U-Zr-Nb alloys are also represented by γ_3 . The term γ_3 is purposely adopted here for U-Nb and U-Zr-Nb alloys (i.e., Nb-containing alloys) in order to avoid confusion with the γ_2 of the U-Zr system. The term γ° is used to describe the non-equilibrium tetragonal phase. Several variants of alpha phase are described by different notations like α , α' and α'' . The α -phase is basically an equilibrium orthorhombic phase. The non-equilibrium orthorhombic phase is referred to as α' with some deviation from equilibrium orthorhombic structure. The α'' notation defines the non-equilibrium monoclinic structure of uranium alloys.

3.4. Results

3.4.1. Structural Characterization

3.4.1.1. Furnace-cooled samples

The X-ray diffraction data of furnace-cooled U-6Zr, U-4Zr-2Nb, U-2Zr-4Nb and U-6Nb alloy samples are collectively presented in Fig. 3.1. The furnace-cooled U-6Zr alloy

consists predominantly of α phase that corresponds to orthorhombic α -U phase (space group Cmc_m). According to the binary U-Zr phase diagram (Fig. 1.2, Chapter 1), the equilibrium phases of U-rich U-6Zr alloy are orthorhombic α -U and hexagonal δ -UZr₂ at room temperature. However, most of the XRD peaks of δ -UZr₂ phase overlap with different peaks of α -U phase except few low intensity peaks at 2θ values of $\sim 46.5^\circ$ and $\sim 71.6^\circ$ corresponding to (111) and (112) planes of δ -phase, respectively. The magnified XRD plot of furnace-cooled U-6Zr alloy (Fig. 3.2) resolves the presence of very small peaks at 46.54° and 71.64° due to formation of small fraction δ -phase formation during furnace cooling. The XRD data of all the furnace-cooled samples were further subjected to analyses by Rietveld refinement to determine the lattice parameters, phase fraction of various phases formed in the samples and the refinement results are summarized in Table 3.1. The Rietveld refinement plot of U-6Zr alloy is presented in Fig. 3.3a. The phase fraction of δ -UZr₂ is found to be around 8 vol%. The XRD pattern of furnace-cooled U-4Zr-2Nb alloy corresponds to orthorhombic α -U phase. The non-overlapping peaks of δ -UZr₂ phase are absent in the XRD pattern. In addition to that, no additional peaks of bcc gamma phase are observed. The furnace-cooled U-2Zr-4Nb alloy is biphasic in nature consisting of orthorhombic α (space group Cmc_m) and bcc γ_3 (space group Im-3m) phases and the peaks of bcc γ_3 phase are marked by asterisk in the XRD data (Fig. 3.1). The Rietveld refinement results show that the γ_3 phase formed in furnace-cooled U-2Zr-4Nb alloy has lattice parameter of 3.445 Å and phase fraction of around 11 vol%. Similarly, furnace-cooled U-6Nb alloy also consists of orthorhombic α -U and bcc γ_3 phases and the γ_3 -phase peaks are more prominent here. In this case, the lattice parameter of the γ_3 -phase is 3.441 Å and its phase fraction is ~ 32 vol%. The

Rietveld refinement plot of U-2Zr-4Nb alloy is shown in Fig. 3.3b as a representative of two phase furnace-cooled alloys with α and γ_3 -phases.

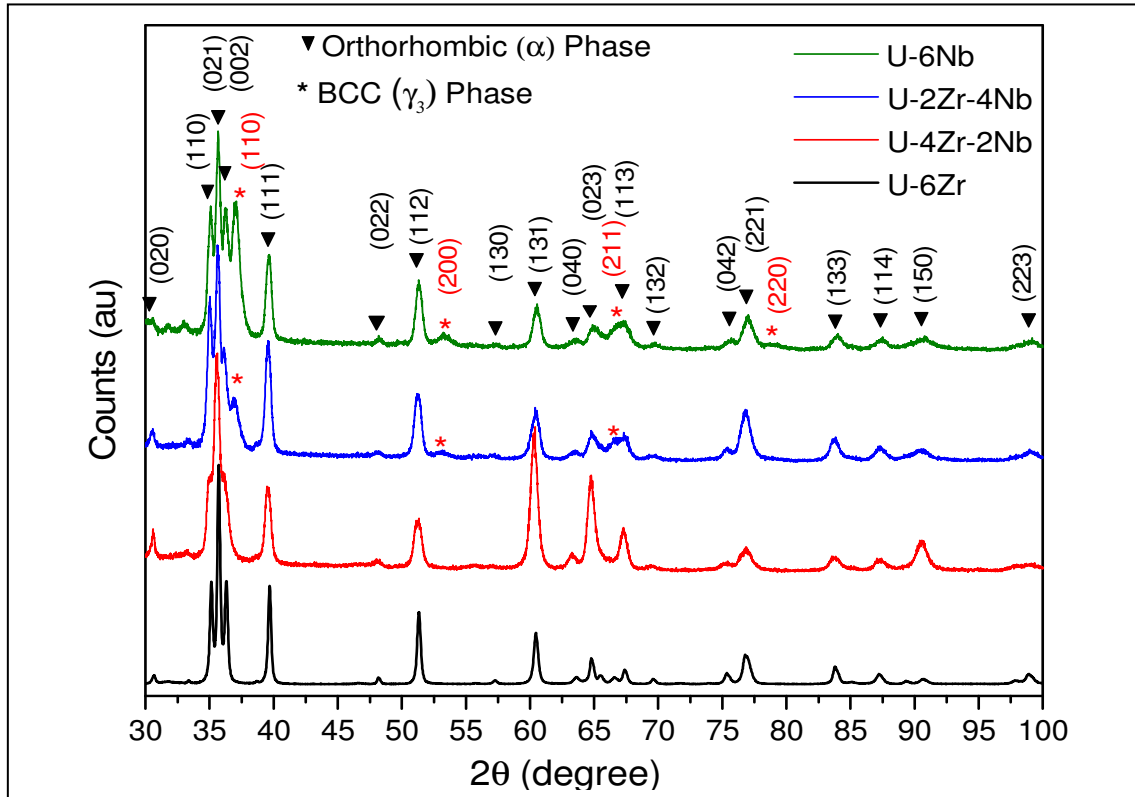


Fig. 3.1 X-ray diffraction patterns of furnace-cooled alloy samples.

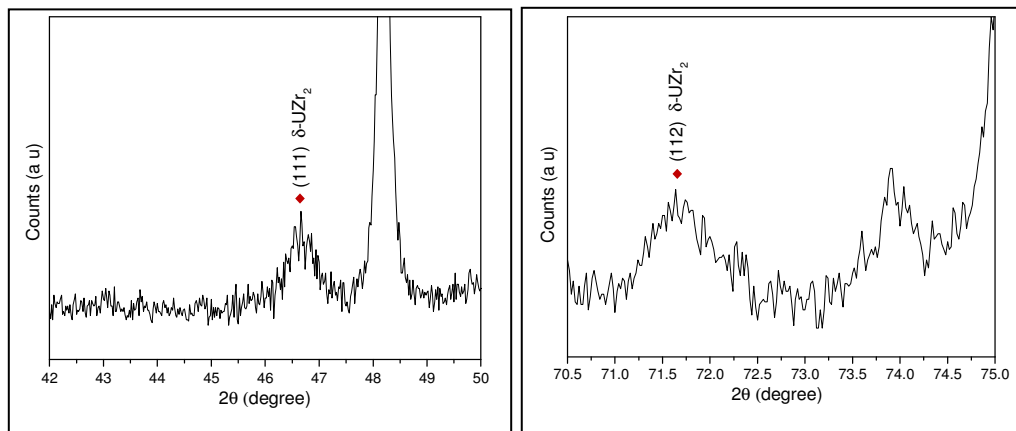


Fig. 3.2 Magnified XRD data of furnace-cooled U-6Zr alloy showing low intensity (111) and (112) peaks of δ -UZr₂ phase.

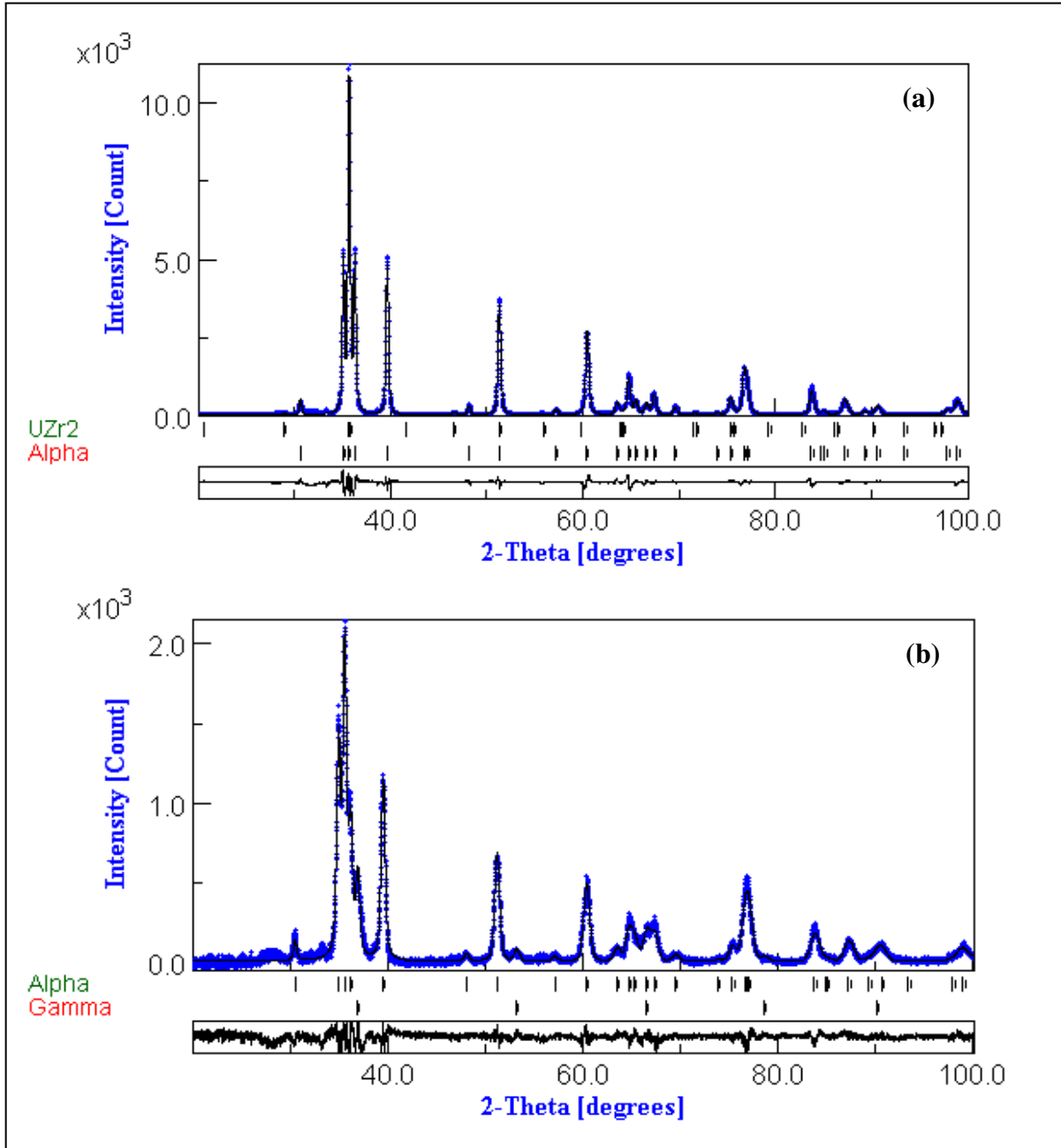


Fig. 3.3 Rietveld refinement of XRD data of furnace-cooled (a) U-6Zr alloy showing experimental (blue dots), calculated (black line) and difference pattern (bottom line) along with the peak positions of α -U and δ -UZr₂ phases, and (b) U-2Zr-4Nb alloy showing experimental (blue dots), calculated (black line) and difference pattern (bottom line) along with the peak positions of α and γ_3 phases.

Sample (furnace-cooled)	Phase(s)	Space group	Phase fraction (vol %)	Lattice Parameters (Å, degree)					
				<i>a</i>	<i>b</i>	<i>c</i>	α	β	γ
U-6Zr	Orthorhombic (α)	Cmcm	92	2.856	5.869	4.972	90	90	90
	Hexagonal (δ)	P6/mmm	8	5.035	5.035	3.102	90	90	120
U-4Zr-2Nb	Orthorhombic (α)	Cmcm	100	2.858	5.873	4.963	90	90	90
U-2Zr-4Nb	Orthorhombic (α)	Cmcm	89	2.858	5.863	4.966	90	90	90
	BCC (γ_3)	Im-3m	11	3.445	3.445	3.445	90	90	90
U-6Nb	Orthorhombic (α)	Cmcm	68	2.856	5.863	4.967	90	90	90
	BCC (γ_3)	Im-3m	32	3.441	3.441	3.441	90	90	90

3.4.1.2. Water-quenched samples

Fig. 3.4 shows the XRD patterns of water-quenched U-6Zr, U-4Zr-2Nb, U-2Zr-4Nb and U-6Nb samples. The U-6Zr, U-4Zr-2Nb, U-2Zr-4Nb alloys exhibit similar XRD patterns that corresponds to orthorhombic α -U phase. The refinement results including the space group and lattice parameter are given in Table 3.2. However, there are notable differences among the α -U phases of water-quenched and corresponding furnace-cooled samples in terms of their lattice parameter. The crystal structure of the water-quenched alloys is explained by a distorted orthorhombic α phase which has higher 'a' and 'c' parameters and lower 'b' parameter as compared to their furnace-cooled part. The orthorhombic crystal structure with slightly different lattice parameter is named as α' . Since, the alloys were water quenched from the γ -phase region at 1173 K, the alloys contain certain lattice distortion depending upon their composition. The

refinement plot of U-6Zr is presented in Fig. 3.5a as a representative of the three alloys with similar structure (α'). The XRD pattern of the water-quenched U-6Nb alloy is totally different and its crystal structure is characterized by a monoclinic unit cell, i.e., α'' modification. The refinement was carried out with space group $P2_1/m$ (11) and Axis b as unique axis; the lattice parameters are found to be $a = 3.288 \text{ \AA}$, $b = 4.988 \text{ \AA}$, $c = 3.171 \text{ \AA}$ and $\beta = 126.38^\circ$. Fig. 3.5b shows the Rietveld refinement plot of water-quenched U-6Nb alloy.

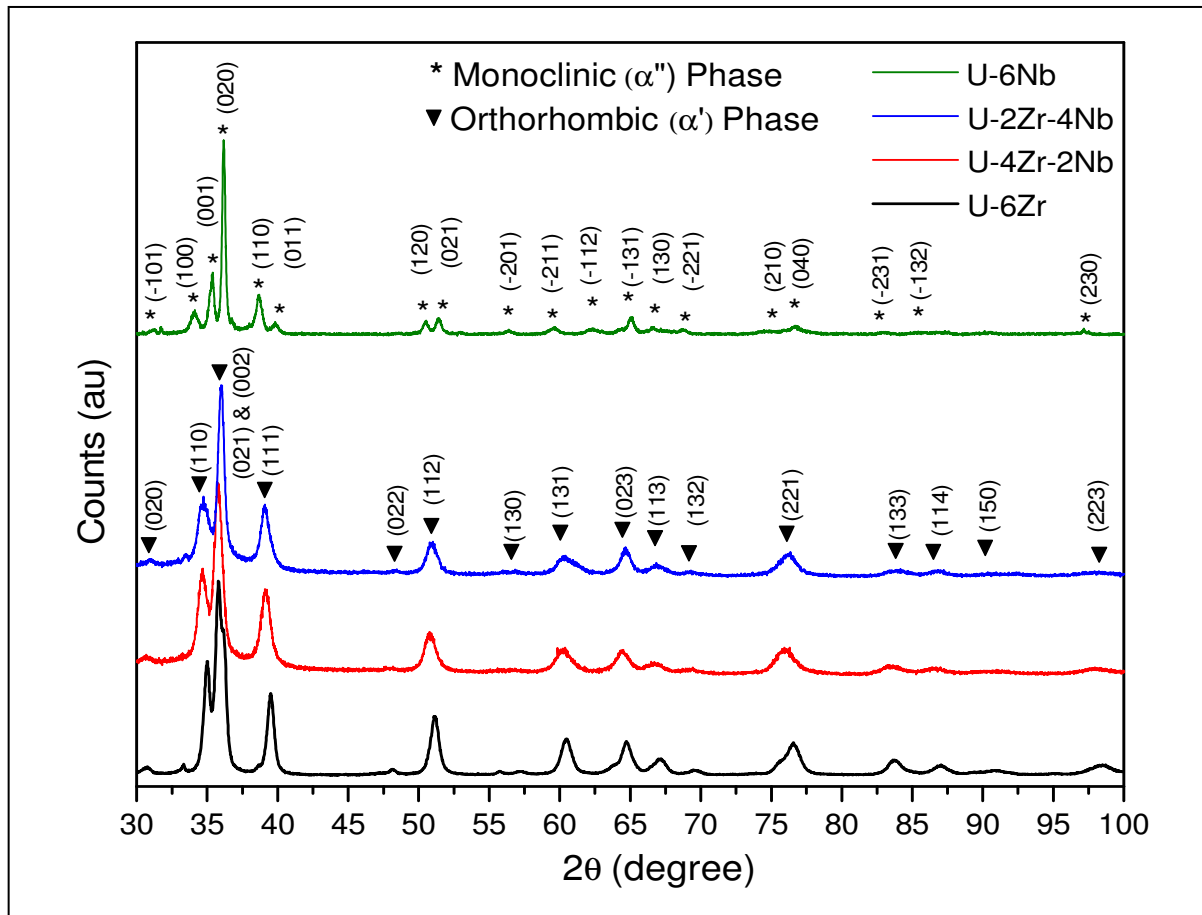


Fig. 3.4 X-ray diffraction patterns of water-quenched alloy samples.

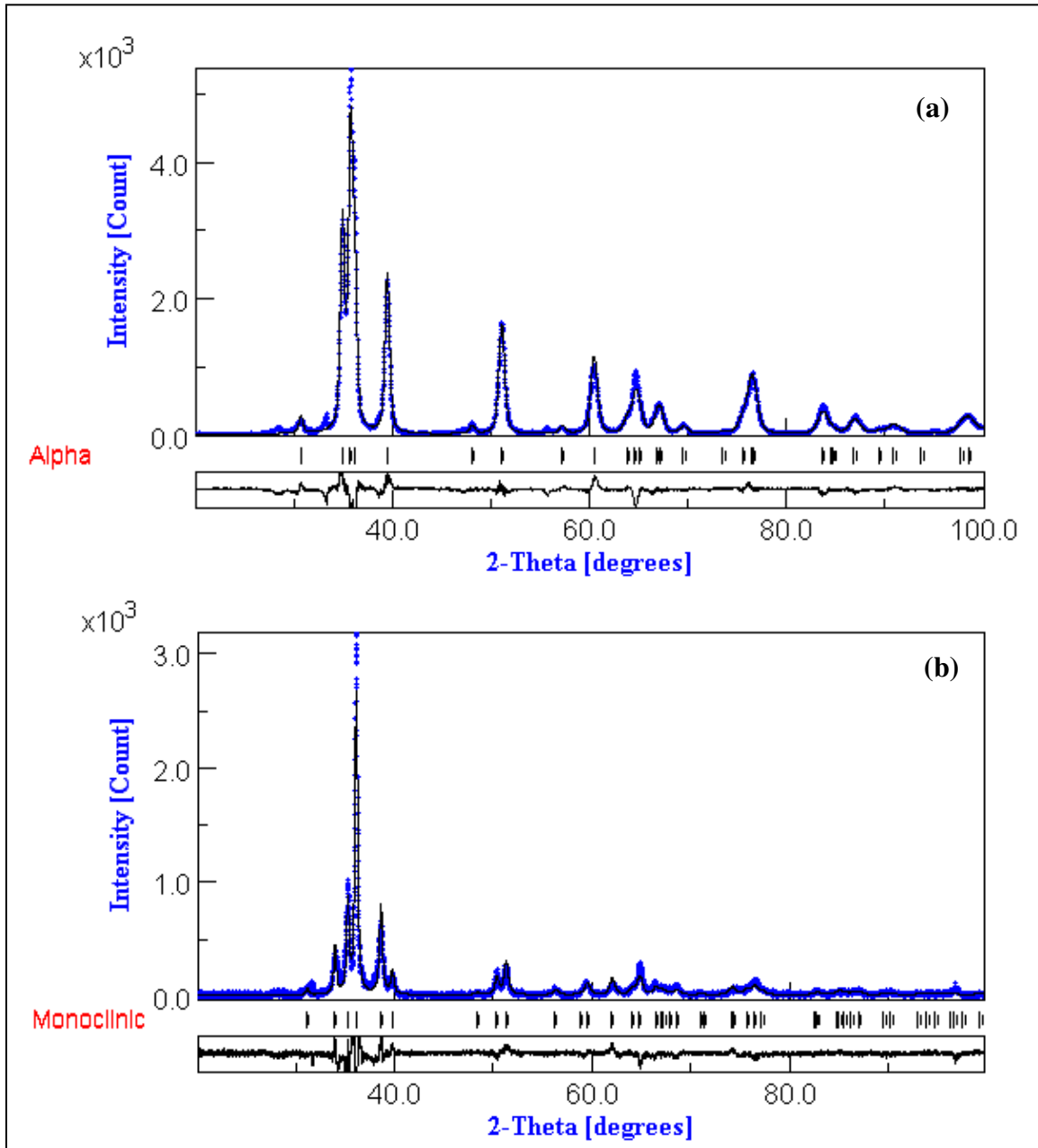


Fig. 3.5 Rietveld refinement of XRD data of water-quenched (a) U-6Zr alloy showing experimental (blue dots), calculated (black line) and difference pattern (bottom line) along with the peak positions of orthorhombic α' phase, (b) U-6Nb alloy showing experimental (blue dots), calculated (black line) and difference pattern (bottom line) along with the peak positions of monoclinic α'' phase.

Table 3.2 Lattice parameter of phases formed in water-quenched alloy samples

Sample (water- quenched)	Phase	Space group	Lattice parameter (Å, degree)					
			<i>a</i>	<i>b</i>	<i>c</i>	α	β	γ
U-6Zr	Orthorhombic (α')	Cmcm	2.873	5.845	4.986	90	90	90
U-4Zr-2Nb	Orthorhombic (α')	Cmcm	2.885	5.816	4.990	90	90	90
U-2Zr-4Nb	Orthorhombic (α')	Cmcm	2.896	5.772	4.978	90	90	90
U-6Nb	Monoclinic (α'')	P2 ₁ /m	3.288	4.988	3.171	90	126.38	90

3.4.2. Microstructural characterization

3.4.2.1. Furnace-cooled samples

The microstructure of furnace-cooled U-6Zr alloy (Fig. 3.6(a-b)) exhibits a fine lamellar type structure with inter-lamellar spacing of approximately in the range of 250-350 nm. The prior γ grain boundaries are also visible in the microstructure. The X-ray line profile of U-M α and Zr-L α lines on the fine lamellar structure (Fig. 3.6b) shows a segregation of Zr into Zr-rich lamellae and Zr-lean matrix phase. The lamellar structure is characteristic of invariant reactions (monotectoid, eutectoid) occurred during furnace cooling of the alloys from high temperature bcc γ -phase. However, it is difficult to determine the exact composition on Zr-rich lamellae and matrix phases using EDS as the size of lamellae is smaller than the interaction volume of the beam electrons and therefore the elements from the adjacent layer may partially interfere during composition analysis. It may be noted here that the average Zr content of Zr-rich lamellae was found to be approximately 25 at%. The formation of δ -UZr₂ intermetallic phase in furnace-cooled U-6Zr alloy could not be resolved by SEM/EDS.

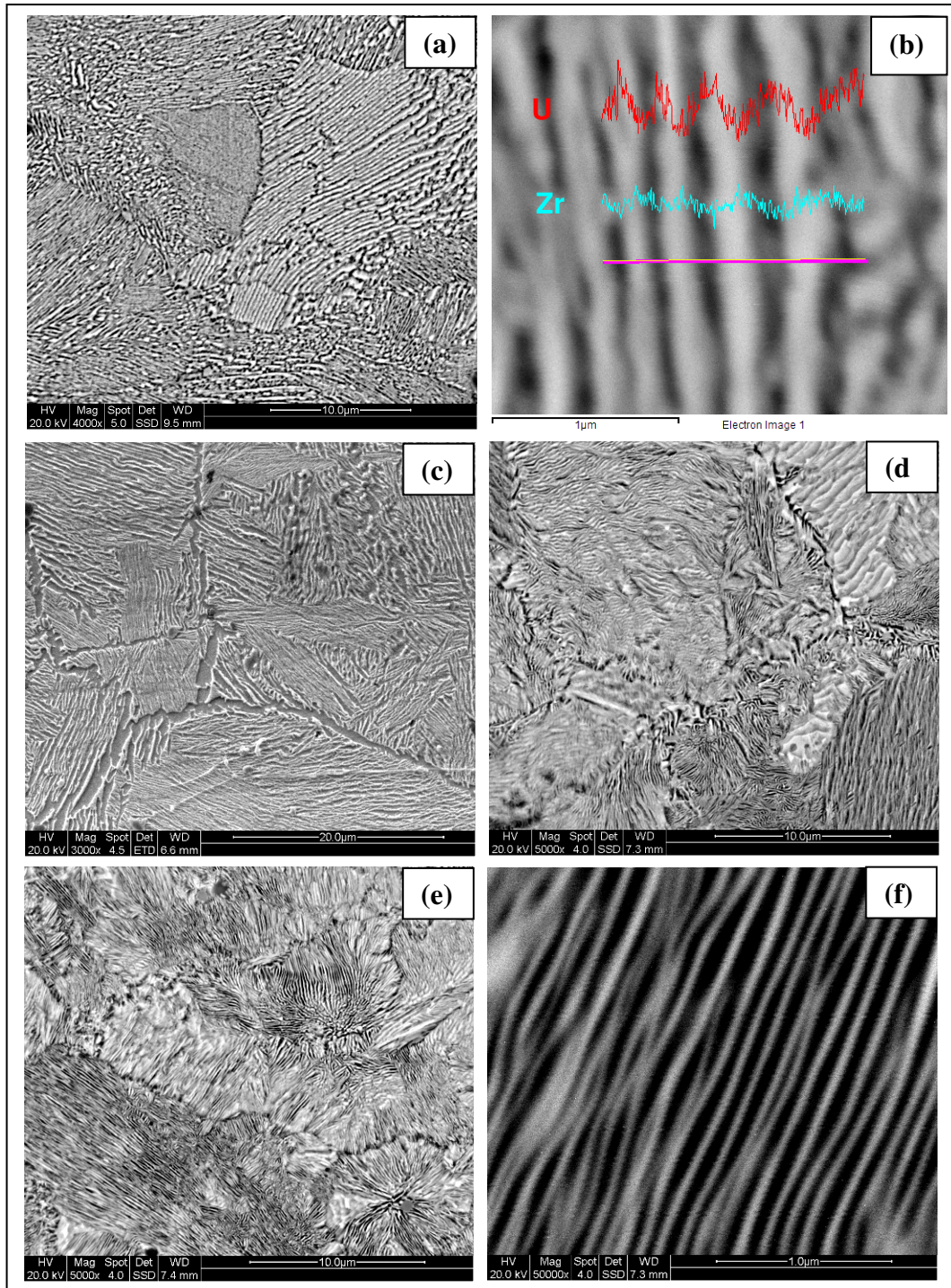


Fig. 3.6 (a & b) SEM micrographs & Intensity profiles of U-M α , Zr-L α X-ray lines on the lamellar structure of furnace-cooled U-6Zr alloy; (c, d & e) SEM micrographs of furnace-cooled U-4Zr-2Nb, U-2Zr-4Nb and U-6Nb alloys, respectively; (f) Magnified micrograph of U-2Zr-4Nb alloy showing very fine lamellar.

The micrograph of furnace-cooled U-4Zr-2Nb alloy (Fig. 3.6c) reveals grain boundary allotriomorphs (GBA) along the prior γ grain with elemental composition almost 100 at.%U which is α -U phase with negligible solute content. At relatively higher magnification, lamellar type of structure with segregation of Zr/Nb in the alternative layers was revealed within the prior γ -grain. The layer rich in solute content (i.e., Zr+Nb) had approximately 22 at.% (14 at.% Zr + 8 at.% Nb). In addition to that the formation of δ -UZr₂ phase formation has not been observed in the microstructure of furnace-cooled U-4Zr-2Nb alloy. Both the furnace-cooled U-2Zr-4Nb and U-6Nb alloys are having similar type of fine lamellar microstructures (Fig. 3.6(d-f)) throughout the sample with inter-lamellar distance in the range of 100-150 nm. Both the furnace-cooled samples are biphasic containing orthorhombic α -U and bcc γ_3 phases as revealed by the XRD results. Hence, the lamellar structure is composed of alternative layers of α -U and bcc γ_3 phases which are formed due to decomposition of γ -phase through invariant reaction. The average (Nb+Zr) or Nb content in the γ_3 phase is found to be around 25-30 at.% which might be lower than the actual value as the inter-lamellar spacing is lower than the actual interaction volume of the SEM electron beam.

3.4.2.2. Water-quenched samples

The microstructures of water-quenched alloy samples are presented in Fig 3.7(a-f). The microstructure of U-6Zr alloy (Fig. 3.7(a-b)) shows prior γ grain boundaries and acicular martensitic plates within the grains. The average size of prior γ -grain is approximately 40-50 μ m. The acicular martensitic phase can be designated as α'_a where subscript 'a' stands for acicular morphology and superscript 'prime' indicates distorted orthorhombic phase. The internal twinning within the martensitic plates is also visible in the magnified image (Fig. 3.7b).

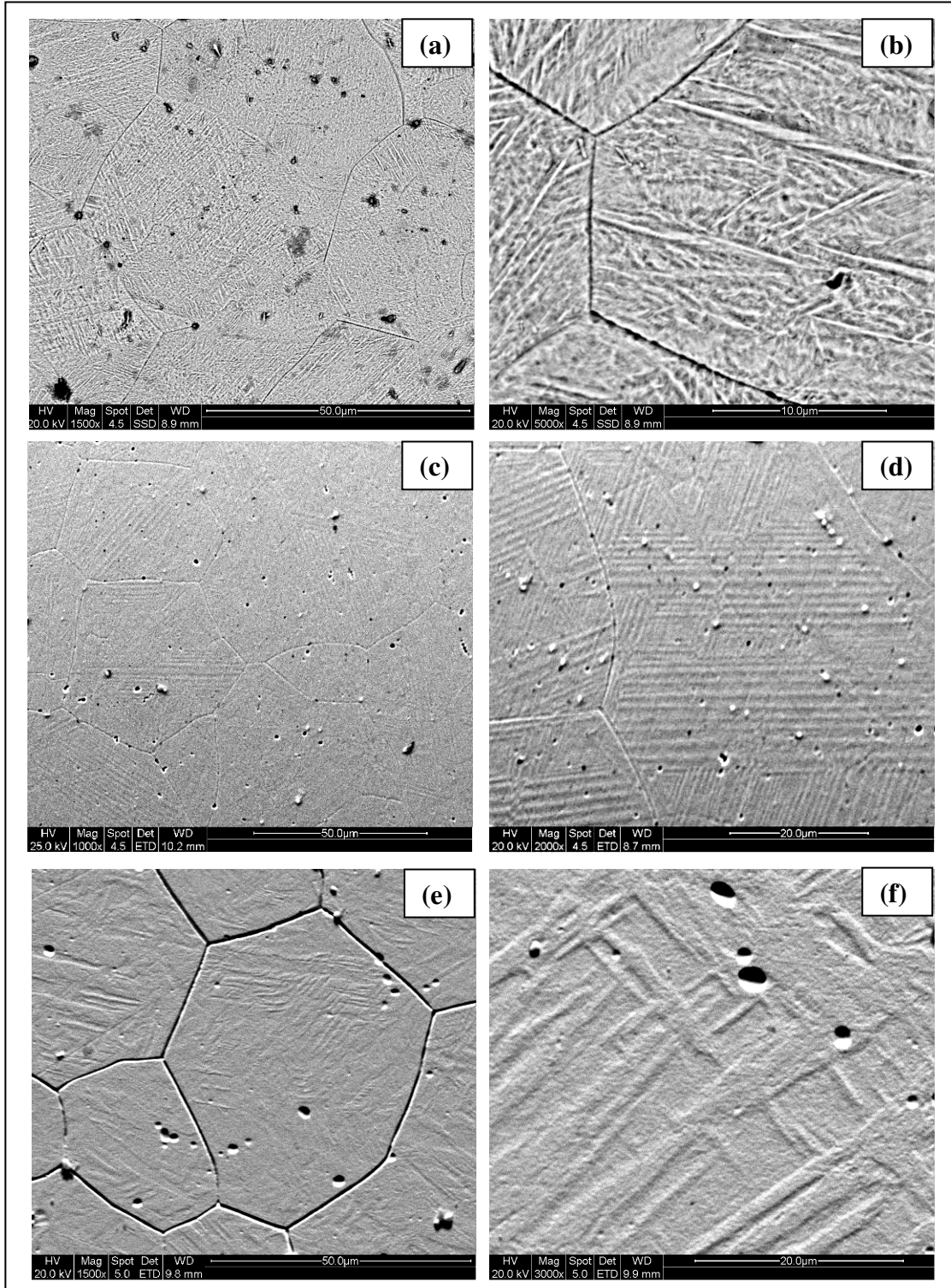


Fig. 3.7 SEM micrographs at different magnification for water-quenched alloy samples, (a & b) U-6Zr, (c & d) U-4Zr-2Nb, (e & f) U-6Nb showing martensitic structures.

The martensitic plates were formed due to rapid cooling of the sample during water quenching. The compositional characterization by EDS reveals a homogeneous distribution of Zr throughout the sample. The elemental compositions of the water-quenched samples are presented in Table 3.3. The water-quenched U-4Zr-2Nb and U-2Zr-4Nb alloys exhibit similar microstructure with well-defined grain boundaries and banded martensitic morphology within the grain, each band being an individual martensite plate. The representative micrographs of U-4Zr-2Nb alloy at two different magnifications are shown in (Fig.3.7(c-d)). Both the alloys have single-phase distorted orthorhombic crystal structures as already confirmed by XRD and therefore the martensitic phases can be designated as α'_b , where b stands for banded morphology. The micrographs of water-quenched U-6Nb alloy also exhibit banded martensitic structure inside grains (Fig. 3.7(e-f)). The water quenching of the U-6Nb alloy leads to formation of martensitic monoclinic structure (α'') of banded morphology. All the water-quenched samples were found to be single phasic and homogeneous with respect to Zr or Nb distribution. The single phase microstructures were formed via diffusionless shear dominated martensitic transformation.

Table 3.3 Chemical composition of water-quenched alloys by EDS

Sample	Zr (wt%)	Nb (wt%)
U-6Zr	5.93	-
U-4Zr-2Nb	3.86	2.00
U-2Zr-4Nb	1.95	3.99
U-6Nb	-	6.08

3.4.3. Differential thermal analysis

3.4.3.1. Furnace-cooled sample

The DTA curves of furnace-cooled alloys during heating and cooling cycles at a scanning rate of 10 K min⁻¹ are collectively presented in Fig. 3.8a and Fig. 3.8b, respectively. The

solidus/liquidus temperatures and other phase transformation temperatures were determined from the DTA curves. In general, the onset of a peak appeared in the heating curve was chosen as transformation temperature. Similarly, the onset of melting peak in the heating curve was taken as solidus temperature. It is customary to select the peak temperature of melting during heating as liquidus temperature as metals/alloys are prone to supercooling prior to initial nucleation of solid from melt during cooling. Sometimes, the liquidus temperature was measured from the cooling curve when it was not resolved properly in the heating curve.

The DTA curve of U-6Zr alloys exhibits three distinct peaks at 860 K, 960 K and 1465 K during heating. The solidus and liquidus temperatures of U-6Zr alloy are found to be at 1465 K and 1548 K, respectively (Fig. 3.8a). Each peak appeared in the thermogram is associated with a phase transformation of alloy. As depicted in the U-Zr equilibrium phase diagram (Fig.1.2, Chapter 1), the first peak at 860 K may be attributed to $\alpha + \delta \rightarrow \alpha + \gamma_2$ transformation. The peak at 960 K may be related to $\alpha + \gamma_2 \rightarrow \gamma$ following $\alpha + \gamma_2 \rightarrow \beta + \gamma_2 \rightarrow \gamma_1 + \gamma_2 \rightarrow \gamma$ steps. It seems that the intermediate transformation may not be resolved properly at a heating rate of 10 K min^{-1} . The DTA run was then repeated with a lower heating rate of 5 K min^{-1} up to 1273 K to resolve overlapping thermal events if any. The repeat run of U-6Zr alloy shows peaks at 860 K, 947 K, 958 K and 975 K (Fig. 3.8c). Two additional low intensity peaks appeared here at 947 K and 975 K were not resolved/visible at higher heating rate. The several peaks appeared with lower scanning rate may be due to those multiple intermediate phase transitions. A detail discussion will be carried out to explain the origin of those multiple peaks. The DTA curve of U-4Zr-2Nb alloy during heating reveals peaks at 900 K and 1478 K (Fig. 3.8a). A similar peak at 900 K (Fig. 3.8c) was also observed when DTA run was repeated with a lower heating rate up to 1273 K.

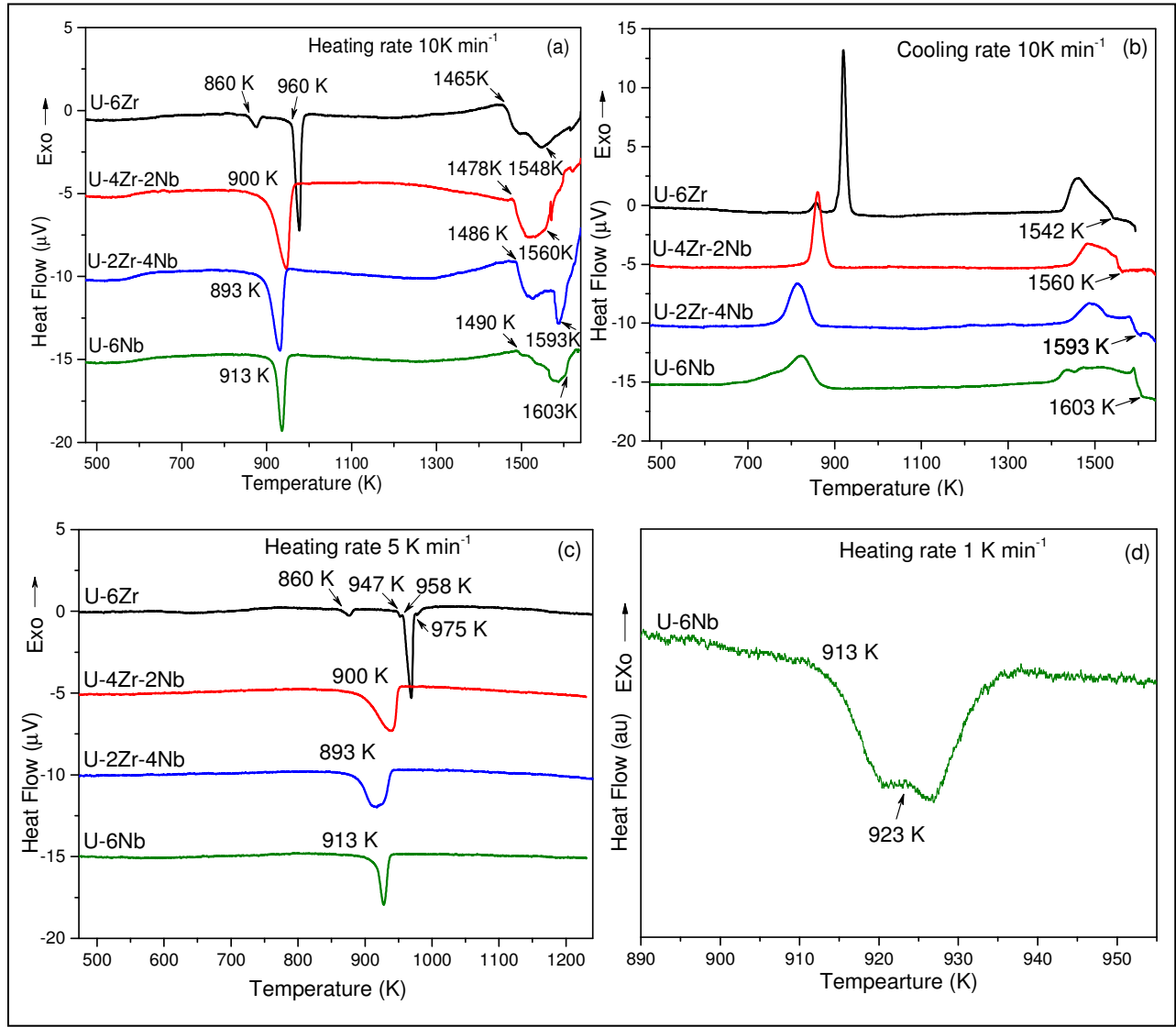


Fig. 3.8 (a & b) DTA curves of furnace-cooled alloy samples during heating and cooling cycles, respectively at scanning rate of 10 K min⁻¹, (c) DTA curves of repeat runs at scanning rate of 5 K min⁻¹, (d) Magnified view of DTA peak of U-6Nb alloy at 1 K min⁻¹.

The solidus and liquidus temperatures of U-4Zr-2Nb alloy are found to be 1478 and 1560 K, respectively. The furnace-cooled U-2Zr-4Nb alloy also exhibits a similar type of DTA curves with peaks appeared at 893 and 1486 K during heating. The solidus and liquidus temperatures appeared at 1486 and 1593 K, respectively, are somewhat higher than that of U-4Zr-2Nb alloy.

The first peaks at 900 K (for U-4Zr-2Nb) and 893 K (for U-2Zr-4Nb) during heating may be attributed to $\alpha + \gamma_3 \rightarrow \gamma$ type phase transformations or the temperature at which the single γ -phase forms. The heating curve of U-6Nb alloy shows peaks at 913 and 1490 K (Fig. 3.8a). The solidus and liquidus temperatures at 1490 and 1603 K, respectively, are found to be higher than for U-6Zr and two U-Zr-Nb alloys. The peak at 913 K appeared as single peak during heating (Fig. 3.8a). However, the appearance of small shoulder in the same peak during cooling (Fig. 3.8b) indicates/suggests overlapping thermal events. The overlapping reactions were not resolved even at heating rate of 5 K min^{-1} (Fig. 3.8c). The DTA experiment was further repeated with a lower heating rate of 1 Kmin^{-1} and two overlapping peaks were resolved at 913 and 923 K (Fig. 3.8d) which may be attributed to $\alpha + \gamma_3 \rightarrow \beta + \gamma_3$ and $\beta + \gamma_3 \rightarrow \gamma$ transformation, respectively. These are basically two close invariant reactions i.e., eutectoid ($\beta \leftrightarrow \alpha + \gamma_3$) at 913 K and monotectoid ($\gamma \leftrightarrow \beta + \gamma_3$) at 923 K as depicted in the U-Nb phase diagram (Fig.1.3, Chapter 1).

3.4.3.2. Water-quenched sample

The DTA curves of water-quenched alloys during heating are collectively shown in Fig. 3.9a. The repeat runs of the alloys with a heating rate of 5 K min^{-1} are presented in Fig. 3.9b. The nature of the cooling curves of both the furnace-cooled (Fig. 3.9b) and water-quenched samples was found to be identical and therefore the cooling curves of water-quenched alloys are not presented here to avoid repetition. The DTA curve of water-quenched U-6Zr alloy (Fig. 3.9a) is found to be similar to that of the furnace-cooled sample with endothermic peaks at 860, 960 and 1465 K. The DTA curve of water-quenched U-6Nb alloy (Fig. 3.9a) shows one exothermic transformation peak at 725 K and two endothermic peaks at 913 and 1490 K. The exothermic peak at 725 K was not observed in the DTA thermogram of the furnace-cooled sample (Fig. 3.8a) and it disappeared in the repeat run of the water-quenched sample (Fig. 3.9b). The other two

peaks at 913 and 1490 K are similar to the peaks in the furnace-cooled alloy. Similarly, DTA thermograms of both the water-quenched U-4Zr-2Nb and U-2Zr-4Nb alloys (Fig. 3.9a) also exhibit one additional exothermic peak along with two endothermic peaks. The endothermic peaks of water-quenched alloys are almost similar to their furnace-cooled part. The exothermic peaks were observed at 775 K for U-4Zr-2Nb and 765 K for U-2Zr-4Nb alloys. No exothermic peaks were observed in the repeat run (Fig. 3.9b). In the water-quenched U-4Zr-2Nb sample, the exothermic peak is not so prominent and a small exothermic effect with little enthalpy change was observed. The exothermic effect gets gradually diminished with increasing Zr content in the alloys. In fact, no exothermic peak was identified in case of U-6Zr alloy. The exothermic peaks of water-quenched sample may be attributed to phase transformation of non-equilibrium phases.

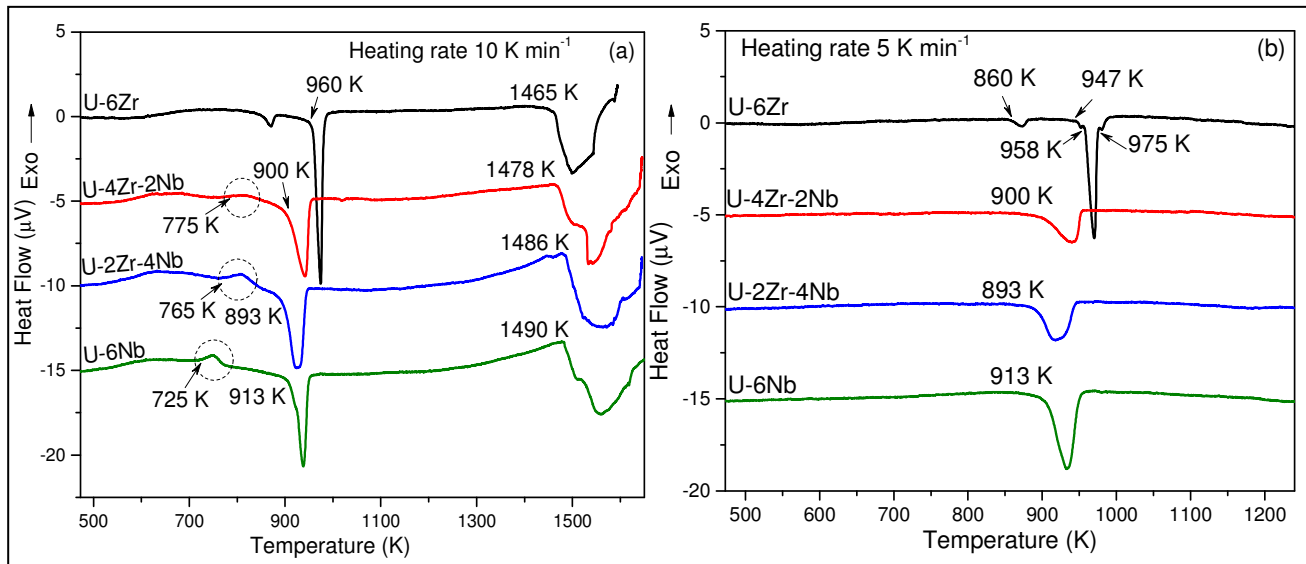


Fig. 3.9 (a) DTA curves of water-quenched alloy samples during heating cycle at scanning rate of 10 K min⁻¹, (b) DTA curves of repeat run at scanning rate of 5 K min⁻¹.

3.4.4. Dilatometry

The thermal expansion curves of furnace-cooled alloys are presented together in Fig. 3.10a in which the length changes (%) are plotted against temperature. The sudden change in length in the expansion curves is attributed to the phase transition. The expansion curves apparently show single phase transition and the temperatures associated with phase change are mentioned in Fig. 3.10a. The expansion curve of U-6Zr alloy reveals a single transition at 960 K. However, the first derivative plot of expansion curve against temperature of U-6Zr alloy (Fig. 3.10b) reveals two phase transitions at approximately 860 K and 960 K. The phase transition at 860 K was not clearly resolved in Fig. 3.10a. The dilatometry expansion experiment of U-6Zr was further repeated employing a heating rate of 5 K min⁻¹ to check various expected intermediate transformations in U-Zr alloys. The expansion curve and its first derivative as shown in Fig. 3.10c reveal the three transformations at 947, 958 and 975 K which are similar to DTA results. The thermal expansion curve of U-4Zr-2Nb shows single phase transition at 900 K and the extent of expansion is almost similar to that of U-6Zr alloy. It indicates that the replacement of 2wt% Zr in U-6Zr alloy with 2wt%Nb does not cause any remarkable effect on the overall expansion except the transformation temperature. The expansion of U-2Zr-4Nb alloy shows that is comparable with U-4Zr-2Nb alloy and its transformation temperature (i.e., 893 K) is slightly lower. The thermal expansion of U-6Nb alloy is substantially lower than the rest of the alloys and transformation temperature was found to be at 915 K. The two consecutive transformations may not be resolved at heating 10 or 5 K min⁻¹ as discussed in the previous section (section 3.4.3.1). It indicates that the Nb-rich alloy exhibits lower coefficient of thermal expansion (CTE) than the Zr-rich alloy.

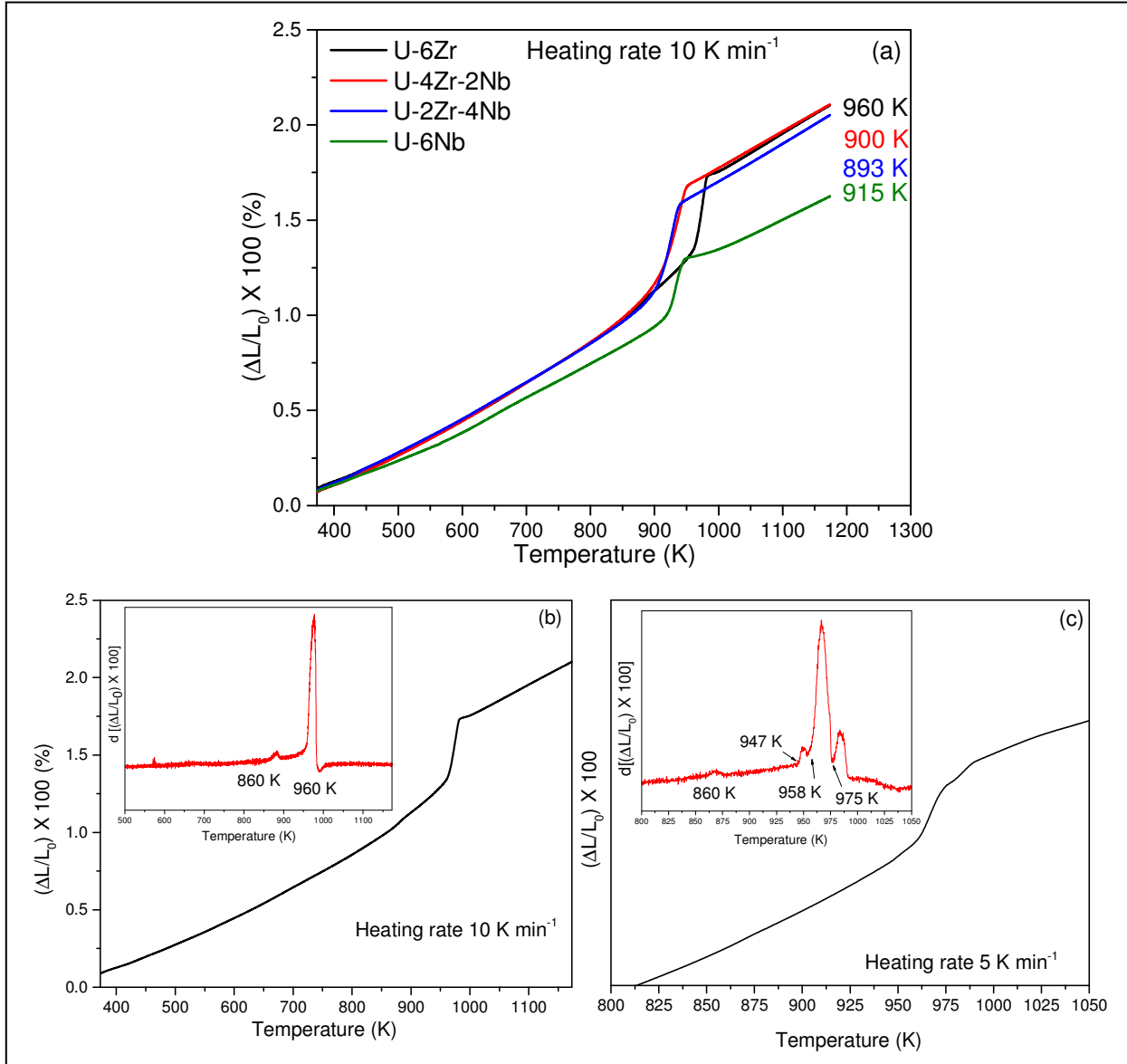


Fig. 3.10 (a) Thermal expansion curves of alloy samples, (b & c) Expansion curves of U-6Zr alloy at different heating rates, the first derivative plots of the expansion curves are shown in inset.

The dilatometric curves can be fitted by second degree polynomials as follows:

U-6Zr alloy:

$$\Delta L/L_0 (\%) = -0.247 + 0.479 \times 10^{-3} T + 1.129 \times 10^{-6} T^2 \quad (373 \text{ K} \leq T \leq 873 \text{ K}) \quad (3.1)$$

$$\Delta L/L_0 (\%) = -0.152 + 1.800 \times 10^{-3} T + 0.108 \times 10^{-6} T^2 \quad (998 \text{ K} \leq T \leq 1173 \text{ K}) \quad (3.2)$$

U-4Zr-2Nb alloy:

$$\Delta L/L_0 (\%) = -0.315 + 0.633 \times 10^{-3} T + 1.050 \times 10^{-6} T^2 \quad (373 \text{ K} \leq T \leq 873 \text{ K}) \quad (3.3)$$

$$\Delta L/L_0 (\%) = -0.215 + 2.040 \times 10^{-3} T - 0.055 \times 10^{-6} T^2 \quad (973 \text{ K} \leq T \leq 1173 \text{ K}) \quad (3.4)$$

U-2Zr-4Nb alloy:

$$\Delta L/L_0 (\%) = -0.358 + 0.872 \times 10^{-3} T + 0.805 \times 10^{-6} T^2 \quad (373 \text{ K} \leq T \leq 873 \text{ K}) \quad (3.5)$$

$$\Delta L/L_0 (\%) = 0.230 + 1.010 \times 10^{-3} T + 0.460 \times 10^{-6} T^2 \quad (973 \text{ K} \leq T \leq 1173 \text{ K}) \quad (3.6)$$

U-6Nb alloy:

$$\Delta L/L_0 (\%) = -0.258 + 0.559 \times 10^{-3} T + 0.867 \times 10^{-6} T^2 \quad (373 \text{ K} \leq T \leq 873 \text{ K}) \quad (3.7)$$

$$\Delta L/L_0 (\%) = 1.239 - 1.170 \times 10^{-3} T + 1.283 \times 10^{-6} T^2 \quad (973 \text{ K} \leq T \leq 1173 \text{ K}) \quad (3.8)$$

where, L_0 is initial length (at 298 K) and ΔL is the difference between the instantaneous length (at any temperature T) and L_0 .

3.4.5. Molar heat capacity

Three alloys i.e., U-6Zr, U-2Zr-4Nb and U-6Nb alloys were chosen to measure their molar heat capacity employing DSC. The molar heat capacity data of U-6Zr, U-2Zr-4Nb and U-6Nb alloys were measured in the temperature range of 323-823 K, below the phase transition temperature observed in the DTA and Dilatometer curves. The molar heat capacity ($C_{p,m}^0$) values of the alloy samples are collectively presented in Table 3.4 and Fig. 3.11. The $C_{p,m}^0(T)$ values of the alloys are least squares fitted with second order polynomial in two different temperature ranges for best fitting.

The least squares fitted expressions of the alloy samples are given as follows:

U-6Zr alloy:

$$C_{p,m}^0 (\text{J} \cdot \text{mol}^{-1} \cdot \text{K}^{-1}) = 22.945 + 1.732 \times 10^{-2} T - 0.6605 \times 10^{-5} T^2, \quad (323 \leq T/\text{K} \leq 598) \quad (3.9)$$

$$C_{p,m}^0 \text{ (J}\cdot\text{mol}^{-1}\cdot\text{K}^{-1}) = 33.798 - 3.231\times 10^{-2} T + 4.608\times 10^{-5} T^2, \quad (598 \leq T/\text{K} \leq 823) \quad (3.10)$$

U-2Zr-4Nb alloy:

$$C_{p,m}^0 \text{ (J}\cdot\text{mol}^{-1}\cdot\text{K}^{-1}) = 20.359 + 2.937\times 10^{-2} T - 2.184\times 10^{-5} T^2, \quad (323 \leq T/\text{K} \leq 598) \quad (3.11)$$

$$C_{p,m}^0 \text{ (J}\cdot\text{mol}^{-1}\cdot\text{K}^{-1}) = 10.447 + 3.914\times 10^{-2} T - 1.029\times 10^{-5} T^2, \quad (598 \leq T/\text{K} \leq 823) \quad (3.12)$$

U-6Nb alloy:

$$C_{p,m}^0 \text{ (J}\cdot\text{mol}^{-1}\cdot\text{K}^{-1}) = 20.516 + 2.812\times 10^{-2} T - 2.041\times 10^{-5} T^2, \quad (323 \leq T/\text{K} \leq 598) \quad (3.13)$$

$$C_{p,m}^0 \text{ (J}\cdot\text{mol}^{-1}\cdot\text{K}^{-1}) = -4.185 + 8.881\times 10^{-2} T - 5.282\times 10^{-5} T^2, \quad (598 \leq T/\text{K} \leq 823) \quad (3.14)$$

Table 3.4 Experimental molar heat capacity data of U-6Zr, U-2Zr-4Nb and U-6Nb alloys

T (K)	$C_{p,m}^0 \text{ (J}\cdot\text{mol}^{-1}\cdot\text{K}^{-1})$		
	U-6Zr	U-2Zr-4Nb	U-6Nb
323	27.84	27.50	27.42
348	28.22	27.94	27.78
373	28.44	28.27	28.15
398	28.76	28.70	28.58
423	29.09	28.92	28.87
448	29.41	29.14	29.09
473	29.74	29.35	29.24
498	29.96	29.57	29.31
523	30.17	29.68	29.53
548	30.39	29.79	29.74
573	30.61	30.00	29.96
598	31.04	30.22	30.11
623	31.47	30.66	30.47
648	32.13	31.53	31.12
673	32.99	32.18	31.78
698	33.65	32.83	32.21
723	34.51	33.49	32.43
748	35.60	33.92	32.65
773	36.25	34.36	32.80
798	37.34	35.00	32.90
813	37.99	35.44	33.08
823	38.42	35.87	33.29

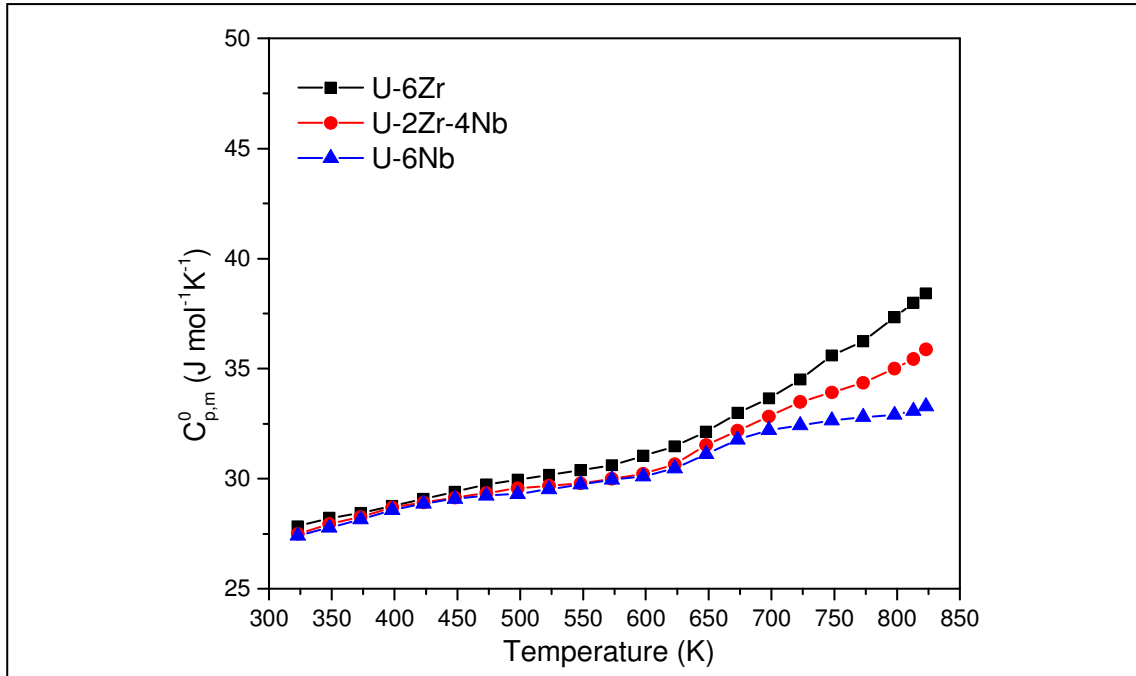


Fig. 3.11 Measured molar heat capacity data of U-6Zr, U-2Zr-4Nb and U-6Nb alloys.

3.4.6. Microhardness

The microhardness data of furnace-cooled and water-quenched alloy samples are presented in Table 3.5. Among the furnace-cooled samples, microhardness of U-2Zr-4Nb and U-6Nb alloys are found to be higher than that of U-6Zr and U-4Zr-2Nb alloys. The hardness data of U-6Zr and U-4Zr-2Nb alloys are in the range of 360-380 VHN whereas that of U-4Zr-2Nb and U-6Nb alloys are in the range of 415-425 VHN. The variation in the hardness data can be explained on the basis of phase stability, crystal structure and effect of alloying elements. In this case, U-6Zr and U-4Zr-2Nb alloys consist of predominantly α -U phase. On the other hand, U-2Zr-4Nb and U-6Nb alloys are biphasic in nature consisting of α -U and γ_3 phases in fine lamellar fashion. Also, the γ_3 -phases are rich in solute content. The higher hardness of furnace-cooled U-2Zr-4Nb and U-6Nb alloys could be explained due to the formation of significant amount of second phase with fine lamellar structure. In the water-

quenched alloys, the hardness gradually decreases with increasing Nb content in the samples. The hardness of U-6Zr alloy is 565 VHN whereas it is only 160 VHN for U-6Nb alloy. The water-quenched samples are martensitic in nature. The replacement of Zr with Nb remarkably reduces hardness. The hardening of U-6Zr alloy is due to the formation of martensite with distorted orthorhombic structure (α'). The hardness of the alloys can be explained on the basis of solid-solution strengthening mechanism where the strength of a metal increases with the addition of alloying elements. Zr and Nb form substitutional solid solution with uranium and exhibit limited solubility at lower temperature which may lead to formation of supersaturated solid solution. The substitutional alloying elements produce strain in the crystalline lattice of solvent structure because of difference in atomic sizes. The resulting distortion, or strain energy, may create a barrier to dislocation motion. It may be noted here that the atomic radii of U, Zr and Nb are 1.53, 1.60 and 1.46Å, respectively.

Table 3.5 Microhardness data of different U-Zr-Nb alloy samples

Sample	Load (gm)	Dwell time (s)	Hardness value (VHN) (kg/mm ²)	
			Furnace-cooled	Water-quenched
U-6Zr	200	10	377 ± 20	565 ± 10
U-4Zr-2Nb			363 ± 14	369 ± 13
U-2Zr-4Nb			425 ± 12	262 ± 10
U-6Nb			415 ± 15	160 ± 15

3.5. Discussion

The purpose of this study is to develop a good alternative metallic fuel for fast reactor. Among many choices, U-Zr-Nb alloys can be considered as a good alternative fuel due to many attractive characteristics of zirconium and niobium as mentioned earlier. Therefore, in this study, a combination of Zr and Nb were alloyed with uranium to create a ternary U-Nb-Zr alloy. Also,

the combined addition of Zr and Nb were purposely restricted to 6wt% to order to achieve higher breeding ratio, density. With this background, various heat treated U-Zr-Nb alloys (Zr+Nb = 6wt%) with different combination of Nb and Zr have been analyzed in terms of their crystal structure, microstructure, phase content, microhardness and thermophysical properties.

The XRD analysis of the alloy samples reveals that the furnace-cooled U-6Zr alloy consists of mainly α -U phase with few non-overlapping low intensity peaks for δ -UZr₂ phase and its microstructure consists of fine lamellar structure with segregation of Zr in alternate layers. On the other hand, water-quenched U-6Zr alloy has distorted orthorhombic crystal structure with acicular martensitic morphology (α'_a). As per the U-Zr phase diagram (Fig. 1.2), the equilibrium phases of U-rich U-Zr alloys are orthorhombic α -U with limited Zr solubility and hexagonal δ -UZr₂ intermetallic at room temperature. It was reported in few earlier studies that the as-cast U-rich U-Zr alloy samples have supersaturated α -phase at room temperature and the samples do not contain any δ -phase. The sluggish nature of formation of δ -phase in U-rich U-Zr alloy has been highlighted by Basak et al. [37, 38]. However, the propensity for precipitation of δ -phase in the supersaturated solutions is evident in other literature where the coexistence of α and δ phase in as-cast U-rich U-Zr alloys were reported by authors using TEM analysis [42, 43]. The presence of the δ -phase in the XRD results of as-cast U-Zr alloys with a Zr content exceeding 8 wt.% was also reported by Zhang et al.[45]. In this present study, small fraction (~8 vol%) of δ -UZr₂ phase in the furnace-cooled U-6Zr alloy was revealed by Rietveld refinement of XRD data and this volume fraction is found to be less than the equilibrium value. However, the same could not be resolved by SEM analysis. Hence, it may not be appropriate to conclude on the phase stability and phase transformation behaviour of U-6Zr alloy based on the above results. One attempt was made to investigate the structural, microstructural, phase transformation

behaviour of U-6Zr alloy under near equilibrium condition to reveal to the δ -phase and associated phase transformations. In order to attain the equilibrium phases the alloy was subjected to step cooling with isothermal holding at various temperatures. For that, a portion of the sample was heated to 1173 K for 50 h and then furnace stepwise cooled to RT by holding the sample at 1073, 973, 923, 873, 823 and 773 K for 100, 100, 250, 250, 500 and 550 h, respectively. The heat treatment was planned in such a way to allow sufficient time at various temperatures for transformation to occur. The sample is treated as a step-cooled sample. The microstructural analysis (Fig. 3.12a) shows that the alloy is biphasic in nature where δ -phase is uniformly distributed in the α -U matrix. The EDS analysis of δ -phase revealed the elemental composition of 72 at.% Zr and 28 at.% U, as expected for UZr_2 whereas the Zr-content in the matrix phase (α -U) is negligibly small and therefore could not be detected by EDS (Fig. 3.12(b-c)). The presence of α -U and δ - UZr_2 phases in the alloy is also supported by the XRD analysis. The results are in good agreement with the equilibrium phase diagram. The detail characterization of this alloy will be discussed in Chapter 5.

As already mentioned, α -U has orthorhombic crystal structure (space group Cmcm) while δ phase (UZr_2) has C32-AlB_2 type hexagonal structure (space group P6/mmm). The structure of δ -phase is related to metastable ω phase as found in Zr and Ti alloys [102]. In the δ -phase, a Zr atom occupies the Al position (0,0,0) of the hexagonal cell and a random mixture of U and Zr atoms occupies the B positions $(1/3, 2/3, 1/2)$, and $(2/3, 1/3, 1/2)$. In U-Zr alloys, the bcc γ -phase transforms to hexagonal δ -phase via the ω transformation mechanism. During ω transformation, two intermediate $(111)_\gamma$ planes collapse to form an intermediate $(0001)_\omega$ plane by moving a distance of $1/12[111]a_\gamma$ in opposite directions [103]. In as-cast alloy, the incomplete collapse of

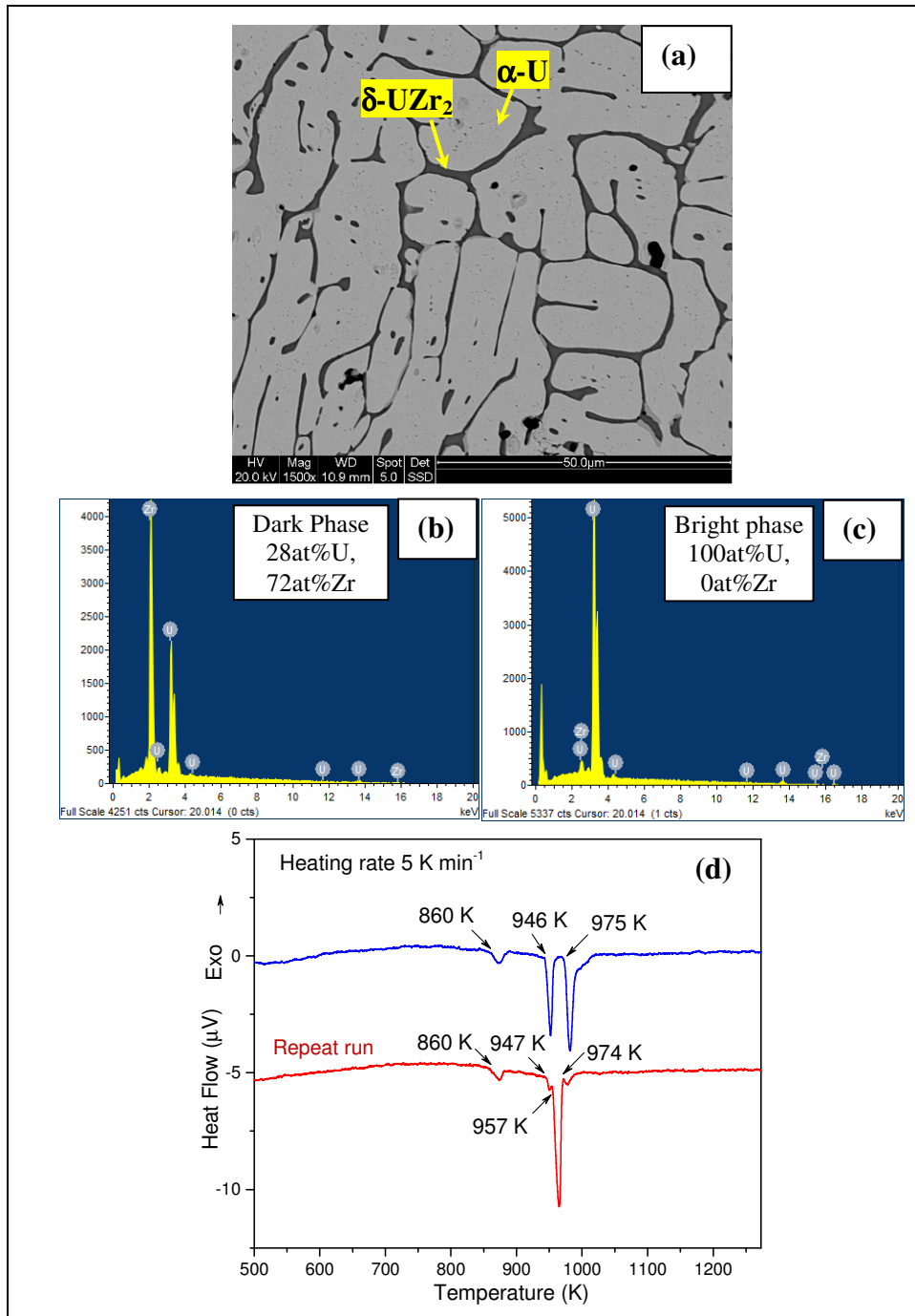


Fig. 3.12 (a) SEM micrograph of equilibrium cooled U-6Zr sample showing δ -phase and α -matrix, (b & c) Typical EDS spectra of δ -phase (dark phase) and α -matrix (bright phase), respectively, showing the elemental composition; (d) DTA curves of step-cooled U-6Zr sample during heating cycle at scanning rate of 5 K min⁻¹.

the $(111)_\gamma$ planes results in formation of ω with lack of long range ordering. This could be the probable reason of absence of δ -phase peaks in the XRD data of most of studies on as-cast U-rich U-Zr alloy [103]. On the other hand, the continuous slow cooling or step cooling from γ -phase may cause complete collapse of $(111)_\gamma$ planes and partial ordering of Zr atoms. This results in formation of δ -phase which is considered as a partially ordered ω . The above explanation justifies appearance of δ -phase in furnace-cooled sample and its absence in the quenched sample.

The furnace-cooled and water-quenched U-6Zr alloys exhibit multiple phase transformation peaks in DTA thermograms with first endothermic peak at ~ 860 K and a sharp endothermic peak at 960 K. Two additional weak overlapping peaks at 947 and 975 K were also revealed at a lower heating rate. As per the U-Zr equilibrium phase diagram, the expected sequences of phase transformation in U-6Zr alloy are $\alpha + \delta \rightarrow \alpha + \gamma_2 \rightarrow \beta + \gamma_2 \rightarrow \gamma_1 + \gamma_2 \rightarrow \gamma$. The first transition peak at 860 K appeared for both the furnace-cooled and water-quenched samples was found to substantially lower than the equilibrium phase diagram where the room temperature phases ($\alpha + \delta$) transform to ($\alpha + \gamma_2$) at 890 K. In addition to that, a substantial variation in the various transition temperatures for similar type of U-rich U-Zr alloy samples has also been reported in the literature. The DTA peaks associated with phase transformation of an alloy may be affected by several factors like thermal history of the sample, phase fraction, homogeneity and heating rate etc. Hence, the actual sequences of phase transformations of U-6Zr alloy can be ensured by analyzing the step-cooled U-6Zr alloy sample using DTA. The DTA curve of step-cooled U-6Zr alloy (Fig. 3.12d) shows three distinct peaks at 860, 946 and 975 K. The step-cooled sample contains α -phase and δ -phase (Fig. 3.12a) and therefore, the first peak at 860 K is attributed to transformation of δ -phase, i.e., $\alpha + \delta \rightarrow \alpha + \gamma_2$, which is basically

dissolution of δ -phase. The other peaks at 946 and 975 K are due to the $\alpha + \gamma_2 \rightarrow \beta + \gamma_2 \rightarrow \gamma$ reactions, respectively. The three distinct peaks at 860, 946 and 975 K are basically three invariant reactions i.e., $\alpha + \gamma_2 \leftrightarrow \delta$ (Peritectoid), $\beta \leftrightarrow \alpha + \gamma_2$ (Eutectoid) and $\gamma \leftrightarrow \beta + \gamma_2$ (Monotectoid). The $\gamma_1 + \gamma_2 \rightarrow \gamma$ transformation associated to miscibility gap is revealed by a small shoulder at 993 K in DTA peak. When the repeat run was conducted with the same step-cooled sample, the peaks at 946 and 975 K became weak and in addition one strong peak at ~957 K appeared. The finding of repeat run is almost identical to that of furnace-cooled and water-quenched alloys (Fig. 3.8c and Fig. 3.9b). During the repeat run, the sample lost its initial thermal history (i.e., step-cooled) and became equivalent to furnace-cooled alloy. In the step-cooled sample, the orthorhombic α -U phase had almost negligible Zr solubility and the major part of α -U phase is expected to become supersaturated with Zr during furnace cooling. The supersaturated alloy follows the transformation sequence of $\alpha + \delta \rightarrow \alpha + \gamma_2 \rightarrow \gamma$ at 860, 960 K, respectively, without undergoing the intermediate transitions. This effect was found to be more prominent when DTA run of furnace-cooled/water-quenched alloys were taken with 10 K min^{-1} (Fig. 3.8a and Fig. 3.9a) where a sharp peak appeared at ~960 K without the resolving intermediate transitions (i.e., at 947 and 975 K). It indicates that the supersaturated α -U phase of the sample might have transformed to γ -phase without the intermediate transitions. Therefore, the strong endothermic peak at 960 K may be attributed to $\alpha + \gamma_2 \rightarrow \gamma$ transformation reaction in the supersaturated alloy. At relatively lower heating rate, the intermediate peaks at 947 K for $\alpha + \gamma_2 \rightarrow \beta + \gamma_2$ and at 975 K for $\beta + \gamma_2 \rightarrow \gamma$ reactions become visible in DTA thermogram. It is noteworthy to mention here that the furnace-cooled alloy may also exhibit similar type of thermogram as observed in case of step-cooled sample under extremely slow heating rate following almost equilibrium condition.

The effects of Nb on U-Zr alloys in terms of their crystal structure, microstructures etc. are discussed in the following paragraphs. The furnace-cooled U-4Zr-2Nb contained α -U phase with lattice parameters $a = 2.858\text{\AA}$, $b = 5.873\text{\AA}$, $c = 4.963\text{\AA}$, and the microstructure exhibited lamellar morphology with segregation of Zr/Nb. The lamellar structure is formed due to $\gamma \rightarrow \alpha + \gamma_3$ monotectoid reaction at higher temperature. During cooling, the γ_3 phase may not get stabilized at RT as it does not contain enough solute to permit retention. Probably, the γ_3 phase transforms into α -phase during cooling keeping the lamellae intact and therefore could not be detected in XRD. However, the formation of α and γ_3 phases were detected in the furnace-cooled U-2Zr-4Nb alloy because of higher Nb content in the γ_3 phase. On the other hand, both the water-quenched U-4Zr-2Nb and U-2Zr-4Nb alloys formed distorted orthorhombic (α'_b) structure via martensitic transformation.

In a similar type investigation with water-quenched U-rich U-(7-y)Zr-yNb alloys (y = 0, 2, 3.5, 5, 7 in wt%), Ghoshal et al. [27] reported formation of metastable α' -phase for U-7Zr and U-5Zr-2Nb alloys; α'' and γ° structures in U-2Zr-5Nb and U-7Nb alloys, respectively. However, the retention of single bcc γ -phase in water-quenched alloys was not reported in their study which is in good agreement with the present result. Eckelmeyer [104] has also found a banded martensitic structure (α'_b) for water-quenched U-0.75Zr-0.75Nb-0.75Mo-0.50Ti alloy and its crystal structure of α'_b is considered as strained variant of α -U with lattice parameter of $a = 2.877\text{\AA}$, $b = 5.830\text{\AA}$, $c = 4.985\text{\AA}$. The structure and morphology are very similar to the martensitic structure of water-quenched U-4Zr-2Nb and U-2Zr-4Nb alloys of our present study. Lopes et al. [20, 53] has reported that U-2.5Zr-7.5Nb alloy water-quenched from 1273 K has typical bcc structure with lattice parameter of 3.481\AA . The bcc γ -phase was stabilized in the

water-quenched U-2.5Zr-7.5Nb alloy due to its higher Nb content. However, the γ -phase transformed to α'' -phase having twinned morphology during isothermal annealing at 573 K for 6 h, a pearlite structure of α (orthorhombic) + γ_3 (bcc) at 773 K. Pais et al. [54] also found that the microstructures of U-3Zr-9Nb and U-2.5Zr-7.5Nb alloys gradually transformed from single γ -phase to a pearlitic phase ($\alpha + \gamma_3$) when the alloys were treated isothermally at 873 K. Similar type of lamellar structure composed of α and γ_3 was formed during furnace cooling of U-2Zr-4Nb alloy in the present study.

The furnace-cooled U-6Nb alloy also contains fine lamellar structure of α -U and γ_3 phases, while water-quenched U-6Nb alloy exhibited banded martensitic with monoclinic structure (α''). The U-rich U-Nb alloys generally form a wide variety of metastable structures during quenching. At low Nb contents (0–8 at.%), γ transforms directly to a metastable orthorhombic phase, referred to as α' . At Nb contents (9–15 at.%), a monoclinically distorted structure (α'') is formed. At still higher Nb contents (16–20 at.%), a tetragonally distorted version of the metastable γ^0 phase is formed [47]. The monoclinic crystal structure (α'') of U-6Nb alloy is closely related to the orthorhombic α -U structure. The monoclinic structure (α'') can be defined either by natural space group of $P2_1/m$ or by an artificial space group $C2_1/m$ [105]. Axis b is considered as unique axis in standard $P2_1/m$ setting whereas axis c is the unique axis for $C2_1/m$ setting. The β angle in the $P2_1/m$ symmetry and γ angle for $C2_1/m$ symmetry are not 90° . It may be noted here that some Rietveld refinement software packages cannot handle unusual settings during crystal structure analysis. In the present investigation, the refinement of monoclinic α'' structure of water-quenched U-6Nb alloy was carried out using natural space group of $P2_1/m$. The lattice parameters are $a = 3.288 \text{ \AA}$, $b = 4.988 \text{ \AA}$, $c = 3.171 \text{ \AA}$ and the β angle

was found to be around 126.38° and the atomic positions are $x = 0.855$, $y = 0.25$ and $z = 0.071$. The lattice parameters of as-quenched U-Nb alloys were determined by Brown et al. [51] using neutron diffraction and the monoclinic α'' structure have been characterized by the non-conventional space group of $C2_1/m$ to avoid a cell transformation and to facilitate comparison with orthorhombic (α , α') structure. As per their study, the α'' lattice parameters (with space group $C2_1/m$) are $a = 2.914 \text{ \AA}$, $b = 5.718 \text{ \AA}$, $c = 4.965 \text{ \AA}$ and $\gamma = 93.26$ for U-6.25Nb alloy. Vandermeer [23] also characterized the water-quenched U-6Nb alloy and the lattice parameters of monoclinic α'' phase were $a = 2.893 \text{ \AA}$, $b = 5.752 \text{ \AA}$, $c = 4.977 \text{ \AA}$ and $\gamma = 92.38^\circ$ and α'' was thought to transform martensitically in two steps during rapid quenching from γ -phase i.e., γ (bcc) $\rightarrow \gamma^\circ$ (tetragonal) $\rightarrow \alpha''$ (monoclinic). The data reveals a substantial decrease in lattice parameter b of monoclinic α'' (space group $C2_1/m$) in U-6Nb alloy when compared to α -U phase (space group $Cmcm$).

In the present study, the lattice parameters data of water-quenched U-6Zr, U-4Zr-2Nb and U-2Zr-4Nb alloys, all having α' phase (space group $Cmcm$), also reveal a remarkable decrease in lattice parameter b with gradual addition of Nb (Table 3.2). It indicates that the lattice parameter 'b' is very sensitive to the solute content. The uranium atom has ellipsoidal shape with the long axis parallel to the [010] direction i.e., along b axis. The substitution of some ellipsoidal U atoms by more spherical solutes results in a contraction of the 'b' parameter [59].

The microstructures of as-cast, quenched and slow-cooled U-6Nb alloy were also studied by Kelly et al. [50]. The quenched sample exhibited prior γ grain boundaries with a very detailed herringbone twinned martensite while the slow-cooled samples revealed lamellar structure. Their results are consistent with our observation. Another important observation is that the inter-lamellar spacing becomes smaller in the furnace-cooled alloys having more Nb (Fig. 3.6). The γ -

stabilizing effect of Nb is more than that of Zr. As Nb content increases, the monotectoid reaction ($\gamma \rightarrow \alpha + \gamma_3$) takes place during cooling at relatively lower temperature due to more undercooling and that may lead to reduction in the inter-lamellar spacing. More under cooling was observed in alloys containing a higher amount of Nb, which is also evident in the DTA cooling curve (Fig. 3.8b). From the above results and discussion, it is evident that U-6(Zr+Nb) alloys form different crystal structures and microstructures associated with several phase transformations. However, a total alloying content of 6wt% (Zr or Nb or both) is not sufficient to retain the high-temperature bcc γ -phase at room temperature by water quenching from 1173 K.

In the present study, DTA has been employed extensively to determine the phase transformation temperatures including solidus/liquidus of U-Zr-Nb alloys. The solidus temperature of the fuel is considered as an important parameter which depends primarily on the fuel alloy composition (at fixed pressure). The solidus/liquidus temperatures of U-6Nb alloy (1490/1603 K) are found to be higher than that of U-6Zr alloy (1465/1548 K) and the replacement of Zr by Nb in U-Zr-Nb alloy gradually increases the solidus/liquidus temperatures. The solidus/liquidus temperatures (1489/1631 K) of U-8.4Zr alloy measured by Leibowitz et al. [106] using DTA are found to be higher than that of present data due to higher Zr-content. The solidus/liquidus temperatures (1468 K/1550 K) of U-6Zr alloy reported by Balakrishnan et al. [73] using spot-technique are in good agreement with the present data.

Several important features of the ternary alloy have been revealed from the present investigation. The additions of both Zr and Nb lower the temperature at which γ is stable as a single phase and the γ -stabilizing effect of Nb is more than that of Zr. In fact, DTA thermograms of U-Zr-Nb alloys showed a substantial decrease in the transformation temperature at which the single γ -phase forms via $\alpha + \gamma_3 \rightarrow \gamma$ reaction. In contrast to U-6Zr alloy, the DTA thermograms

of the ternary alloys do not show any transformation peak associated with δ -UZr₂ phase as well as β -phase. The water-quenched samples have martensitic orthorhombic structure (α') or monoclinic structure (α'') and therefore additional exothermic peaks appeared in the water-quenched alloys, at 725 (for U-6Nb), 765 (for U-4Zr-2Nb), and 775 K (for U-2Zr-4Nb) are associated with the non equilibrium martensitic to equilibrium phase transformation i.e., $\alpha'' \rightarrow \alpha + \gamma_3$ for U-6Nb alloy and $\alpha' \rightarrow \alpha + \gamma_3$ for ternary alloys.

The coefficient of thermal expansion (CTE) of nuclear fuel is considered as an important parameter for modelling fuel behaviour in reactors. The thermal expansion of alloys strongly depends on their composition and phase(s). Here, the overall extent of thermal expansion of U-6Zr and U-4Zr-2Nb alloys are similar whereas it gradually decreases with increasing Nb content. In U-6Zr alloy, the transition in $\Delta L/L_0$ (%) versus temperature plot at 860 K and 960 K are associated with the $\alpha + \delta \rightarrow \alpha + \gamma_2 \rightarrow \gamma$ transformations which was already discussed using DTA result. The intermediate transitions were also resolved at a lower heating rate. On the other hand, the transition in length changes at 900 K (for U-4Zr-2Nb), 893 K (U-2Zr-4Nb) and 913 K (U-6Nb) are due to $\alpha + \gamma_3 \rightarrow \gamma$ transformation reaction. The dilatometer expansion curve also indicates that Nb addition lowers the temperatures of $\alpha + \gamma_3 \rightarrow \gamma$ transformation in the ternary alloys. The phase transition temperatures are in excellent agreement with the DTA results. The average coefficients of thermal expansion of U-6Zr, U-4Zr-2Nb, U-2Zr-4Nb, and U-6Nb alloys in the temperature range of 300–873 K were found to be 18.13×10^{-6} , 18.41×10^{-6} , 17.92×10^{-6} and $15.37 \times 10^{-6} \text{ K}^{-1}$, respectively. The CTE values of U-6Zr, U-4Zr-2Nb, and U-2Zr-4Nb alloys are close to each. The variation in CTE values may be due to variation in phase content and phase transformation temperatures. The CTE of U-6Nb alloy is remarkably lower

than the rest of the three alloys. The dilatometer thermal expansion of as-cast U-6Zr alloy has been reported in the earlier study with average CTE value of $18.28 \times 10^{-6} \text{ K}^{-1}$ in the temperature range 298–823 K [15]. This value is in good agreement with the present data. The thermal expansion coefficients reported for U-8Nb and U-10Nb alloys are found to be 14.2×10^{-6} and $13.5 \times 10^{-6} \text{ K}^{-1}$, respectively, which also indicates that CTE gradually decreases with increasing niobium [72]. Therefore, the thermal expansion results of the present study are consistent with those previously reported for U-Zr and U-Nb alloys.

Molar heat capacity is another important thermophysical property of fuel. The molar heat capacity of the U-6(Zr+Nb) alloys increases with temperature and decreases with increasing Nb content. The molar heat capacities of U-2Zr-4Nb and U-6Nb alloys were found to be lower than that of U-6Zr alloy. In general, the molar heat capacity should decrease with increase in Zr or Nb, due to the lower molar heat capacity value of Zr or Nb compared to U. In addition to this, Zr is having higher molar heat capacity than that of Nb and therefore the gradual replacement of Zr with equivalent amount of Nb should decrease the molar heat capacity value. It is also reflected in the present results where the molar heat capacity values of U-6Nb alloy are slightly lower than that of U-2Zr-4Nb alloy.

The molar heat capacity data of various U-rich U-Zr alloys of similar compositions are presented together in Fig. 3.13 for comparison. The data reported by Fedorov and Smirnov [75] was found to be higher than that of present result. On the other hand, the molar heat capacity data reported by Takahashi et al. [76] for U-5.87Zr alloy shows a reasonably good agreement with the present result of U-6Zr alloy. The similarity in the results is due to similar nature of samples in terms of heat treatment and phase content. The sample (U-5.87Zr) used by Takahashi et al. [76] was first annealed at 1100 K for 30 min and the room temperature phases were U(α) and δ -

UZr₂ which are similar to the present study. Unlike U-rich U-Zr alloys, the data on the molar heat capacity of U-Nb and U-Zr-Nb alloys were limited. Dash et al. [78] measured the specific heat capacities of U-7Zr, U-7Nb, U-5Zr-2Nb, U-3.5Zr-3.5Nb and U-2Zr-5Nb alloys where the total alloying content was limited to 7 wt%. The data reported by Dash et al. [78] are found to be substantially higher than that of the present results. The authors used water-quenched samples were for measurement whereas alloys used in the present study were furnace-cooled and therefore the phase contents of samples are expected to be different. The variation in the molar heat capacity data is probably due to the variation in phase content in the alloys resulting from their different thermal history/heat treatment prior to measurement.

The molar heat capacities of U-6Zr, U-2Zr-4Nb and U-6Nb alloys were also calculated from the reported molar heat capacity data of pure U, Zr and Nb metals [107] employing the Neumann-Kopp (NK) rule. The experimental and calculated results are presented collectively in Fig. 3.14 which reveals that the experimental molar heat capacity data are lower than that calculated from the NK rule. The difference between the experimental and estimated data can be correlated with the phase stability. As for example of U-6Zr alloy, the molar heat capacity values were estimated from $0.8572 C_{p,m}^0(\text{U})$ and $0.1428 C_{p,m}^0(\text{Zr})$ using additivity law where $C_{p,m}^0(\text{U})$ and $C_{p,m}^0(\text{Zr})$ are the molar heat capacities of U and Zr, respectively. However, the alloy is biphasic in nature containing α -U phase and δ -UZr₂. Hence, the experimental data reflects the measured molar heat capacity of the two-phase mixture of $\alpha\text{U} + \delta\text{-UZr}_2$ instead of $\alpha\text{-U} + \alpha\text{-Zr}$. Similarly, both the U-2Zr-4Nb and U-6Nb alloys are biphasic in nature containing orthorhombic α -U and bcc γ_3 phases and the experimental data are basically measured molar heat capability of two phase mixture of $\alpha\text{-U} + \gamma_3$ instead of $\alpha\text{-U} + \alpha\text{-Zr} + \text{Nb}$ (for U-2Zr-4Nb)

or α -U + Nb (for U-6Nb alloy). The difference between the experimental and estimated values may be attributed to their difference in phases under consideration.

In the present study, the thermodynamic functions such as molar enthalpy increment $H_m^0(T) - H_m^0(298.15 \text{ K})$ and molar entropy increment $S_m^0(T) - S_m^0(298.15 \text{ K})$ of the alloy samples were computed in the temperature range of 298.15 – 800 K using the fitted molar heat capacity equations (Eqs. 3.9 – 3.14). The relations used for the calculation of thermodynamic functions are given as follows:

$$H_m^0(T) - H_m^0(298.15 \text{ K}) = \int_{298.15}^T C_{p,m}^0(T) dT \quad (3.15)$$

$$S_m^0(T) - S_m^0(298.15 \text{ K}) = \int_{298.15}^T \left(\frac{C_{p,m}^0(T)}{T} \right) dT \quad (3.16)$$

It may be noted here that the $C_{p,m}^0(298.15 \text{ K})$ of samples were calculated through the extrapolation of fitted equations valid in the lower temperature range (i.e., $323 \leq T/\text{K} \leq 598$). The computed thermodynamic functions for U-6Zr, U-2Zr-4Nb and U-6Nb alloys are provided in Tables 3.6, 3.7 and 3.8, respectively. The reported thermodynamic functions of pure uranium metal have also been highlighted in Table 3.9 for comparing with the present results and it was found that the calculated molar enthalpy increment and molar entropy increment data of the alloy samples in the temperature range of 298.15–800 K are comparable to those of pure uranium.

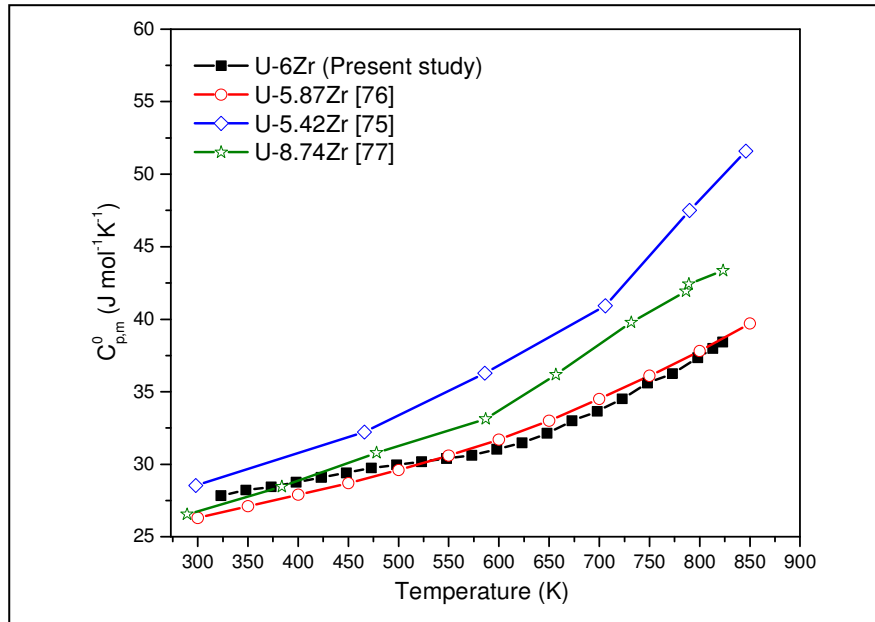


Fig. 3.13 Molar heat capacity data of various U-rich U-Zr alloys of similar compositions as a function of temperature for comparison with the present data of U-6Zr alloy.

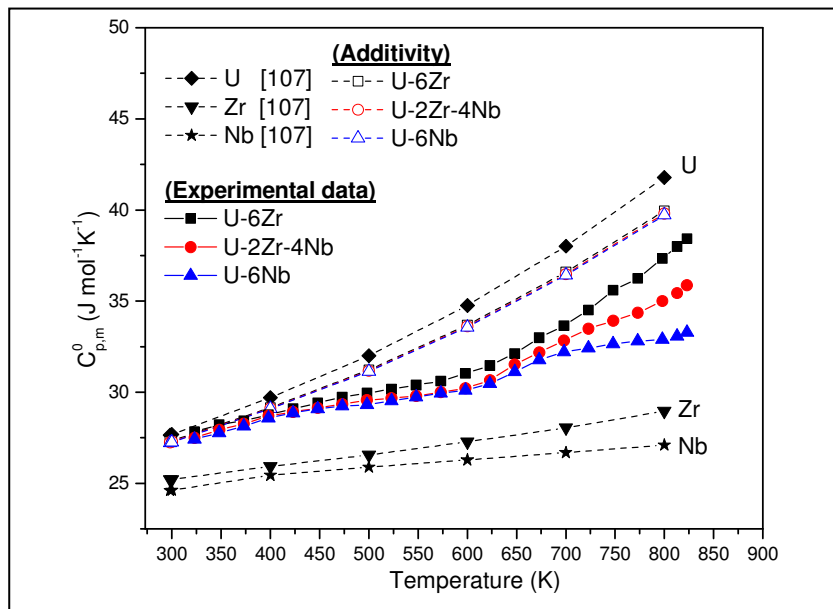


Fig. 3.14 The experimental and calculated molar heat capacities of U-6Zr, U-2Zr-4Nb and U-6Nb alloys along with the reported molar heat capacities of pure constituent elements (i.e., U, Zr and Nb) are plotted collectively as a function of temperature.

Table 3.6 Thermodynamic functions for U-6Zr alloy.

T (K)	$C_{p,m}^0$ ($J \cdot mol^{-1} \cdot K^{-1}$)	$H_m^0(T) - H_m^0(298.15)$ ($J \cdot mol^{-1}$)	$S_m^0(T) - S_m^0(298.15)$ ($J \cdot mol^{-1} \cdot K^{-1}$)
298.15	27.52	0	0
300	27.55	50.9	0.17
350	28.20	1444.7	4.47
400	28.82	2870.1	8.27
450	29.40	4325.8	11.70
500	29.95	5809.8	14.83
550	30.47	7320.6	17.71
600	31.00	8856.6	20.38
650	32.27	10437.3	22.91
700	33.76	12087.0	25.35
750	35.49	13817.1	27.74
800	37.44	15639.3	30.09

Table 3.7 Thermodynamic functions for U-2Zr-4Nb alloy.

T (K)	$C_{p,m}^0$ ($J \cdot mol^{-1} \cdot K^{-1}$)	$H_m^0(T) - H_m^0(298.15)$ ($J \cdot mol^{-1}$)	$S_m^0(T) - S_m^0(298.15)$ ($J \cdot mol^{-1} \cdot K^{-1}$)
298.15	27.17	0	0
300	27.20	50.3	0.17
350	27.96	1429.9	4.42
400	28.61	2844.8	8.20
450	29.15	4289.4	11.60
500	29.58	5758.3	14.69
550	29.91	7246.0	17.53
600	30.23	8747.2	20.14
650	31.54	10291.6	22.61
700	32.80	11900.4	25.00
750	34.01	13571.0	27.30
800	35.17	15301.0	29.54

Table 3.8 Thermodynamic functions for U-6Nb alloy.

T (K)	$C_{p,m}^0$ ($\text{J}\cdot\text{mol}^{-1}\cdot\text{K}^{-1}$)	$H_m^0(T) - H_m^0(298.15)$ ($\text{J}\cdot\text{mol}^{-1}$)	$S_m^0(T) - S_m^0(298.15)$ ($\text{J}\cdot\text{mol}^{-1}\cdot\text{K}^{-1}$)
298.15	27.09	0	0
300	27.12	50.1	0.17
350	27.86	1424.9	4.40
400	28.50	2834.2	8.17
450	29.04	4273.0	11.56
500	29.47	5736.2	14.64
550	29.81	7218.7	17.46
600	30.09	8715.4	20.07
650	31.23	10249.2	22.52
700	32.10	11833.5	24.87
750	32.71	13454.8	27.11
800	33.06	15100.1	29.23

Table 3.9 Reported data of thermodynamic functions for uranium metal [107].

T (K)	$C_{p,m}^0$ ($\text{J}\cdot\text{mol}^{-1}\cdot\text{K}^{-1}$)	$H_m^0(T) - H_m^0(298.15)$ ($\text{J}\cdot\text{mol}^{-1}$)	$S_m^0(T) - S_m^0(298.15)$ ($\text{J}\cdot\text{mol}^{-1}\cdot\text{K}^{-1}$)
298.15	27.654	0	0
300	27.690	51	0.171
400	29.701	2920	8.409
500	32.007	6002	15.277
600	34.760	9336	21.348
700	38.012	12970	26.944
800	41.785	16956	32.261

The microhardness of an alloy generally depends upon the composition, type of heat treatment, phase content and crystal structure. In the present investigation, a substantial variation in the microhardness data has been observed from 160 VHN (water-quenched U-6Nb) to 565 VHN (water-quenched U-6Zr alloy). The hardness of as-cast U-6Zr alloy was reported earlier in the temperature range of 300–973 K [15] where the room temperature hardness (380 ± 20 VHN)

is found to be very close to that of furnace-cooled U-6Zr alloy (377 ± 20 VHN) of this study. Pais et al. [54] found that the Vickers microhardness data of U-2.5Zr-7.5Nb and U-3Zr-9Nb alloys aged at 573 K and 873 K varies in the range 245–530 VHN. Lopes et al. [108] analyzed the hardness behaviour of U-2.5Zr-7.5Nb alloy with respect to recovery, recrystallization, and precipitation phenomena by varying different process variables i.e., degree of deformation, temperature, and time. According to them, annealing of the 50 % deformed sample at 723 K for 2.5 h resulted in $\alpha + \gamma_3$ phase precipitation with hardness value of 482.4 (± 9.48) HV. In this study, a similar increasing trend in microhardness data in the furnace-cooled U-2Zr-4Nb (425 VHN) and U-6Nb (415 VHN) alloys was also observed due to formation of $\alpha + \gamma_3$ phases. Masrukan et al. [55] measured the hardness of selected U-Zr-Nb alloys and the variation of hardness data of U-6Zr-2Nb (375 HVN), U-6Zr-5Nb (523 HVN) and U-6Zr-8Nb (319 HVN) alloys was explained on the basis of different rates of nucleation and grain growth mechanism depending on Nb content in the alloys. Morais et al. [71] assessed the microhardness of as-cast and heat treated U-3Zr-9Nb, U-6Zr-6Nb and U-9Zr-3Nb alloys by dividing them into two categories i.e., cubic (bcc) and non-cubic (orthorhombic and monoclinic) crystal structures and reported that the cubic-gamma phase alloys are softer than non-cubic phase alloys. The hardness of cubic U-Zr-Nb alloys are in the range 235-270 VHN, whereas the monoclinic phases (α'') have hardness data in the range 330-440 VHN. The as-cast U-9Zr-3Nb alloy with distorted orthorhombic (α') structure shows hardness of 525 VHN. In general, Zr is considered as hardener and Nb is a softener alloying element.

3.6. Summary and Conclusions

The present study delivers useful data on the crystal structures of phases with their lattice parameter and phase fraction, microstructural characteristic, phase transformation behaviour, solidus/liquidus temperature, expansion behaviour, molar heat capacity and hardness data of the uranium rich U-6Zr, U-4Zr-2Nb, U-2Zr-4Nb and U-6Nb alloys. The following important observations are summarized based on the present study:

- The replacement of Zr in U-6Zr alloy with Nb leads to the disappearance of δ -UZr₂ phase. The fraction of bcc γ_3 -phase is found to be higher in alloy with higher Nb content.
- A total alloying content of 6wt% (Zr or Nb or both) is not sufficient to retain the high temperature bcc γ -phase at RT by water quenching from 1173 K.
- The solidus and liquidus temperatures gradually increase with increasing Nb content. The expansion data indicates that Nb addition decreases the coefficient of thermal expansion.
- The addition of 6wt% alloying element (Zr or Nb) into uranium metals leads to decrease in molar heat capacity. The gradual replacement of Zr with equivalent amount of Nb leads to decrease in molar heat capacity. The measured molar heat capacity of the alloys is found to be lower than the values estimated by the Neumann-Kopp additivity rule.
- The hardness data of water-quenched samples gradually decreases with increasing Nb content in the alloy.
- During water quenching, the martensitic transformation leads to the contraction of lattice parameter b, and the extent of contraction gradually increases with increasing Nb content.
- Furnace cooling of the alloys leads to the formation of fine lamellar microstructure with segregation of alloying element(s). The water quenching lead to formation of the

martensitic microstructure of the U-6Zr alloy having acicular morphology and the alloys containing Nb having banded structure.

- In water-quenched samples containing Nb, an exothermic transformation was observed in the temperature range 725-775 K which is associated with the non-equilibrium martensitic to equilibrium phase transformation.

Chapter 4

Structural, microstructural characterization and thermal properties of U-(6-x)Zr-xMo alloys (x = 0, 2, 4, 6 wt%)

4.1. Introduction

Like U-Zr-Nb alloys, uranium-rich uranium-zirconium-molybdenum (U-Zr-Mo) alloys are also considered as good alternative fuel for fast breeder reactors due to their many favourable properties. In the present investigation, U-6Zr, U-4Zr-2Mo, U-2Zr-4Mo and U-6Mo alloys with total alloying content of 6 wt% were chosen by gradually replacing Zr in U-6Zr alloy with equivalent quantity of Mo to find out the effect of Mo addition. This chapter describes structural and microstructural characterization, thermal analysis and thermophysical property evaluation, phase transformation behaviour and microhardness data of these alloys. All the results have been thoroughly discussed and compared with the reference alloy composition of U-6Zr.

4.2. Experimental procedure

This present chapter also deals with furnace-cooled and water-quenched samples of U-6Zr, U-4Zr-2Mo, U-2Zr-4Mo and U-6Mo alloys. The detailed experimental procedure of sample preparation, heat treatment, structural and microstructural characterization, thermal analysis and thermophysical properties measurement, and microhardness of the samples have been presented in Chapter 2.

4.3. Results

4.3.1. Structural Characterization

4.3.1.1. Furnace-cooled samples

The XRD data of the furnace-cooled U-6Zr, U-4Zr-2Mo, U-2Zr-4Mo and U-6Mo alloys are presented together in Fig. 4.1. The Rietveld refinement results of XRD data of all the furnace-cooled samples are summarized in Table 4.1. The XRD data of furnace-cooled U-6Zr

alloy comprises of mainly orthorhombic α -U phase with a small fraction of δ -UZr₂ phase. The formation of small fraction of δ -UZr₂ phase was ascertained by identifying the non overlapping low intensity peaks of (111) and (112) planes at around 46.5° and 71.6°, respectively, as already discussed in the previous chapter. The XRD pattern of furnace-cooled U-4Zr-2Mo alloy reveals the peaks of orthorhombic α -phase (space group Cmcm) and bcc γ -phase (space group Im-3m). The γ -phase was revealed by the appearance of shoulder of (110) peak in the XRD pattern as highlighted by an asterisk. The cubic γ -phase has lattice parameter of 3.446 Å and the phase fraction of around 4 vol%. Similarly, the furnace-cooled U-2Zr-4Mo alloy consists of orthorhombic α -U and bcc γ phases and the peaks of γ -phase are more intense. In this case, the lattice parameter of γ -phase is 3.426 Å and phase fraction is around 38 vol%. The Rietveld refinement plots of furnace-cooled U-4Zr-2Mo and U-2Zr-4Mo alloys are shown in Fig. 4.2a and Fig. 4.2b, respectively. The furnace-cooled U-6Mo alloy comprises predominantly of the bcc γ phase. Few peaks of orthorhombic α -phase were also visible in the magnified XRD plot of U-6Mo alloy (Fig. 4.1b) and the phase fraction of α -phase was found to be ~9 vol%.

4.3.1.2. Water-quenched samples

Fig. 4.3a shows the XRD data of water-quenched U-6Zr, U-4Zr-2Mo, U-2Zr-4Mo and U-6Mo alloy samples. The refinement results including the phases with their space group and lattice parameter are presented in Table 4.2. The water-quenched U-6Zr and U-4Zr-2Mo alloys exhibited similar XRD patterns which belong to distorted orthorhombic crystal structure of α -phase with higher 'a' and 'c' parameters and lower 'b' parameter as compared to their furnace-cooled part. The orthorhombic crystal of α -phase with slightly different lattice parameter is designated as α' . The Rietveld refinement plot of XRD data of U-4Zr-2Mo alloy is shown in

Fig. 4.4a as a representative of the two similar alloys. The XRD pattern of the water-quenched U-2Zr-4Mo alloy is significantly different and the crystal structure is characterized by a monoclinic unit cell, i.e., α'' modification. The Rietveld refinement analysis using space group $P2_1/m$ (11) revealed the lattice parameters as $a = 3.265 \text{ \AA}$, $b = 4.951 \text{ \AA}$, $c = 3.159 \text{ \AA}$ and $\beta = 126.60^\circ$. Fig. 4.4b shows the refinement plot of U-2Zr-4Mo alloy. The XRD data of water-quenched U-6Mo sample apparently shows the peaks of bcc γ -phase. The magnified view of $\gamma(110)$ plane (Fig. 4.3b) revealed a weak shoulder-like feature (indicated by an arrow). However, the splitting of the (110) plane and other high angle reflections was not visible in the XRD pattern. It indicates that the U-6Mo alloy consists predominantly of bcc γ -phase retained in a metastable state during quenching rapid cooling. The weak shoulder-like feature in $\gamma(110)$ plane may be attributed to trace amount of intermediate tetragonal (γ°) phase formation. It is interesting to note here that the γ -phases of both the furnace-cooled and water-quenched U-6Mo alloys exhibit almost identical lattice parameters.

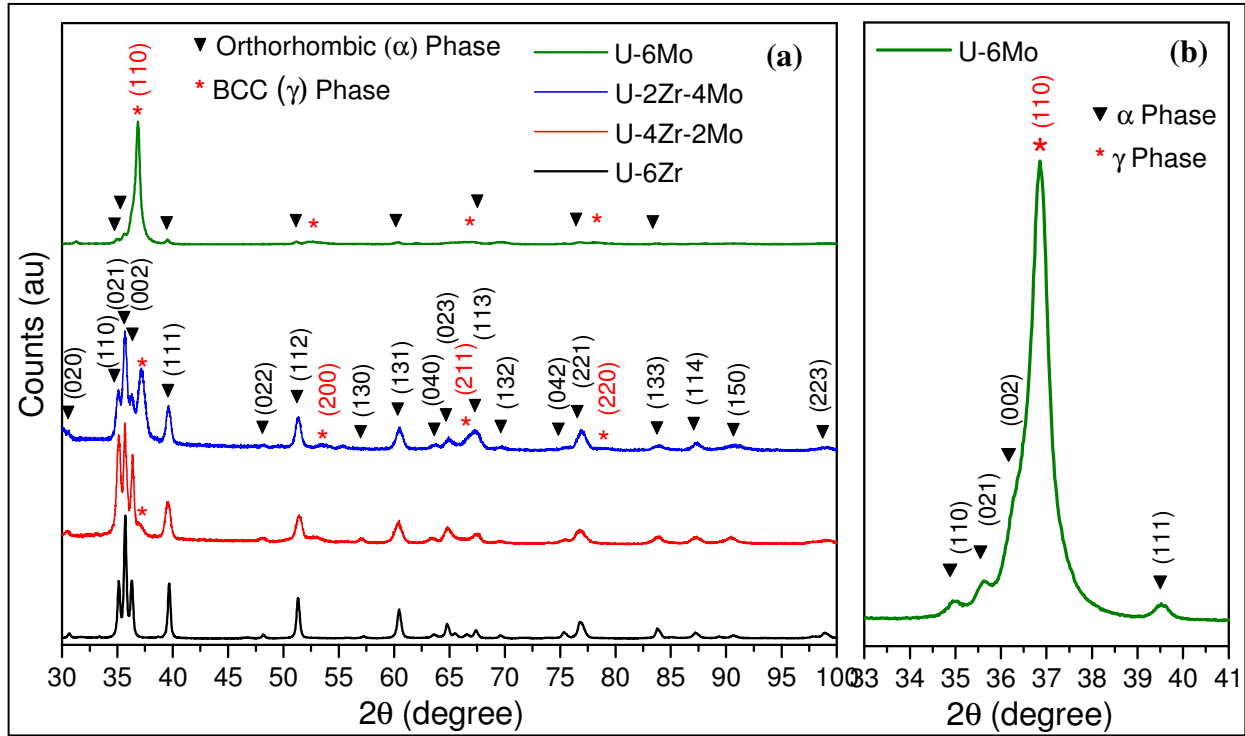


Fig. 4.1 (a) X-ray diffraction patterns of furnace-cooled alloy samples, (b) Magnified XRD data of U-6Mo alloy showing low intensity peaks of orthorhombic α U phase along with bcc γ -phase.

Table 4.1 Lattice parameter, phase fraction of different phases formed in furnace-cooled alloys

Sample (furnace-cooled)	Phase(s)	Space group	Phase fraction (vol %)	Lattice Parameters (\AA , degree)					
				a	b	c	α	β	γ
U-6Zr	Orthorhombic (α)	Cmcm	92	2.856	5.869	4.972	90	90	90
	Hexagonal (δ)	P6/mmm	8	5.035	5.035	3.102	90	90	120
U-4Zr-2Mo	Orthorhombic (α)	Cmcm	96	2.857	5.876	4.962	90	90	90
	BCC (γ)	Im-3m	4	3.446	3.446	3.446	90	90	90
U-2Zr-4Mo	Orthorhombic (α)	Cmcm	62	2.854	5.856	4.960	90	90	90
	BCC (γ)	Im-3m	38	3.426	3.426	3.426	90	90	90
U-6Mo	Orthorhombic (α)	Cmcm	9	2.852	5.843	4.963	90	90	90
	BCC (γ)	Im-3m	91	3.445	3.445	3.445	90	90	90

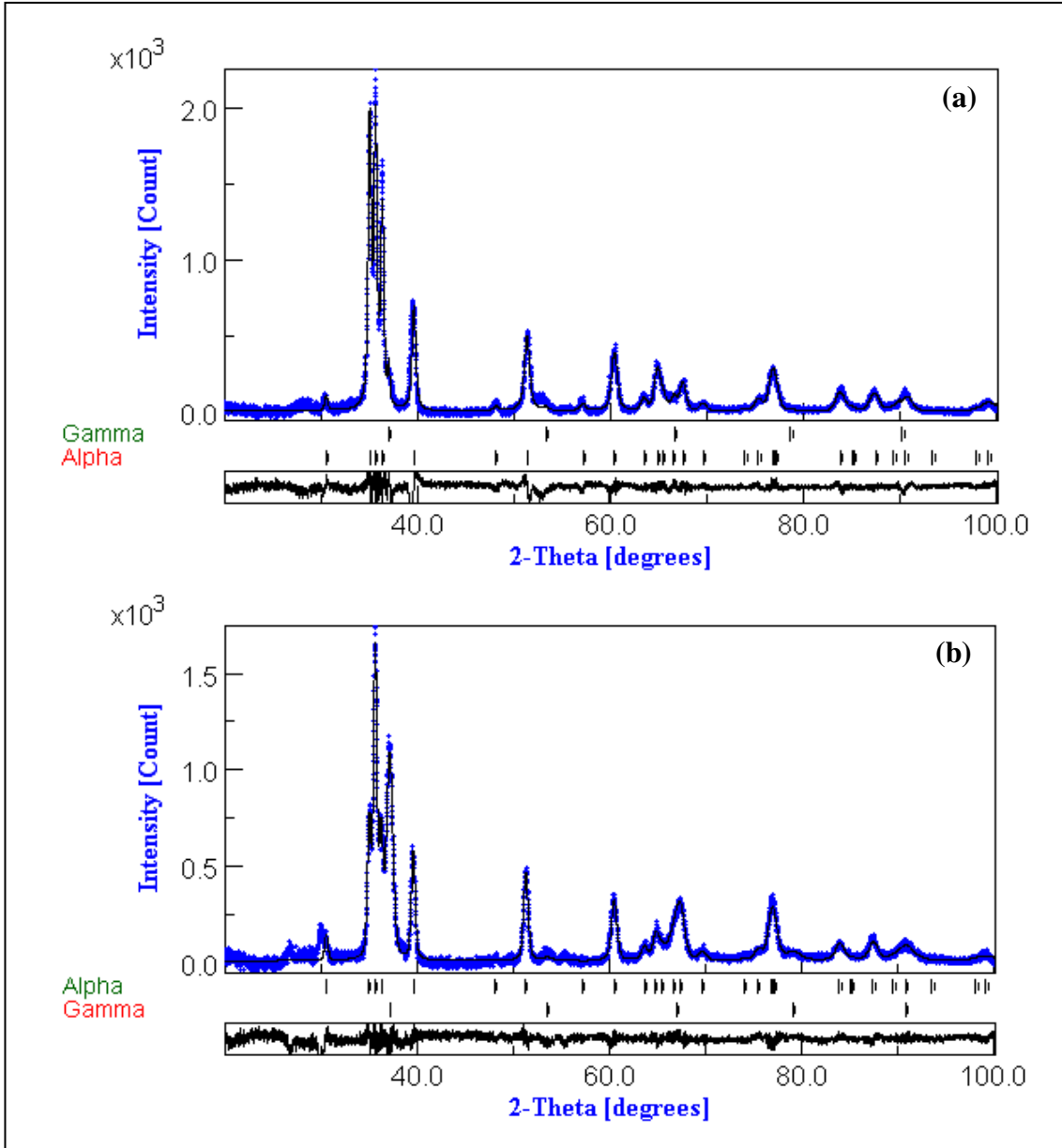


Fig. 4.2 Rietveld refinement of XRD data of furnace-cooled (a) U-4Zr-2Mo alloy showing experimental (blue dots), calculated (black line) and difference pattern (bottom line) along with the peak positions of α -U and γ phases, and (b) U-2Zr-4Mo alloy showing experimental (blue dots), calculated (black line) and difference pattern (bottom line) along with the peak positions of α and γ phases.

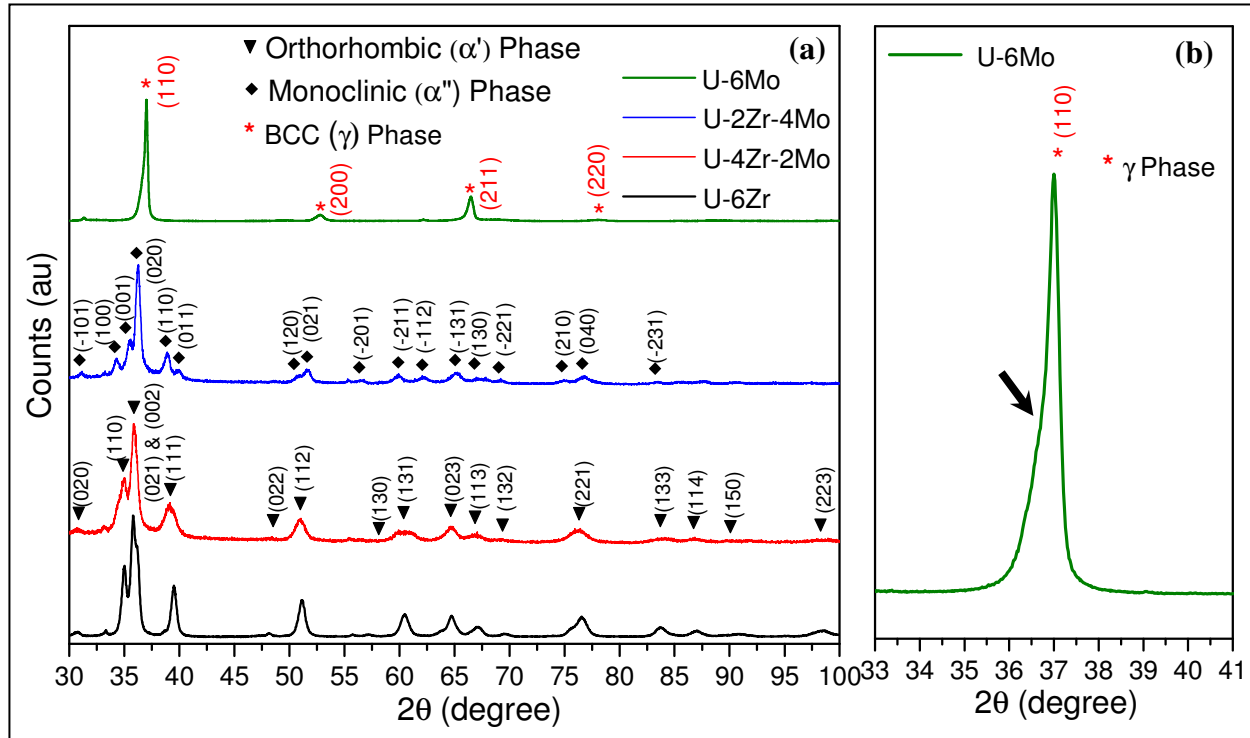


Fig. 4.3 (a) X-ray diffraction patterns of water-quenched alloy samples, and (b) Magnified XRD data of U-6Mo alloy showing (110) peak of bcc γ -phase.

Table 4.2 Lattice parameter of phases formed in water-quenched alloys

Sample (water- quenched)	Phase	Space group	Lattice parameter (\AA , degree)					
			a	b	c	α	β	γ
U-6Zr	Orthorhombic (α')	Cmcm	2.873	5.845	4.986	90	90	90
U-4Zr-2Mo	Orthorhombic (α')	Cmcm	2.901	5.796	4.979	90	90	90
U-2Zr-4Mo	Monoclinic (α'')	P2 ₁ /m	3.265	4.951	3.159	90	126.6 0	90
U-6Mo	BCC (γ)	Im-3m	3.444	3.444	3.444	90	90	90

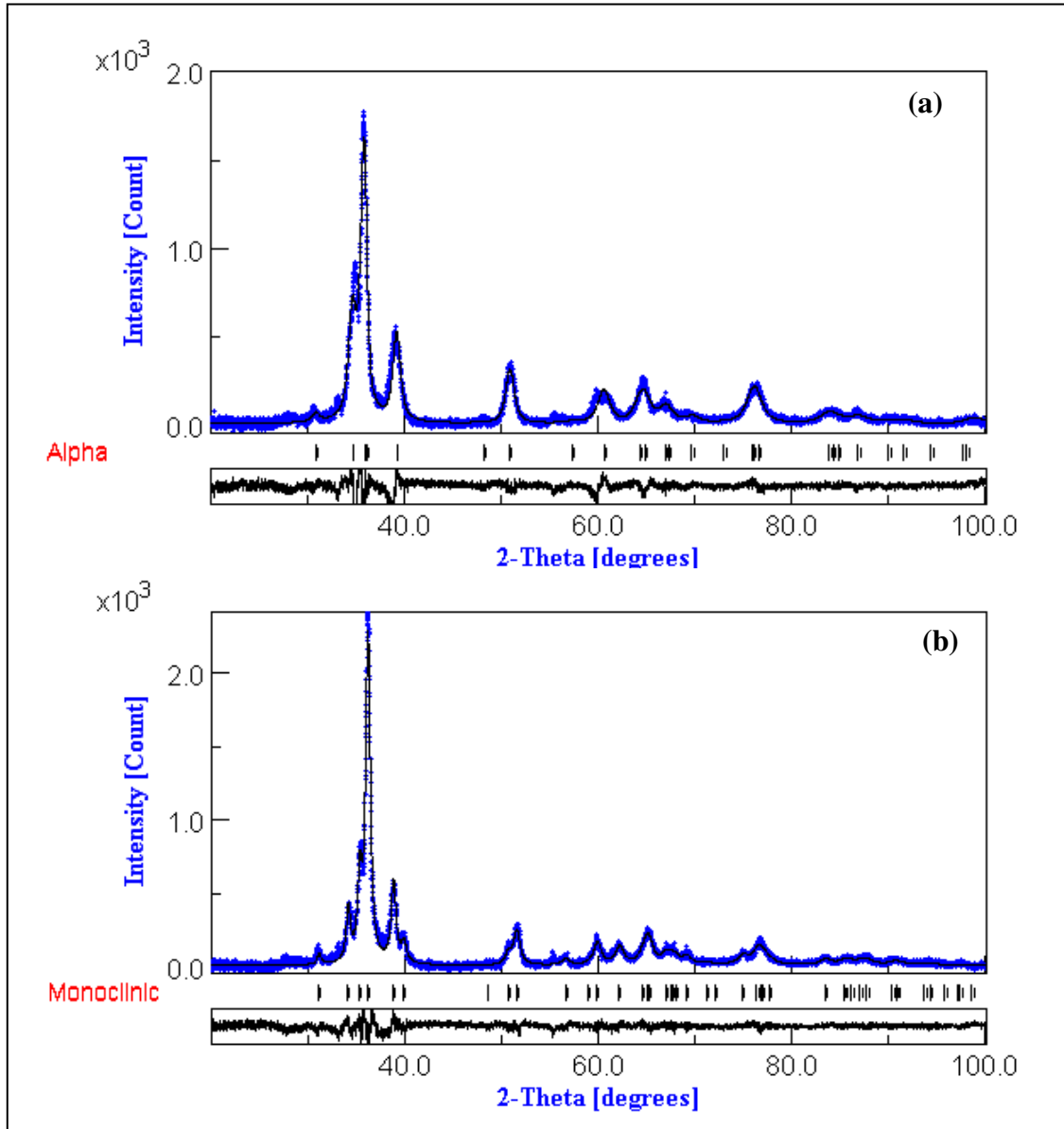


Fig. 4.4 Rietveld refinement of XRD data of water-quenched (a) U-4Zr-2Mo alloy showing experimental (blue dots), calculated (black line) and difference pattern (bottom line) along with the peak positions of orthorhombic α' phase, (b) U-2Zr-4Mo alloy showing experimental (blue dots), calculated (black line) and difference pattern (bottom line) along with the peak positions of monoclinic α'' phase.

4.3.2. Microstructural characterization

4.3.2.1. Furnace-cooled samples

The furnace-cooled U-6Zr sample has fine lamellar type microstructure with segregation of Zr in the alternative layers (Fig. 4.5(a-b)) as discussed in the previous chapter. The furnace-cooled U-4Zr-2Mo alloy exhibits Widmanstatten type microstructure within the prior γ grains (Fig. 4.5c). The micrograph also shows the grain boundary allotriomorphs (GBA) along the prior γ -grain boundaries with elemental composition of approximately 97at.%U, 3at.%Zr which corresponds to α -U phase with small fraction of soluble Zr. Furthermore, a lamellar type microstructure with segregation of Zr/Mo in the alternative layers was also visible in the magnified micrographs (Fig. 4.5(d-e)). The microstructure of U-2Zr-4Mo alloy (Fig. 4.5f) also contains fine lamellar morphology throughout the sample with Zr/Mo segregation inside the lamellar structure. The magnified view of fine lamellar structure (Fig. 4.5g) reveals the inter-lamellar distance of around 200 nm. The inter-lamellar spacing is found to be lower than the actual interaction volume of the SEM electron beam and therefore the exact composition of each layer cannot be determined accurately. The microstructures of the furnace-cooled U-6Mo alloy (Fig. 4.5h) shows the decomposition of high temperature bcc γ -phase at multiple regions and the decomposition is more along the prior γ grain boundary areas. The magnified micrograph of the decomposed region (Fig. 4.5i) revealed fine lamellar microstructure of ($\alpha + \gamma$) with an inter-lamellar spacing well below 1 μm . The prior γ -grain boundaries act as nucleation site of the lamellar product and the growth of reaction products was observed on both sides of the grain boundaries. The presence of un-decomposed bright matrix phase (which is basically metastable γ -phase) indicates that the decomposition event did not proceed to completion during furnace

cooling. The average Mo concentration in the γ matrix was found to be ~6 wt%. However, EDS elemental analysis did not reveal any phase that may correspond to γ' -U₂Mo) intermetallic phase.

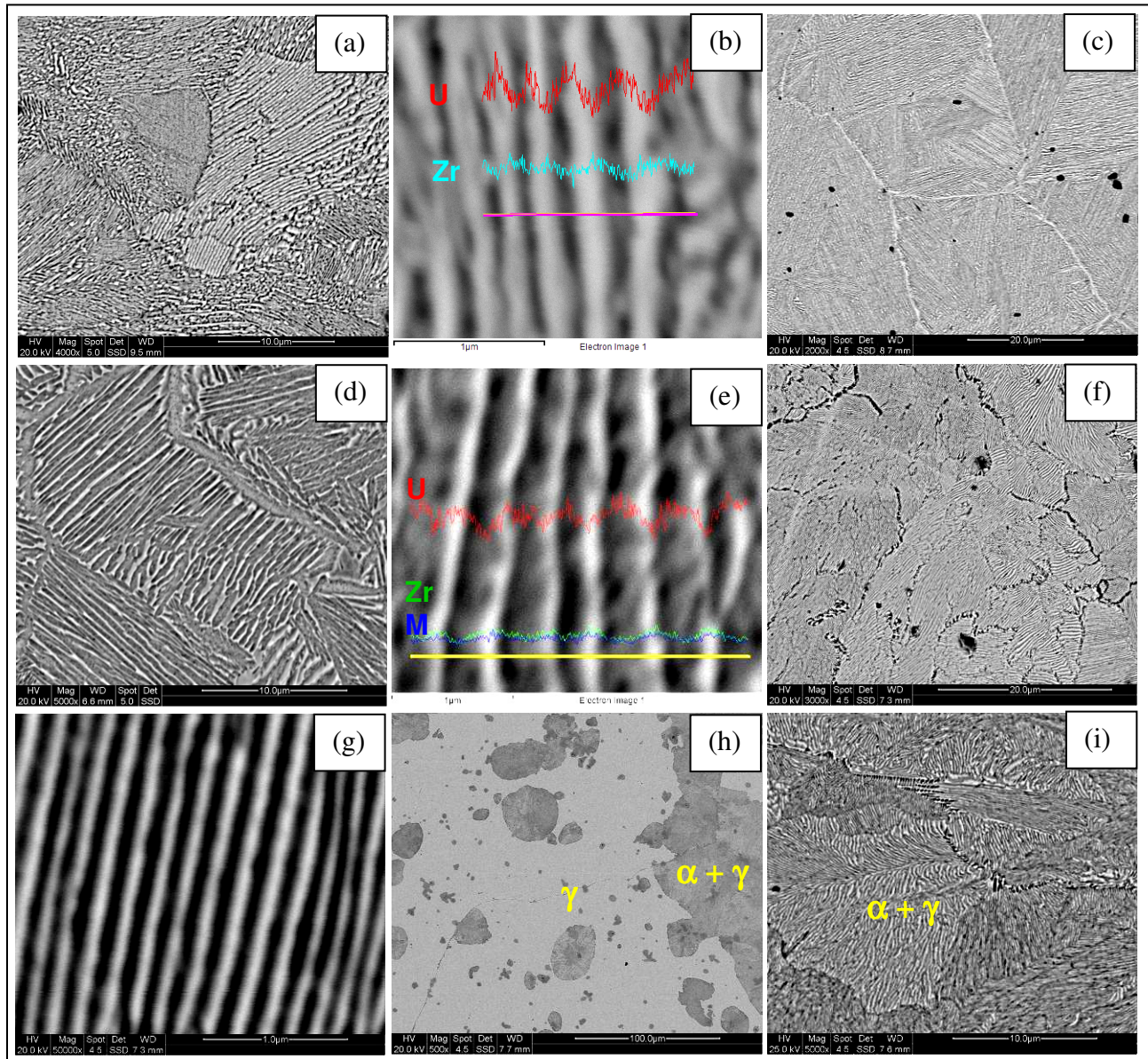


Fig. 4.5 (a & b) SEM images & intensity profiles of U-Mo, Zr-L α X-ray lines on the lamellar structure of furnace-cooled U-6Zr alloy; (c, d & e) SEM images & U-Mo, Zr-L α , Mo-L α X-ray lines scan on the furnace-cooled U-4Zr-2Nb alloy; (f & g) Micrographs of U-2Zr-4Mo at various magnifications showing fine lamellar structure; (h & i) SEM images of U-6Mo alloys showing partial decomposition of γ -phase and magnified view of the decomposition product.

4.3.2.2. Water-quenched samples

The microstructures of water-quenched alloy samples are collectively presented in Fig. 4.6. The microstructures of U-6Zr alloy (Fig. 4.6(a-b)) contain acicular martensitic morphology within prior γ grain grains and the acicular martensitic phase with distorted orthorhombic structure is represented by α'_a which was already discussed earlier. The microstructures of both U-4Zr-2Mo and U-2Zr-4Mo alloys exhibit well-defined grain boundaries (Fig. 4.6(c, e)). In U-4Zr-2Mo alloy, a banded martensitic morphology was found to be formed inside grains (Fig. 4.6d) and the banded martensitic phase of orthorhombic lattice (α) is represented by α'_b where b stands for banded morphology. In U-6Mo alloy, the rapid cooling during quenching from γ -phase region leads to the retention of single γ phase microstructure and the grain boundaries were not resolved properly (Fig. 4.6f). No indication of γ phase decomposition was found in the microstructure of water-quenched U-6Mo alloy which resembles well with the XRD result. All the water-quenched alloy samples were found to be homogeneous with respect to solute (Zr, Mo) distribution. The elemental compositions of all the water-quenched alloys based on EDS results are summarized in Table 4.3.

Table 4.3 EDS results of chemical composition of water-quenched alloys

Sample	Zr (wt%)	Mo (wt%)
U-6Zr	5.93	-
U-4Zr-2Mo	3.93	2.13
U-2Zr-4Mo	1.91	4.05
U-6Mo	-	6.12

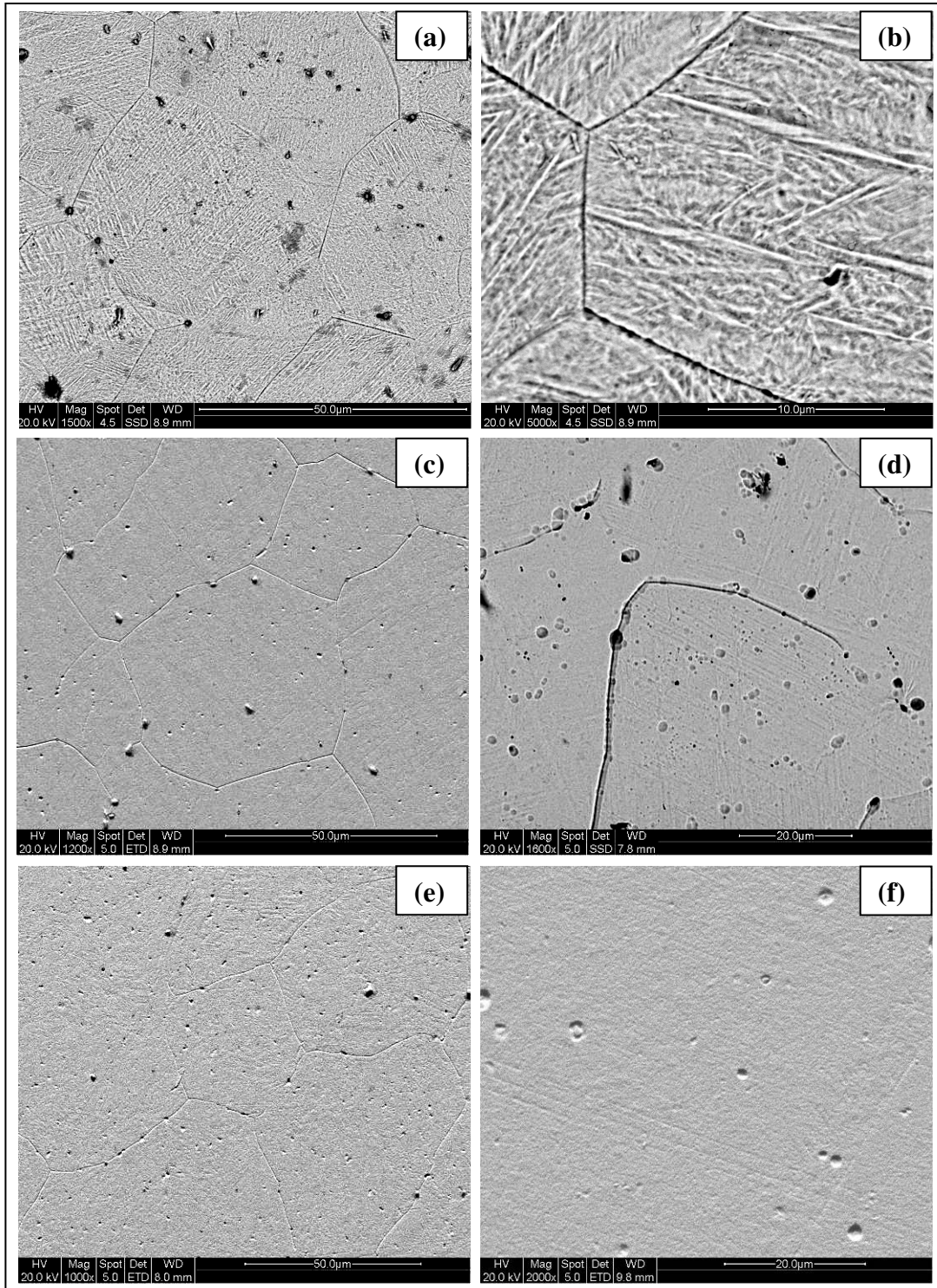


Fig. 4.6 SEM micrographs at different magnification for water-quenched alloys, (a & b) U-6Zr, (c & d) U-4Zr-2Mo, (e) U-2Zr-4Mo and (f) U-6Mo alloys.

4.3.3. Differential thermal analysis

4.3.3.1. Furnace-cooled sample

The DTA curves of furnace-cooled samples during heating and cooling cycles at a scanning rate of 10 K min⁻¹ are collectively presented in Fig. 4.7a and Fig. 4.7b, respectively. In DTA curve, the onset of peak in the heating curve was chosen here as transformation temperature which is similar to convention used in the previous chapter for U-Zr-Nb alloys. The phase transformation behaviour of U-6Zr alloy based on DTA result has already been explained earlier and therefore the same are not repeated here. The overall finding is that U-6Zr alloy exhibits the phase transformation sequences of $\alpha + \delta \rightarrow \alpha + \gamma_2 \rightarrow \beta + \gamma_2 \rightarrow \gamma$ reactions during heating at 860, 946 and 975 K, respectively. The solidus and liquidus temperatures are found to be at 1465 K and 1548 K, respectively (Fig. 4.7a). The DTA curve of U-4Zr-2Mo alloy (Fig. 4.7a) shows peaks at 890 K and 1433 K during heating. The repeat run with a lower heating rate also reveals a similar peak at 890 K (Fig. 4.7c). The solidus and liquidus temperatures are found to be 1433 and 1470 K, respectively. In furnace-cooled U-2Zr-4Mo alloy, the transformation peaks at 869 and 1420 K are slightly lower than that of U-4Zr-2Mo alloy. The solidus and liquidus temperatures of U-2Zr-4Mo alloy are observed at 1420 and 1450 K, respectively. Both the U-Zr-Mo alloys contain α and γ phase at room temperature as revealed by XRD and therefore the first peaks at 890 K (for U-4Zr-2Mo) and 869 K (for U-2Zr-4Mo) in the heating curve may be explained due to $\alpha + \gamma \rightarrow \gamma$ transformation. In the cooling curve, the peaks appeared below 900 K could be explained on the basis of γ -phase decomposition phenomena. For U-2Zr-4Mo alloy, this decomposition peak is not sharp (Fig. 4.7b) and covers a wide temperature range. The DTA peaks of U-6Mo alloy during heating were found to be at 855 and 1412 K (Fig. 4.7a) which are lower than that of other three alloys. The solidus and liquidus

temperatures of U-6Mo alloy are 1412 and 1450 K, respectively. The cooling curve of U-6Mo alloy shows only a single peak corresponding to the solidification (liquidus/solidus) and the low temperature peak disappeared unlike other alloys. In the repeat run, a weak peak appeared in the temperature range of 850-900 K (Fig. 4.7c).

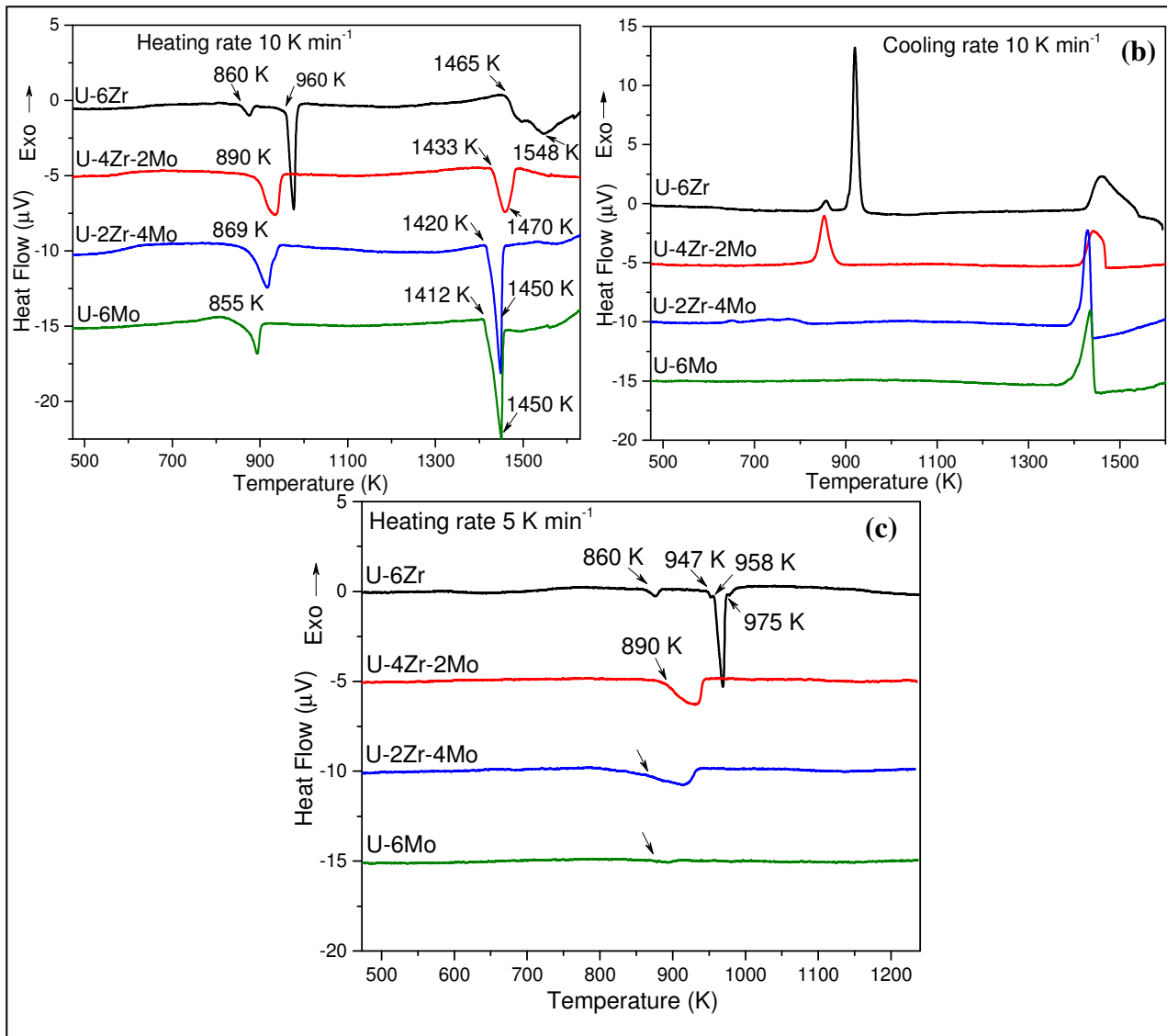


Fig. 4.7 (a & b) DTA curves of furnace-cooled alloys in heating and cooling cycles, respectively, at scanning rate of 10 K min⁻¹, (c) DTA curves of repeat runs at scanning rate of 5 K min⁻¹.

4.3.3.2. Water-quenched sample

The DTA thermograms of water-quenched alloys in the heating cycle are presented in Fig. 4.8a. DTA curves of the repeat runs using a heating rate of 5 K min^{-1} are presented in Fig. 4.8b. Both furnace-cooled and water-quenched alloys exhibit almost identical DTA thermogram (Fig. 4.7b) in the cooling cycle and therefore the same for water-quenched alloys are not presented to avoid repetition. The DTA curve of water-quenched U-4Zr-2Mo alloy shows peaks at 889 and 1436 K which are comparable to that of furnace-cooled sample. In water-quenched U-2Zr-4Mo alloy, DTA thermogram has three distinct peaks at 673, 869 and 1420 K (Fig. 4.8a). The peak at 673 K, exothermic in nature, has disappeared in the repeat run (Fig. 4.8b). The same peak was not observed in case of furnace-cooled sample (Fig. 4.7a). The other two endothermic peaks at 869 and 1420 K resemble well with that of furnace-cooled sample. The thermogram of water-quenched U-6Mo alloy exhibits a very weak peak at $\sim 855 \text{ K}$ and the melting peak at 1412 K (Fig. 4.8a). In the repeat run (Fig. 4.8b), the weak peak disappeared.

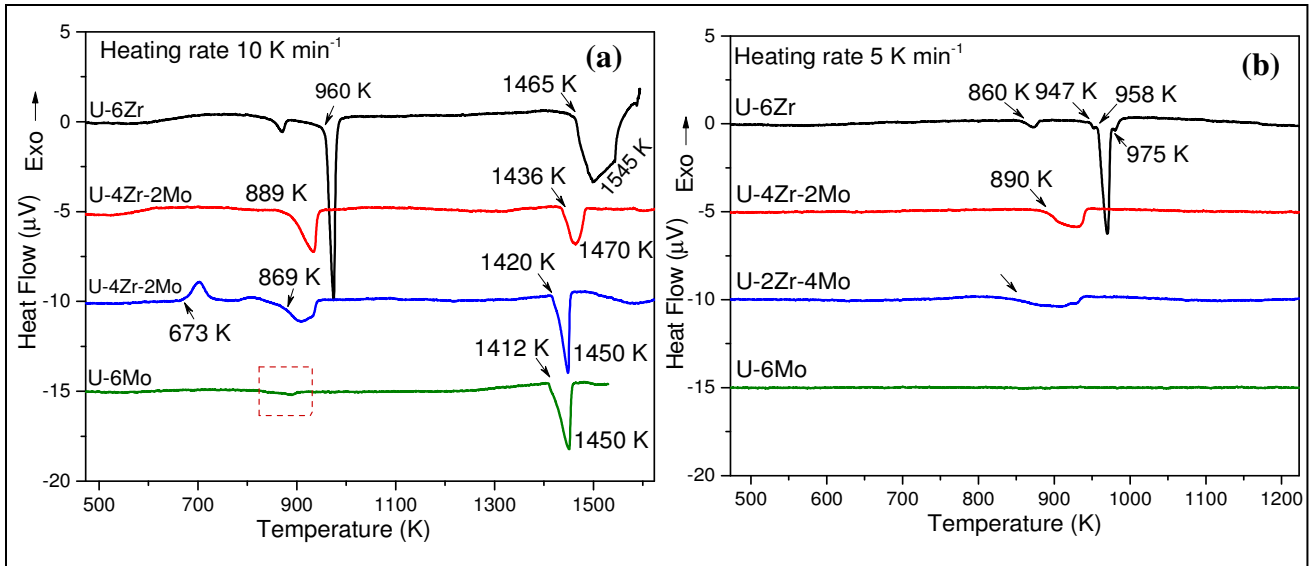


Fig. 4.8 (a) DTA curves of water-quenched alloy samples during heating cycle at scanning rate of 10 K min^{-1} , (b) DTA curves of repeat run at scanning rate of 5 K min^{-1} .

4.3.4. Dilatometry

The dilatometry thermal expansion curves of furnace-cooled alloys are collectively presented in Fig. 4.9a. In the length changes (%) versus temperature plot, the phase transition is associated with sudden change in slope and the temperatures associated with phase transition are mentioned in Fig. 4.9a. The various features of expansion curves of U-6Zr alloy have already been discussed earlier. The expansion curve of U-4Zr-2Mo alloy shows single phase transition at 890 K and the overall extent of expansion is comparable to that of U-6Zr alloy. On the other hand, the expansion curve of U-2Zr-4Mo alloy exhibits a phase transformation at 869 K and its overall thermal expansion is found to be substantially lower than that of U-6Zr and U-4Zr-2Mo alloys. Like U-2Zr-4Mo alloy, U-6Mo also exhibits similar type of expansion curve upto ~773 K and above the temperature, a non-linearity in expansion curve was observed. Also the change in the length during phase transition was not sharp. However, the nonlinearity and phase transition in the expansion curve disappeared when a repeat run was carried out with the same U-6Mo alloy (Fig. 4.9b).

The dilatometric expansion curves are fitted by second degree polynomials as follows:

U-6Zr alloy:

$$\Delta L/L_0 (\%) = -0.247 + 0.479 \times 10^{-3} T + 1.129 \times 10^{-6} T^2 \quad (373 \text{ K} \leq T \leq 873 \text{ K}) \quad (4.1)$$

$$\Delta L/L_0 (\%) = -0.152 + 1.800 \times 10^{-3} T + 0.108 \times 10^{-6} T^2 \quad (998 \text{ K} \leq T \leq 1173 \text{ K}) \quad (4.2)$$

U-4Zr-2Mo alloy:

$$\Delta L/L_0 (\%) = -0.376 + 0.900 \times 10^{-3} T + 0.798 \times 10^{-6} T^2 \quad (373 \text{ K} \leq T \leq 873 \text{ K}) \quad (4.3)$$

$$\Delta L/L_0 (\%) = 0.073 + 1.440 \times 10^{-3} T + 0.270 \times 10^{-6} T^2 \quad (973 \text{ K} \leq T \leq 1173 \text{ K}) \quad (4.4)$$

U-2Zr-4Mo alloy:

$$\Delta L/L_0 (\%) = -0.167 + 0.285 \times 10^{-3} T + 1.127 \times 10^{-6} T^2 \quad (373 \text{ K} \leq T \leq 823 \text{ K}) \quad (4.5)$$

$$\Delta L/L_0 (\%) = 0.031 + 1.110 \times 10^{-3} T + 0.398 \times 10^{-6} T^2 \quad (973 \text{ K} \leq T \leq 1173 \text{ K}) \quad (4.6)$$

U-6Mo alloy:

$$\Delta L/L_0 (\%) = -0.396 + 1.040 \times 10^{-3} T + 0.540 \times 10^{-6} T^2 \quad (373 \text{ K} \leq T \leq 773 \text{ K}) \quad (4.7)$$

$$\Delta L/L_0 (\%) = -0.350 + 1.170 \times 10^{-3} T + 0.397 \times 10^{-6} T^2 \quad (923 \text{ K} \leq T \leq 1173 \text{ K}) \quad (4.8)$$

U-6Mo alloy (Repeat run):

$$\Delta L/L_0 (\%) = -0.410 + 1.110 \times 10^{-3} T + 0.411 \times 10^{-6} T^2 \quad (373 \text{ K} \leq T \leq 1173 \text{ K}) \quad (4.9)$$

where, L_0 is initial length (at 298 K) and ΔL is the difference between the instantaneous length (at any temperature T) and L_0 .

4.3.5. Molar heat capacity

Like U-Zr-Nb system, three samples i.e., U-6Zr, U-4Zr-2Mo and U-2Zr-4Mo alloys were considered here for molar heat capacity measurement. The molar heat capacity data of U-6Zr, U-4Zr-2Mo and U-2Zr-4Mo alloys measured in the temperature range of 323-823 K are collectively presented in Fig. 4.10 and Table 4.4. The $C_{p,m}^0(T)$ values of the samples are least squares fitted with second order polynomial in two different temperature ranges for best fitting. The fitted expression for U-6Zr has been given in Equations 3.9-3.10 (Chapter 3) and the same for two other samples are given as:

U-4Zr-2Mo alloy:

$$C_{p,m}^0 (\text{J} \cdot \text{mol}^{-1} \cdot \text{K}^{-1}) = 23.589 + 1.622 \times 10^{-2} T - 1.127 \times 10^{-5} T^2, \quad (323 \leq T/\text{K} \leq 598) \quad (4.10)$$

$$C_{p,m}^0 (\text{J} \cdot \text{mol}^{-1} \cdot \text{K}^{-1}) = 75.718 - 15.012 \times 10^{-2} T + 12.168 \times 10^{-5} T^2, \quad (598 \leq T/\text{K} \leq 823) \quad (4.11)$$

U-2Zr-4Mo alloy:

$$C_{p,m}^0 (\text{J} \cdot \text{mol}^{-1} \cdot \text{K}^{-1}) = 26.550 + 0.203 \times 10^{-2} T + 0.2749 \times 10^{-5} T^2, \quad (323 \leq T/\text{K} \leq 598) \quad (4.12)$$

$$C_{p,m}^0 (\text{J} \cdot \text{mol}^{-1} \cdot \text{K}^{-1}) = 36.918 - 3.724 \times 10^{-2} T + 3.959 \times 10^{-5} T^2, \quad (598 \leq T/\text{K} \leq 823) \quad (4.13)$$

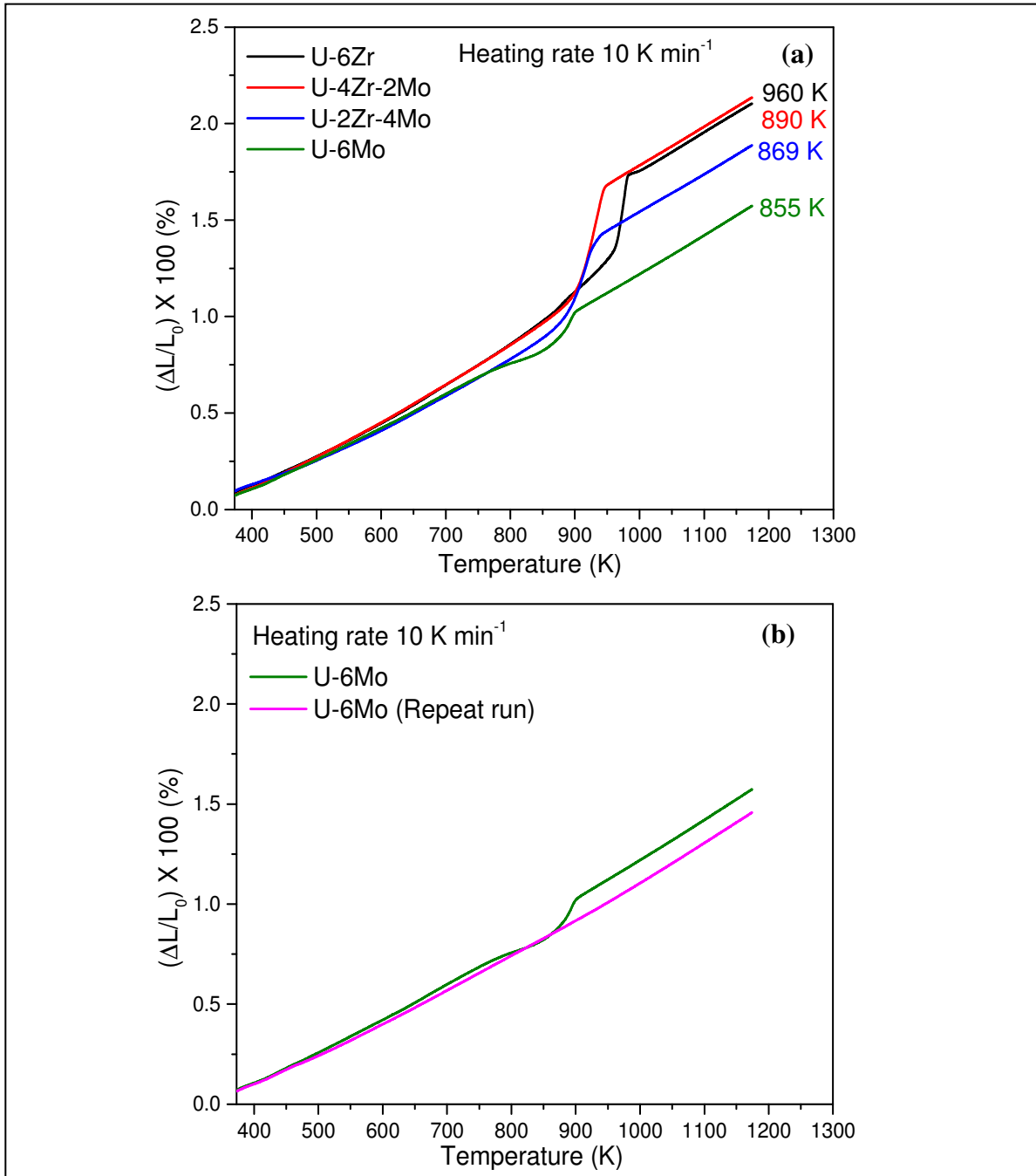


Fig. 4.9 (a) Thermal expansion curves of alloy samples, (b) Thermal expansion curves of the first run and repeat run of U-6Mo alloy.

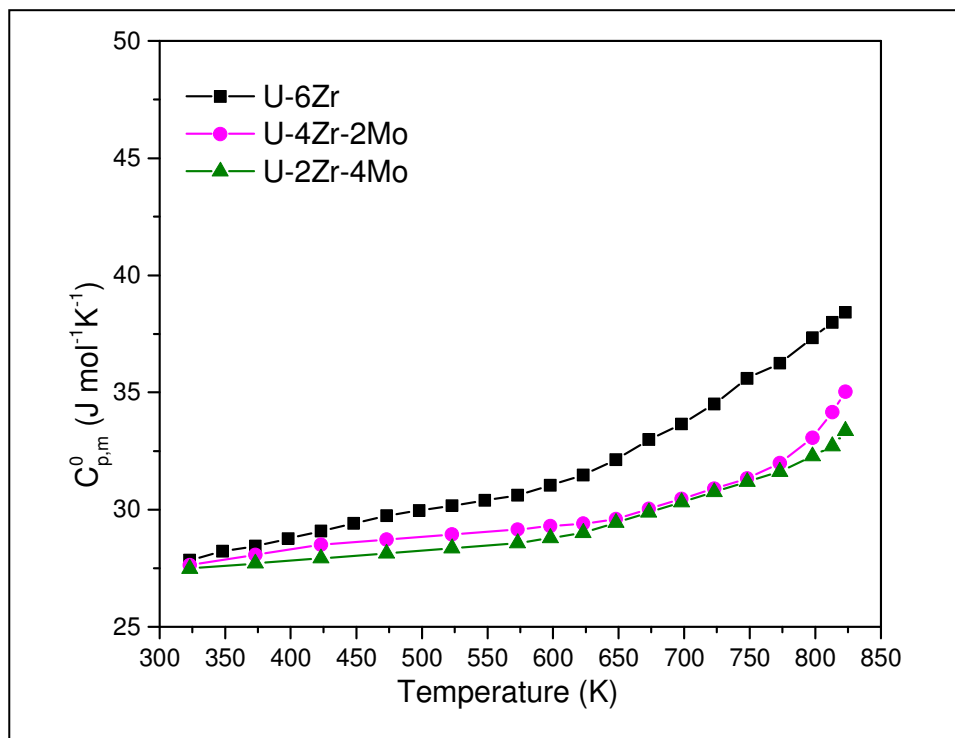


Fig. 4.10 Measured molar heat capacity data of U-6Zr, U-4Zr-2Mo and U-2Zr-4Mo alloys.

Table 4.4 Experimental molar heat capacity data of U-4Zr-2Mo and U-2Zr-4Mo alloys

T (K)	$C_{p,m}^0$ ($J \cdot mol^{-1} \cdot K^{-1}$)	
	U-4Zr-2Mo	U-2Zr-4Mo
323	27.63	27.48
373	28.07	27.70
423	28.50	27.92
473	28.72	28.13
523	28.94	28.35
573	29.15	28.57
598	29.30	28.79
623	29.40	29.01
648	29.59	29.44
673	30.03	29.88
698	30.46	30.32
723	30.90	30.75
748	31.33	31.19
773	31.98	31.62
798	33.07	32.28
813	34.16	32.71
823	35.03	33.37

4.3.6. Microhardness

Microhardness of both furnace-cooled and water-quenched alloys are summarized in Table 4.5. The furnace-cooled U-4Zr-2Mo and U-2Zr-4Mo alloys are having higher microhardness values than that of U-6Zr alloy. In furnace-cooled U-6Mo alloy, significant variations in the hardness data between matrix phase and lamellar region were observed where the lamellar region was found to be remarkably harder than the matrix phase. The lamellar phases of both the furnace-cooled U-2Zr-4Mo and U-6Mo alloys exhibit almost similar hardness values (475–480 VHN) which is slightly higher than that of U-4Zr-2Mo alloy. The hardness data of furnace-cooled alloys indicate that the replacement of Zr with Mo leads to increase in their microhardness. The water-quenched alloys also exhibit substantial variations in their microhardness data ranging from ~200 to 565 VHN. U-2Zr-4Mo and U-6Mo alloys have similar hardness in the range of 200-215 VHN whereas it is around 565 VHN for U-6Zr alloy. In water-quenched alloys, the replacement of Zr with Mo remarkably reduces hardness.

Table 4.5 Microhardness data of different U-Zr-Mo alloy samples

Sample	Load (gm)	Dwell time (s)	Hardness value (VHN) (kg/mm^2)	
			Furnace-cooled	Water-quenched
U-6Zr	200	10	377 ± 20	565 ± 10
U-4Zr-2Mo			433 ± 23	342 ± 14
U-2Zr-4Mo			476 ± 17	202 ± 06
U-6Mo			480 ± 13 ($\alpha + \gamma$) 272 ± 7 (γ)	215 ± 04

4.4. Discussion

The purpose of the present study is to investigate U-Zr-Mo system with 6% alloying content from the perspective of an alternative metallic fuel for fast reactor. The data on U-rich

part of U-Zr-Mo alloys was found to be limited in the literature. Therefore, in this study, various heat treated U-Zr-Mo alloys (Zr+Mo = 6wt%) with different combinations of Zr and Mo have been analyzed in terms of their crystal structure, microstructure, phase content, microhardness and thermophysical properties.

The structural, microstructural characteristics and phase transformation behaviour of furnace-cooled and water-quenched U-6Zr alloys have been discussed and explained in detailed in chapter 3. The effects of Mo on U-Zr alloys are addressed in the following paragraphs by comparing the results of U-6Zr with U-Zr-Mo alloys. Unlike U-6Zr, both the furnace-cooled U-4Zr-2Mo and U-2Zr-4Mo alloys are biphasic in nature with orthorhombic α -U and bcc γ -phase. The γ -phase fraction of U-2Zr-4Mo alloy (~38 vol%) is substantially higher than that of U-4Zr-2Mo alloy (~4 vol%). The lattice parameter of γ -phase of U-2Zr-4Mo alloy (3.426 Å) was found to be smaller than that of U-4Zr-2Mo alloy (3.446 Å). During furnace cooling, the U-Zr-Mo alloys undergoes segregation of alloying elements in the alternative layers and forming (Zr,Mo)-lean/depleted and (Zr,Mo)-rich layers which are basically orthorhombic α and bcc γ phases formed in a lamellar fashion via $\gamma \rightarrow \alpha + \gamma$ transformation reaction. The high temperature bcc γ -phase is decomposed as γ -U with higher solute content and α -U during cooling. The increased Mo-content in the U-2Zr-4Mo alloy resulted in formation of higher fraction of the (Zr,Mo)-rich bcc γ -phase at room temperature. Furthermore, the Mo-content in the (Zr,Mo)-rich γ -phase is more for U-2Zr-4Mo alloy. The replacement of Zr with smaller Mo atom in the γ -phase reduces the lattice parameter. The reduced lattice parameter in the γ -phase of U-2Zr-4Mo alloy is due to its higher content smaller Mo atom. In addition, few tiny dark spots were also seen in the SEM micrograph of U-Zr-Mo alloys (Fig. 4.5c, Fig. 4.5f). The elemental

composition of those dark phases were found to be approximately 80-84 at.% Zr, 1-2 at.% Mo and 15-19 at.% U (for U-4Zr-2Mo) and 65-78 at.% Zr, 8-12 at.% Mo and 10-25 at.% U (for U-2Zr-4Mo) which do not resemble to any of the probable intermetallic phases i.e., δ -UZr₂, γ -U₂Mo and ZrMo₂. It may be noted here that the formation of any of the intermetallics in the furnace-cooled alloys was also not revealed by XRD analysis. The tiny dark phases are basically Zr-rich precipitates.

Like water-quenched U-6Zr alloy, the water-quenched U-4Zr-2Mo alloy has similar distorted orthorhombic structure (α') where a noticeable variation in the lattice parameters was observed when compared to α -phase of their furnace-cooled counterpart. The α' phase is formed during quenching as the result of shear transformation. On the other hand, the water quenching of U-2Zr-4Mo alloy resulted in formation of monoclinic structure of α'' modification. As already mentioned in chapter 3 that the monoclinic structure (α'') can be defined either by natural space group of P2₁/m (with axis b as unique axis) or by an artificial space group C2₁/m (with axis c as unique axis) [105]. The β angle in P2₁/m symmetry and γ angle in C2₁/m symmetry are not 90°. In this study, the Rietveld refinement of monoclinic α'' phase of water-quenched U-2Zr-4Mo alloy using space group of P2₁/m revealed the lattice parameters as a = 3.265 Å, b = 4.951 Å, c = 3.159 Å, angle β = 126.60° and the atomic positions of x = 0.856, y = 0.25, z = 0.069. The data are comparable with the lattice parameters for monoclinic structure (α'') of water-quenched U-6Nb alloy. A similar type of result has been reported by Dabush et al [105] for the crystal structure of monoclinic α'' phase of U-3.83Mo alloy.

The U-rich U-Mo alloys also exhibit microstructural and structural variations depending on their chemical composition, heat treatment etc. As per U-Mo binary phase diagram (Fig. 1.5,

Chapter 1) [32], the equilibrium phases of U-rich U–Mo alloys comprise of α -U and γ' -U₂Mo at room temperature. The high-temperature bcc γ -phase (space group Im-3m) decomposes into orthorhombic α -U (space group Cmcm) and body-centered tetragonal γ' -U₂Mo (space group I4/mmm) via a eutectoid reaction. In the present work, U–6Mo alloy undergoes partial decomposition of the γ -phase into α and γ phases rather than formation of γ' -U₂Mo phase during furnace cooling and the decomposed products form a lamellar microstructure along prior γ -grain boundaries. This type of decomposition reaction may be considered as discontinuous precipitation reaction (or cellular reaction). The cellular reaction was also reported in the decomposition of metastable γ -phase of U–9Mo alloy during isothermal ageing by Neogy et al. [65]. According to them, the cellular decomposition of the γ -phase initiates at the grain boundaries and the partially transformed cellular colonies contain either α -lamellae or γ' (U₂Mo) lamellae with a compositionally different γ -phase as the interlamellar region. A similar type cellular-type decomposition mechanism was also found during annealing of U–10Mo alloy at sub-eutectoid temperatures by Jana et al. [67, 68]. It indicates that the eutectoid decomposition in U-rich U–Mo alloys initiates through a cellular reaction, and the resulting lamellar microstructure comprises of α -U and γ -UMo interlamellar region. Therefore, it is expected that the U–Mo alloy would attain a microstructure consisting of α -U and γ' -U₂Mo, as indicated by the equilibrium phase diagram, only after longer-duration annealing. The present result indicates that single bcc γ -phase cannot be retained fully as metastable phase in the furnace-cooled U–6Mo alloy. It may be noted here that under normal furnace cooling condition (or as-cast), the retention of single γ -phase has been reported for U–Mo alloy with minimum 8 wt% Mo [61]. Pedrosa et al. [66] reported the retention of γ -phase in the as-cast state of U–7Mo and U–10Mo

alloys and not in U-5Mo alloy. The reported results about the γ -stability in the furnace-cooled or as-cast condition of U-rich U-Mo alloys are in close proximity with the present observation.

The high-temperature solid solution of bcc γ -phase of U-rich U-Mo alloys can be retained as metastable phase at RT by rapid cooling. It has been reported that the U-Mo alloys containing up to 4.75 wt% Mo, when water quenched from the γ -phase region, form metastable α' and α'' phases which are slight variations of orthorhombic lattice of α -U and therefore, these alloys may be called “ α -phase” alloys. Similarly, alloys containing more than 4.75 wt% Mo may be called “ γ -phase” alloys, as the phase structures formed after quenching are related to the bcc γ -phase of pure uranium [59, 70, 109]. In the present work, the water-quenched U-6Mo alloy consists predominantly of retained bcc γ -phase in a metastable state and any indication of γ phase decomposition was not revealed in the microstructure. A single γ -phase structure was reported in the U-6Mo alloy after heating in the γ -phase region and subsequent annealing [24]. The single γ -phase state of U-5.4Mo alloy was also found by Lee et al. [69] when the alloy was annealed at 973 K for 48 h followed by cooled in air and the lattice parameter of the γ -phase was reported as ‘a’ = 3.445 Å. In a recent study, Kim-Ngan et al. [63] reported that the splat cooled U-Mo alloys with 4.75–5.21 wt% Mo exhibited a stable body centered tetragonal γ^2 -phase, while those with 5.68–7.63 wt% Mo had a pure γ -phase at RT. Therefore, the present observation of U-6Mo alloy is found to be consistent with the reported results. Another important observation is that the lattice parameter of γ -phase of water-quenched U-6Mo alloy (3.445 Å) is almost similar to that of the furnace-cooled alloy (3.444 Å). Although the partial decomposition of γ -phase was revealed in the SEM micrograph of furnace-cooled sample, the presence of any compositionally different γ -phase product could not be resolved in the XRD data,

presumably because of the low area fraction of transformed regions. Therefore, the above lattice parameters correspond to the metastable γ -phase. Addition of Mo in uranium decreases the lattice parameter of γ -phase as the atomic radius of Mo is much smaller as compared to uranium. Burkes et al. [60] reported the lattice parameters of the U-Mo alloys (7–12 wt% Mo) as a function of Mo content with an empirical relation $a = 3.4812 - 0.0066x$ where x is in wt%. The calculated lattice parameter for U-6Mo alloy based on the above relation is found to be $a = 3.4416 \text{ \AA}$ which is in good agreement with present result.

DTA has been employed extensively in this study to determine various phase transformation temperatures of U-Zr-Mo alloys. The solidus/liquidus temperatures of U-6Zr alloy (1465/1548 K) are found to be higher than that of U-6Mo alloy (1412/1450 K) and the gradual replacement of Zr in U-6Zr alloy with Mo leads to decrease in solidus/liquidus temperatures. As already mentioned earlier, the furnace-cooled U-4Zr-2Mo, U-2Zr-4Mo and U-6Mo alloys are biphasic in nature with orthorhombic α -U and bcc γ phases. For these alloys, the first DTA peak in the heating cycle could be attributed to $\alpha + \gamma \rightarrow \gamma$ transformation or the temperature at which single γ -phase forms. It was found that the transformation temperature gradually decreases with increasing Mo content in the alloy. In addition, there is a slight bulge or shoulder in the DTA peak of U-2Zr-4Mo alloy at around 933 K before signal return to baseline. This is probably due to dissolution of small amount of ZrMo_2 intermetallic phase which might be formed during heating. However, it cannot be concluded based on the above result as the formation of ZrMo_2 phase was not ascertained in the XRD and SEM analysis and therefore, it requires further investigation. In water-quenched U-2Zr-4Mo alloy, an exothermic thermal event occurs at 673 K in the heating curve and after this transition both the water-quenched and furnace-cooled samples exhibited similar thermogram. Unlike the furnace-cooled U-2Zr-4Mo

sample (with $\alpha + \gamma$ phases), the water-quenched alloy is having a martensitic monoclinic structure (α'') and therefore, the additional exothermic peak could be attributed to phase decomposition of non equilibrium α'' martensite to equilibrium α and γ phases (i.e. $\alpha'' \rightarrow \alpha + \gamma$). This is followed by $\alpha + \gamma \rightarrow \gamma$ transition at 869 K similar to furnace-cooled sample. The peak related to decomposition of γ phase (i.e., $\gamma \rightarrow \alpha + \gamma$) during cooling was observed in both the U-Zr-Mo alloys (Fig. 4.7b). However, the absence of similar type of peak in the cooling curve of U-6Mo alloy is attributed to stability of bcc γ -phase at lower temperature. In U-rich U-Mo alloy, the temperature of the invariant point of eutectoid reaction (i.e., $\gamma \rightarrow \alpha + \gamma'$ -U₂Mo) was reported in the range of 828–838 K [32, 110-112]. In the furnace-cooled U-6Mo sample, the peak due to $\alpha + \gamma \rightarrow \gamma$ during heating was observed in the range 815-910 K with extrapolated peak onset temperature of ~855 K which is higher than the reported eutectoid temperature.

Several important features of U-Zr-Mo alloys have been revealed from the DTA results of the present investigation. Additions of both Zr and Mo lower single γ -phase stabilization temperature and Mo is found to be more effective than Zr. Unlike Zr, addition of Mo as an alloying element in the fuel is not a good option for increasing the solidus temperature of fuel. Furthermore, Mo addition leads to decrease in the liquidus/solidus separation (freezing range). In contrast to U-6Zr alloy, DTA thermograms of the ternary alloys do not show any transformation peak associated with δ -UZr₂ phase. In the present investigation, DTA experiments were conducted with the alloy samples homogenized in single γ phase region at 1173 K and then water-quenched or furnace cooled to RT. The above heat treatment does not guarantee the equilibrium structure at lower temperature. Therefore, it is expected that the DTA themogram of equilibrated sample after long-time annealing at lower temperatures may differ from the present

result of furnace-cooled/water-quenched samples. In fact, a notable variation has been observed when the DTA thermograms of step-cooled and furnace-cooled U-6Zr samples were compared.

The coefficient of thermal expansion (CTE) is considered as an important thermal property of fuel. The overall extent thermal expansion of U-6Zr and U-4Zr-2Mo alloys are found to be similar and it decreases with further increasing Mo content. The dilatometric expansion curves with transition in length changes at 890 K (for U-4Zr-2Mo), 869 K (U-2Zr-4Mo) and 855 K (U-6Mo) are due to $\alpha + \gamma \rightarrow \gamma$ transition and these phase transition temperatures are in excellent agreement with the DTA peak. Like DTA, dilatometer expansion curves also indicated that the addition of Mo decreases the transformation temperature at which single γ -phase forms. The average coefficients of thermal expansion of U-6Zr, U-4Zr-2Mo, U-2Zr-4Mo and U-6Mo alloys in the temperature range of 300–773 K were found to be 16.84×10^{-6} , 16.80×10^{-6} , 15.35×10^{-6} and $15.26 \times 10^{-6} \text{ K}^{-1}$, respectively. The dilatometric expansion curve of the repeat run of U-6Mo alloy does not show any phase transition because of thermal stability of retained γ -phase. Therefore, the expansion curve of U-6Mo alloy in the repeat run may correspond to expansion of the metastable γ -phase which has slightly lower CTE value of $\sim 14.70 \times 10^{-6} \text{ K}^{-1}$ than that of alloy containing $\alpha + \gamma$ phase. The thermal expansion data of a series of U-Zr and U-Mo alloys have been reported by Saller et al. [74]. They measured the dilation of U-Mo alloys in both gamma quenched and partially transformed conditions. It was found that U-7Mo alloy which is close to present alloy composition has CTE (293–773K) value of $14.23 \times 10^{-6} \text{ K}^{-1}$ when water quenched from 1073 K and $15.66 \times 10^{-6} \text{ K}^{-1}$ when furnace cooled after soaking at 773 K for 100 h. Similarly, the U-5Mo has CTE (293–773 K) data of $15.30 \times 10^{-6} \text{ K}^{-1}$ when furnace-cooled with a soaking at 773 K for 24 h. All these reported data are found to be in

excellent agreement and comparable with the CTE values of γ -stabilized and partially decomposed U-6Mo alloys of the present work. Furthermore, the temperatures at the beginning of transformation of U-Mo alloys (Mo = 3.5–9 wt %) during heating were reported in the range of 848–898 K which is also comparable with present result.

In U-Zr-Mo alloys, the molar heat capacity increases with temperature and decreases with increasing Mo content. The molar heat capacities of U-4Zr-2Mo and U-2Zr-4Mo alloys are lower than that of U-6Zr alloy. The molar heat capacity of pure Mo metal is found to be lower than that of both U and Zr metals in the temperature range investigated [107] and therefore, the gradual replacement of Zr in U-6Zr alloy with equivalent amount of Mo causes decrease in molar heat capacity value. In general, reports on ternary U-Zr-Mo alloy system are limited in the literature and moreover, the molar heat capacity data of U-Zr-Mo alloys has not been reported in the literature to compare. The molar heat capacity data of U-Zr-Mo alloys of the present study could be compared with reported data of few uranium-rich binary U-Mo alloys. Figure 4.11 compares the molar heat capacity data of U-4Zr-2Mo and U-2Zr-4Mo alloys with reported data of various U-Mo alloys of similar compositions. The data of U-8Mo alloy reported by Parida et al. [79] and U-9.15Mo alloy by Matsui et al. [77] are lower and the values obtained by Burkes et al. [21] on DU-10Mo alloy are slightly higher than the present result. It is expected that the replacement of Mo with Zr in U-Mo alloy will increase the molar heat capacity data as the Zr has higher molar heat capacity than Mo. On the other hand, the molar heat capacity of U-Mo alloy should decrease with increasing Mo, because of lower molar heat capacity of Mo compared to U. The present results follow the expected trend when compared with the data reported by Parida et al. [79] and Matsui et al. [77]. In this context it is noteworthy to mention

that the molar heat capacity of alloys may vary depending on the phase content in the sample resulting from variation in the sample preparation, heat treatment etc. As for example, Matsui et al. [77] annealed/homogenized U-9.15Mo alloy at 773 K for 3 days and cooled down to RT over a period of one day and the slow cooling resulted in formation of two-phase mixture of α -U + γ -U₂Mo. On the other hand, Burkes et al. [21] heated U-10Mo alloy at 923 K for 2 h and cooled which guaranties metastable γ phase. In the present work, both the U-4Zr-2Mo and U-2Zr-4Mo alloys are homogenized at 1173 K for 50 h then furnace cooled to RT prior to heat capacity measurement and both the samples are biphasic in nature with α + γ phases. The variation in phase stability depending on the heat treatment could be the probable reason for substantial difference in measured molar heat capacity data of similar type alloys.

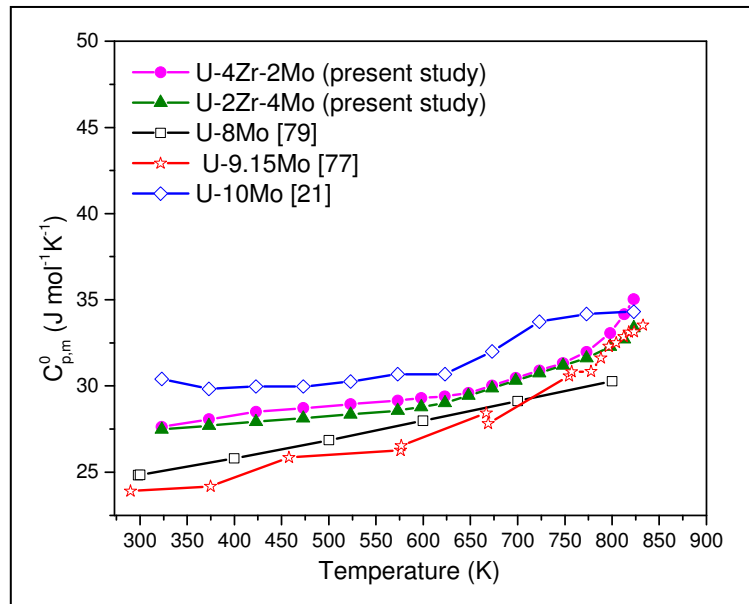


Fig. 4.11 A comparison among molar heat capacity data of present U-Zr-Mo alloys with that of U-Mo alloys reported in the literature.

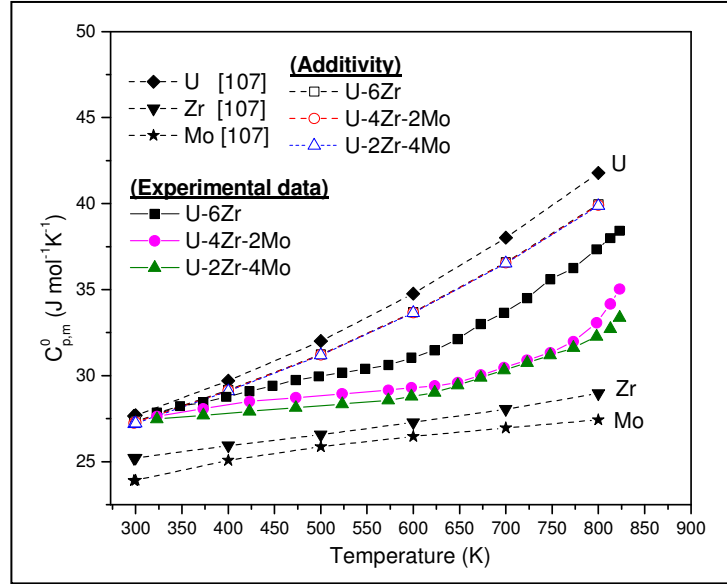


Fig. 4.12 The experimental and calculated molar heat capacities of U-6Zr, U-2Zr-4Mo and U-4Zr-2Mo alloys along with the reported molar heat capacities of pure constituent elements (i.e., U, Zr and Mo) are plotted collectively as a function of temperature.

The molar heat capacities of U-4Zr-2Mo and U-2Zr-4Mo were also calculated (from the reported molar heat capacity data of pure U, Zr and Mo metals) employing the Neumann-Kopp (NK) rule. The experimental and calculated molar heat capacities of U-6Zr, U-4Zr-2Mo and U-2Zr-4Mo alloys along with the reported data of pure U, Zr and Mo metals are compared in Fig. 4.12. The experimental molar heat capacity data are found to be lower than that calculated from the NK rule. It may be noted here that the values of molar heat capacity were estimated from $0.8592C_{p,m}^0(\text{U})$, $0.0954C_{p,m}^0(\text{Zr})$ and $0.0454C_{p,m}^0(\text{Mo})$ (for U-4Zr-2Mo) and $0.8613C_{p,m}^0(\text{U})$, $0.0478C_{p,m}^0(\text{Zr})$, and $0.0909C_{p,m}^0(\text{Mo})$ (for U-2Zr-4Mo) using additivity law where $C_{p,m}^0(\text{U})$, $C_{p,m}^0(\text{Zr})$ and $C_{p,m}^0(\text{Mo})$ are the molar heat capacities of the U, Zr and Mo, respectively. However, the alloys consist of two-phase mixture of $\alpha + \gamma$ phases and therefore, the experimental data are the measured molar heat capacity of the two phase mixture of $\alpha\text{-U} + \gamma$ instead of $\alpha\text{-U} + \alpha\text{-Zr} +$

Mo. Consequently, one can expect a deviation between the estimated and experimental results. The computed thermodynamic functions i.e., molar enthalpy increment $H_m^0(T) - H_m^0(298.15\text{ K})$ and molar entropy increment $S_m^0(T) - S_m^0(298.15\text{ K})$ of U-4Zr-2Mo and U-2Zr-4Mo alloys in the temperature range of 298.15 – 800 K are summarized in Tables 4.6 and 4.7, respectively.

Table 4.6 Thermodynamic functions for U-4Zr-2Mo alloy.

T (K)	$C_{p,m}^0$ (J·mol ⁻¹ ·K ⁻¹)	$H_m^0(T) - H_m^0(298.15)$ (J·mol ⁻¹)	$S_m^0(T) - S_m^0(298.15)$ (J·mol ⁻¹ ·K ⁻¹)
298.15	27.42	0	0
300	27.44	50.7	0.17
350	27.89	1434.1	4.43
400	28.27	2838.4	8.18
450	28.61	4260.6	11.53
500	28.88	5698.0	14.56
550	29.10	7147.8	17.33
600	29.45	8607.5	19.87
650	29.55	10080.0	22.22
700	30.26	11572.6	24.43
750	31.57	13115.9	26.56
800	33.50	14740.1	28.66

Table 4.7 Thermodynamic functions for U-2Zr-4Mo alloy.

T (K)	$C_{p,m}^0$ (J·mol ⁻¹ ·K ⁻¹)	$H_m^0(T) - H_m^0(298.15)$ (J·mol ⁻¹)	$S_m^0(T) - S_m^0(298.15)$ (J·mol ⁻¹ ·K ⁻¹)
298.15	27.40	0	0
300	27.41	50.7	0.17
350	27.60	1425.7	4.40
400	27.80	2810.7	8.11
450	28.02	4206.1	11.39
500	28.25	5612.9	14.36
550	28.50	7031.6	17.06
600	28.83	8463.1	19.55
650	29.44	9918.9	21.88
700	30.25	11410.2	24.09
750	31.26	12947.1	26.21
800	32.46	14539.3	28.27

The hardness data of the alloys varies significantly with composition and heat treatment condition. In this study, the hardness values of the alloys vary from 202 VHN (water-quenched U-2Zr-4Mo) to 565 VHN (water-quenched U-6Zr). The relative strength of U-Zr, U-Mo alloys of various compositions and heat treatments was examined through measurement of hardness by Saller et al. [74]. It was reported that the room-temperature hardness of U-Zr alloys water quenched from 1073 K is much greater than hardnesses obtained by any other method of heat treatment and is in good agreement with the values obtained in the present study. The hardening of water-quenched U-6Zr alloy could be explained due to the formation of martensite with distorted orthorhombic structure (α'). For U-Mo alloys, the room-temperature hardness with transformed γ structures are greater than those of similar alloys containing retained γ structures [74]. According to the report, the RT hardness of water-quenched U-7Mo alloy is 248 VHN whereas the value increased to 448 when the same alloy was furnace cooled after soaking at 773 K for 100 h. This is in good agreement with the hardness values of U-6Mo alloy of this study, where the water-quenched sample has hardness value of 215 VHN and furnace-cooled sample with decomposed γ phase has hardness value of 480 VHN. The higher hardness of furnace-cooled sample is explained to be due to the formation of second phase with fine lamellar microstructure. It may also be noted here that the furnace-cooled U-6Mo alloy has partially decomposed γ -phase structure in which the hardness of the decomposed lamellar phase (480 VHN) is substantially higher than that of the un-decomposed γ -phase (272 VHN). The hardness values of U-Mo alloys in the composition range 0-14 wt% Mo have been reported by Waldron et al. [113]. The room temperature hardness of the U-Mo γ -solid solutions retained by quenching from 1173 K increases almost linearly with Mo content and varies from 255 DPH for 6.6Mo to a value of 365 DPH for 13.5Mo content. On the other hand, the fine structure of γ' (or metastable γ)

and α formed during soaking below the eutectoid temperature causes significant increase in hardness value. Pedrosa et al. [66] also reported the microhardness of as-cast and aged U-Mo alloys. According to them, the as-cast U-7Mo alloy with γ -phase has hardness value of around 280 VHN; however, a substantial increase in the hardness value was observed due to precipitation of α and γ' phases in the U-7Mo alloy aged at sub-eutectoid temperature. The reported hardness data are comparable with the present results.

The furnace-cooled and water-quenched U-Zr-Mo alloys also showed a substantial variation in their hardness values. Morais et al. [71] assessed the microhardness of as-cast and homogenized U-9Zr-3Mo, U-6Zr-6Mo and U-3Zr-9Mo alloys where all the U-Zr-Mo alloys exhibited bcc structure except as-cast U-9Zr-3Mo. The bcc U-Zr-Mo alloys have hardness data approximately in the range of 300-340 VHN, whereas the orthorhombic phase of as-cast U-9Zr-3Mo alloy has hardness value of approximately 590VHN.

4.5. Summary and conclusions

The present study generates useful data on the crystal structures of phases with their lattice parameter, microstructural characteristic, phase transformation behaviour, solidus/liquidus temperatures, molar heat capacity, thermal expansion, and microhardness of U-6Zr, U-4Zr-2Mo, U-2Zr-4Mo and U-6Mo alloys. The following important observations are summarized based on the findings of this study:

- The replacement of Zr in U-6Zr alloy with Mo causes disappearance of δ -UZr₂ phase and favours the formation of bcc γ -phase. The phase fraction of γ gradually increases with increasing Mo content in the alloy.
- No evidence of formation of intermetallic phases i.e., U₂Mo and Mo₂Zr phases was observed in the furnace-cooled as well as in water-quenched alloys.

- The solidus temperature gradually decreases with increasing Mo content in the alloy. The addition of Mo reduces the coefficient of thermal expansion (CTE).
- The addition of 6wt% alloying element (Zr or Mo) into uranium metals leads to decrease its molar heat capacity.
- The gradual replacement of Zr with equivalent amount of Mo leads to decrease in molar heat capacity value. The measured molar heat capacities of the alloys are found to be lower than the values estimated by the Neumann-Kopp additivity rule.
- The room temperature hardness of water-quenched samples gradually decreases with increasing Mo content.
- Mo was found to be a better stabilizer of the γ -phase than Zr. Also Mo addition reduces the temperature at which single γ -phase forms via $(\alpha + \gamma \rightarrow \gamma)$ transition.
- In water-quenched U-2Zr-4Mo alloy, an exothermic transformation at ~ 673 K temperature is associated with non-equilibrium martensitic (α'') to equilibrium $(\alpha + \gamma)$ phase transformation.
- Furnace cooling of U-6Mo alloy leads to partial decomposition of high temperature γ -phase via cellular decomposition whereas water quenching results in almost complete retention of γ -phase as metastable state.

Chapter 5

Phase stability of U-(6-x)Zr-xNb and U-(6-x)Zr-xMo alloys under near-equilibrium condition (x = 0, 2, 4, 6 wt%)

5.1. Introduction

In the last two chapters, the phase stability of furnace-cooled and water-quenched U-(6-x)Zr-xNb and U-(6-x)Zr-xMo alloys (x = 0, 2, 4, 6 wt%) has been discussed. The microstructural investigation of the furnace-cooled alloys shows segregation of alloying element (Zr, Nb/Mo) in the alternative layer of fine lamellar structure with interlamellar spacing in the range of approximately 200-300 nm and therefore, the composition of each layer could not be determined precisely. Furthermore, the formation of various intermetallic phases i.e., δ -UZr₂, ZrMo₂ and γ -U₂Mo could not be revealed in microstructural investigation. It appears that the microstructures and phases do not correspond to the equilibrium structure probably due to the sluggish diffusion kinetics in U-alloys. It may be noted here that the fuel material will attain equilibrium microstructure during prolonged reactor operation and therefore, it is important to understand the phase stability of the alloys under equilibrium condition. The near-equilibrium microstructure and phases of U-rich U-7Zr alloy has been reported earlier by Basak et al. [40]. However, studies on phase stability and microstructural evolution of U-Zr-Nb and U-Zr-Mo alloys under equilibrium condition are very limited in the literature. This chapter aims to describe the structural and microstructural characterization, phase transformation behaviour under near-equilibrium conditions for these alloys.

5.2. Experimental procedure

In order to attain the equilibrium phases the samples were subjected to step cooling with isothermal holding at various temperatures. For that, all the alloy samples were heated to 1173 K for 50 h and then stepwise cooled to room temperature by keeping the samples at 1073, 973, 923,

873, 823 and 773 K for 100, 100, 250, 250, 500 and 550 h, respectively. The heat treatment was planned in such a way as to allow sufficient time at various temperatures for transformation to occur. The samples were treated as step-cooled alloys under near-equilibrium condition. The phase characterization of the alloy samples were then characterized using XRD, SEM/EDS.

5.3. Results

5.3.1. U-Zr-Nb alloys (Zr+Nb = 6 wt%)

5.3.1.1 Structural Characterization

The XRD patterns of U-6Zr, U-4Zr-2Nb, U-2Zr-4Nb and U-6Nb alloys are presented collectively in Fig. 5.1. The U-6Zr alloy consists orthorhombic α phase (space group Cmcm) and hexagonal δ -UZr₂ phase (space group P6/mmm). As most of the peaks of δ -UZr₂ phase overlap with various peaks of α -U phase, the non-overlapping δ -UZr₂ phase peaks were shown in the magnified XRD plot (Fig 5.2). The Rietveld refinement analysis of the XRD data to determine the lattice parameters, phase fraction of various phases formed are summarized in Table 5.1. The phase fraction of δ -UZr₂ phase is found to be around 20 vol%. The XRD pattern of U-4Zr-2Nb alloy corresponds to orthorhombic α -U phase. The non-overlapping peaks of δ -UZr₂ phase as well as any additional peaks of bcc gamma phase could not be identified. On the other hand, both U-2Zr-4Nb and U-6Nb alloys are biphasic in nature consisting of α and bcc γ_3 phases. The phase fraction of γ_3 phase is around 8 and 22 vol% in U-2Zr-4Nb and U-6Nb samples, respectively. The lattice parameter of the γ_3 -phase is 3.429 Å and 3.368 Å for U-2Zr-4Nb and U-6Nb alloys, respectively.

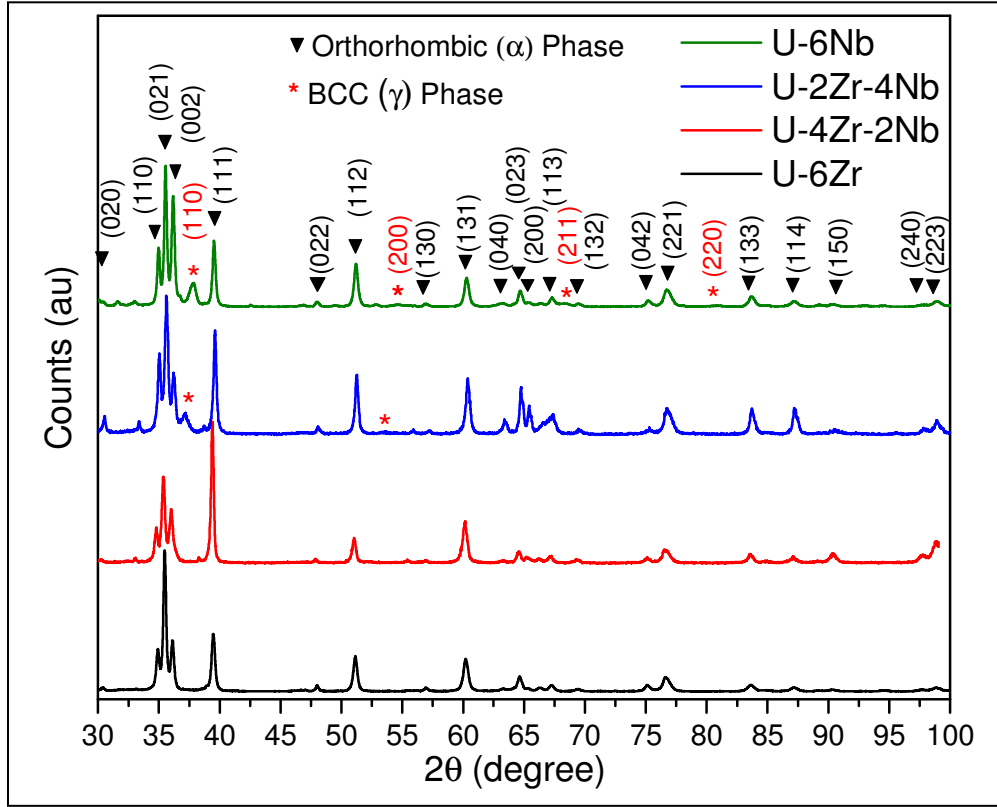


Fig. 5.1 XRD patterns of step-cooled U-6Zr, U-4Zr-2Nb, U-2Zr-4Nb and U-6Nb alloys.

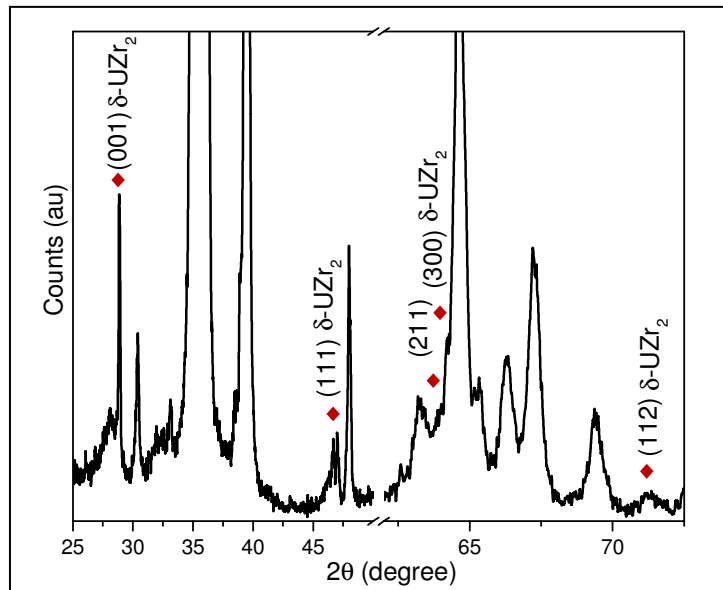


Fig. 5.2 Magnified XRD data of step-cooled U-6Zr alloy showing few non-overlapping low intensity peaks of δ -UZr₂ phase.

Table 5.1 Lattice parameter, phase fraction of phases formed in step-cooled U-6Zr, U-4Zr-2Nb, U-2Zr-4Nb and U-6Nb alloys under near-equilibrium condition.

Sample (Equilibrium-cooled)	Phase(s)	Space group	Phase fraction (vol %)	Lattice Parameters (Å, degree)					
				<i>a</i>	<i>b</i>	<i>c</i>	α	β	γ
U-6Zr	Orthorhombic (α)	Cmcm	80	2.854	5.872	4.965	90	90	90
	Hexagonal (δ)	P6/mmm	20	5.039	5.039	3.090	90	90	120
U-4Zr-2Nb	Orthorhombic (α)	Cmcm	-	2.852	5.870	4.968	90	90	90
	BCC (γ)	Im-3m	-	-	-	-	90	90	90
U-2Zr-4Nb	Orthorhombic (α)	Cmcm	92	2.856	5.870	4.967	90	90	90
	BCC (γ_3)	Im-3m	8	3.429	3.429	3.429	90	90	90
U-6Nb	Orthorhombic (α)	Cmcm	78	2.854	5.870	4.967	90	90	90
	BCC (γ_3)	Im-3m	22	3.368	3.368	3.368	90	90	90

5.3.1.2. Microstructure

The SEM micrographs of U-6Zr, U-4Zr-2Nb, U-2Zr-4Nb and U-6Nb alloys are presented in Fig. 5.3. U-6Zr alloy (Fig. 5.3(a-b)) exhibits biphasic microstructure with δ -phase network and α -matrix phase. The network of δ -phase is uniformly distributed in the α -U matrix. Few tiny δ -phase particles within α -matrix were also observed. After longer holding time at and below 873 K, the δ -particles coalesce together to form a network structure. The elemental compositions of various phases formed are presented in Table 5.2. Zr-content of the δ -network was found to be around 72 at.% whereas Zr-content in α -matrix is negligibly small and therefore could not be detected by EDS. The results are in good agreement with the equilibrium phase diagram. The U-4Zr-2Nb alloy exhibits lamellar microstructure (Fig. 5.3(c,f)) with significant segregation of alloying elements in the alternative layers. The solute-rich layer has average

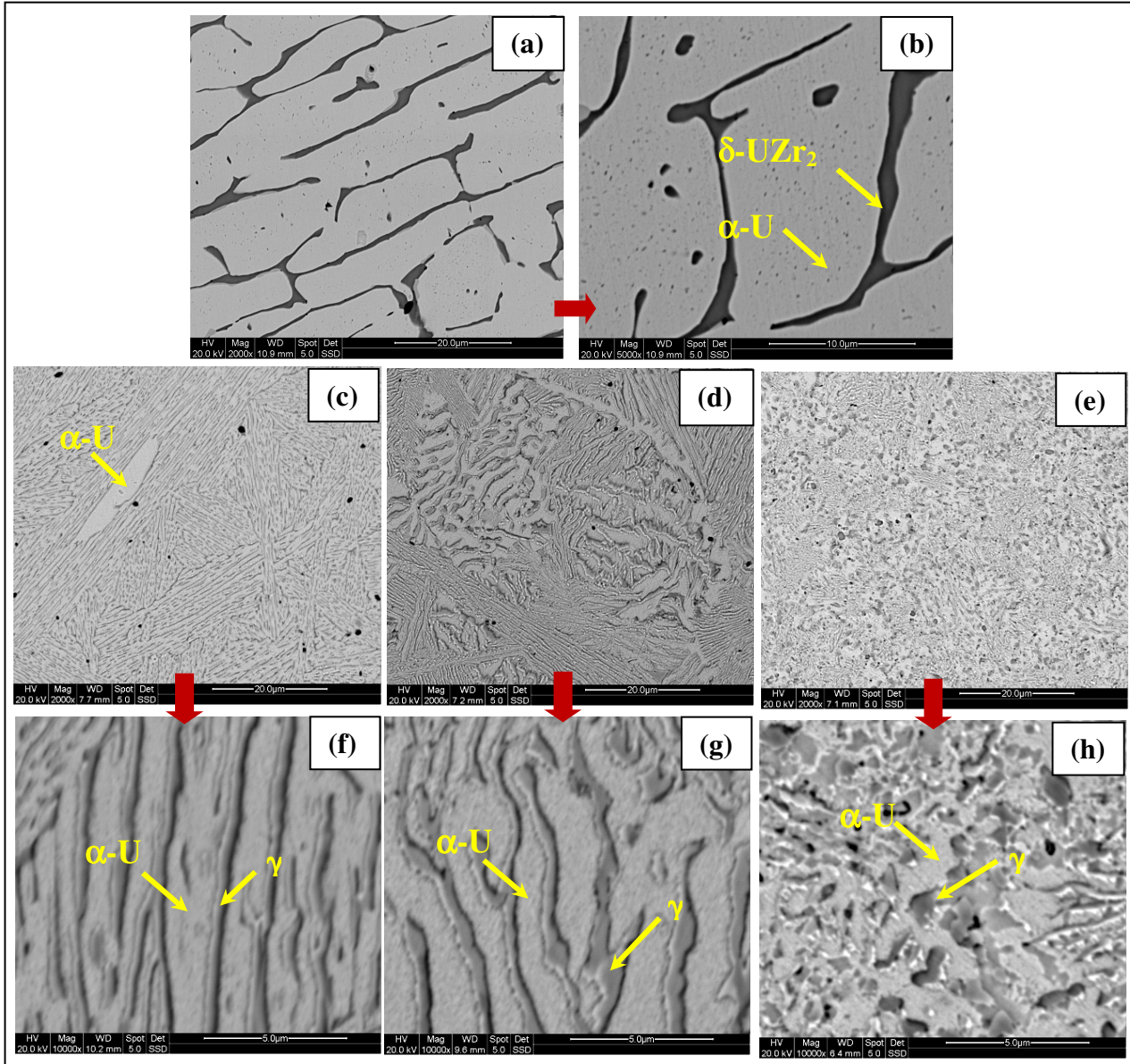


Fig. 5.3 SEM micrographs of step-cooled alloys at different magnifications (a & b) U-6Zr alloy showing α -U and δ -UZr₂ phases; (c & f) U-4Zr-2Nb, (d & g) U-2Zr-4Mo, (e & h) U-6Nb alloy showing alternative layers of α -U and γ -phases.

composition of approximately 30 at.%Zr, 20 at.%Nb and 50 at.%U whereas solute content in other phase is negligibly small and was not detected. The two phases of the lamellar structure are basically bcc γ_3 (solute-rich) and α -U (negligible solute). The microstructure of U-4Zr-2Nb

alloy also contains island of α -U phase (Fig. 5.3c). Since, the bcc γ_3 phase was not identified by XRD and the solute-rich phase was further characterized with electron back scattered diffraction (EBSD) attached to SEM. For EBSD analysis, the sample was first metallographically polished up to 1 μm surface finish and then the final polishing was carried out with 0.025 μm colloidal silica for an hour. The EBSD patterns (Kikuchi patterns) was acquired by point mode analysis and then matched with the crystal structure of the probable phases of interest (i.e., orthorhombic α -U, bcc γ , hexagonal δ -UZr₂, etc.). The experimental and indexed EBSD patterns of (Fig. 5.4) revealed that the solute-rich layer is bcc- γ phase (space group Im-3m). A similar type of lamellar microstructure of α -U phase and γ_3 -phase was also observed in the U-2Zr-4Nb alloy (Fig. 5.3(d,g)). In this case, the solute-rich γ_3 phase contains approximately 10 at.%Zr, 35 at.%Nb and 55 at.%U. The coarsening of lamellae in many regions could also be noticed in the microstructures of the alloy samples due to long time annealing. The U-6Nb alloy (Fig. 5.3(e,h)) also exhibits similar type of phases where the γ_3 phase is highly enriched in solute of approximately 66 at %Nb. The microstructure shows coarsening of lamellar morphology and also spheroidization of the solute-rich γ_3 phase.

Table 5.2 Elemental compositions of various phases formed in different alloys.

Sample	Phase(s)	Element (at.%)		
		U	Zr	Nb
U-6Zr	α	100	0	-
	δ	28	72	-
U-4Zr-2Nb	α	100	0	0
	γ_3	50	30	20
U-2Zr-4Nb	α	100	0	0
	γ_3	55	10	35
U-6Nb	α	100	-	0
	γ_3	34	-	66

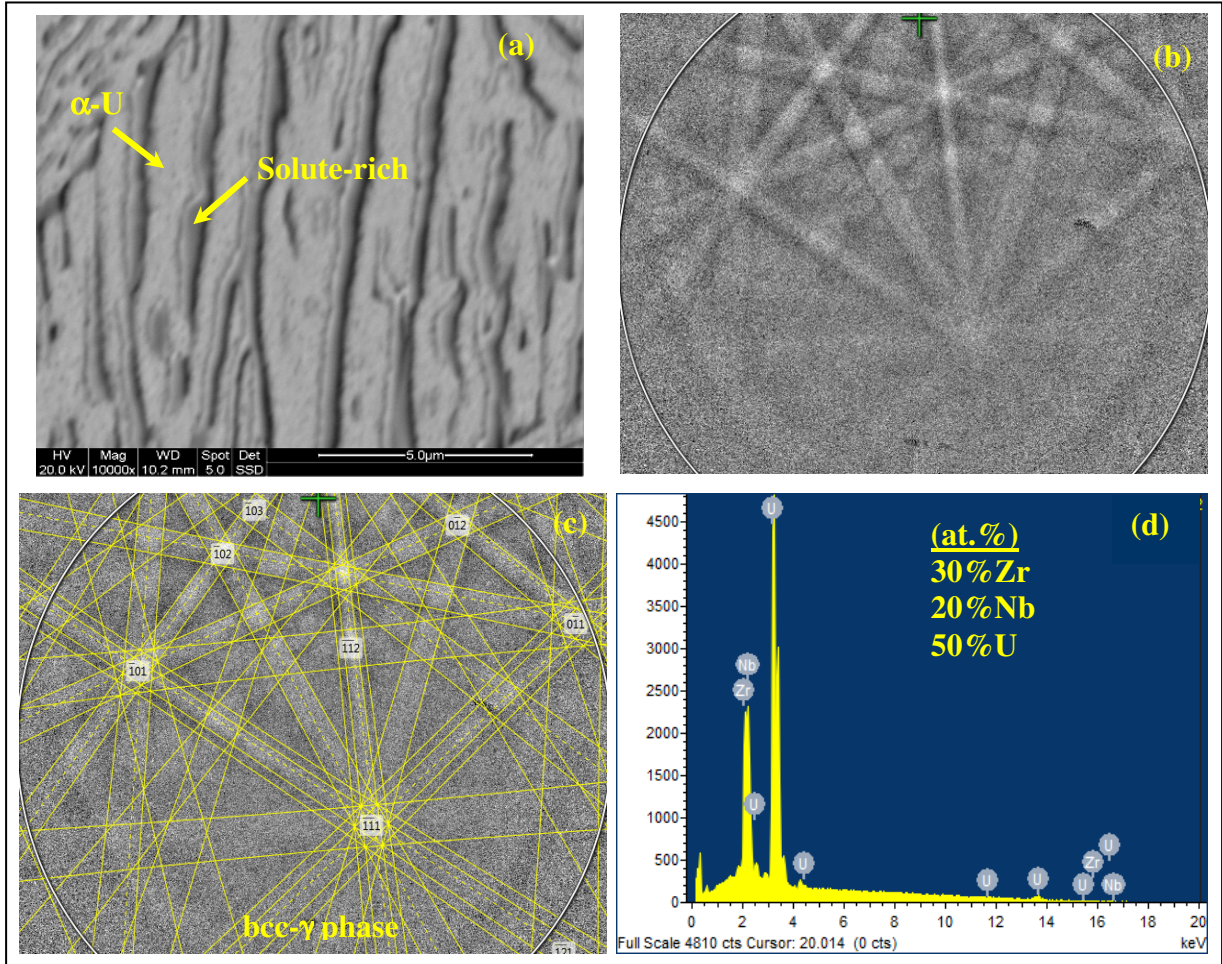


Fig. 5.4 (a) SEM image of U-4Zr-2Nb alloy; (b) experimental EBSD pattern on the solute-rich phase; (c) indexed EBSD pattern on b corresponds to bcc γ -phase (Im-3m); (d) EDS spectrum on the solute-rich γ -phase showing chemical composition.

5.3.1.3. Differential thermal analysis

The DTA curves of the alloy samples at a heating rate of 5 K min⁻¹ are collectively presented in Fig. 5.5a. The DTA curve of U-6Zr alloy exhibits three distinct peaks at 860 K, 946 K and 975 K. In addition, there is a shoulder in DTA peak at around 993 K before signal return to baseline. As already explained in Chapter 3, the peaks are due to three invariant reactions i.e., $\alpha + \gamma_2 \leftrightarrow \delta$ (Peritectoid), $\beta \leftrightarrow \alpha + \gamma_2$ (Eutectoid) and $\gamma \leftrightarrow \beta + \gamma_2$ (Monotectoid). The small

shoulder at 993 K denotes the $\gamma_1 + \gamma_2 \rightarrow \gamma$ transformation associated to miscibility gap. The DTA curve of U-4Zr-2Nb alloy (Fig. 5.5a) exhibits a strong peak at 909 K and a weak peak at 972 K. On the other hand, The DTA curves of U-4Zr-2Nb and U-6Nb alloys exhibit single peak at 916 K and 930 K, respectively. The DTA peaks of step-cooled alloys are found to be slightly higher than that of furnace-cooled alloys. However, DTA responses of all the samples in the repeat run (Fig. 5.5b) are found to be almost identical to their furnace-cooled part.

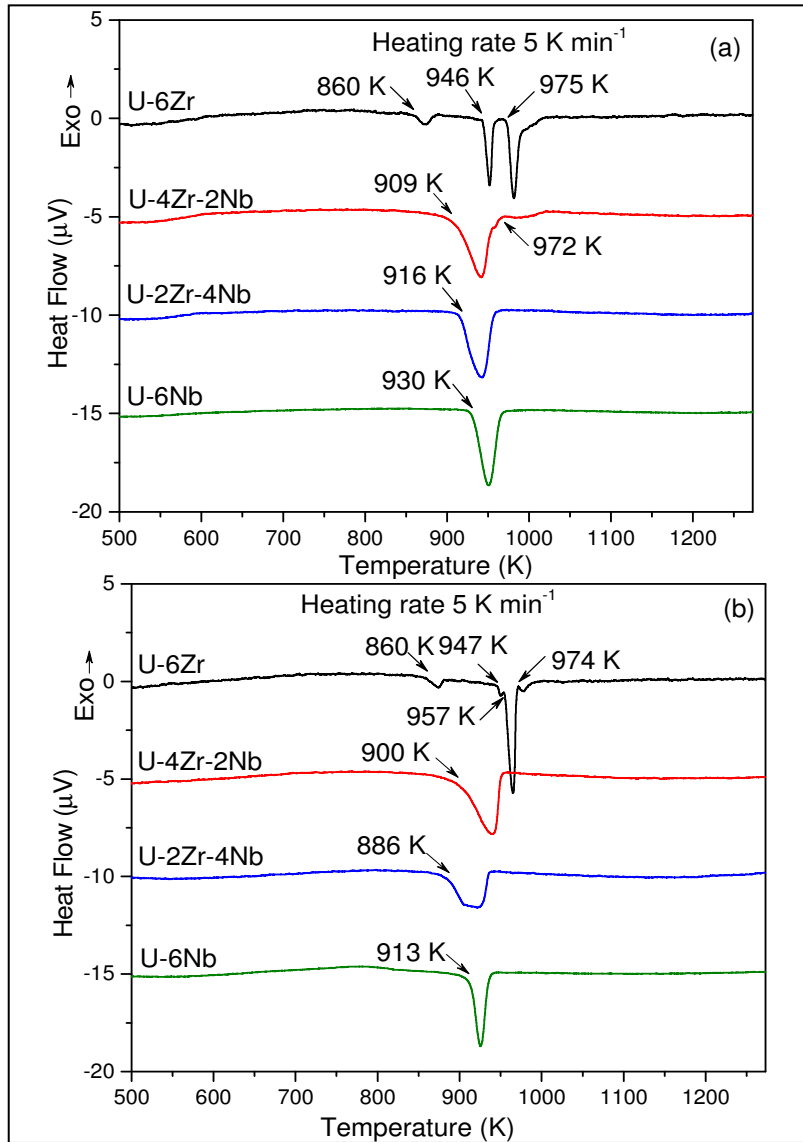


Fig. 5.5 (a) DTA curves of step-cooled of U-6Zr, U-4Zr-2Nb, U-2Zr-4Nb and U-6Nb alloys during heating, and (b) DTA curves of repeat runs at scanning rate of 5 K min^{-1}

5.3.2. U-Zr-Mo alloys (Zr+Mo = 6 wt%)

5.3.2.1 Structural Characterization

The XRD patterns of U-6Zr, U-4Zr-2Mo, U-2Zr-4Mo and U-6Mo alloys are presented in Fig. 5.6. The Rietveld refinement results of the XRD data of all the samples is summarized in Table 5.3. The XRD pattern of U-4Zr-2Mo alloy reveals the peaks of orthorhombic α -phase along with fcc $ZrMo_2$ intermetallic phase (space group Fd-3m). However, the non overlapping peaks of bcc gamma phase and δ -phase could not be identified. The U-2Zr-4Mo alloy consists of orthorhombic α -U, bcc γ phase and $ZrMo_2$ intermetallic. On the other hand, the U-6Mo alloy is biphasic in nature consisting of α -U and tetragonal γ - U_2Mo intermetallic and the phase fraction of γ - U_2Mo phase is around 39 vol%.

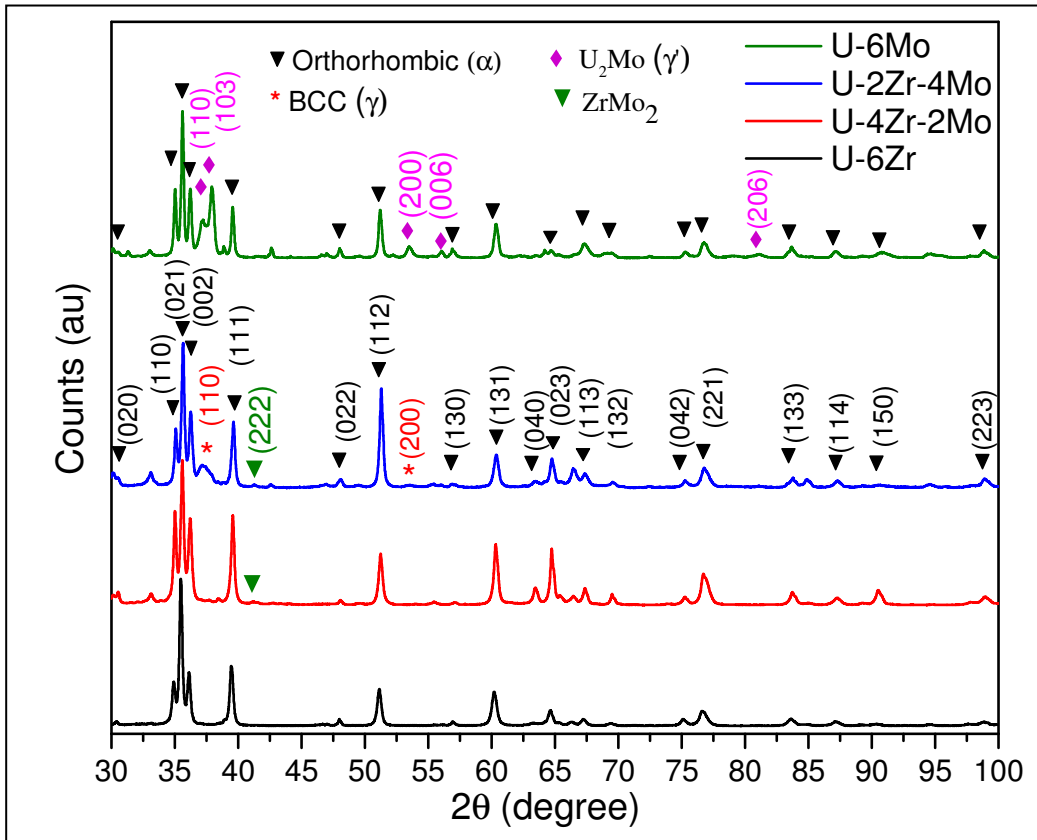


Fig. 5.6 XRD patterns of step-cooled U-6Zr, U-4Zr-2Mo, U-2Zr-4Mo and U-6Mo alloys.

Table 5.3 Lattice parameter, phase fraction of phases formed in step-cooled U-6Zr, U-4Zr-2Mo, U-2Zr-4Mo and U-6Mo alloys.

Sample (Equilibrium-cooled)	Phase(s)	Space group	Phase fraction (vol %)	Lattice Parameters (Å, degree)					
				<i>a</i>	<i>b</i>	<i>c</i>	α	β	γ
U-6Zr	Orthorhombic (α)	Cmcm	80	2.854	5.872	4.965	90	90	90
	Hexagonal (δ)	P6/mmm	20	5.039	5.039	3.090	90	90	120
U-4Zr-2Mo	Orthorhombic (α)	Cmcm	-	2.855	5.870	4.964	90	90	90
	BCC (γ)	Im-3m	-	-	-	-	90	90	90
	ZrMo ₂	Fd-3m	-	7.608	7.608	7.608	90	90	90
U-2Zr-4Mo	Orthorhombic (α)	Cmcm	-	2.855	5.875	4.967	90	90	90
	BCC (γ)	Im-3m	-	3.420	3.420	3.420	90	90	90
	ZrMo ₂	Fd-3m	-	7.601	7.601	7.601	90	90	90
U-6Mo	Orthorhombic (α)	Cmcm	61	2.857	5.871	4.973	90	90	90
	U ₂ Mo (γ)	I4/mmm	39	3.429	3.429	9.904	90	90	90

5.3.2.2. Microstructure

SEM micrographs of U-6Zr, U-4Zr-2Mo, U-2Zr-4Mo and U-6Mo are shown in Fig. 5.7. The U-4Zr-2Mo alloy exhibits lamellar microstructure of α -U (with negligible solute content) and solute-rich phases and the precipitates of ZrMo₂ intermetallic (Fig. 5.7 (c,f)). The ZrMo₂ precipitates are uniformly distributed throughout the sample. The solute-rich phases have two different compositions as indicated by types A and B in Fig. 5.7f in which type B phases contain higher amount of (Zr+Mo) (~55 at.%) as compared to type A (~40 at.%). The chemical compositions of various phases formed are presented in Table 5.4. The microstructures of U-2Zr-4Mo alloy (Fig. 5.7 (d,g)) also exhibit similar type of phases i.e., α -U, γ -phase and ZrMo₂ intermetallics. In this case, the γ phase contains approximately 20 at.% Mo, and 80 at.% U. The

microstructure of U-6Mo alloy (Fig. 5.7(e,h)) shows a fully lamellar morphology of α -U (with almost no Mo) and γ -U₂Mo intermetallic. The sample does not have any undecomposed region of retained high temperature γ -phase. The coarsening of lamellae could also be observed in microstructures of all the alloys.

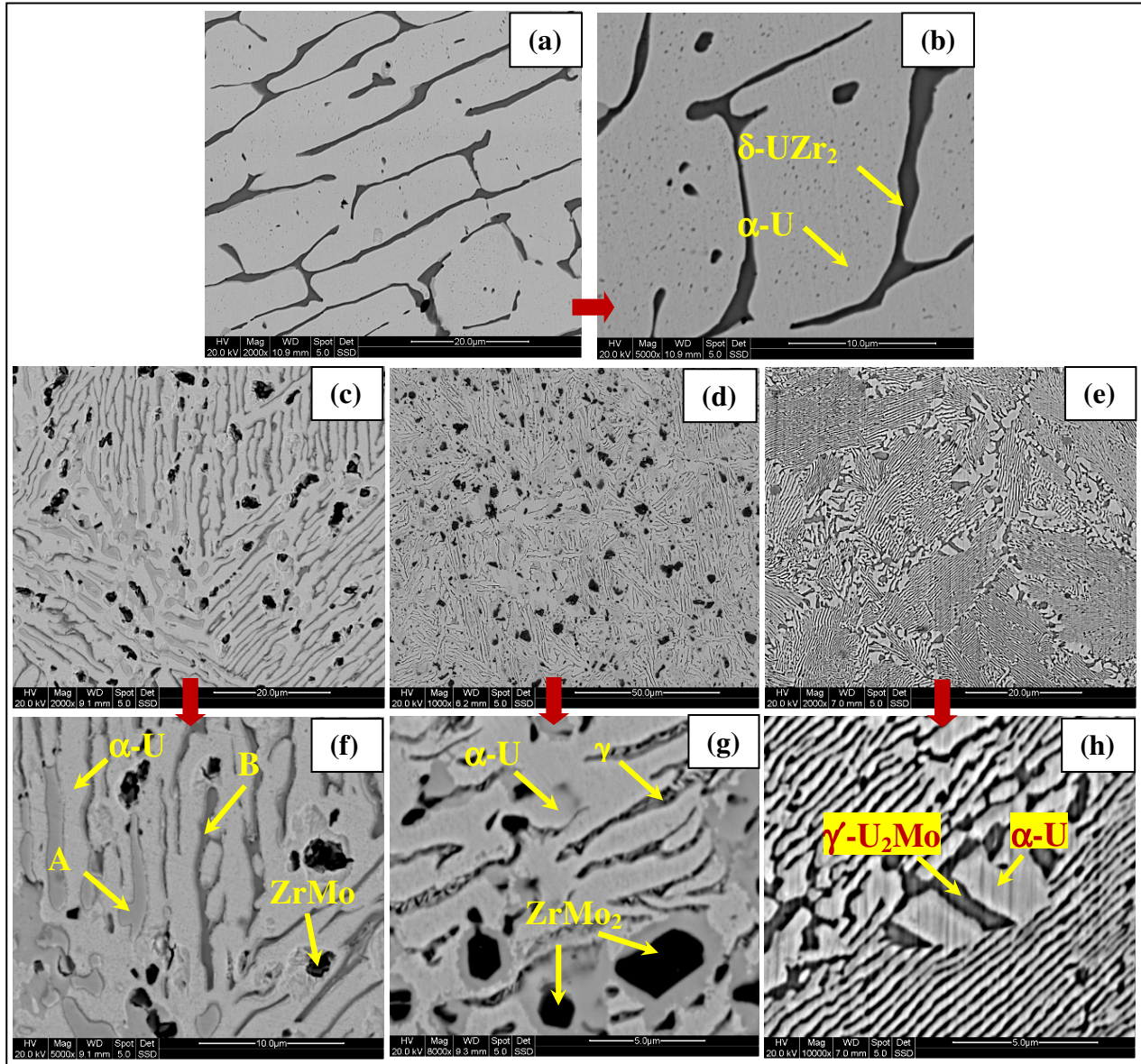


Fig. 5.7 SEM micrographs of step-cooled alloys at different magnifications (a & b) U-6Zr alloy showing α -U and δ -UZr₂ phases; (c & f) U-4Zr-2Nb, (d & g) U-2Zr-4Mo, (e & h) U-6Nb alloy showing formation of various phases.

Table 5.4 Elemental compositions of various phases formed in different alloys.

Sample	Phase(s)	Element (at.%)		
		U	Zr	Mo
U-6Zr	α	100	0	-
	δ	28	72	-
U-4Zr-2Mo	α	100	0	0
	A	62	30	08
	B	45	40	15
	ZrMo ₂	12	34	54
U-2Zr-4Mo	α	100	0	0
	γ	80	0	20
	ZrMo ₂	02	36	62
U-6Mo	α	100	-	0
	γ -U ₂ Mo	33	-	67

5.3.1.3. Differential thermal analysis

The DTA thermograms of all the samples are collectively presented in Fig. 5.8a. In U-4Zr-2Mo alloy, the DTA curve of (Fig. 5.8a) exhibits two peaks at 935 K and 960 K. A similar type of DTA curve was also observed for U-2Zr-4Mo alloy with transformation peak at 913 K and 959 K where the first transformation is somewhat lower than that of U-4Zr-2Mo. It may be noted here that DTA curves all these furnace-cooled alloys (Fig. 4.7, Chapter 4) had only single peak up to 1273 K with peak temperatures substantially lower than that of step-cooled alloys. The U-6Mo alloy has transition peak at 871 K. The DTA response of all the samples in the repeat run (Fig. 5.8b) are found to be similar to their furnace-cooled counterpart. The peak appeared in U-6Mo alloy becomes weak in the repeat run.

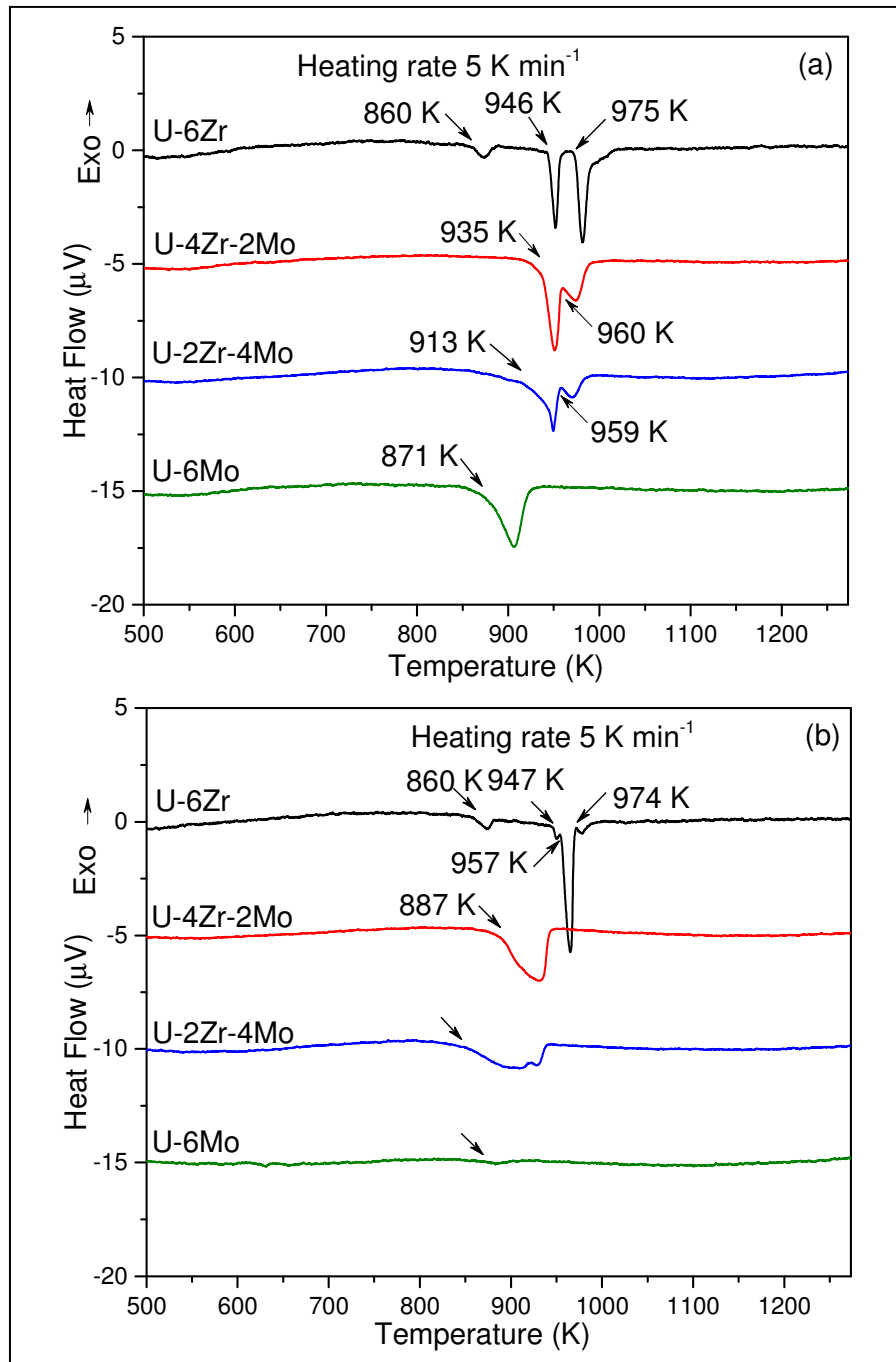


Fig. 5.8 (a) DTA curves of step-cooled U-6Zr, U-4Zr-2Mo, U-2Zr-4Mo and U-6Mo alloys samples during heating at scanning rate of 5 K min^{-1} , (b) DTA curves of repeat runs at scanning rate of 5 K min^{-1} .

5.4. Discussion

The purpose of the present study is to investigate the phase stability of U-6%(Zr+Nb), U-6%(Zr+Mo) alloys under near-equilibrium condition. Generally, the literature data on the phase stability of the uranium based alloys under equilibrium condition is scanty. The present study evaluates the phase stability of those alloys by analyzing their microstructure, phase content, phase transformation behaviour.

The phase stability results indicate that the major phase in all step-cooled samples is orthorhombic α -U phase under near-equilibrium condition. The solute content in α -U phase was found to be negligibly small and therefore could not be detected by EDS elemental analysis. The result is also supported by the equilibrium phase diagrams where the solubilities of Zr or Nb or Mo in α -U phase were reported to be <1 at. %. In U-6Zr alloy, the Rietveld analysis shows that the phase fraction of δ -UZr₂ phase is around 20 vol% which is equivalent to approximately 12 wt%. The phase fraction of δ -UZr₂ was also calculated from equilibrium U-Zr phase diagram (Fig. 1.2, Chapter 1) applying lever rule and the equilibrium concentration of Zr in δ -UZr₂ was taken as 72 at.% (equivalent to 50 wt%) based on EDS result. The weight fraction of α and δ would be ~88.35% and 11.64% respectively which are in close agreement with values obtained from XRD data. It indicates that the sample may be in close proximity to the equilibrium state. In U-4Zr-2Nb alloy, the phase fraction of α -U and γ_3 phases could not be determined from XRD data as peaks of γ_3 phase were not identified. The compositional analysis showed that the γ_3 phase in U-4Zr-2Nb alloy is rich in Zr with approximately 30 at.% Zr, 20 at.% Nb, 50 at.% U. In general, lattice parameter of bcc γ -phase increases with increase in Zr content and the $\gamma(110)$ peak shifts towards lower 2θ value. Therefore, the absence of $\gamma(110)$ could be explained due to overlap with (002) peak of α -U phase. The same peak is clearly visible in both the U-2Zr-4Nb

and U-6Nb alloys. The lattice parameter of γ_3 phase in U-6Nb alloy is substantially lower than that of U-4Zr-2Nb alloy. The lattice parameter of γ_3 phase should decrease with increasing Nb content as the atomic radius of Nb is smaller as compared to uranium. In U-6Nb alloy, the γ_3 phase is highly enriched with Nb (~66 at.% or ~43 wt%) and that results in decrease in lattice parameter. As per the U-Nb phase diagram (Fig. 1.3, Chapter 1), the equilibrium composition of solute-rich γ_3 is approximately 25 at.%U and 75at.%Nb which indicates that the U-6Nb sample did not reach the equilibrium composition. Therefore, it may not be appropriate to compare the phase fraction α and γ_3 applying lever rule on the U-Nb equilibrium diagram. Another important observation is that the lattice parameters of γ_3 phases in furnace-cooled samples were found to significantly higher than that of step-cooled samples. This attributes to lesser amount of Nb-content in the γ_3 phase of furnace-cooled alloys. Therefore, it can be concluded that γ_3 phase is gradually getting enriched with Nb with increasing the annealing time.

The phase transformation behaviour of step-cooled U-6Zr alloy has already been discussed and compared with furnace-cooled and water quenched alloys in chapter 3 based on DTA results and therefore the same is not discussed here in order to avoid repetition. The DTA results of step-cooled U-Zr-Nb alloys indicated that U-4Zr-2Nb alloy undergoes two phase transition at 909 and 972 K whereas U-4Zr-2Nb alloy undergoes only single phase transformation at 916 K. The sequence of phase transformation in step-cooled U-4Zr-2Nb and U-2Zr-4Nb alloys can be best explained with the help of vertical sections of ternary U-Zr-Nb diagram as reported by Dwight and Mueller [22]. The vertical sections relevant to present alloy composition are presented in Fig. 5.9 (a-b). The two transition peaks at 909 and 972 K of U-4Zr-2Nb alloy could be due to $\alpha + \gamma_3 \rightarrow \beta + \gamma_3 \rightarrow \gamma$, respectively. The second transition peak found in U-4Zr-2Nb alloy is due to appearance of β phase. On the other hand, the phase

transition at 916 K in U-2Zr-4Nb alloy is due to $\alpha + \gamma_3 \rightarrow \gamma$ where the β -U phase does not appear. It indicates that the formation of β -U phase is eliminated in ternary U-2Zr-4Nb alloy. The results were further supported by microstructural analysis where U-4Zr-2Nb alloy contains islands of uranium with almost no Zr/Nb which may correspond to β -U phase formed during isothermal annealing at 923 K and later on it was converted to α -U during cooling of the alloy. In case of U-2Zr-4Nb alloy, this type of feature was not observed in the microstructure. It may be noted here that the transition peak of β -U phase has not appeared in the DTA curve of furnace-cooled alloy. The furnace cooling of the sample does not allow sufficient time for the segregation of alloying constituent in α and γ_3 phases like step-cooled samples and therefore the solute content in the α -phase might be higher than the solubility limit of <1at.% leading to formation of supersaturated α -U phase. It is well known that the alloying constituent Nb is effective stabilizer of γ phase and as a result of that the β -U phase may be suppressed and at the same time γ -phase may appear at a lower temperature. In fact, the temperatures at which single γ phase forms or the temperatures of $\alpha + \gamma_3 \rightarrow \gamma$ transition for furnace-cooled alloys are found to be lower than that of step-cooled sample. It was also observed in the repeat run of the step-cooled sample. After the first run completed, the equilibrium cooled sample lost its initial thermal history and behaves like furnace-cooled sample. The step-cooled U-6Nb alloy undergoes transition at 930 K due to $\alpha + \gamma_3 \rightarrow \gamma$ reaction where β -U phase formation could not be revealed and this transition temperature is slightly higher than that of U-2Zr-4Nb alloy.

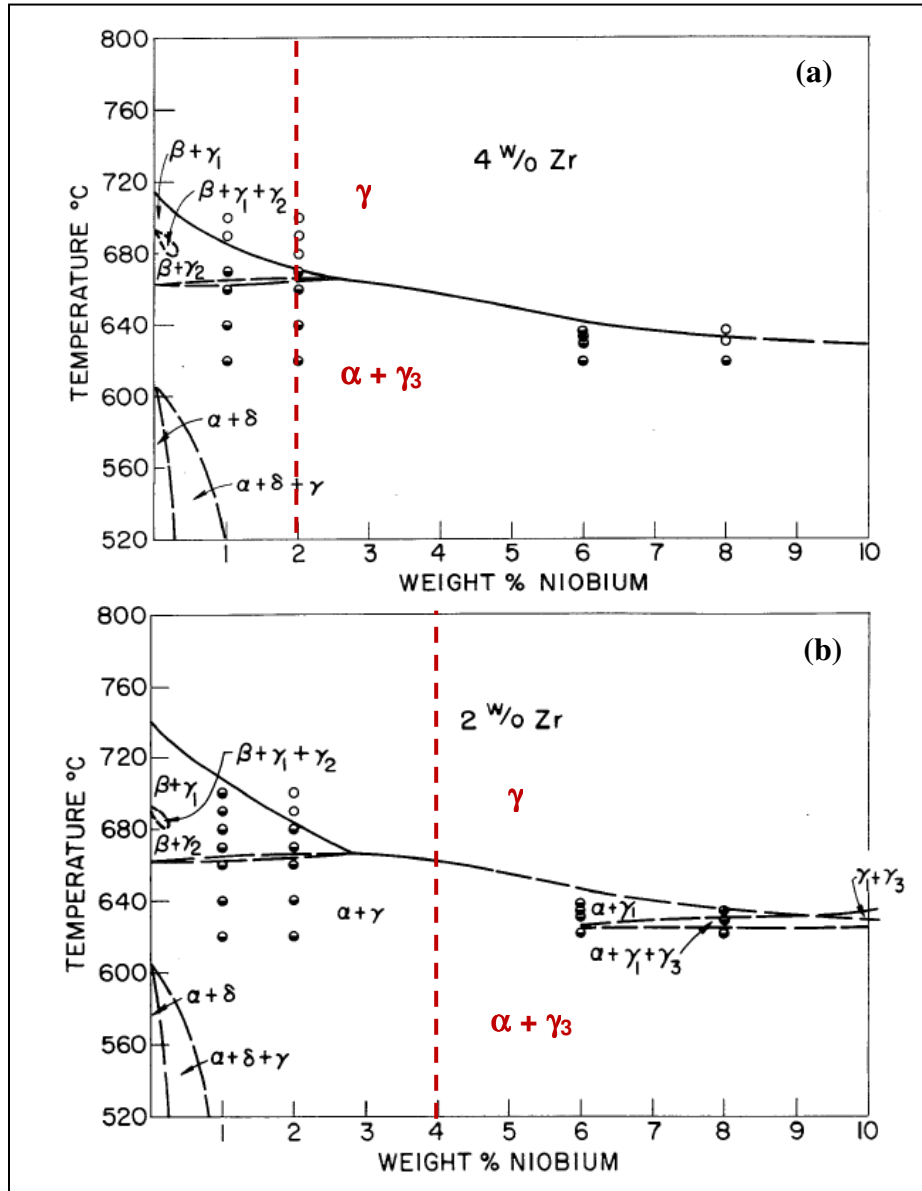


Fig. 5.9 The vertical sections of ternary U-Zr-Nb diagram at (a) 4 wt% Zr and (b) 2 wt% Zr as reported by Dwight and Mueller [22]. The composition of U-4Zr-2Nb and U-2Zr-4Nb are shown by lines. The (Zr+Nb)-rich bcc γ phases in U-Zr-Nb alloys is represented by γ_3 .

The phase stability results of step-cooled U-4Zr-2Mo alloys showed that the alloy contains multi-phase microstructure with α -U (with almost no solute content), ZrMo_2 intermetallic and solute enriched phases with two different compositions (type A and B as

indicated in Fig. 5.7f). The type A phases have composition of approximately 62 at.%U, 30 at.%Zr and 8at.%Mo whereas type B phases contain around 45 at.%U, 40 at.%Zr and 15 at.%Mo. According to the U–Zr–Mo ternary phase diagram (Fig. 5.10) [56, 114], various intermetallic or solid solution phases such as U_6Zr_3Mo , U_4Zr_5Mo may be formed at lower temperature in addition to various binary intermetallic phases (e.g. δ -UZr₂, γ -U₂Mo and ZrMo₂). Based on the compositional analysis, the type A phases may be referred to as U_6Zr_3Mo which might be developed by the local ordering of solute-rich γ phase (i.e., $\gamma \rightarrow U_6Zr_3Mo$), below 923 K [56, 114]. On other hand, the type B phases with relatively higher solute content may be either developed as U_4Zr_5Mo predicted by U–Zr–Mo phase diagram below 848 K [114] or stabilized as solute-rich γ -phase. Although, U_6Zr_3Mo , U_4Zr_5Mo phases are predicted by the calculated phase diagram, the crystallographic data are not available in the literature. Moreover, Zr-rich γ -phase could also not be identified in the XRD data as the lattice parameter of bcc γ -phase increases with increase in Zr content (due to its higher atomic radius as compared to uranium) leading to $\gamma(110)$ peak shift towards lower 2θ value and the peak may overlap with α -U(002) peak. It appears that in step-cooled U–4Zr–2Mo alloy, solute enrichment of γ -phase followed by local ordering during long time annealing may give rise to formation of either various intermetallic phases (U_6Zr_3Mo , U_4Zr_5Mo) or stabilize as solute rich γ -phase.

The step-cooled U–2Zr–4Mo alloy contains three-phase microstructure with α -U (negligible solute content) and γ phase (solute enriched) and ZrMo₂ intermetallic. The solute-rich γ -phase was identified in the XRD data of U–2Zr–4Mo alloy. The lattice parameter should decrease with increasing Mo content as the atomic radius of Mo is smaller as compared to uranium. In U–2Zr–4Mo alloy, the γ phase contains approximately 20 at.% Mo and 80 at %U and almost negligible Zr. Therefore, the $\gamma(110)$ peak shifts towards higher 2θ value and clearly

visible in XRD pattern. It may be noted here that there is possibility of formation of γ -U₂Mo intermetallic phase inside solute enriched γ phase during long time annealing at and below 823 K. However, the γ -U₂Mo phase formation could not be ascertained based on the present result.

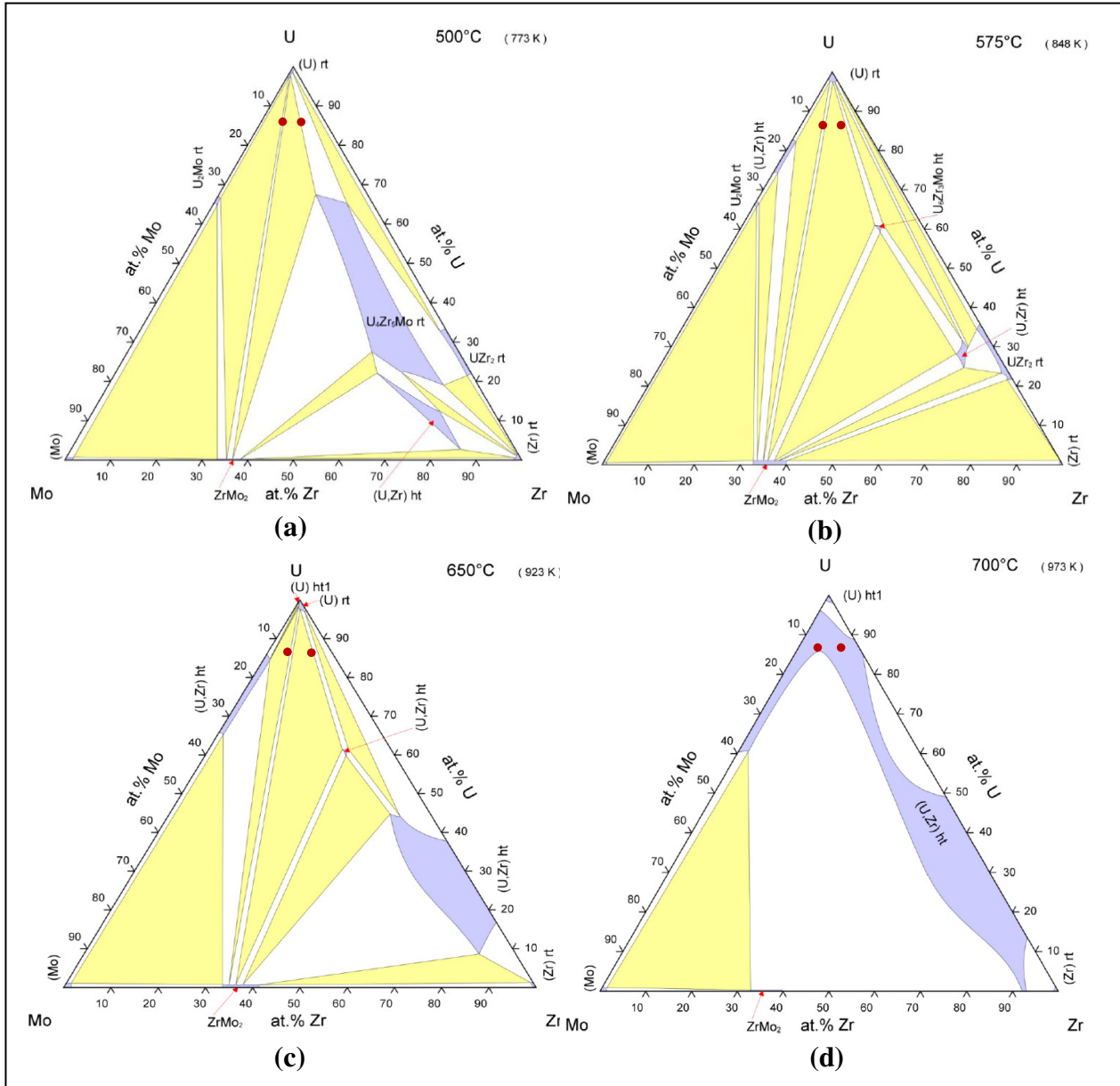


Fig. 5.10 Isothermal section of ternary U–Zr–Mo phase diagrams at (a) 773 K, (b) 848 K, (c) 923 K and (d) 973 K [56,114]. The compositions of U–Mo–Zr alloys in this study are marked by dots.

The U-6Mo alloy exhibited biphasic microstructure of α -U and γ' -U₂Mo with phase fractions of approximately 61 vol% (~65wt%) and 39 vol % (~35 wt%), respectively. The phase fractions of α -U and γ' -U₂Mo were also calculated from U-Mo phase diagram (Fig. 1.5, Chapter 1) using level rule. The weight fractions of α and γ' would be ~67% and 33% respectively which matches well with values obtained from XRD data. As expected, the U-Mo alloy after long time annealing during step cooling attained a microstructure consisting of α -U and γ' -U₂Mo which resemble well with the equilibrium phase diagram. The γ' -U₂Mo phase was not formed in the furnace-cooled sample implying the sluggish nature of eutectoid transformation (i.e., $\gamma \rightarrow \alpha + \gamma'$ -U₂Mo). In U-rich U-Mo alloys, the eutectoid decomposition initiates through a cellular reaction, resulting in a lamellar microstructure of α -U and γ (higher Mo content) rather than α -U and γ' -U₂Mo as expected for a normal eutectoid reaction. The long time annealing at sub-eutectoid temperature (823, 773 K) would lead to transformation of Mo-rich γ -phase into tetragonal γ' -U₂Mo phase. This leads to progressive evolution of high temperature γ -phase into lamellar microstructure of α -U + Mo-rich γ -phase which is followed by α -U + Mo-rich γ -phase + γ' -U₂Mo finally a biphasic α -U + γ' -U₂Mo microstructure as indicated by equilibrium phase diagram (i.e., $\gamma \rightarrow \alpha + \gamma \rightarrow \alpha + \gamma + \gamma' \rightarrow \alpha + \gamma'$) [64, 68, 115]. It is also supported by the present result, where the partial decomposition of high temperature γ -phase in the furnace-cooled sample lead to formation $\alpha + \gamma$ microstructure and the step-cooled sample exhibited equilibrium microstructure of $\alpha + \gamma'$ -U₂Mo.

The DTA results of step-cooled U-Zr-Mo alloys indicated that U-4Zr-2Mo alloy undergoes two phase transitions at 935 and 960 K whereas U-2Zr-4Mo undergoes transitions at 913 and 959 K. The phase transformation sequence of the sample can be evaluated by comparing

the results with the phase stability of U-Zr-Mo alloys using the isothermal section of ternary phase diagram (Fig. 5.9). According to the phase diagram, the alloys form a bcc solid solution at and above 973 K whereas at relatively lower temperatures i.e., 848 K and 923, the equilibrium phases of the alloy compositions are $\alpha + \text{ZrMo}_2 + \text{U}_6\text{Zr}_3\text{Mo}/\gamma$ (for U-4Zr-2Mo) and $\alpha + \text{ZrMo}_2 + \gamma$ (for U-2Zr-4Mo). The present alloys also exhibit similar type multi-phase microstructures. Based on the ternary phase diagram, it can be predicted that the U-Zr-Mo alloy follow the transformation sequence of $\alpha + \text{ZrMo}_2 + \gamma \rightarrow \gamma + \text{ZrMo}_2 \rightarrow \gamma$. The lower DTA peaks at 913 K (for U-4Zr-2Mo) and 935 K (for U-2Zr-4Mo) are due to $\alpha + \gamma + \text{ZrMo}_2 \rightarrow \gamma + \text{ZrMo}_2$ whereas the DTA peak ~960 K for both the alloys corresponds to $\gamma + \text{ZrMo}_2 \rightarrow \gamma$. It may be noted here that the DTA curve of U-4Zr-2Mo did not reveal any peak at lower temperature that can be correlated with transformation/dissolution of $\text{U}_6\text{Zr}_3\text{Mo}$, $\text{U}_4\text{Zr}_5\text{Mo}$ phases. The result indicate that the U-Zr-Mo alloys form single γ -phase at relatively higher temperature due to presence of ZrMo_2 intermetallic which has higher thermally stability. Therefore, it is expected that the high temperature γ -phase will be depleted in Zr and Mo relative to its overall alloy composition before complete dissolution of ZrMo_2 . Unlike U-Zr-Mo alloys, the U-6Mo alloy exhibited peak at 871 K in the absence of Zr. According to the U-Mo equilibrium phase diagram (Fig. 1.5, chapter 1), the U-6Mo alloy should follow the phase transformation sequences of $\alpha + \gamma' - \text{U}_2\text{Mo} \rightarrow \alpha + \gamma \rightarrow \gamma$ where the first reaction is eutectoid reaction (i.e., $\gamma \leftrightarrow \alpha + \gamma'$) and the second transformation corresponds to solvus line which may not be resolved. In U-6Mo alloy, the single peak observed at 871 K is attributed to eutectoid reaction. The DTA results indicate that the phase transition temperatures of the alloys may vary significantly depending on their phase stability resulting from variation in the heat treatment prior to DTA run.

5.5. Summary and conclusions

This work provides a thorough understanding on the phase stability of U-6(Zr+Nb) and U-6(Zr+Mo) alloys. The following important observations are summarized based on the findings of this study:

- Microstructure of U-6Zr alloy reveals presence of distinct α -U and δ -UZr₂ phases under near-equilibrium condition.
- U-4Zr-2Nb, U-2Zr-4Nb and U-6Nb alloys are all biphasic in nature comprised of bcc γ phase with higher solute content and α -U phase.
- U-4Zr-2Mo and U-4Zr-2Mo alloys exhibit multiphase microstructure with α -U, ZrMo₂ intermetallic and solute enriched phases whereas U-6Mo alloy attained a microstructure consisting of α -U and γ -U₂Mo.
- In all step-cooled samples, the solute content in α -U phase was not detected by EDS. Therefore, the solubilities of Zr or Nb or Mo in α -U phase under near-equilibrium condition were found to be negligibly small.
- Intermetallic δ -UZr₂ phase formation was not observed in ternary U-Zr-Nb and U-Zr-Mo alloys under near-equilibrium condition.
- In U-Zr-Mo alloys, single γ -phase forms at relatively higher temperature due to presence of ZrMo₂ intermetallic. The formation of ZrMo₂ phase may lead to decrease in solute content in the bcc γ phase. The precipitation of such type of phases is always undesirable.
- The phase stability of under near-equilibrium condition differs significantly from furnace-cooled alloys.

Chapter 6

Fuel-cladding chemical interaction (FCCI) between U–Zr alloy and T91 steel cladding

6.1. Introduction

The fuel-cladding chemical interaction (FCCI) between the metallic fuel and steel cladding is considered as a potential problem area in metallic fuelled fast reactors. This chapter describes the chemical compatibility between U–Zr alloy and T91 grade cladding steel from the prospective of their application in fast reactor. For compatibility test, U–Zr alloy with relatively higher Zr content (10 wt %) was purposely chosen here to explore the role of Zr in fuel-cladding interaction. It may also be noted here the maximum allowable concentration of Zr in metallic fuel is also limited to approximately 10 wt% as higher Zr addition would result in formation of an alloy whose liquidus temperatures may exceed the softening point of the quartz molds used for fabrication of actual fuel rod. Therefore, in the present investigation, a detail investigation on chemical compatibility of U–10Zr alloy with T91 steel has been carried out by differential thermal analysis followed by diffusion couple test at various temperatures relevant to normal and off-normal thermal events of reactor. The compatibility test will give feedback about FCCI at nominal steady-state operating conditions and further at elevated temperatures during off-normal reactor events. Finally, the chemical compatibility of our reference composition of U–6Zr alloy with T91 has been checked by diffusion couple test.

6.2. Experimental procedure

U–10Zr sample used for this experiment was taken from the alloy slug prepared using nuclear grade uranium and 99.95% pure crystal bar of zirconium by following injection casting route [116]. The U–10Zr alloy was at first characterized with XRD and SEM/EDS for phase and

compositional analyses before conducting compatibility experiment. T91 grade steel was used in the standard normalized and tempered condition. The chemical composition of T91 steel is given in Table 1.6 (Chapter 1). As already mentioned, the chemical interaction between U–10Zr and T91 steel was investigated by differential thermal analysis and diffusion couple experiment and the detailed experimental procedure have been presented in Chapter 2. The diffusion couple experiment between U–6Zr alloy and T91 steel has also been carried out at few selected temperatures. The heat treatment schedule of the couples is given in Table 6.1.

Table 6.1 Annealing temperature and time of the diffusion couple experiments.

Couple	Temperature (K)	Time (h)
U–10Zr/T91	823	1500
	923	1000
	973	500
	1003	200
U–6Zr/T91	973	500
	1023	100

6.3. Results

6.3.1. Structural and microstructural characterization of U–10Zr alloy

The X-ray diffraction pattern of U–10Zr alloy (Fig. 6.1) corresponds to orthorhombic α -U phase (space group Cmc_m) with lattice parameters of $a = 2.860\text{\AA}$, $b = 5.865\text{\AA}$, $c = 4.980\text{\AA}$. The formation of δ -phase cannot be stated here conclusively from the XRD result of the alloy as most of the peaks of δ -UZr₂ phase overlap with that of α -U phase and non overlapping low intensity peaks at $\sim 46.5^\circ$ and $\sim 71.6^\circ$ corresponding to (111) and (112) planes of δ -phase are not properly revealed. The alloy exhibits Widmanstatten type microstructure (Fig. 6.2a) and like U–6Zr alloy, the δ -UZr₂ phase could not be resolved by SEM. A representative EDS spectrum for the compositional analysis is shown in Fig. 6.2b.

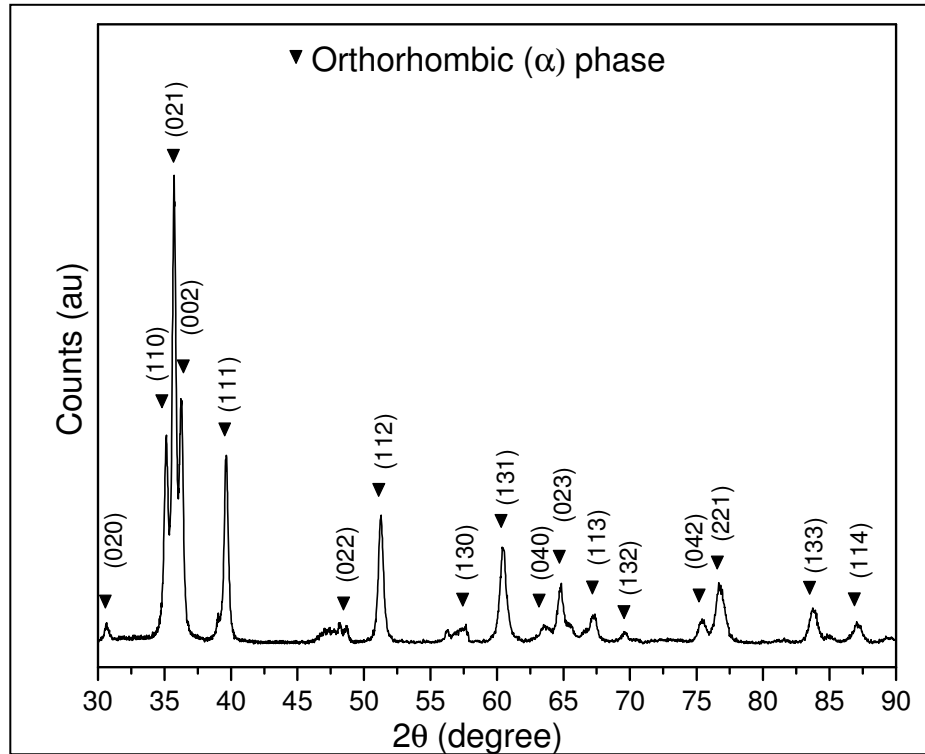


Fig. 6.1 XRD pattern of U–10Zr alloy showing peaks of orthorhombic α -U phase.

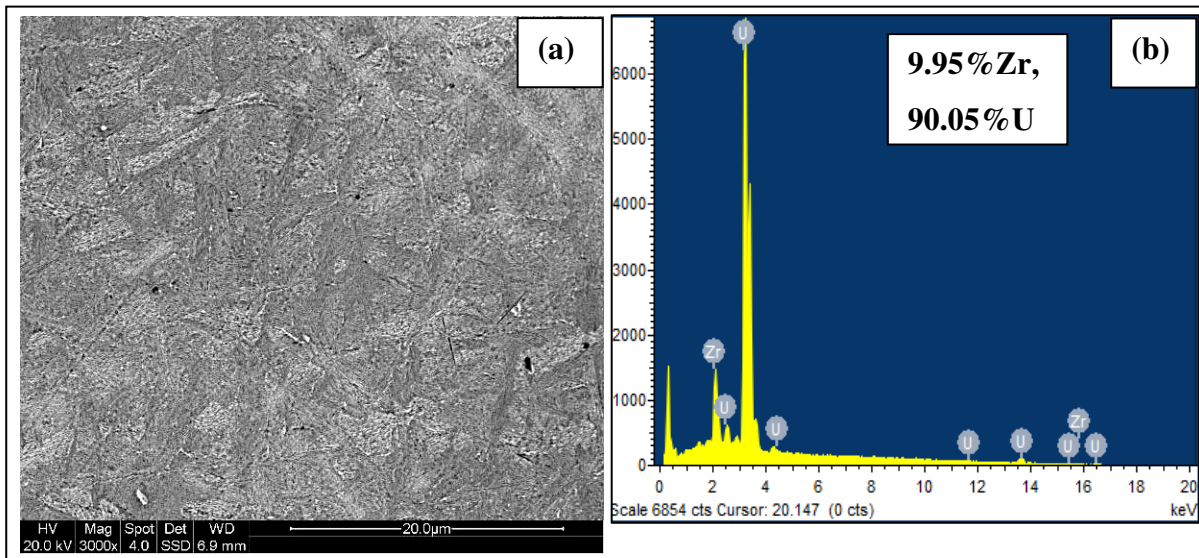


Fig. 6.2 (a) SEM micrograph of U–10Zr alloy, (b) A representative EDS spectrum showing chemical composition.

6.3.2. Chemical interaction by differential thermal analysis

At first, the phase transformation temperatures U–10Zr alloy, T91 steel and U metal samples were examined separately with DTA and the corresponding DTA thermograms are collectively presented in Fig. 6.3. For pure uranium metal, DTA peaks observed at 941, 1046 and 1393 K are attributed to phase transformation sequence of $\alpha \rightarrow \beta \rightarrow \gamma \rightarrow$ melting, respectively. For T91, the peak at 1015 K is due to the ferromagnetic to paramagnetic Curie temperature whereas the peak at 1111 K is attributed to the ferrite (α) to austenite (γ) transition. The U–10Zr alloy exhibits DTA thermogram similar to U–6Zr alloy. For U–10Zr alloy, the peak at 860 K is due to the $\alpha + \delta \rightarrow \alpha + \gamma_2$ reaction and the peak at 958 K corresponds to the $\alpha + \gamma_2 \rightarrow \gamma$ transformation (i.e., $\alpha + \gamma_2 \rightarrow \beta + \gamma_2 \rightarrow \gamma_1 + \gamma_2 \rightarrow \gamma$) and the peak at 1510 K corresponds to the solidus temperature. It may be noted here that the intermediate transitions U–10Zr alloy could not be resolved at the heating rate of 10 K min^{-1} . The DTA peaks for different phase transformation are presented in Table 6.2.

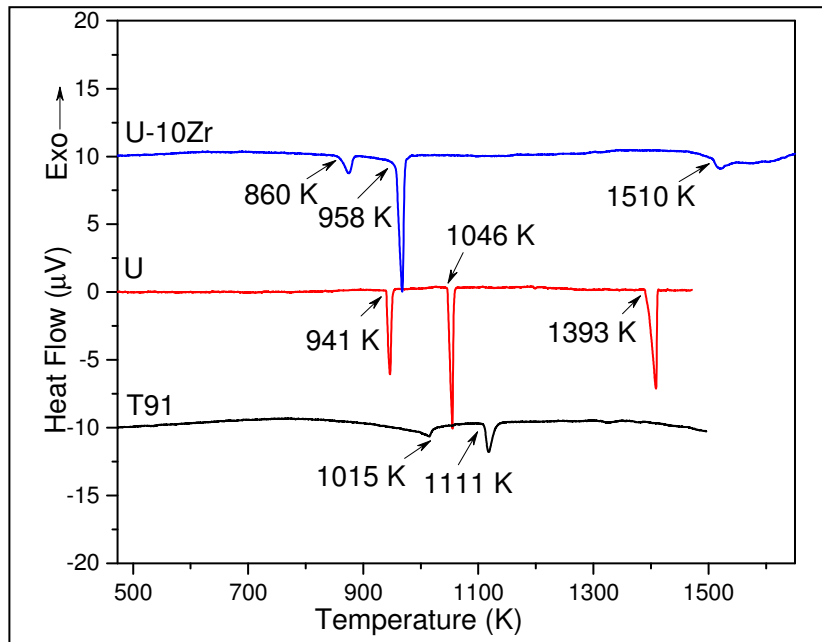


Fig. 6.3 DTA thermograms of U metal, T91 steel, U–10Zr alloy.

Table 6.2 DTA peaks for various phase transitions of U, U–10Zr and T91 during heating

Sample	DTA peak temp (K)	Origin of Peak
U	941	α -U \rightarrow β -U
	1046	β -U \rightarrow γ -U
	1393	Melting point
T91	1015	Curie temperature, (ferromagnetic \rightarrow paramagnetic)
	1111	ferrite (α) \rightarrow austenite (γ)
U–10Zr	860	$\alpha + \delta \rightarrow \alpha + \gamma_2$
	958	$\alpha + \gamma_2 \rightarrow \gamma$ (i.e., $\alpha + \gamma_2 \rightarrow \beta + \gamma_2 \rightarrow \gamma_1 + \gamma_2 \rightarrow \gamma$)
	1510	Solidus temperature

With this background, DTA experiments were carried out with U+T91 composite (small discs of U and T91) as well as U–10Zr+T91 composite (small discs of U–10Zr and T91). The DTA experiment of U+T91 composite was carried out for comparison. The DTA curves of U+T91 composite up to 1473 K in both heating and cooling cycles were presented together in Fig. 6.4(a-b). In the first heating cycle (Fig. 6.4a), the endothermic peaks at 941, 1015, 1046 and 1111 K are due to the phase transformations of uranium and T91 as explained above. Apart from these, the U+T91 composite exhibits one intense exothermic peak at 1383 K which is followed by an endothermic peak at 1387 K. The intense exothermic peak is indicative of strong chemical reaction between the two whereas the peak at 1387 K is due to the melting of unreacted uranium metal. However, only two peaks at 1313 and 988 K were observed in the cooling cycle (Fig. 6.4a). In the repeat DTA run with same sample, both the heating and cooling curves (Fig. 6.4b) show only two peaks.

In DTA thermograms of U–10Zr+T91 composite (Fig. 6.4(c-d)), the endothermic peaks at 861 and 958 K are due to the phase transformation of U–10Zr alloy whereas the peaks at 1015

and 1111 K are due to Curie temperature and ferrite to austenite transition of T91, respectively. In this case, the exothermic reaction peak appears at 1495 K which is significantly higher than that observed in U+T91 composite. The exothermic peak was followed by an endothermic peak at 1503 K. In the cooling curve, two peaks were identified at 1383 and 978 K. In the heating cycle of the repeat run, the first peak appeared at 995 K and other peak was not resolved properly. The cooling curves of both the first and repeat runs are almost identical in nature.

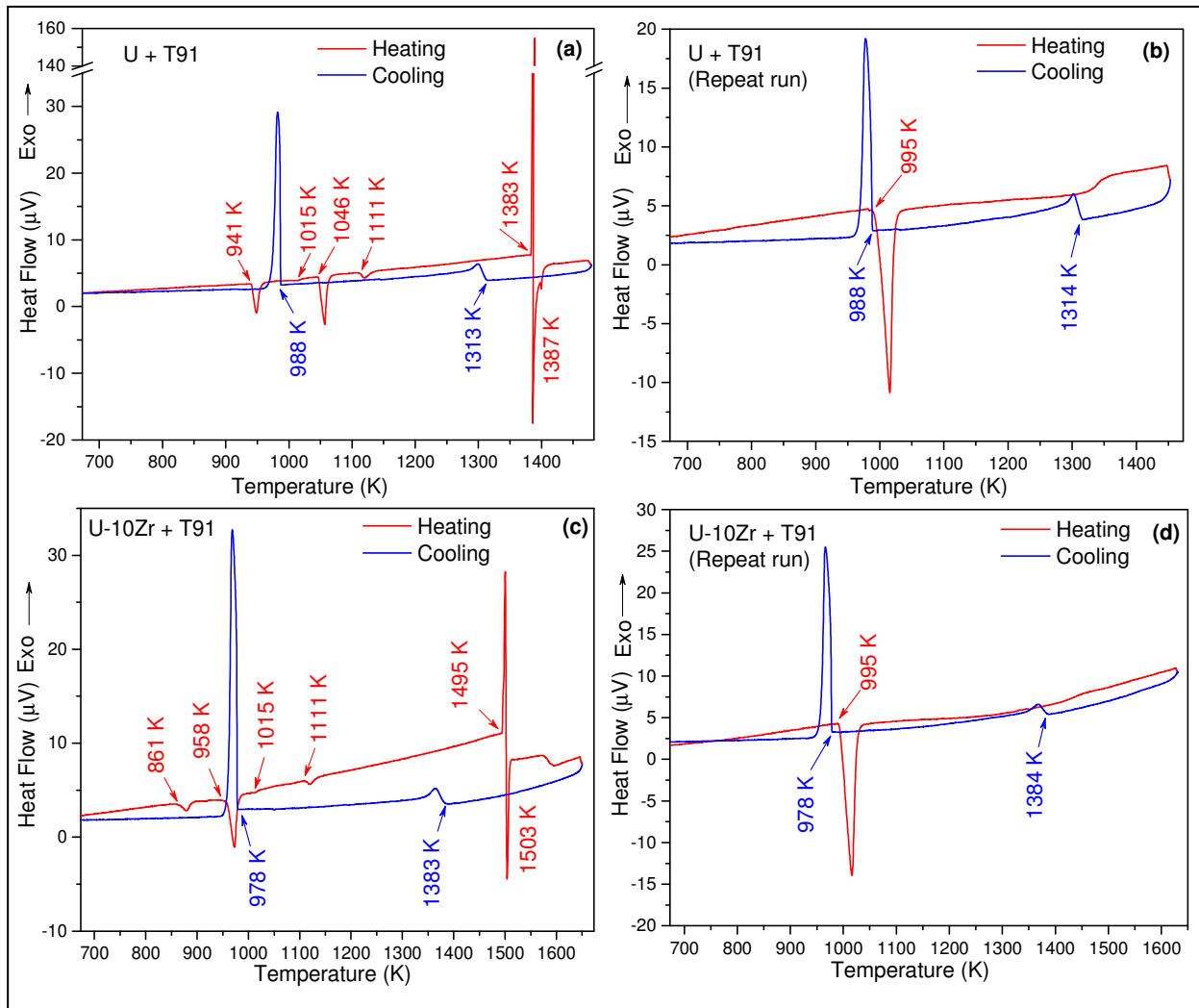


Fig. 6.4 DTA curves of (a & b) U+T91 composite, and (c & d) U–10Zr+T91 composite in both heating and cooling cycles at a scanning rate of 10 K min⁻¹.

The BSE image of the reaction products of the U+T91 and U–10Zr+T91 composites are shown in Fig. 6.5(a-d). The microstructures of the reaction products do not contain any unreacted starting materials. The reaction product of U+T91 composite (Fig. 6.5(a-b)) contained two distinct phases i.e., bright and grey. The larger grey phases are uniformly distributed in the sample and the lamellar matrix had alternative layer of grey and bright phases. On the other hand, the reaction product of U–10Zr+T91 composite had three distinct phases which appear as bright, grey and dark in Fig. 6.5(c-d). The magnified micrographs (Fig. 6.5d) revealed that the dark phases are surrounded by grey phases and the matrix contained bright and grey phases.

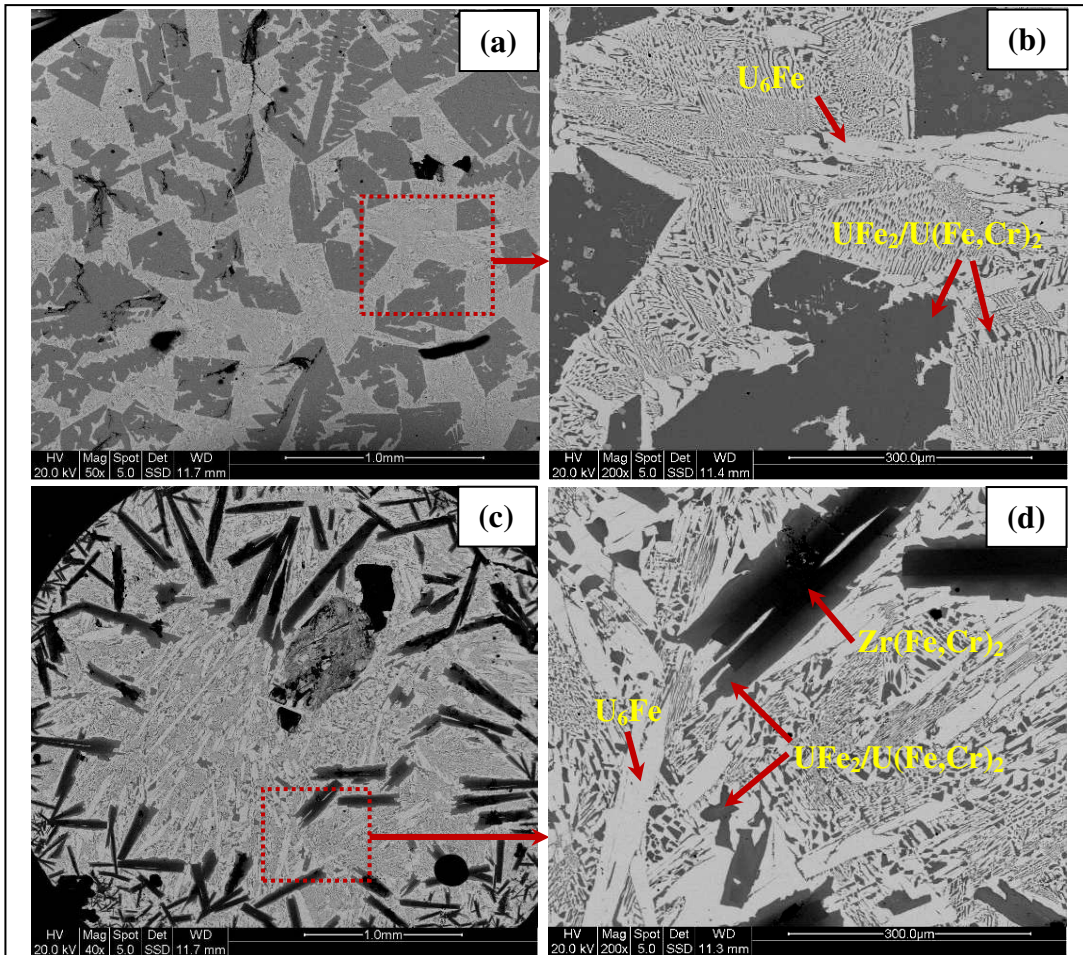


Fig. 6.5 Microstructures of reaction products of (a & b) U+T91, and (c & d) U–10Zr+T91 composites at different magnifications showing different phases (i.e., bright, grey and dark).

The phases were further characterized with EBSD and EDS attached to SEM. For EBSD sample preparation, standard metallographic processes of sectioning, grinding and polishing were carried out up to 1 μm surface finish and then the final polishing was carried out with 0.025 μm colloidal silica for about an hour to ensure that the sample surface is free of any sectioning damage. For EBSD analysis, the samples were tilted approximately 70° with respect to the incident beam and the accelerating voltage of 20 kV was applied. The EBSD patterns (Kikuchi patterns) of different phases were acquired by point mode analysis and then matched with the crystal structure of the probable phases of interest (i.e., UFe_2 , U_6Fe , ZrFe_2 , $\text{Zr}(\text{Fe,Cr})_2$ etc.). The electron forescatter images of U+T91 reaction product at different magnifications were shown in Fig. 6.6(a-b). The experimental and indexed EBSD patterns (Fig. 6.6(c-f)) revealed two types of phases i.e., cubic UFe_2 -type (space group Fd-3m) and tetragonal U_6Fe (space group I4/mcm). The elemental analysis (Fig. 6.6(g-h)) revealed that the amount of Cr in U_6Fe phase is negligible and could not be detected in EDS. On the other hand, the UFe_2 phase with soluble Cr can be represented as $\text{U}(\text{Fe,Cr})_2$. It may be noted here that both UFe_2 and $\text{U}(\text{Fe,Cr})_2$ compounds have cubic Laves structure (space group Fd-3m) [117]. The electron forescatter images of the U–10Zr+T91 reaction product were shown in Fig. 6.7(a-b). The experimental and indexed EBSD patterns (Fig. 6.7(c-h)) revealed three types of phases i.e., hexagonal $\text{Zr}(\text{Fe,Cr})_2$ (space group $\text{P6}_3/\text{mmc}$), UFe_2 (Fd-3m) and U_6Fe (I4/mcm). The EDS spectra of the three phases are shown in Fig. 6.7(i-k). The solubility of Cr in the U_6Fe phase is negligible and the UFe_2 phase with small fraction of soluble Cr can be represented as $\text{U}(\text{Fe,Cr})_2$ similar to U+T91 reaction product. The Cr content in the $\text{Zr}(\text{Fe,Cr})_2$ phase was found to be higher than that of the $\text{U}(\text{Fe,Cr})_2$ phase. The $\text{Zr}(\text{Fe,Cr})_2$ phase has significant amount of soluble U and the $\text{U}(\text{Fe,Cr})_2$ phase has significant amount of soluble Zr. It may be noted here that the solubilities of Zr in UFe_2 and U in ZrFe_2 have

also been reported in the U–Zr–Fe phase diagram [118]. The results indicate that the bright, grey and dark phases in the BSE micrographs of the reaction product (Fig. 6.5(a-d)) are U_6Fe , $UFe_2/U(Fe,Cr)_2$ and $Zr(Fe,Cr)_2$, respectively.

6.3.3. Diffusion couple experiment

6.3.3.1. Interfacial reaction in U–10Zr/T91 couple at 823 K

The microstructures of the interdiffusion layer at the interfacial region of the U–10Zr/T91 diffusion couple annealed at 823 K for 1500 h are shown in Fig. 6.8(a-b). Fig. 6.8c shows the intensity profiles of U-M α , Zr-L α , Fe-K α , Cr-K α X-ray lines recorded along a line AB marked in Fig. 6.8b. The interdiffusion between U–10Zr and T91 leads to the formation of different reaction layers at the interface namely UFe_2 -type intermetallic, Zr-rich layer, and Zr-depleted layer. The interdiffusion layer adjacent to the T91 contained approximately 29 at.% U, 8 at.% Zr, 57 at.% Fe and 6 at.% Cr and it is most likely to be of UFe_2 -type intermetallic with soluble Zr and Cr. This layer is followed by a thin Zr-rich layer. The Zr-rich layer contains approximately 65 at.% Zr, 12 at.% U, 20 at.% Fe and 3 at.% Cr. The total thickness of the UFe_2 -type and Zr-rich layers as measured from the X-ray line profile was $\sim 1.5 \mu m$. The Zr depleted zone formed at the U–Zr alloy side contains approximately 95 at.% U, 5 at.% Fe. There is no distinct boundary for Zr depleted zone and therefore it was difficult to find the exact width of this layer. In U–Zr alloy side, one could see fine precipitates of δ - UZr_2 phase uniformly distributed in α -U matrix. The detailed microstructural investigation on the U–Zr side of the interfacial region also revealed formation of intermetallic phases τ_2 (6 at.% Fe, 67 at.% U, 27 at.% Zr) in a discrete manner (Fig. 6.8b). It may be noted here that the formation of such intermetallic phase (τ_2) was reported in the ternary U–Zr–Fe system [118].

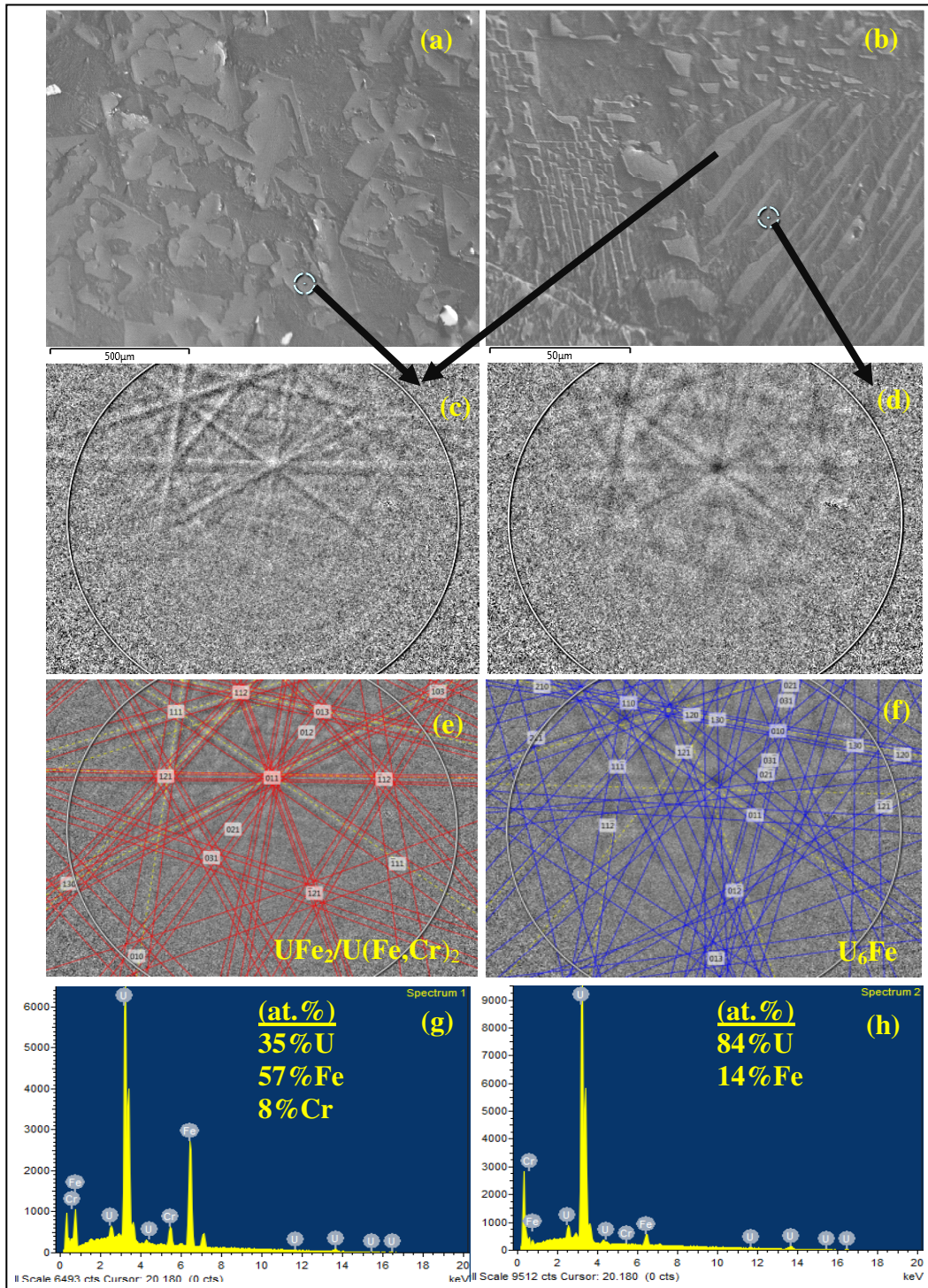


Fig. 6.6(a-b) Electron forescatter images of U+T91 reaction products after DTA run; (c-d) experimental EBSD patterns of phases as indicated by arrows; (e-f) indexed EBSD patterns on c and d correspond to UFe_2 (Fd-3m) and U_6Fe (I4/mcm) phases, respectively; (g-h) EDS spectra of respective phases showing their chemical composition.

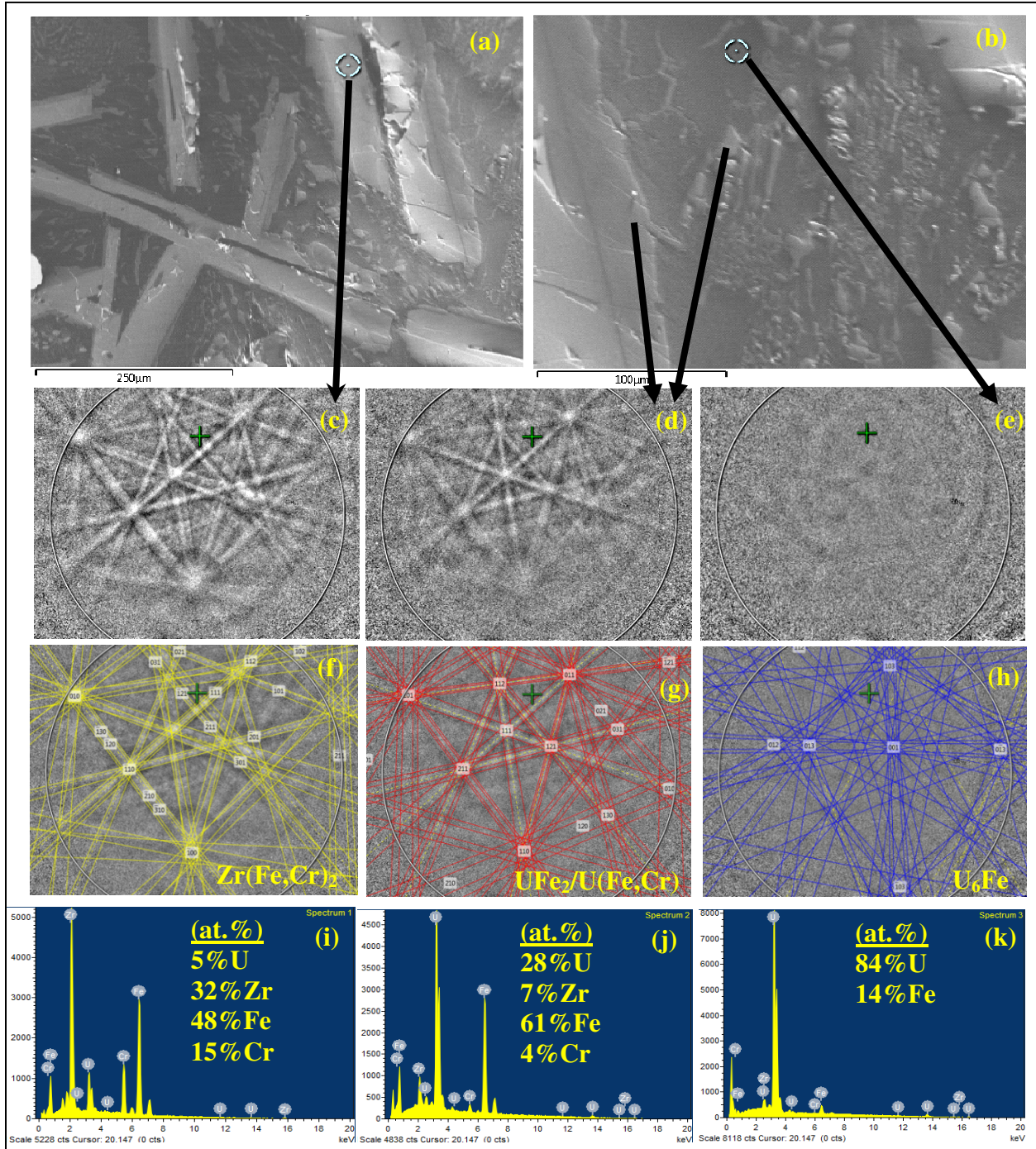


Fig. 6.7(a-b) Electron forescatter images of U-10Zr+T91 reaction product, (c-e) experimental EBSD patterns of various phases as indicated by arrows; (f-h) indexed EBSD patterns on c, d and e correspond to $Zr(Fe,Cr)_2$ ($P6_3/mmc$), UFe_2 ($Fd-3m$) and U_6Fe ($I4/mcm$) phases, respectively; (i-K) EDS spectra of respective phases showing their chemical composition.

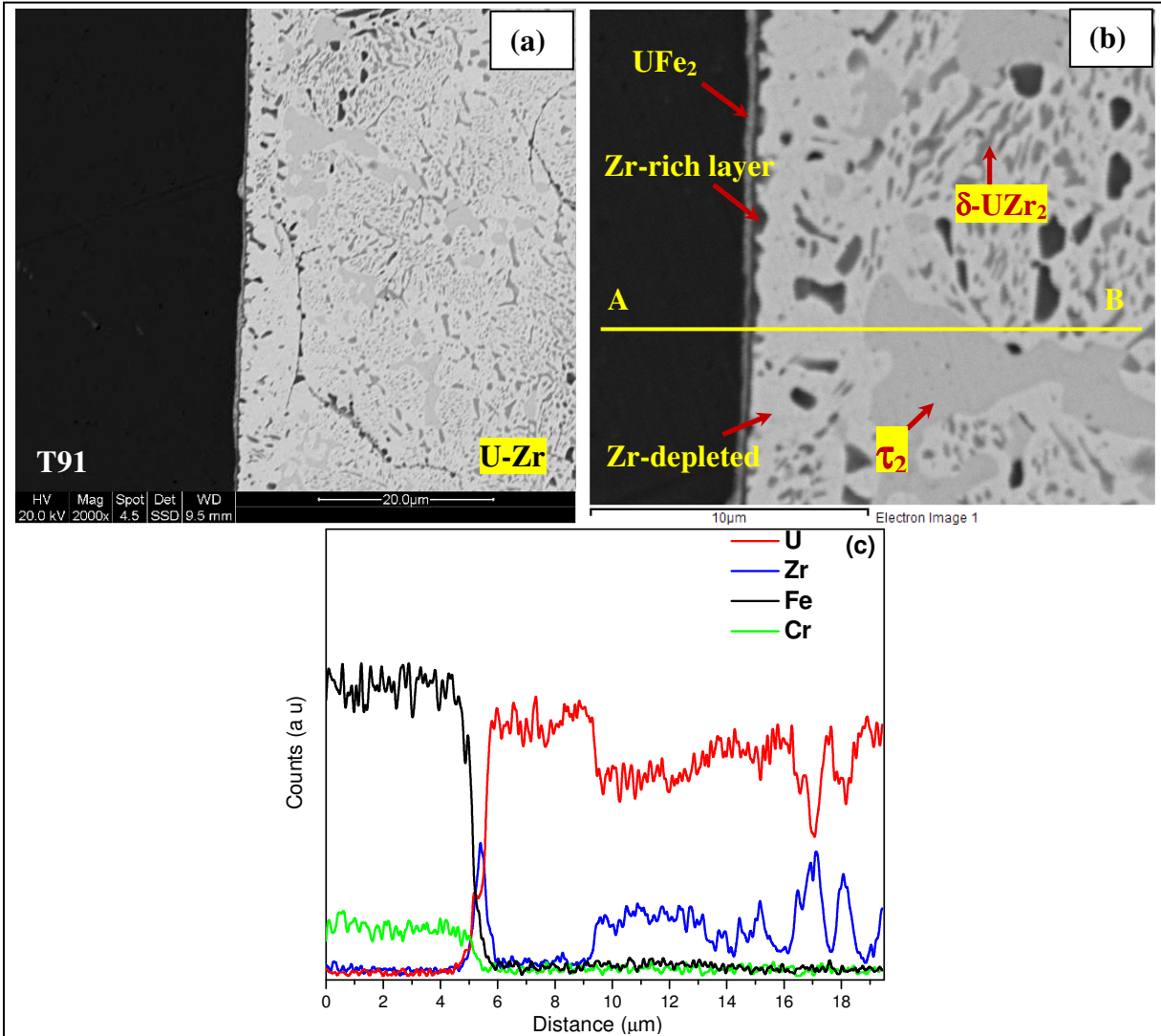


Fig. 6.8 (a & b) SEM micrographs of U–10Zr/T91 couple at 823 K for 1500 h, (c) intensity profiles of U-Mα, Zr-Lα, Fe-Kα and Cr-Kα X-ray lines along line AB marked in Fig. 6.8b

6.3.3.2. Interfacial reaction in U–10Zr/T91 couple at 923 K

The interdiffusion regions at the interface of U–10Zr/T91 couple after heating at 923 K for 1000 h are presented in Fig. 6.9(a-b) which reveal formation of similar types of UFe₂-type intermetallic, Zr-rich layer, and Zr-depleted layer. The Zr-rich layer is not uniform throughout the interfacial region which results in formation of UFe₂-type layer of different thickness (Fig. 6.9a). Fig. 6.9c shows the intensity profiles of U-Mα, Zr-Lα, Fe-Kα, Cr-Kα X-ray lines recorded

along the line CD marked in Fig. 6.9a (with non-uniform Zr-rich layer). Similarly, Fig. 6.9d shows the intensity profiles along the line EF marked in Fig. 6.9b (with uniform Zr-rich layer). These results indicate that the Zr-rich layer plays a crucial role in the overall interdiffusion behaviour. The interfacial region with smaller thickness of Zr-rich layer resulted in formation of thicker UFe_2 -type layer. The combined thickness of these two layers was found to be $\sim 4.5 \mu\text{m}$. The non-uniform/thinner Zr-rich layer had approximately 81 at.% Zr, 10 at.% U, 8 at.% Fe and 1 at.% Cr and the uniform/thicker Zr-rich layer contained ~ 91 at.% Zr, 3 at.% U, 5 at.% Fe and 1 at.% Cr. The Zr depleted zone on the U–Zr alloy side had ~ 98 at.% U, 2 at.% Fe. The formation of intermetallic phase τ_2 (6 at.% Fe, 69 at.% U, 25 at.% Zr) was also observed in the Zr-depleted layer (Fig. 6.9a) and the extent of formation of τ_2 phase is reduced in Fig. 6.9b where the Zr-rich layer is uniform. The microstructure of U–10Zr alloy contains δ - UZr_2 phase in α -U matrix and the δ -phase precipitates are much larger in size when compared with the couple heated at 823 K.

The microstructural investigations revealed that the width of UFe_2 -type layer is close to the depth of X-ray production from interaction volume of electron and therefore, it may not be accurate to assign that phase based on the EDS elemental analysis. The interdiffusion layer was further characterized using electron back scattered diffraction (EBSD) technique. It may be noted here that the information depth of EBSD is of several tenths of nm, depending upon the material's atomic number and density [119]. The diffraction volume in EBSD is significantly smaller than the width of the interdiffusion layer and hence the layer can be characterized using EBSD. Fig. 6.10a shows the electron forescatter image of the diffusion couple annealed at 923 K for 1000 h. The EBSD patterns (Kikuchi patterns) were acquired from the different points across the interface in point mode analysis and then matched with the crystal structure of the probable phases of interest (e.g., UFe_2 , U_6Fe , ZrFe_2 , Zr, Fe etc.). The experimental and indexed EBSD

patterns of interdiffusion layers (Fig. 6.10(b-g)) revealed that the Zr-rich layer is α -Zr phase (space group $P6_3/mmc$) and the thin diffusion layer corresponds to UFe_2 -type phase ($Fd-3m$). The Kikuchi pattern on the T91 steel is indexed with bcc Fe ($Im-3m$). All these indexing were carried out with a mean angle deviation (from the ideal Euler Angle) less than 0.5. The combined EDS and EBSD results confirmed that the crystal structure of thin interface layer is of cubic UFe_2 -type with Zr and Cr present as solute.

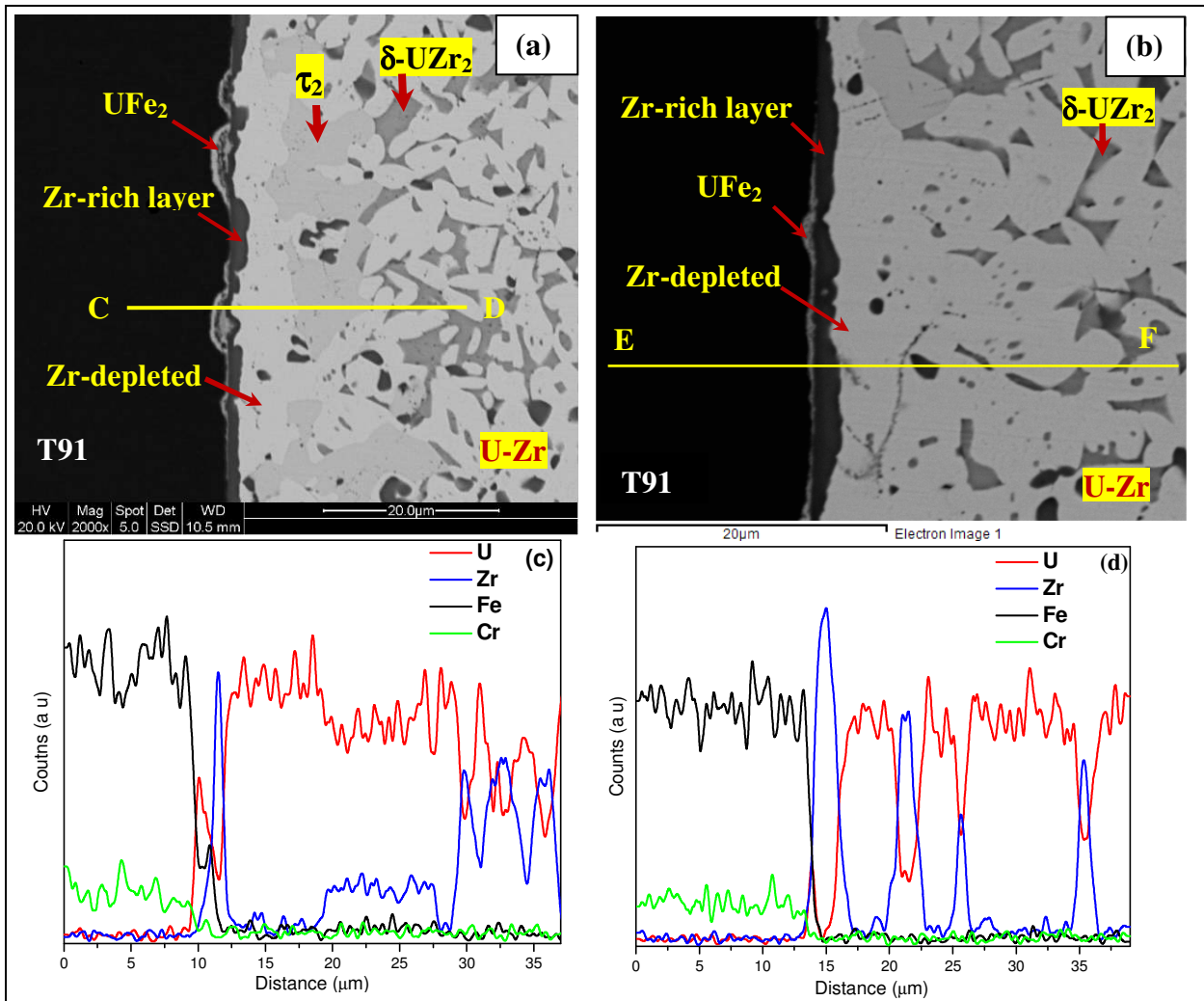


Fig. 6.9 (a & b) SEM image of U-10Zr/T91 couple at 923 K for 1000 h, (c & d) intensity profiles of U-M α , Zr-L α , Fe-K α and Cr-K α X-ray lines along line CD and EF marked in Fig. 6.9a and Fig. 6.9b, respectively.

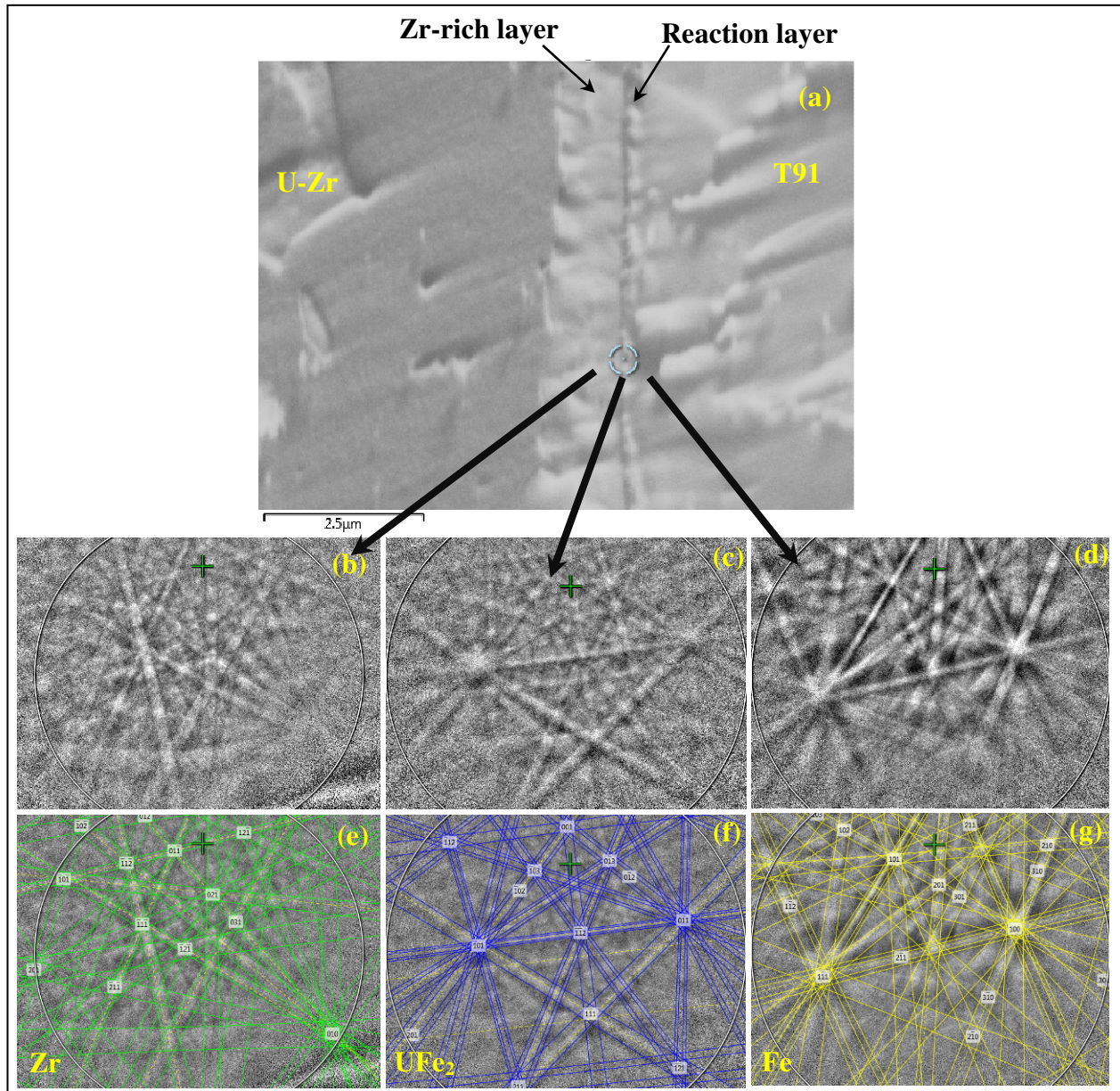


Fig. 6.10(a) The electron forescatter image of the diffusion couple annealed at 923 K for 1000 h; (b-d) the experimental EBSD patterns of different layers as indicated by arrows; (e-g) the indexed EBSD patterns on b, c and d correspond to Zr ($P6_3/mmc$), UFe_2 -type phase ($Fd-3m$) and Fe ($Im-3m$), respectively.

6.3.3.3. Interfacial reaction in U–10Zr/T91 couple at 973 K

The microstructures and intensity profiles of U-M α , Zr-L α , Fe-K α , Cr-K α X-ray lines of the U–10Zr/T91 diffusion couple heated at 973 K for 500 h are presented in Fig. 6.11(a-c). The scheme of the microstructure in the interdiffusion region was found to be similar to that of the couples annealed at 823 and 923 K. However, the Zr-rich layer formed at 973 K is wider and uniform and as a result of that a thin reaction layer of UFe₂-type was formed at the interface.

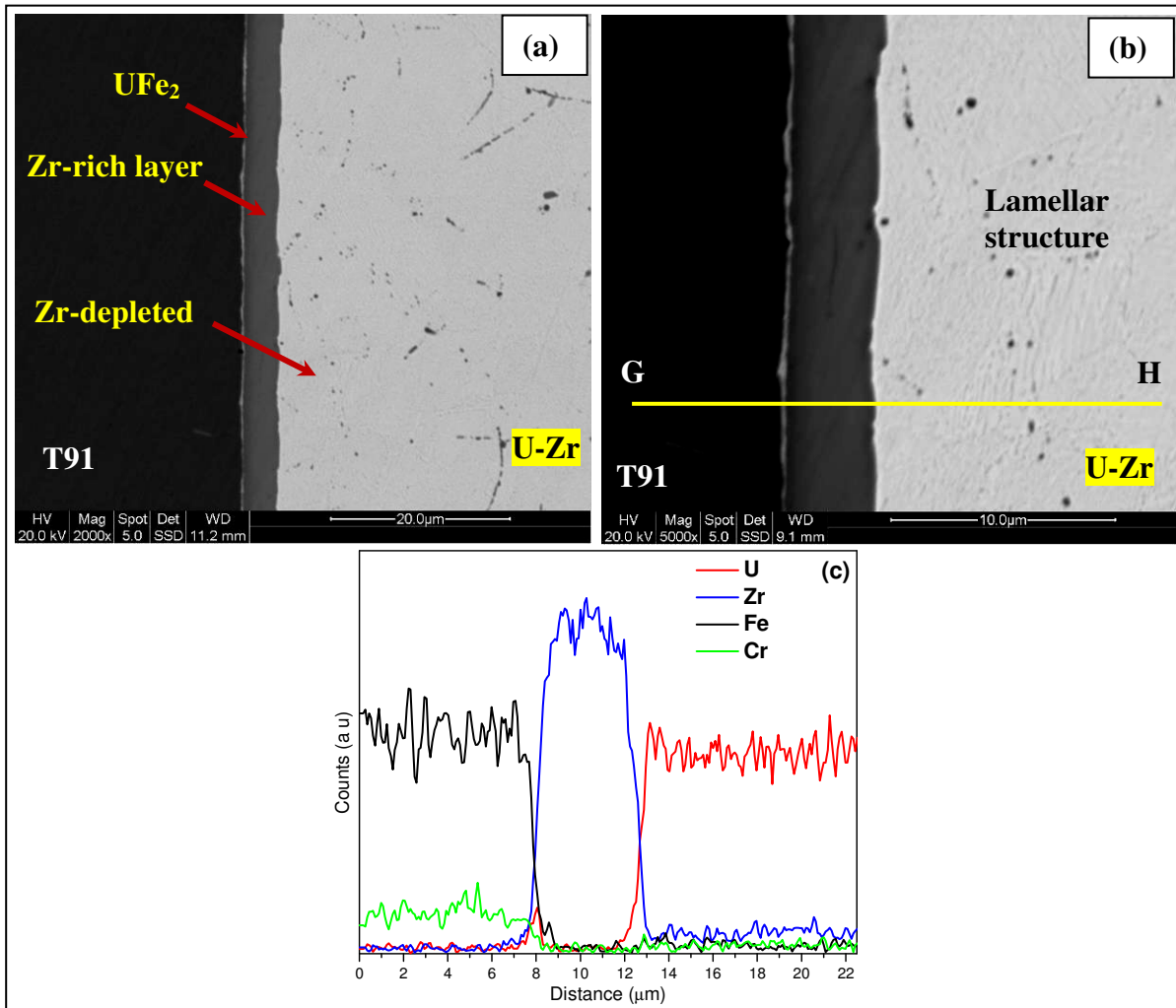


Fig. 6.11 (a & b) SEM images of U–10Zr/T91 diffusion couple annealed at 973 K for 500 h, (c) intensity profiles of U-M α , Zr-L α , Fe-K α and Cr-K α X-ray lines along the line GH marked in Fig. 6.11b.

The Zr-rich layer (containing 97 at.% Zr, 2 at.% Fe, 1 at.% U) acts as a strong barrier layer for the interdiffusion between Fe/Cr and U. It seems that the width of the UFe_2 reaction layer is strongly dependent on the Zr-rich layer. The combined width of the two layers is found to be ~ 6 μm . The Zr-depleted layer formed on the U–Zr alloy side has no sharp boundary and Zr concentration in this layer is gradually increasing towards the bulk U–Zr alloy. In this case, the formation of any U–Zr–Fe intermetallic compound on the U–Zr alloy side was not observed. Rather, a lamellar type microstructure was found to be formed in the U–Zr alloy (Fig. 6.11b). The liquid phase formation at the interface was not evident in the microstructure.

6.3.3.4. Interfacial reaction in U–10Zr/T91 couple at 1003 K

Two types of interfacial reaction zone were formed at the interface of the U–10Zr/T91 diffusion couple heated at 1003 K for 200 h. These can be described as (a) interface with stable Zr-rich layer and (b) interface with broken Zr-rich layer.

(a) Interface with stable Zr-rich layer

The microstructure and intensity profiles of U- $M\alpha$, Zr- $L\alpha$, Fe- $K\alpha$, Cr- $K\alpha$ X-ray lines of this interface are shown in Fig. 6.12(a-c). The interfacial region revealed the formation of UFe_2 -type, Zr-rich and Zr-depleted layers similar to other couples. In the Zr-rich layer, a variation in Zr-concentration across its width was observed. Here, the combined thickness of the UFe_2 , Zr-rich layers is ~ 4 μm .

(b) Interface with broken Zr-rich layer

The microstructure and elemental intensity profiles of the interface are shown in Fig. 6.13(a-c). In few places of the interfacial region, the Zr-rich layer was found to be broken and rounded/curved shape of reaction layer with larger depth of penetration of the constituent elements was observed (Fig. 6.13a). A magnified view of the region is shown in Fig. 6.13b.

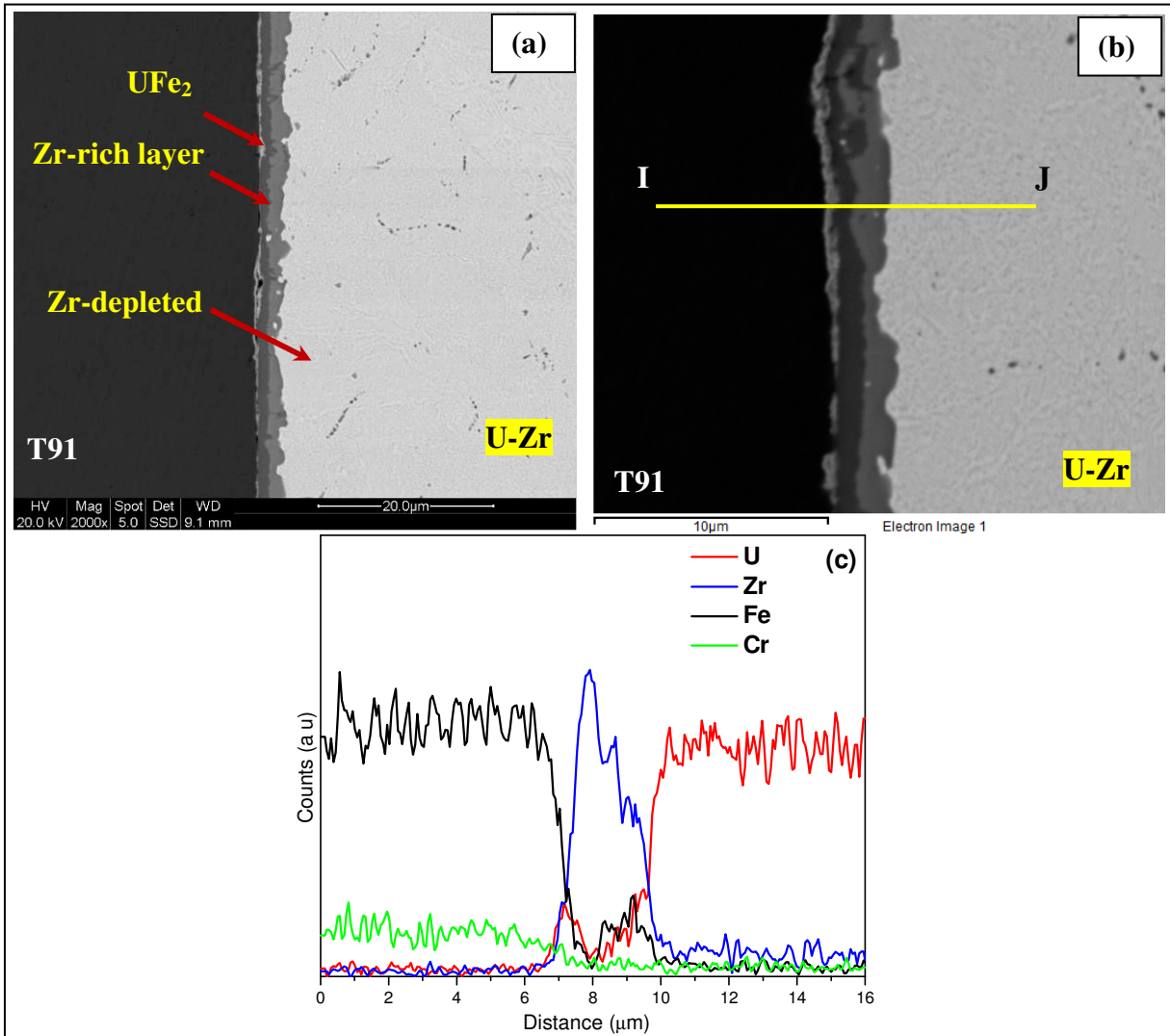


Fig. 6.12 (a & b) SEM images of U–10Zr/T91 couple annealed at 1003 K for 200 h, showing the interface with stable Zr-rich layer, (c) intensity profiles of U-M α , Zr-L α , Fe-K α and Cr-K α X-ray lines along the line IJ marked in Fig. 6.12b.

The accelerated rate of diffusion is due to the formation of liquid phase in those interfacial regions. It appears from the microstructure in Fig.6.13a that solidification of the liquid phase during cooling leads to formation of porous layer.

The interdiffusion region contains number of reaction layers namely (Fig. 6.13b):

(I) U-rich layer (80 at.% U, 17 at.% Fe, 3 at.% Cr) with few black precipitates (69 at.% Fe, 18 at.% Cr, 1 at.% Mo and 12 at.% U) which are relatively rich in Cr (on the T91 side), (II) UFe_2 layer with few tiny bright spots of U_6Fe phase, (III) Zr-rich layer (87 at.% Zr, 9 at.% U, 3 at.% Fe, 1 at.% Cr), (IV) a reaction layer containing U-rich (80 at.% U, 18 at.% Zr, 2 at.% Fe) and Zr-rich (78 at.% Zr, 20 at.% U, 2 at.% Fe) layers, and (V) Zr-depleted layer on the U-Zr alloy side.

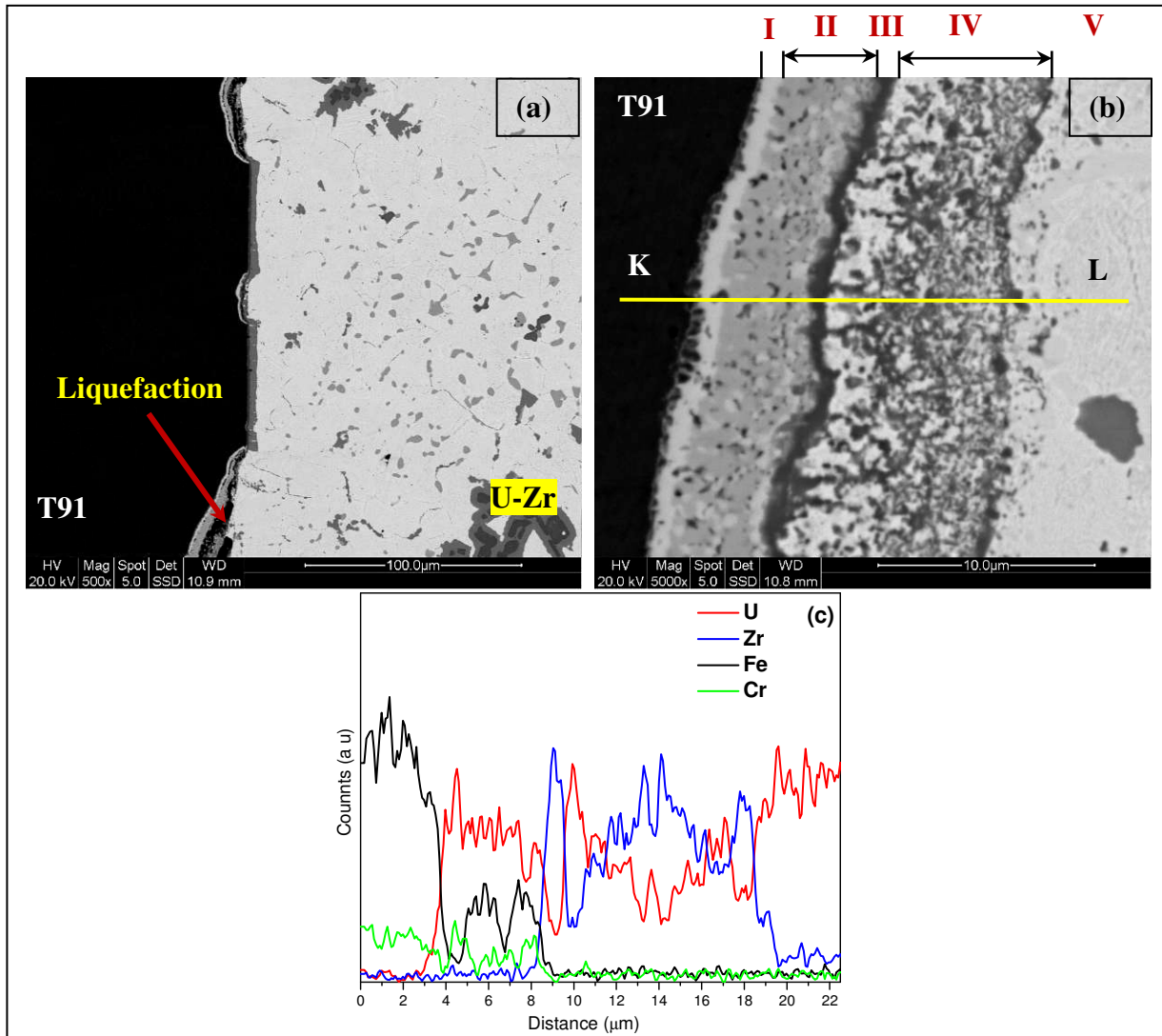


Fig. 6.13 (a) SEM images of U-10Zr/T91 diffusion couple at 1003 K for 200 h, showing the interface with broken Zr-rich layer, (b) magnified image marked with different reaction layers, (c) X-ray line profiles of U, Zr, Fe and Cr along the line KL marked in Fig. 6.13b.

6.4. Discussion:

The purpose of this study is to investigate the chemical compatibility between U–Zr based fuel and T91 cladding for fast breeder reactor. The chemical compatibility between metallic fuel and steel cladding is of major concern as the interdiffusion between fuel and cladding components may result in the formation of relatively low-melting-point compositions. In this background, the results of the present study are discussed below.

6.4.1. Differential thermal analysis

The chemical interaction between U-based metallic fuel and T91 steel cladding could be best evaluated with the help of U–Fe phase diagram. In U–Fe system (Fig. 6.14) [120], there are two intermetallic compounds i.e., U_6Fe which is formed via a peritectic reaction at 1083 K (i.e., $L + (\gamma U) \rightarrow U_6Fe$) and UFe_2 which melts congruently at 1503 K. U_6Fe exhibits a body centered tetragonal structure (space group I4/mcm) while UFe_2 has a cubic Laves structure (Fd-3m). The U–Fe system is comprised of two eutectics i.e., $L \rightarrow UFe_2 + U_6Fe$ at 998 K and $L \rightarrow (\gamma Fe) + UFe_2$ at 1353 K; having eutectic compositions of U–10.2wt%Fe and U–52wt%Fe, respectively.

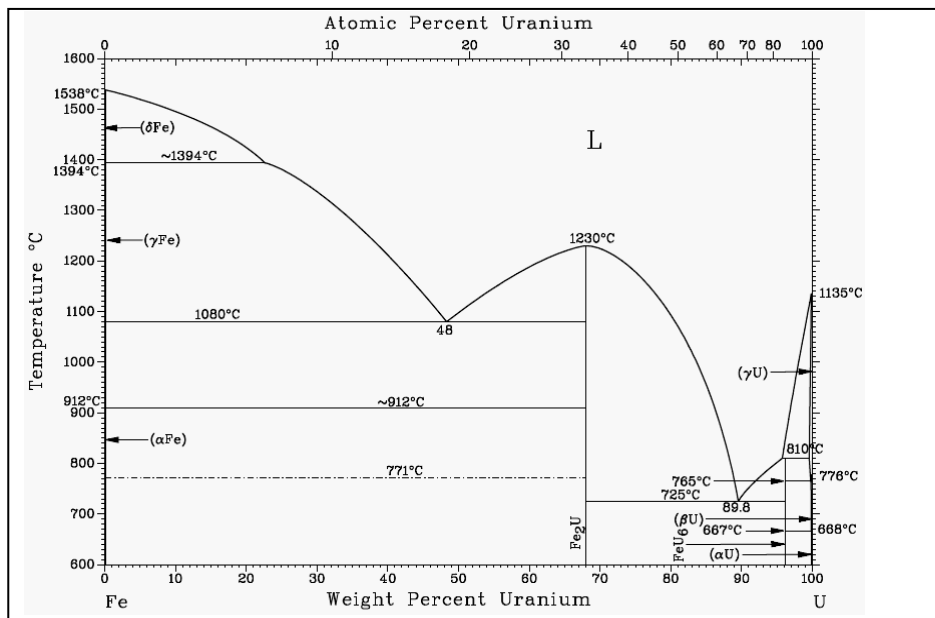


Fig. 6.14 Phase diagram of U–Fe system [120].

In the present study, the DTA experiments of U+T91 and U–10Zr+T91 composites were carried out by taking the fuel (U or U–10Zr) and cladding (T91) components in the mass ratio of around 5:1. This ratio was purposely chosen here in order to focus the uranium rich part of the system, since the U-rich part of U–Fe system exhibits a eutectic reaction only at 998 K. The eutectic liquefaction temperature between fuel and cladding is considered as very critical data for reactor safety. Hence, DTA experiments with U-rich U+T91 and U–10Zr+T91 composites may give an important/useful output on the chemical interaction behaviour between U–Zr and T91. In the first heating cycle, DTA thermogram of U+T91 composite comprises of transformation peaks of both U and T91 and an intense exothermic peak at 1383 K. The exothermic peak is attributed to strong chemical reaction between two. The U–T91 system can be considered here as pseudo binary system by comparing them with binary U–Fe system. The chemical interaction between U and T91 may lead to the formation of UFe_2 and/or U_6Fe types of intermetallics. The Gibbs free energies of formation (ΔG_f°) of the UFe_2 and U_6Fe intermetallics have been reported by Gardie et al. [121]. According to them, the ΔG_f° (UFe_2) data are $-54.1 \text{ kJ mol}^{-1}$ at 998 K and $-52.8 \text{ kJ mol}^{-1}$ at 1500 K, whereas the ΔG_f° (U_6Fe) values are $-31.3 \text{ kJ mol}^{-1}$ at 998 K and $-28.5 \text{ kJ mol}^{-1}$ at 1068 K. These above data indicate that the formation of UFe_2 is thermodynamically more favourable as compared to U_6Fe in the temperature range of our interest. Hence, the intense exothermic peak of U+T91 composite at 1383 K may be attributed to the formation of UFe_2 -type compound. The exothermic peak appeared just below the melting temperature of uranium. After the melting of unreacted uranium, the heating of the composite sample was continued up to 1473 K where the whole sample got converted to liquid phase. In the repeat heating run, the first peak appeared at 995 K and the second peak ($\sim 1314 \text{ K}$) was not sharp (Fig. 6.4b). All the peaks corresponding to pure U and T91 disappeared in the repeat run. By comparing with the reference phase diagram of

U–Fe system [120], it can be concluded that the peak at ~1314 K represents the liquidus temperature and the other peak at 995 K represents the eutectic reaction (i.e., $L \leftrightarrow \text{UFe}_2 + \text{U}_6\text{Fe}$). The above explanation is further supported by the microstructural investigation. The microstructure of U+T91 reaction product (Fig. 6.5(a-b)) comprises of large equiaxed grains of pro-eutectic UFe_2 phase and lamellar eutectic structure of UFe_2 and U_6Fe phases. The UFe_2 phase with soluble Cr can also be represented here as $\text{U}(\text{Fe},\text{Cr})_2$ as already mentioned earlier. The phase transformation sequences in the heating and cooling cycles of U+T91 composite are presented in Table. 6.3. Similarly, the DTA curve of U–10Zr+T91 composite (Fig. 6.4c) also shows the transformation peaks for both U–10Zr and T91 in the first heating cycle and in this case the exothermic reaction peak appeared at 1495 K is approximately 110 K higher than that of U+T91 composite. The intense exothermic peak is most likely due to the formation of UFe_2 -type compound. The higher reaction temperature is because of the higher solidus temperature of U–10Zr alloy than the melting temperature of uranium metal. The exothermic peak was followed by an endothermic melting of unreacted U–10Zr alloy at 1503 K. After that, the DTA curves repeatedly showed only two peaks (i.e., 995 K and 1384 K). The microstructure of the reaction product revealed three phases namely U_6Fe , $\text{UFe}_2/\text{U}(\text{Fe},\text{Cr})_2$ and $\text{Zr}(\text{Fe},\text{Cr})_2$. The DTA run was carried out by taking U–10Zr and T91 in the ratio of 5:1, therefore, the resultant U–10Zr+T91 composite sample contained approximately 75wt%U, 8wt%Zr and 17wt%Fe (where the sum of concentrations of Fe, Cr, Mo etc. of the T91 steel is taken as one concentration variable). According to the reported ternary phase diagram of U–Zr–Fe system at 853 K [118], the equilibrium phases of U–Zr–Fe alloy of the above composition are U_6Fe , UFe_2 and ZrFe_2 which are similar to the phases formed in the present study. By combining all the finding, it can be concluded here that the peak at 995 K corresponds to the liquefaction temperature of the eutectic

type reaction and the peak at 1384 K represents the liquidus temperature. The details of all the reactions are shown in Table 6.3. Nakamura et al. [122] investigated the equilibrium phase relations in the U–Zr–Fe ternary alloys using DTA and electron probe microanalysis. According to their study, U–7.6Zr–16.3Fe alloy followed the phase transformations of $U_6Fe + UFe_2 + ZrFe_2 \rightarrow ZrFe_2 + L \rightarrow L$ at 995 and 1273 K, respectively. This alloy composition is similar to that of our sample and therefore, followed the phase transformation sequences which are consistent with the present results. They also reported the minimum temperature at which the liquid phase appeared i.e., the liquefaction temperature of around 994–995 K which is found to be almost identical to the eutectic reaction temperature of present study. Kutty et al. [87] also studied the chemical interaction behaviour of metal fuels such as U, U–Zr alloy with T91 steel using DTA and DSC and observed similar type of exothermic reactions before actual melting.

Several important features of the fuel-cladding chemical reaction between U-based fuel and T91 cladding have been revealed from the DTA results of the present investigation. The addition of Zr increases the temperature of the exothermic reaction between U-based fuel and T91 cladding. This could be due to the increase in solidus temperature which may indirectly affect the diffusivity. In fact, it was reported that the diffusivity decreases with addition of Zr in U–Zr alloy [87, 123]. However, the eutectic liquefaction temperature has not been altered with the addition of 10wt%Zr. Similarly, alloying elements of T91 grade steel i.e. Cr, Mo, V, Nb etc. have no remarkable effect on the eutectic temperature. In both the U-rich U+T91 and U–10Zr+T91 composites, the eutectic liquefaction temperatures are found to be identical (995 K) and the eutectic temperatures are in good agreement with the literature data. Hence, one can conclude here that the presence of Zr (~ 10wt%) in the fuel or Cr, Mo etc. in the cladding steels will not have much effect on eutectic reaction temperature of fuel-cladding interaction since the main

contributors to the fuel-cladding eutectic reaction are U of the U-based fuel and Fe of the cladding.

Table 6.3 Phase transformation sequences of U+T91 and U–10Zr+T91 composites samples.

Sample	Heating sequence	DTA peak temp (K)	Nature of peak	Origin of Peak
U+T91*	Heating cycle	941	Endothermic	$\alpha\text{-U} \rightarrow \beta\text{-U}$
		1015		Curie temperature (T91)
		1046		$\beta\text{-U} \rightarrow \gamma\text{-U}$
		1111		ferrite (α) \rightarrow austenite (γ) (T91)
		1383	Exothermic	Reaction peak for UFe_2 formation
		1387	Endothermic	Melting peak
	Cooling cycle	1313	Exothermic	Liquidus ($\text{L} \rightarrow \text{UFe}_2 + \text{L}$)
		988		$\text{UFe}_2 + \text{L} \rightarrow \text{UFe}_2 + \text{U}_6\text{Fe}$
U+T91* (Repeat)	Heating cycle	995	Endothermic	$\text{UFe}_2 + \text{U}_6\text{Fe} \rightarrow \text{UFe}_2 + \text{L}$
		~1314 (not sharp)		$\text{UFe}_2 + \text{L} \rightarrow \text{L}$
	Cooling cycle	1314	Exothermic	Liquidus ($\text{L} \rightarrow \text{UFe}_2 + \text{L}$)
		988		$\text{UFe}_2 + \text{L} \rightarrow \text{UFe}_2 + \text{U}_6\text{Fe}$
U–10Zr+T91**	Heating cycle	861	Endothermic	$\alpha + \delta \rightarrow \alpha + \gamma_2$ (U–10Zr)
		958		$\alpha + \gamma_2 \rightarrow \gamma$ (U–10Zr) (i.e., $\alpha + \gamma_2 \rightarrow \beta + \gamma_2 \rightarrow \gamma_1 + \gamma_2 \rightarrow \gamma$)
		1015		Curie temperature (T91)
		1111		Ferrite (α) \rightarrow austenite (γ) (T91)
		1495	Exothermic	Reaction peak for UFe_2 formation
		1503	Endothermic	Melting peak
	Cooling cycle	1383	Exothermic	Liquidus ($\text{L} \rightarrow \text{Zr}(\text{Fe,Cr})_2 + \text{L}$)
		978	Exothermic	$\text{L} + \text{Zr}(\text{Fe,Cr})_2 \rightarrow \text{UFe}_2 + \text{U}_6\text{Fe} + \text{Zr}(\text{Fe,Cr})_2$
U–10Zr+T91** (Repeat)	Heating cycle	995	Endothermic	$\text{UFe}_2 + \text{U}_6\text{Fe} + \text{Zr}(\text{Fe,Cr})_2 \rightarrow \text{L} + \text{Zr}(\text{Fe,Cr})_2$
		~1384 (not sharp)		$\text{L} + \text{Zr}(\text{Fe,Cr})_2 \rightarrow \text{L}$
	Cooling cycle	1384	Exothermic	Liquidus ($\text{L} \rightarrow \text{Zr}(\text{Fe,Cr})_2 + \text{L}$)
		978		$\text{L} + \text{Zr}(\text{Fe,Cr})_2 \rightarrow \text{UFe}_2 + \text{U}_6\text{Fe} + \text{Zr}(\text{Fe,Cr})_2$

* For U+T91: UFe_2 phase contains soluble Cr,

** For U–10Zr+T91: UFe_2 phase contains soluble Zr and Cr; $\text{Zr}(\text{Fe,Cr})_2$ contains soluble U

6.4.2. Interfacial reactions in U–10Zr/T91 couples

Based on the feedback from the DTA results, the isothermal diffusion couple experiments between U–10Zr and T91 were carried out in the temperature range of 823–1003 K which covers both normal and accidental scenarios. The temperature and time schedules were chosen in such a way so that there is a measurable amount of diffusion after reasonable length of time. The extensive studies will provide useful output on chemical compatibility at reactor operating condition as well as in the transient accidental situation.

The results of diffusion couple tests indicated that the interdiffusion between U–10Zr alloy and T91 leads to formation of three layers namely UFe_2 -type intermetallic, Zr-rich layer and Zr-depleted layer at the interface. Similar type of interdiffusion layers at the interface of diffusion couple between U–19Pu–10Zr alloy fuel and HT9 ferritic steel cladding at 973 K was also reported earlier by Hofman and Walters [8]. According to them, a Zr-rich layer containing interstitial nitrogen is first formed at the interface of U–19Pu–10Zr and HT9. Then U and Pu of the fuel diffuse through the Zr-rich layer and interact with the cladding components resulting in formation of U_6Fe and UFe_2 type phases in a single zone on the cladding side of the Zr-rich layer. Keiser and Dayananda [91] reported that the interdiffusion between U–10Zr alloy and HT9 steel at 973 K resulted in formation of similar type of reaction layers i.e., $\text{U}(\text{Fe},\text{Cr})_2$, Zr-rich phases at the interface. The diffusion behaviour of U–10Zr alloy and HT9 steel was also studied by Lee et al. at 973 and 1003 K [93]. According to them, the $\delta\text{-UZr}_2$ phases in the vicinity of the interface would decompose into U and Zr in the first step. The U in the matrix would interact with cladding components and form $(\text{U},\text{Zr})(\text{Fe},\text{Cr})_2$ phase. At the same time, the decomposed Zr is saturated to form a Zr-rich layer which acts as an interdiffusion barrier layer. These studies

indicate that both the HT9 and T91 ferritic steels follow similar interdiffusion behaviour with U–Zr alloy.

All the results indicate that there is a propensity of Zr-segregation towards the interfacial region. The phenomenon of Zr-segregation plays a vital role in the overall interdiffusion mechanism. In a recent work, the segregation in the U–Zr solid solution and the interaction of cladding elements (Fe, Ni, Cr) with U–Zr fuel have been interpreted by atomistic simulations using the concepts of strain and chemical energy underlying the Bozzolo–Ferrante–Smith (BFS) method [124, 125]. The segregation in U–Zr solid solution is strongly dependent on lattice parameter, temperature, concentration of Zr and surface energy. According to Bozzolo et al. [124, 125], at low Zr concentration, ($0 < x_{\text{Zr}} < 22.45$ (at.%) (U–10 wt% Zr)), a slightly favorable Zr surface energy and small negative lattice deviation from their average value lead to enhanced Zr segregation to the surface as the low value of the bulk lattice parameter increases the BFS strain of Zr atoms. On the other hand, as the concentration of Zr increases the lattice parameter expands above average values, fast approaching bulk Zr values, thus reducing the BFS strain energy of Zr atom and U finds itself in a high BFS strain environment which favours U segregation to the surface. The enrichment of Zr at the surface of U–8.74Zr (U–20at.%Zr) alloy during vacuum annealing above 550 K has been reported by Paukov et al. [126]. As per their study, a Zr-depleted zone was formed just below the Zr-rich overlayer at surface. The Zr content in the Zr-rich surface layer of was $\sim 80\text{at}\%$ in the temperature range of 673–973 K. There may be even a tendency to have more Zr-rich material at the very surface, as the atomic diameter of Zr is larger than that of U [126].

In this context, an attempt has been made to explain the typical interdiffusional behaviour between U–10Zr and T91 steel by combining the reported and present observations. For low Zr

containing U–Zr alloy/U-rich U–Zr alloy, there is a tendency of Zr segregation towards the surface to minimize the lattice strain of Zr atoms as well as favorable Zr surface energy [124, 125]. The segregation of Zr toward the surface is further accelerated in the presence of interstitial impurity atom in the steel, since Zr has strong affinity towards the interstitial impurity atoms. The segregation of Zr towards the surface leads to the formation of Zr-rich layer at the interface. As a consequence of that, a Zr-depleted layer on the U–10Zr side was formed to maintain mass balance of Zr element. As the temperature increases from 823 to 973 K the diffusivity of Zr increases which may result in formation of very strong and thicker Zr-rich layer. It may be noted that the Zr-rich layer contained approximately 97 at.% Zr, 2 at.% Fe, 1 at.% U at 973 K and the EBSD analysis confirmed that the Zr-rich layer is α -Zr phase (space group $P6_3/mmc$). It acts as a diffusion barrier by reducing the penetration of Fe and Cr elements towards fuel lattice. The thickness of the interfacial Zr-rich layer at 823 and 923 K is not uniform and as a result, the penetration of Fe through it towards fuel lattice leads to the formation of low Fe-containing intermetallic phase τ_2 (6 at.% Fe, 67 at.% U, 27 at.% Zr) on the U–Zr side. The absence of τ_2 phase in the diffusion couple at 973 K is because of the thicker and uniform Zr-rich diffusion barrier layer. Due to strong interaction of U with Fe of T91 steel, U diffuses through the Zr rich layer and comes in contact with Fe of the steel. This results in formation of an UFe_2 -type layer on the T91 side. The thickness of UFe_2 layer gradually decreases as the thickness of Zr-rich layer increases with temperature. Another important aspect is that any notable interaction between Zr-rich layer and T91 has not been revealed even though there are many intermetallic compounds, viz. $ZrFe_2$, Zr_2Fe and Zr_3Fe in the Zr–Fe system [127]. The unusual nature demonstrates the sluggish nature of diffusion reaction between Zr and Fe. The diffusion reaction experiments by

Bhanumurthy et al. [128] also showed that none of these compounds formed at the Zr/Fe interface up to 1073 K.

When the annealing temperature was increased from 973 to 1003 K, the Zr-rich layer could not effectively prevent the interdiffusion. In some interfacial region, the Zr-rich layer was broken and the interaction between U and Fe leads to the formation liquid phase. The annealing temperature (1003 K) is slightly above the liquefaction temperature (i.e., 995 K) of U–10Zr+T91 composite. This particular temperature (i.e., 1003 K) was purposely chosen to investigate whether the Zr-rich layer is able to prevent the liquefaction or not. This result indicates that in any case, if the temperature at fuel-cladding interface reaches above the eutectic liquefaction temperature, the direct contact of U–10Zr and T91 cladding would cause eutectic melting in spite of the formation of Zr-rich layer.

Several important features have been revealed from the diffusion couple experiment of the present study. The Zr plays most crucial role in the interdiffusion between U–Zr alloy and T91 steel. There are few direct and indirect effects of Zr-enrichment at the interface. The Zr-enrichment leads to the formation of Zr-depleted region on U–Zr alloy. Since Zr increases the solidus temperature of U–Zr alloy, it is expected that the Zr-depletion may reduce the solidus temperature at the Zr-depleted region. At the same time, the thermal conductivity at the Zr-depleted layer may be improved. In fact, these effects will be further complicated during actual reactor operation in presence of other fission products. Based on the diffusion couple results, it can be concluded that the compatibility of U–Zr alloy and T91 steel cladding seems to be good at reactor operating temperature because of formation of Zr-rich barrier layer at the interface. However, at any accidental condition if the fuel-cladding interfacial temperature reaches above

the eutectic liquefaction temperature (995 K), the U–Zr fuel will no longer remain compatible with T91 cladding due to liquid phase formation.

It may be noted here that Ryu et al. [94, 95] reported that the interdiffusion between U–10Zr alloy and ferritic martensitic steels (FMS) was inhibited effectively by the presence of thin Zr-foil (~20-30 μm) or thin Zr-layer (~6 μm) even above the eutectic melting temperature of U–Zr alloys and FMS. Eutectic melting between was not observed in the diffusion couples even after annealing at 1073 K for 25 h. The diffusion couple experiment between U and T91 steel with a Zr foil of thickness ~200 μm between them was also carried out by Kaity et al. [16]. The chemical compatibility between U and T91 is significantly improved by Zr liner and liquefaction due the eutectic reaction was not observed even at 1023 K. These are the important observations in support of the concept of using Zr foil as a diffusion barrier between fuel and cladding.

6.4.2.1. Kinetics of the interfacial reaction

In this study, an attempt has been made to calculate the growth kinetics of reaction layers based on total thickness of UFe_2 -type and Zr-rich layers. Here, the combined thickness of the two layers is considered as width of reaction layer. The measured widths of reaction layers (i.e., UFe_2 + Zr-rich layers) are found to be 1.5, 4.5 and 6.0 μm at 823, 923 and 973 K, respectively. It may be noted here that the Zr-depleted layer is not taken into consideration here as it has no sharp boundary and there is a gradient of Zr concentration in this layer as a consequence of Zr segregation towards the interface.

The growth of the reaction layers at the interface of diffusion couples are generally diffusion controlled and hence follow a parabolic relationship [90, 129]. The growth of the reaction layer at the interface can therefore be expressed as [130]:

$$w^2 = kt \quad (6.1)$$

where, w is width of the reaction layer, t is time of the reaction, k is diffusion controlled rate constant. The rate constant k can be written as:

$$k = k_0 \exp (-Q_k/RT) \quad (6.2)$$

where, k_0 is the pre-exponential factor, Q_k is the activation energy for growth, R is the universal gas constant and T is the temperature in absolute scale.

Combining Eqn (1) and (2), $w^2/t = k_0 \exp (-Q_k/RT)$ (6.3)

The pre-exponential factor k_0 can be calculated from the intercept of $\log (w^2/t)$ versus $1/T$ plot. The activation energy Q can be determined from the slope of the plot. The plot of $\log (w/t^{1/2})$ versus $1/T$ is shown in Fig. 6.15. The pre-exponential factor k_0 was found to be $2.698 \times 10^{-8} \text{ m}^2 \text{ s}^{-1}$ and the activation energy Q was found to be 170 kJ mole^{-1} . Hence, the growth of the interdiffusion layers at the interface can be expressed as:

$$w^2 = 2.698 \times 10^{-8} t \exp (-170 \text{ kJ mol}^{-1}/RT) \quad (823 \leq T/K \leq 973) \quad (6.4)$$

Park et al. [90] studied the diffusional interaction between U–10Zr and Fe in the temperature range of 903–953 K and found that the interdiffusion zone had various intermetallic phases with the activation energy of $296.6 \text{ kJ mol}^{-1}$ for the entire diffusion zone. Huang et al. [131] reported the growth rate constants and the activation energies for U/Fe, U/Fe–15Cr and U/Fe–15Cr–15Ni (wt%) diffusion couples where the interdiffusion zone had two reaction layers of U_6Fe and UFe_2 intermetallic phases. According to them, the activation energy for total interdiffusion zone (i.e., $\text{U}_6\text{Fe} + \text{UFe}_2$ layers) of U/Fe, U/Fe–15Cr and U/Fe–15Cr–15Ni couple are 137, 231 and 135 kJ mol^{-1} , respectively. The activation energy of the present study is relatively closer to that of U/Fe, U/Fe–15Cr–15Ni and U/Fe–15Cr couples. However, the comparison of the activation energies of the present study with the above literature data may not suitable as the diffusion behaviour and interdiffusion layers formed between U–Zr and T91 is different from those reported couples. In

this context, it may be noted that the data on the diffusion kinetics between U–Zr and ferritic steel are limited in the literature. Based on the available literature and present studies, it was found that the diffusion couples between U–Zr alloy and ferritic steels (T91, HT9) contained fewer numbers of phases with smaller width at interdiffusion zone when compared to diffusion couples between U–Zr alloy and Fe, Fe–Cr, Fe–Ni, Fe–Ni–Cr, 316SS, D9.

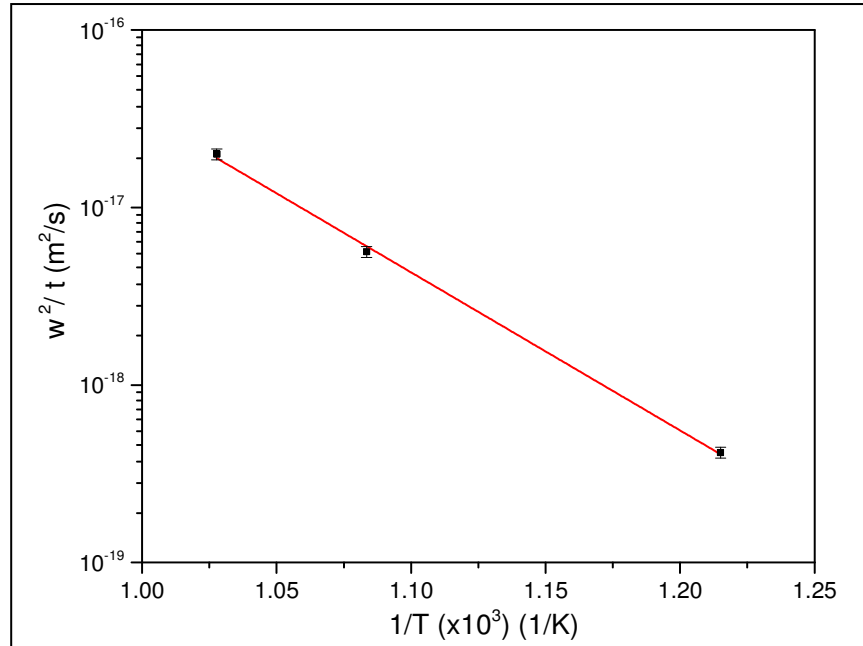


Fig. 6.15 Plot of w^2/t versus $1/T$ for the combined width of UFe_2 and Zr-rich reaction layers.

6.4.3. Interfacial reactions in U–6Zr/T91 couples

The interdiffusion reaction of our reference alloy composition of U–6Zr with T91 steel is expected to be similar to that of U–10Zr/T91 couple. In order to examine the chemical interaction between U–6Zr and T91, diffusion couple tests were carried out at two selective temperatures i.e., 973 K and 1023 K for time duration of 500 and 100 h, respectively. The above temperatures were purposely chosen here to check their diffusion interaction below and above the eutectic liquefaction temperature. Figs. 6.16(a-c) show the microstructures and intensity profiles of U-M α , Zr-L α , Fe-K α , Cr-K α X-ray lines of the U–6Zr/T91 diffusion couple annealed

at 973 K for 500 h. In this case, the interdiffusion region also revealed similar type of three distinct reaction zones i.e., UFe_2 -type, Zr-rich and Zr-depleted layers. The total width of the UFe_2 and Zr-rich layers is found to be approximately $4\ \mu\text{m}$. The Zr-rich layer had approximately 95 at.% Zr, 3 at.% U and 2 at.% Fe and the adjacent Zr-depleted zone had approximately 97 at.% U, 3 at.% Fe. Any evidence of the liquid phase formation due to eutectic melting was not observed at the interfacial region.

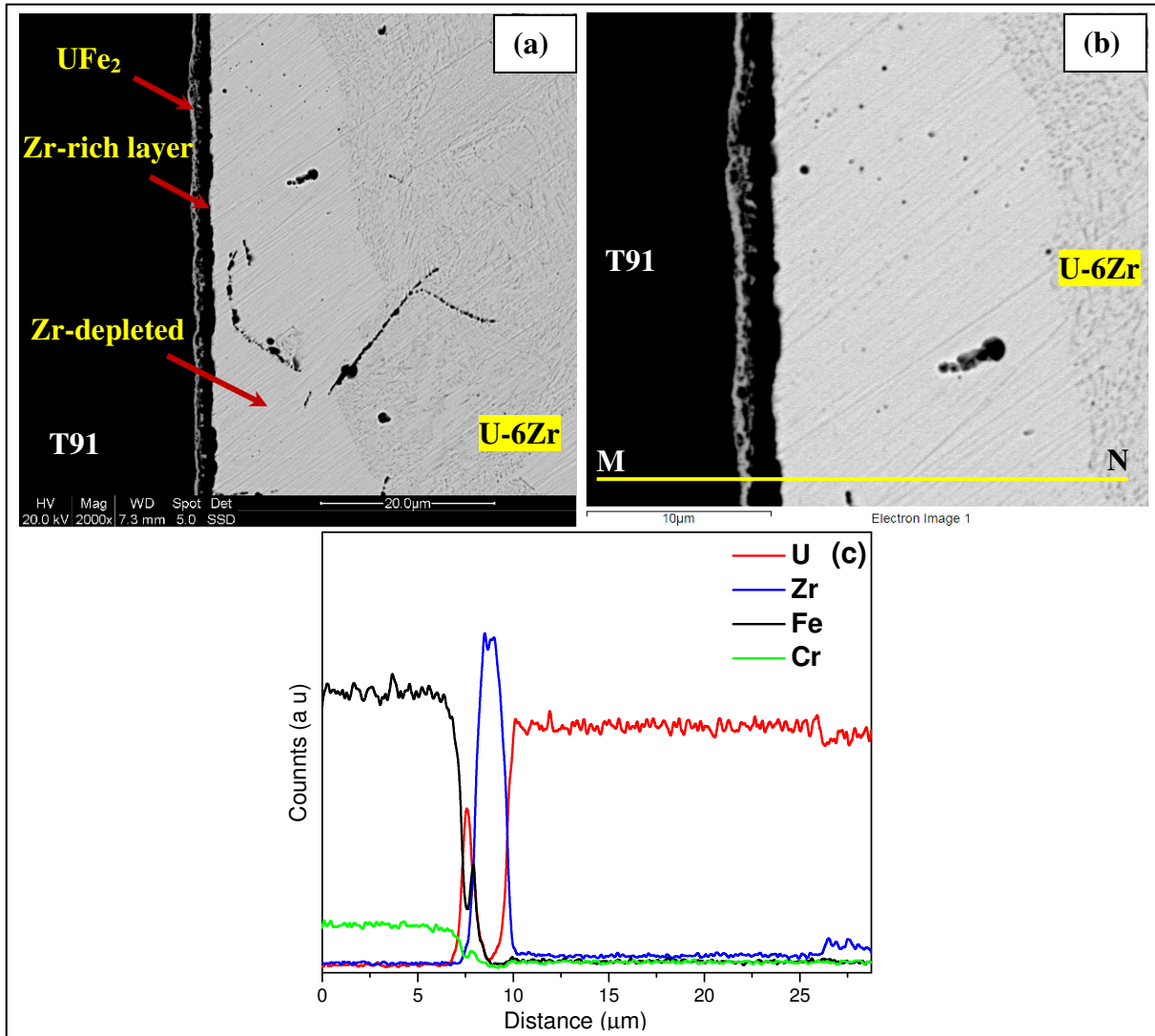


Fig. 6.16 (a & b) SEM image of U–6Zr/T91 diffusion couple at 973 K for 500 h, (c) intensity profiles of U- $\text{M}\alpha$, Zr- $\text{L}\alpha$, Fe- $\text{K}\alpha$ and Cr- $\text{K}\alpha$ X-ray lines along the line MN marked in Fig. 6.16b.

When the temperature was increased to 1023 K, almost complete melt down of the diffusion couple occurred only in 100 h and a eutectic-melted microstructures with various intermetallic i.e., U_6Fe , $U(Fe,Cr)_2$ and $Zr(Fe,Cr)_2$ were formed (Fig. 6.17). These results indicates that the diffusion interaction of U–6Zr alloy with T91 steel follow almost similar trend as found in case of U–10Zr alloy.

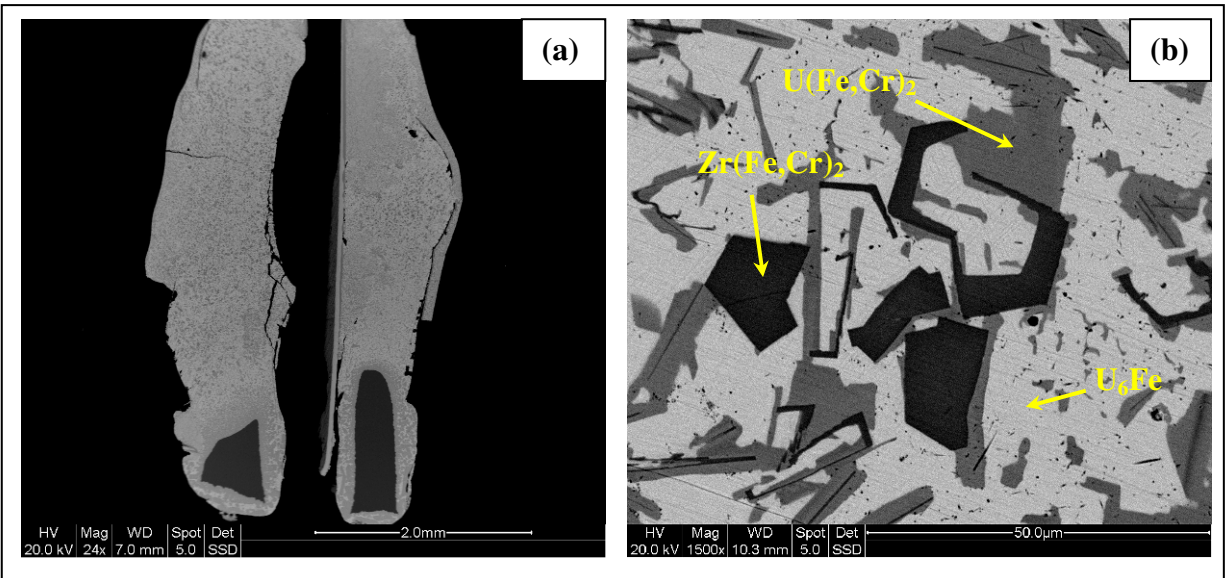


Fig.6.17 (a) Microstructure of U–6Zr/T91 diffusion couple annealed at 1023 K for 100 h showing almost complete meltdown of couple, (b) Magnified micrograph showing the formation of U_6Fe , $U(Fe,Cr)_2$ and $Zr(Fe,Cr)_2$ phases.

6.5. Summary and conclusions:

The present study provides useful output on the fuel-cladding chemical compatibility between U–Zr alloy fuels and T91 steel cladding. The following important observations could be made based on the results of this study:

- An intense exothermic reaction occurred between U/U–Zr alloy and T91 steel just below the melting/solidus temperature of U/U–Zr alloy which could be attributed to UFe_2 -type compound formation.
- The eutectic liquefaction temperatures between U/U–Zr alloy and T91 steel are found to be identical (i.e., 995 K). The microstructures of the reaction product comprise of U_6Fe , $\text{UFe}_2/\text{U}(\text{Fe},\text{Cr})_2$ and $\text{Zr}(\text{Fe},\text{Cr})_2$ intermetallic phases.
- The interdiffusion between U–Zr and T91 leads to formation of three distinct reaction zones at the interface: UFe_2 -type intermetallic, a Zr-rich layer and a Zr-depleted layer.
- The alloying element Zr in the fuel plays an important role in fuel-cladding chemical interaction through the formation of Zr-rich diffusion barrier layer at the interface.
- The growth kinetics of interfacial reaction zone was evaluated using the total width of UFe_2 and Zr-rich reaction layers at different temperatures and the activation energy Q was found to be 170 kJ mol^{-1} .
- The chemical compatibility of U–Zr alloy and T91 steel cladding seems to be good at reactor operating temperature due to the formation of Zr-rich barrier layer at the interface. However, at any accidental condition if the fuel-cladding interfacial temperature reaches above the eutectic liquefaction temperature (995 K), the U–Zr fuel will no longer be compatible with T91 cladding due to the formation of liquid phase.

References:

- [1] B. Raj, H. Kamath, R. Natarajan, P.V. Rao, A perspective on fast reactor fuel cycle in India, *Prog. Nucl. Energy* 47 (2005) 369-379.
- [2] B. Raj, History and Evolution of Fast Breeder Reactor Design in India—a Saga of Challenges and Successes, *IGC Newsletter* 69 (2006) 1-7.
- [3] K.S. Kumar, A. Babu, B. Anandapadmanaban, G. Srinivasan, Twenty five years of operating experience with the fast breeder test reactor, *Energy Procedia* 7 (2011) 323-332.
- [4] P. Tsvetkov, A. Waltar, D. Todd, Sustainable Development of Nuclear Energy and the Role of Fast Spectrum Reactors, *Fast Spectrum Reactors*, Springer 2012, pp. 3-22.
- [5] J. Kittel, B. Frost, J. Mustelier, K. Bagley, G. Crittenden, J. Van Dievoet, History of fast reactor fuel development, *J. Nucl. Mater.* 204 (1993) 1-13.
- [6] D.E. Burkes, R.S. Fielding, D.L. Porter, D.C. Crawford, M.K. Meyer, A US perspective on fast reactor fuel fabrication technology and experience part I: metal fuels and assembly design, *J. Nucl. Mater.* 389 (2009) 458-469.
- [7] D.C. Crawford, D.L. Porter, S.L. Hayes, Fuels for sodium-cooled fast reactors: US perspective, *J. Nucl. Mater.* 371 (2007) 202-231.
- [8] G.L. Hofman, L.C. Walters, Metallic fast reactor fuels, in: B.R.T. Frost (Ed.), Vol. 10A, *Nuclear Materials, Materials Science and Technology*, VCH Publishers Inc., New York, 1994, pp. 1–43.
- [9] C. Lahm, J. Koenig, R. Pahl, D. Porter, D. Crawford, Experience with advanced driver fuels in EBR-II, *J. Nucl. Mater.* 204 (1993) 119-123.
- [10] L. Walters, Thirty years of fuels and materials information from EBR-II, *J. Nucl. Mater.* 270 (1999) 39-48.
- [11] IAEA, Status and Trends of Nuclear Fuels Technology for Sodium Cooled Fast Reactors, International Atomic Energy Agency, 2011.

- [12] A. Sengupta, R. Bhagat, J. Banerjee, S. Kaity, K. Khan, R. Singh, H. Kamath, Development of Metallic Fuels for Indian Fast Breeder Reactor Programme, Fast Reactors and Related Fuel Cycles: Challenges and Opportunities (FR09). Proceedings of an International Conference, 2012.
- [13] K. Devan, A. Bachchan, A. Riyas, T. Sathiyasheela, P. Mohanakrishnan, S. Chetal, Physics design of experimental metal fuelled fast reactor cores for full scale demonstration, Nucl. Eng. Des. 241 (2011) 3058-3067.
- [14] H. Kamath, Recycle fuel fabrication for closed fuel cycle in India, Energy Procedia 7 (2011) 110-119.
- [15] S. Kaity, J. Banerjee, M.R. Nair, K. Ravi, S. Dash, T.R.G. Kutty, A. Kumar, R.P. Singh, Microstructural and thermophysical properties of U-6wt.% Zr alloy for fast reactor application, J. Nucl. Mater. 427 (2012) 1-11.
- [16] S. Kaity, T.R.G. Kutty, R. Agarwal, A. Laik, A. Kumar, Chemical compatibility of uranium based metallic fuels with T91 cladding, Nucl. Eng. Des. 250 (2012) 267-276.
- [17] IAEA-TECHDOC 1374, Development status of metallic, dispersion and non-oxide advanced and alternative fuels for power and research reactors, International Atomic Energy Agency (2003).
- [18] H.L. Yakel, Crystal structures of transition phases formed in U/16.60 at% Nb/5.64 at% Zr alloys, J. Nucl. Mater. 33 (1969) 286-295.
- [19] G.L. Hofman, M.K. Meyer, A.E. Ray, Design of high density gamma-phase uranium alloys for LEU dispersion fuel applications, Argonne National Lab., IL (US), October 18-23, 1998.
- [20] D.A. Lopes, T.A.G. Restivo, A.F. Padilha, Mechanical and thermal behaviour of U-Mo and U-Nb-Zr Alloys, J. Nucl. Mater. 440 (2013) 304-309.

- [21] D.E. Burkes, C.A. Papesch, A.P. Maddison, T. Hartmann, F.J. Rice, Thermo-physical properties of DU–10 wt.% Mo alloys, *J. Nucl. Mater.* 403 (2010) 160-166.
- [22] A. Dwight, M. Mueller, Constitution of the uranium-rich U-Nb and U-Nb-Zr systems, ANL-5581 Argonne National Lab., 1957, pp. 1-74.
- [23] R. Vandermeer, Phase transformations in a uranium+ 14 at.% niobium alloy, *Acta Metallurgica* 28(3) (1980) 383-393.
- [24] A. Vatulin, A. Morozov, V. Suprun, Y.I. Petrov, Y.I. Trifonov, High-density U-Mo fuel for research reactors, *Metal science and heat treatment* 46(11-12) (2004) 484-489.
- [25] S. Kaity, J. Banerjee, S.C. Parida, V. Bhasin, Structural, microstructural and thermal analysis of U–(6-x) Zr– xNb alloys (x= 0, 2, 4, 6), *J. Nucl. Mater.* 504 (2018) 234-250.
- [26] S. Kaity, J. Banerjee, S.C. Parida, P.G. Behere, V. Bhasin, Structural, microstructural and thermal analysis of U–(6-x) Zr– xMo alloys (x= 0, 2, 4, 6), *J. Nucl. Mater.* 532 (2020) 152046.
- [27] K. Ghoshal, S. Kaity, S. Mishra, A. Kumar, Microstructural investigation of uranium rich U–Zr–Nb ternary alloy system, *J. Nucl. Mater.* 446 (2014) 217-223.
- [28] C. Jacob, B. Warren, The crystalline structure of uranium, *Journal of the American Chemical Society* 59(12) (1937) 2588-2591.
- [29] H.L. Yakel, Review of x-ray diffraction studies in uranium alloys, Oak Ridge National Lab., Tenn.(USA), 1973.
- [30] C. Woolum, Fabrication and Characterization of Uranium-Molybdenum-Zirconium Alloys, Texas A&M University, 2014.
- [31] R. Sheldon, D. Peterson, The U-Zr (uranium-zirconium) system, *Bulletin of Alloy Phase Diagrams* 10(2) (1989) 165-171.
- [32] T.B. Massalski, H. Okamoto, P.R. Subramanian, L. Kacprzak, *Binary Alloy Phase Diagrams*, second ed., ASM International, Materials Park, Ohio, 1990.

- [33] J. Koike, M. Kassner, R. Tate, R. Rosen, The Nb-U (niobium-uranium) system, *Journal of phase equilibria* 19(3) (1998) 253-260.
- [34] X. Liu, Z. Li, J. Wang, C. Wang, Thermodynamic modeling of the U-Mn and U-Nb systems, *J. Nucl. Mater.* 380 (2008) 99-104.
- [35] G. Lagerberg, Phase transformations in a uranium-zirconium alloy containing 2 weight per cent zirconium, *J. Nucl. Mater.* 9 (1963) 261-276.
- [36] R.F. Hills, B.R. Butcher, B.W. Howlett, D. Stewart, The effect of cooling rate on the decomposition of the γ -phase in uranium-zirconium alloys, *J. Nucl. Mater.* 16 (1965) 25-38.
- [37] C. Basak, G. Prasad, H. Kamath, N. Prabhu, An evaluation of the properties of As-cast U-rich U-Zr alloys, *J. Alloys Compd.* 480 (2009) 857-862.
- [38] C.B. Basak, R. Keswani, G. Prasad, H. Kamath, N. Prabhu, Phase transformations in U-2 wt% Zr alloy, *J. Alloys Compd.* 471 (2009) 544-552.
- [39] C. Basak, R. Keswani, G. Prasad, H. Kamath, N. Prabhu, S. Banerjee, Investigation on the martensitic transformation and the associated intermediate phase in U-2 wt% Zr alloy, *J. Nucl. Mater.* 393 (2009) 146-152.
- [40] C.B. Basak, Microstructural evaluation of U-rich U-Zr alloys under near-equilibrium condition, *J. Nucl. Mater.* 416 (2011) 280-287.
- [41] S. Ahn, S. Irukuvarghula, S.M. McDeavitt, Thermophysical investigations of the uranium-zirconium alloy system, *J. Alloys Compd.* 611 (2014) 355-362.
- [42] A.K. Rai, R. Subramanian, R.N. Hajra, H. Tripathy, M. Rengachari, S. Saibaba, Calorimetric study of phase stability and phase transformation in U-xZr (x= 2, 5, 10 wt pct) alloys, *Metallurgical and Materials Transactions A* 46(11) (2015) 4986-5001.
- [43] J.T. McKeown, S. Irukuvarghula, S. Ahn, M.A. Wall, L.L. Hsiung, S. McDeavitt, P.E.A. Turchi, Coexistence of the α and δ phases in an as-cast uranium-rich U-Zr alloy, *J. Nucl. Mater.* 436 (2013) 100-104.

- [44] S. Irukuvarghula, S. Ahn, S. McDeavitt, Decomposition of the γ phase in as-cast and quenched U–Zr alloys, *J. Nucl. Mater.* 473 (2016) 206-217.
- [45] Y. Zhang, X. Wang, G. Zeng, H. Wang, J. Jia, L. Sheng, P. Zhang, Microstructural investigation of as-cast uranium rich U–Zr alloys, *J. Nucl. Mater.* 471 (2016) 59-64.
- [46] K. Tangri, D. Chaudhuri, Metastable phases in uranium alloys with high solute solubility in the BCC gamma phase. Part I—the system U–Nb, *J. Nucl. Mater.* 15 (1965) 278-287.
- [47] R. Field, D. Thoma, P. Dunn, D. Brown, C. Cady, Martensitic structures and deformation twinning in the U–Nb shape-memory alloys, *Philosophical Magazine A* 81(7) (2001) 1691-1724.
- [48] D. Brown, M. Bourke, M. Stout, P. Dunn, R. Field, D. Thoma, Uniaxial tensile deformation of uranium 6 wt pct niobium: a neutron diffraction study of deformation twinning, *Metallurgical and Materials Transactions A* 32(9) (2001) 2219-2228.
- [49] H.M. Volz, R.E. Hackenberg, A.M. Kelly, W. Hulst, A. Lawson, R. Field, D. Teter, D. Thoma, X-ray diffraction analyses of aged U–Nb alloys, *J. Alloys Compd.* 444 (2007) 217-225.
- [50] A. Kelly, R. Field, D. Thoma, Metallographic preparation techniques for U–6 wt.% Nb, *J. Nucl. Mater.* 429 (2012) 118-127.
- [51] D.W. Brown, M.A.M. Bourke, A.J. Clarke, R.D. Field, R.E. Hackenberg, W.L. Hulst, D.J. Thoma, The effect of low-temperature aging on the microstructure and deformation of uranium-6 wt% niobium: An in-situ neutron diffraction study, *J. Nucl. Mater.* 481 (2016) 164-175.
- [52] M. Karnowsky, R. Rohde, The transformation behavior of a U-16.4 at% Nb-5.6 at% Zr alloy, *J. Nucl. Mater.* 49 (1973) 81-90.
- [53] D.A. Lopes, T.A.G. Restivo, A.F. Padilha, Phase transformation studies in U–Nb–Zr alloy, *Nucl. Eng. Des.* 265 (2013) 619-624.

- [54] R.W.D. Pais, A.M.M. Dos Santos, F.S. Lameiras, W.B. Ferraz, Isothermal phase transformation of U-Zr-Nb alloys for advanced nuclear fuels, *Current Research in Nuclear Reactor Technology in Brazil and Worldwide* (2013) 55.
- [55] M. Masrukan, M.H. Al Hasa, J. Setiawan, S. Pribadi, Effect Of Nb Element Content In U-Zr Alloy On Hardness, Microstructure and Phase Formation, *Urania Jurnal Ilmiah Daur Bahan Bakar Nuklir* 21(2) (2015).
- [56] O. Ivanov, G. Bagrov, Isothermal cross sections of the triple system uranium-molybdenum-zirconium at 1000 C-625 C, *Struct. Alloys Certain Syst. Cont. Uranium Thorium* (1963) 131.
- [57] N. Eriksson, Phase Transformations and Microstructural Evolution in the U-10 wt.% Mo Alloy with Various Zr Additions at 900C and 650C, University of Central Florida Orlando, Florida, 2015.
- [58] R. Hills, B. Butcher, J. Heywood, A study of the effect of cooling rate on the decomposition of the γ -phase in uranium-low molybdenum alloys, *Journal of the Less Common Metals* 3(2) (1961) 155-169.
- [59] K. Tangri, G. Williams, Metastable phases in the uranium molybdenum system and their origin, *J. Nucl. Mater.* 4 (1961) 226-233.
- [60] D.E. Burkes, T. Hartmann, R. Prabhakaran, J.F. Jue, Microstructural characteristics of DU-xMo alloys with x= 7-12 wt%, *J. Alloys Compd.* 479 (2009) 140-147.
- [61] V. Sinha, P. Hegde, G. Prasad, G. Dey, H. Kamath, Effect of molybdenum addition on metastability of cubic γ -uranium, *J. Alloys Compd.* 491 (2010) 753-760.
- [62] V. Sinha, P. Hegde, G. Prasad, G. Dey, H. Kamath, Phase transformation of metastable cubic γ -phase in U-Mo alloys, *J. Alloys Compd.* 506 (2010) 253-262.

- [63] N.-T. Kim-Ngan, I. Tkach, S. Maškova, A. Goncalves, L. Havela, Study of decomposition and stabilization of splat-cooled cubic γ -phase U–Mo alloys, *J. Alloys Compd.* 580 (2013) 223-231.
- [64] S. Neogy, M. Saify, S. Jha, D. Srivastava, M. Hussain, G. Dey, R. Singh, Microstructural study of gamma phase stability in U–9 wt.% Mo alloy, *J. Nucl. Mater.* 422 (2012) 77-85.
- [65] S. Neogy, M. Saify, S. Jha, D. Srivastava, G. Dey, Ageing characteristics of the metastable gamma phase in U–9 wt.% Mo alloy: experimental observations and thermodynamic validation, *Philosophical Magazine* 95(26) (2015) 2866-2884.
- [66] T.A. Pedrosa, A.M.M. dos Santos, F.S. Lameiras, P.R. Cetlin, W.B. Ferraz, Phase transitions during artificial ageing of segregated as-cast U–Mo alloys, *J. Nucl. Mater.* 457 (2015) 100-117.
- [67] S. Jana, N. Overman, T. Varga, C. Lavender, V.V. Joshi, Phase transformation kinetics in rolled U-10 wt.% Mo foil: Effect of post-rolling heat treatment and prior γ -UMo grain size, *J. Nucl. Mater.* 496 (2017) 215-226.
- [68] S. Jana, A. Devaraj, L. Kovarik, B. Arey, L. Sweet, T. Varga, C. Lavender, V. Joshi, Kinetics of cellular transformation and competing precipitation mechanisms during sub-eutectoid annealing of U10Mo alloys, *J. Alloys Compd.* 723 (2017) 757-771.
- [69] J.-S. Lee, C.-H. Lee, K.H. Kim, V. Em, Neutron diffraction study of U–5.4 wt% Mo alloy, *J. Nucl. Mater.* 280 (2000) 116-119.
- [70] B.-S. Seong, C.-H. Lee, J.-S. Lee, H.-S. Shim, J.-H. Lee, K.H. Kim, C.K. Kim, V. Em, Neutron diffraction study of U–10 wt% Mo alloy, *J. Nucl. Mater.* 277 (2000) 274-279.
- [71] N.W.S. Morais, M.A. Tunes, V.O.d. Santos, C.G. Schon, R.G. Gomide, Influence of Zr, Mo, and Nb on microstructure of ternary uranium alloys, September 2015.

- [72] J. Fackelmann, A. Bauer, D. Moak, LITERATURE SURVEY ON DILUTE URANIUM ALLOYS FOR SANDIA BOOSTER CONCEPT TO SANDIA CORPORATION, Battelle Memorial Inst., Columbus, Ohio, 1969.
- [73] S. Balakrishnan, K. Ananthasivan, K.H. Kumar, Measurement of the Solidus and Liquidus in the U-Zr System by the Spot-Technique, *J. Alloys Compd.* 689 (2016) 751-758.
- [74] H.A. Saller, R.F. Dickerson, W.E. Murr, Uranium Alloys for High-Temperature Application, Battelle Memorial Inst., Columbus, Ohio, 1956.
- [75] G. Fedorov, E. Smirnov, Heat capacity of uranium-zirconium systems, *Soviet Atomic Energy* 25(1) (1968) 795-797.
- [76] Y. Takahashi, K. Yamamoto, T. Ohsato, H. Shimada, T. Terai, M. Yamawaki, Heat capacities of uranium-zirconium alloys from 300 to 1100 K, *J. Nucl. Mater.* 167 (1989) 147-151.
- [77] T. Matsui, T. Natsume, K. Naito, Heat capacity measurements of U_{0.80}Zr_{0.20} and U_{0.80}Mo_{0.20} alloys from room temperature to 1300 K, *J. Nucl. Mater.* 167 (1989) 152-159.
- [78] S. Dash, K. Ghoshal, T. Kutty, Thermodynamic investigations of uranium-rich binary and ternary alloys, *J. Therm. Anal. Calorim.* 112 (2013) 179-185.
- [79] S.C. Parida, S. Dash, Z. Singh, R. Prasad, V. Venugopal, Thermodynamic studies on uranium–molybdenum alloys, *J. Phys. Chem. Solids* 62 (2001) 585-597.
- [80] R. Klueh, A.T. Nelson, Ferritic/martensitic steels for next-generation reactors, *J. Nucl. Mater.* 371 (2007) 37-52.
- [81] R. Klueh, Elevated temperature ferritic and martensitic steels and their application to future nuclear reactors, *International Materials Reviews* 50(5) (2005) 287-310.
- [82] S. Kaity, M. Nair, A. Sengupta, A. Kumar, Transient plane source technique for measurement of thermal conductivity of U and T91 for fast reactor application, *Proc. of THERMANS 2010*, Kurukshetra University, 2010, pp. 144-146.

- [83] G. Roux, R. Billardon, Identification of thermal boundary conditions and thermo-metallurgical behaviour of X10CrMoVNb9-1 steel during simple tig welding tests, 2006.
- [84] L. Leibowitz, R. Blomquist, Thermal conductivity and thermal expansion of stainless steels D9 and HT9, *International journal of thermophysics* 9(5) (1988) 873-883.
- [85] D.D. Keiser Jr., M.A. Dayananda, Interdiffusion between U-Zr fuel and selected Fe-Ni-Cr alloys, *J. Nucl. Mater.* 200 (1993) 229-243.
- [86] A.B. Cohen, H. Tsai, L.A. Neimark, Fuel/cladding compatibility in U-19Pu-10Zr/HT9-clad fuel at elevated temperatures, *J. Nucl. Mater.* 204 (1993) 244-251.
- [87] T.R.G. Kutty, S.K. Rakshit, A. Laik, A. Kumar, H.S. Kamath, C.B. Basak, Studies of the reaction between metal fuels and T91 cladding, *J. Nucl. Mater.* 412 (2011) 53-61.
- [88] T. Ogata, M. Kurata, K. Nakamura, A. Itoh, M. Akabori, Reactions between U-Zr alloys and Fe at 923 K, *J. Nucl. Mater.* 250 (1997) 171-175.
- [89] K. Nakamura, T. Ogata, M. Kurata, A. Itoh, M. Akabori, Reactions of U-Zr alloy with Fe and Fe-Cr alloy, *J. Nucl. Mater.* 275 (1999) 246-254.
- [90] Y. Park, K. Huang, A. Paz Y Puente, H.S. Lee, B.H. Sencer, J.R. Kennedy, Y.H. Sohn, Diffusional Interaction Between U-10 wt pct Zr and Fe at 903 K, 923 K, and 953 K (630° C, 650° C, and 680° C), *Metallurgical and Materials Transactions A* 46A(1) (2015) 72-82.
- [91] D.D. Keiser Jr., M.A. Dayananda, Interdiffusion between U-Zr fuel vs selected cladding steels, *Metallurgical and Materials Transactions A* 25A(8) (1994) 1649-1653.
- [92] D.D. Keiser Jr., M.C. Petri, Interdiffusion behavior in U-Pu-Zr fuel versus stainless steel couples, *J. Nucl. Mater.* 240 (1996) 51-61.
- [93] C.T. Lee, H. Kim, T.K. Kim, C.B. Lee, Diffusion behavior in an interface between U-10Zr alloy and HT-9 steel, *J. Nucl. Mater.* 395 (2009) 140-144.
- [94] H.J. Ryu, B.O. Lee, S.J. Oh, J.H. Kim, C.B. Lee, Performance of FCCI barrier foils for U-Zr-X metallic fuel, *J. Nucl. Mater.* 392 (2009) 206-212.

- [95] J.H. Kim, H.J. Ryu, J.H. Baek, S.J. Oh, B.O. Lee, C.B. Lee, Y.S. Yoon, Performance of a diffusion barrier under a fuel-clad chemical interaction (FCCI), *J. Nucl. Mater.* 394 (2009) 144-150.
- [96] S.W. Yang, H.J. Ryu, J.H. Kim, B.O. Lee, C.B. Lee, FCCI barrier performance of electroplated Cr for metallic fuel, *J. Nucl. Mater.* 401 (2010) 98-103.
- [97] B.D. Cullity, *Elements of X-ray Diffraction*, Addison-Wesley Publishing, 1956.
- [98] A.R. West, *Solid state chemistry and its applications*, John Wiley & Sons, 2014.
- [99] L. Lutterotti, MAUD, *Material Analysis using Diffraction*, Copyright (c) 2008 (1997).
- [100] M.E. Brown, *Introduction to thermal analysis: techniques and applications*, Springer Science & Business Media 2001.
- [101] G. Revankar, *Introduction to Hardness Testing*, Materials Park, OH: ASM International, 2000. (2000) 197-202.
- [102] M. Akabori, A. Itoh, T. Ogawa, F. Kobayashi, Y. Suzuki, Stability and structure of the δ phase of the U-Zr alloys, *J. Nucl. Mater.* 188 (1992) 249-254.
- [103] S. Irukuvarghula, S.M. McDeavitt, Formation mechanism of delta phase in the as-cast U-10wt% Zr alloy, *Transactions of the American Nuclear Society*, Washington, D.C. 109 (2013) 612-615.
- [104] K. Eckelmeyer, The effects of heat treatment on the microstructure and mechanical behavior of U-0.75 wt.% Mo-0.75 wt.% Nb-0.75 wt.% Zr-0.50 wt.% Ti, *J. Nucl. Mater.* 68 (1977) 92-99.
- [105] E. Dabush, J. Sarel, I. Dahan, G. Kimmel, XRD peak broadening effects in U-Mo α phase, *Adv. X Ray Anal.* 45 (2002) 146-151.
- [106] L. Leibowitz, E. Veleckis, R. Blomquist, A. Pelton, Solidus and liquidus temperatures in the uranium-plutonium-zirconium system, *J. Nucl. Mater.* 154 (1988) 145-153.

- [107] I. Barin, P. Gregor, Thermochemical data of pure substances. 3rd, Edition, VCH (1995).
- [108] D.A. Lopes, A.J. de Oliveira Zimmermann, T.A.G. Restivo, A.F. Padilha, Hardness Response Surface for U-7.5 Nb-2.5 Zr Alloy: A Study of Recovery/Recrystallization and Phase Transformation Interactions, Metallurgical and Materials Transactions E 2(3) (2015) 147-156.
- [109] B. Howlett, A study of the shear transformations from the gamma-phase in uranium-molybdenum alloys containing 6.0–12.5 at% molybdenum, J. Nucl. Mater. 35 (1970) 278-292.
- [110] A.E. Dwight, The uranium-molybdenum equilibrium diagram below 900 C, J. Nucl. Mater. 2 (1960) 81-87.
- [111] X. Zhang, Y. Cui, G. Xu, W. Zhu, H. Liu, B. Yin, Z. Jin, Thermodynamic assessment of the U–Mo–Al system, J. Nucl. Mater. 402 (2010) 15-24.
- [112] A. Berche, N. Dupin, C. Guéneau, C. Rado, B. Sundman, J. Dumas, Calphad thermodynamic description of some binary systems involving U, J. Nucl. Mater. 411 (2011) 131-143.
- [113] M. Waldron, R. Burnett, S. Pugh, The mechanical properties of Uranium-Molybdenum alloys, United Kingdom Atomic Energy Authority, Research Group, Atomic Energy Research Establishment, Harwell, Berkshire, 1958.
- [114] O. Ivanov, G. Bagrov, Isothermal Cross Sections at 600 C, 575 C, and 500 C, Polythermal Sections, and the Phase Diagram of the Triple System Uranium-Molybdenum-Zirconium, Struct. Alloys Certain Syst. Cont. Uranium Thorium (1963) 154-176.
- [115] P. Repas, R. Goodenow, R. Hehemann, Transformation characteristics of three Uranium base alloys, The Department of Metallurgy Case Institute of Technology, Cleveland, OH (1963).

- [116] M. Saify, S. Jha, K. Abdulla, A. Kumar, G. Prasad, Fabrication of Metallic Fuel Slugs for Irradiation Experiments in Fast Breeder Test Reactor, (2013).
- [117] E. Beahm, C. Culpepper, O. Cavin, Laves phases of uranium and 3d transition metals, *Journal of the Less Common Metals* 50(1) (1976) 57-71.
- [118] O. Fabrichnaya, Iron–Uranium–Zirconium, in: G. Effenberg, S. Ilyenko (Eds.), Vol. 11, Ternary Alloy Systems Phase Diagrams, Crystallographic and Thermodynamic Data, Subvolume C, Non-Ferrous Metal Systems, Springer Berlin Heidelberg, New York, 2007, pp. 320-327.
- [119] A.J. Schwartz, M. Kumar, B.L. Adams, D.P. Field, *Electron backscatter diffraction in materials science*, Second ed., Springer 2000.
- [120] H. Okamoto, Fe-U (Iron-Uranium), *Phase Diagrams of Binary Iron Alloys* (1993) 429-432.
- [121] P. Gardie, G. Bordier, J. Poupeau, J. Le Ny, Thermodynamic activity measurements of U-Fe and U-Ga alloys by mass spectrometry, *J. Nucl. Mater.* 189 (1992) 85-96.
- [122] K. Nakamura, M. Kurata, T. Ogata, A. Itoh, M. Akabori, Equilibrium phase relations in the U–Zr–Fe ternary system, *J. Nucl. Mater.* 275 (1999) 151-157.
- [123] Y. Adda, J. Philibert, H. Faraggi, Étude des phénomènes de diffusion intermétallique dans le système uranium-zirconium, *Revue de metallurgie* 54(8) (1957) 597-610.
- [124] G. Bozzolo, H. Mosca, A. Yacout, G. Hofman, Y. Kim, Surface properties, thermal expansion, and segregation in the U–Zr solid solution, *Computational Materials Science* 50(2) (2010) 447-453.
- [125] G. Bozzolo, H. Mosca, A. Yacout, G. Hofman, Atomistic modeling of the interaction of cladding elements (Fe, Ni, Cr) with U–Zr fuel, *J. Nucl. Mater.* 414 (2011) 101-108.

- [126] M. Paukov, I. Tkach, F. Huber, T. Gouder, M. Cieslar, D. Drozdenko, P. Minarik, L. Havela, U-Zr alloy: XPS and TEM study of surface passivation, *Applied Surface Science* 441 (2018) 113-119.
- [127] D. Arias, J. Abriata, The Fe– Zr (Iron-Zirconium) system, *Bulletin of Alloy Phase Diagrams* 9(5) (1988) 597-604.
- [128] K. Bhanumurthy, G. Kale, S. Khera, Reaction diffusion in the zirconium-iron system, *J. Nucl. Mater.* 185 (1991) 208-213.
- [129] C. Matthews, C. Unal, J. Galloway, D.D. Keiser Jr, S.L. Hayes, Fuel-Cladding Chemical Interaction in U-Pu-Zr Metallic Fuels: A Critical Review, *Nuclear Technology* 198 (2017) 231-259.
- [130] H.J. Ryu, S.J. Oh, C.T. Lee, K.H. Kim, Y.M. Ko, Y.M. Woo, S.H. Kim, C.H. Hahn, B.O. Lee, C.B. Lee, Fuel-Cladding Chemical Interaction between U-Zr-X Metallic Fuel and Ferritic Martensitic Steels, *Transactions of the Korean Nuclear Society Autumn Meeting* (2007) 245-246.
- [131] K. Huang, Y. Park, L. Zhou, K. Coffey, Y. Sohn, B. Sencer, J. Kennedy, Effects of Cr and Ni on interdiffusion and reaction between U and Fe–Cr–Ni alloys, *J. Nucl. Mater.* 451 (2014) 372-378.

Thesis Highlight

Name of the Student: Santu Kaity

Name of the CI/OCC: BARC, Mumbai

Enrolment No.: CHEM01201604002

Thesis Title: Investigation of physico-chemical properties of fast reactor metallic fuels

Discipline: Chemical Sciences

Sub-Area of Discipline: Nuclear materials

Date of viva voce: 04-06-2021

Metallic fuels based on U–Zr alloys are recognized as promising candidate fuels for fast breeder reactors (FBRs). Metallic fuels with relatively low Zr (~6 wt%) is preferred for achieving higher breeding ratio. The properties of U–Zr alloys can be refined with addition of Nb or Mo due to their various attractive features. In this study, the potential metallic fuel systems, namely, binary U–Zr, U–Nb, U–Mo and ternary U–Zr–Nb, U–Zr–Mo alloys with total alloying content limiting to 6wt% have been investigated for their phase stability, phase transformation, microstructure evolution and thermo-physical properties.

The phase stability of alloys revealed significant variation in crystal structures, lattice parameters, microstructures depending on heat treatment and compositions. The furnace-cooled alloys are far from their equilibrium phase compositions. The water quenching leads to formation of various non-equilibrium phases like distorted orthorhombic, monoclinic via martensitic transformation. Mo has better γ -stabilization power compared to Zr or Nb. The step-cooling of the alloys under near-equilibrium condition leads to the formation of various equilibrium phases i.e., δ -U₂Zr₂, γ -U₂Mo and Mo₂Zr. The ZrMo₂ phase formation is undesirable as it may reduce solute content in the bcc γ phase. The replacement of Zr in U–6Zr alloy with Nb, increases the solidus temperatures whereas, replacement of Zr by Mo decreases the solidus temperatures. Hence, Mo addition is not suitable for increasing melting temperature of fuel. The replacement of Zr in U–6Zr alloy with equivalent amount of Nb or Mo leads to decrease in molar heat capacity value. The lower molar heat capacity will offer an added advantage of less amount of stored energy in the fuel. The replacement of Zr with Nb or Mo decreases the overall thermal expansion. Fuel-cladding chemical interaction (FCCI) between U–Zr fuel and T91 steel cladding leads to formation of Zr-depleted, Zr-rich and UFe₂-type layers at the interface. Their compatibility seems to be good at reactor operating temperature. However, if the interfacial temperature reaches above eutectic liquefaction temperature (995 K), U–Zr fuel will no longer remain compatible with T91.

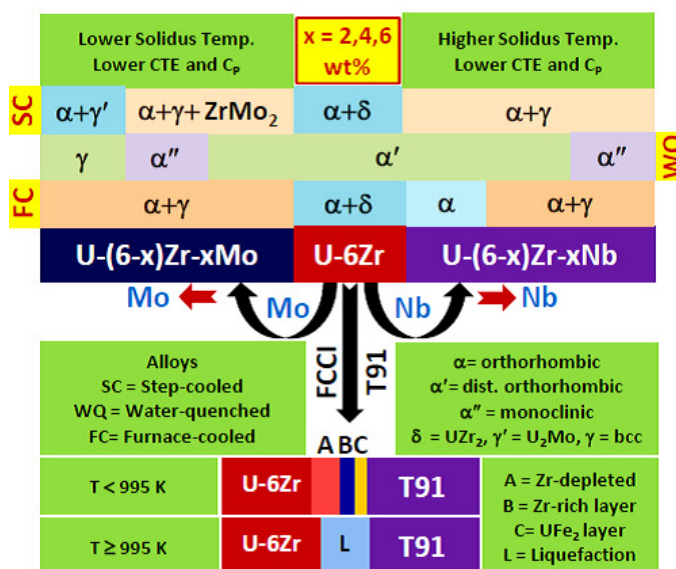


Figure 1. Phase relations, thermo-physical properties and fuel-cladding chemical interaction of U–6Zr based metallic fuel